MULTISCALE MODELING AND SIMULATION OF CLUTTER IN ISAR IMAGING

Dissertation

Jon Mitchell

University of Texas at Arlington
May 2020

ABSTRACT

Clutter is common in applications of radar imaging and can adversely impact target imaging by contributing scattered energy that is not accounted for in target signal models. One potential source of clutter is moving foliage in the vicinity of the target, such as a target embedded in a forest. ISAR imaging of moving clutter results in an equivalent current image that changes over each imaging sample. The stochastic nature of this clutter equivalent current presents challenges in detecting and imaging a weak embedded target using traditional algorithms. This dissertation proposes a multiscale model and analysis method to characterize the multiscale statistical properties of the clutter equivalent current density. It is hypothesized that clutter scattering phenomenon is related to vegetation structure, and the resulting multiscale properties of the projected clutter equivalent current can be modeled and analyzed to reveal these clutter scattering characteristics. Simulation methods are proposed which use these multiscale characteristics to generate additional representative samples of the ISAR clutter equivalent current. The proposed analysis and simulation methods are validated using known simulation data and applied to physical clutter ISAR measurements. Simulation fidelity of the two proposed simulation methods is evaluated with image similarity measures. Hypotheses relating multiscale characteristics of the multiscale model to scattering phenomenon are proposed and tested. Finally, applications for analysis and simulation are presented, demonstrating the value of the proposed methods in a variety of real problems.

ACKNOWLEDGEMENTS

I would like to thank my research advisor Dr. Saibun Tjuatja for his guidance throughout this journey; my wife Angela for her infinite patience and support; my children Aiden, Evan, and Owen for believing in me; my research advisory committee for their time and support; and David J. English, Robert Brakemeier, and Felix Vasquez for their encouragement.

CONTENTS

Abstract i
Acknowledgements ii
1 Introduction 1
  1.1 Related State of the Art Material 1
    1.1.1 ISAR Imaging 2
    1.1.2 Clutter Suppression and Target Detection in Radar Applications 3
    1.1.3 Research in Foliage and Vegetation Clutter 5
    1.1.4 Deep Learning for ISAR and Radar Imaging 5
  1.2 Proposed Clutter Model, Analysis, and Simulation 8
    1.2.1 ISAR Clutter Model 8
    1.2.2 Multiscale Analysis of ISAR Clutter 8
    1.2.3 Simulation of ISAR Clutter 9
  1.3 Dissertation Organization and Approach 10
2 Background Material 12
  2.1 Electromagnetic Scattering and Equivalent Sources 12
    2.1.1 Electromagnetic Scattering 12
    2.1.2 Scattered Field in the Far Zone 13
    2.1.3 Equivalent Sources 15
  2.2 ISAR Imaging 16
    2.2.1 Two-Dimensional ISAR Imaging 16
    2.2.2 Complex ISAR Image and Clutter Equivalent Current 17
    2.2.3 Relationship to Fourier Transform 19
  2.3 ISAR Measurement Setup and Calibration 20
    2.3.1 ISAR Measurement Setup 20
    2.3.2 Sphere Calibration 21
    2.3.3 Calibration Verification 23
    2.3.4 ISAR Measurement Test Articles 24
  2.4 Multiscale Analysis of Complex Stochastic Systems 26
    2.4.1 Multiscale Wavelet Analysis 26
  2.5 Image Similarity Measures 27
    2.5.1 Similarity Measures Introduction and History 27
    2.5.2 Image Similarity Measures 28
3 Multiscale Modeling and Analysis of ISAR Clutter 30

3.1 Multiscale Clutter Model Order 30
3.2 Model Order Validation 30
3.3 Estimation of Multiscale Model Parameters 32
  3.3.1 Multiscale Notation 32
  3.3.1 Multiscale Correlation and Covariance Estimation 32
  3.3.2 Multiscale Covariance vs Correlation 39
3.4 Validation of Multiscale Model Parameter Estimation Method 40
4 Numerical Simulation of ISAR Clutter 45
4.1 Simulation of ISAR Clutter Using Multiscale Model Parameters 45
4.2 Simulation Method 1 – Exponential Correlating Filter 45
  4.2.1 Estimation of Exponential Correlating filter Shape Parameters 45
  4.2.2 Validation of Method 1 Shape Parameter Estimation 49
  4.2.3 Application of Two-Dimensional Exponential Correlating filter 50
  4.2.4 Negative Correlation 51
4.3 Simulation Method 2 – Non-Exponential Correlating filter 52
  4.3.1 Estimation of Correlating Filter Shape Parameters 56
  4.3.2 Validation of Method 2 Shape Parameter Estimation 57
4.4 Experimental Validation of ISAR Clutter Simulation Methods 64
  4.4.1 Simulation of General Correlated Data 64
  4.4.2 Simulation of Physical ISAR Measurements 67
  4.4.3 Similarity Measure Analysis and Conclusions 70
5 Applications for Multiscale Analysis and Simulation 71
5.1 Multiscale Analysis of Scattering Phenomenon in Vegetation Clutter 71
  5.1.1 Multiscale Analysis Hypotheses 71
  5.1.2 Testing Hypothesis 1 – Variance Increases with Motion and Leaf Size 73
  5.1.3 Testing Hypothesis 2 – Correlation Decreases with Pixel Separation 78
  5.1.4 Testing Hypothesis 3 - Correlation Decreases as Decomposition Level Increases. 80
  5.1.5 Testing Hypothesis 4 - Correlation Decreases with Increased Clutter Motion 81
5.2 Multiscale Analysis of Global Ocean Current Data 83
5.3 Deep Learning Convolutional Network Applications for ISAR Clutter 89
  5.3.1 Introduction 89
  5.3.2 Deep Learning Application 1 – Clutter Classification 89
  5.3.3 Sample Mean 93
  5.3.4 Sample Variance 94
  5.3.5 Results for Zero-Mean Measured Clutter Classification 96
  5.3.6 Network Prediction Accuracies on Zero-Mean Clutter Measured Data 96

5.3.7 Results for Zero-Mean, Unit Variance Measured Clutter Classification 98
5.3.8 Deep Learning Application 2 –Target Location 100
5.3.9 Results for Constant Target Location Application 105

6 Conclusions 108

6.1 Multiscale ISAR Clutter Model 108
6.2 Multiscale ISAR Clutter Analysis 108
6.3 Simulation of ISAR Clutter 110
6.4 Relationship of Multiscale Analysis to Scattering and Clutter Structure 112

7 Bibliography 113
Appendix A: Multiscale Analysis of Measured ISAR Clutter 123

Multiscale Components by Plant 124
Multiscale Analysis by Component and Level with Histograms 127

Appendix B: Similarity Plots and Histograms for Generated Samples of Simulated Data......... 132

Samples of Simulated Data Generated with Exponential Correlating function 132
Similarity Metrics Between Samples of Simulated Data with Exponential Correlating function and Generated Samples 139
Samples of Simulated Data Generated with Non-Exponential Correlating function 140
Similarity Metrics Between Samples of Simulated Data with Non-Exponential Correlating function and Generated Samples 147

Appendix C: Similarity Plots for Generated Samples of Measured Data 148

Simulation of Measured Data – Plant D, Light Wind 148
Similarity Metrics for Simulation of Measured Data – Plant D, Light Wind 155
Simulation of Measured Data – Plant D, Medium Wind 156
Similarity Metrics for Simulated Measured Data – Plant D, Medium Wind 163
Simulated Measured Data – Plant E, Light Wind 164
Similarity Metrics for Simulated Measured Data – Plant E, Light Wind 171
Simulation of Measured Data – Plant E, Medium Wind 172
Similarity Metrics for Simulated Measured Data – Plant E, Medium Wind 179

1 INTRODUCTION

Inverse synthetic aperture radar (ISAR) imaging is an active remote sensing technique that estimates spatial locations of concentrated target scattering from the measured backscattered electromagnetic field. When an incident wave hits the target, a current density is excited in the target volume which results in a total radiated field. Inverse techniques are used to find a target equivalent current density that will produce the measured scattered field. The scattered field from a target volume is unique but the equivalent current that produces a measured scattered field is not unique. Many ISAR imaging methods make assumptions about the target to decrease the complexity of the inverse problem. These assumptions and simplifications result in less complex solutions, but may not account for nonlinear interactions and higher-order scattering within the target, resulting in unintended artifacts in the ISAR image [1] [2].

Clutter is present in most radar images due to the presence of non-target scatterers in the vicinity of the target. Mitigation or removal of clutter is one of the primary challenges in target imaging and detection. One possible source of clutter in ISAR imaging is vegetation. Wind causes spatial motion in vegetation, resulting in a backscattered field that changes over image samples. In some applications where the clutter is very strong relative to the target, such as a target embedded in vegetation, the clutter can make detection or imaging of the target difficult. Removal or mitigation of the contributions of scattering from moving vegetation is needed in this case [3]. Multiple scattering and nonlinear interactions within the clutter cause simple scattering models to break down and presents a significant challenge to accurate imaging. This dissertation will show that the estimated two-dimensional projection of the clutter equivalent current in the imaging plane can be estimated by a second-order multiscale model whose parameters are estimated by a proposed multiscale analysis method. This model can then be used to generate additional representative samples that aid in ISAR imaging of targets embedded in clutter and provide representative training data for deep learning applications.

1.1 RELATED STATE OF THE ART MATERIAL

The latest research in topics related to this dissertation are reviewed here with a focus on general ISAR imaging, clutter suppression and target detection in radar applications, research into foliage and vegetation clutter, and deep learning for radar imaging. The intent here is to show that the approaches in this dissertation are novel and applicable to a wide range of ongoing research. Deep learning is being increasingly used to solve complex ISAR and clutter suppression problems and in almost all deep learning applications, performance is based on the availability of representative training data.

1.1.1 ISAR Imaging

ISAR is a broad field and it is appropriate to first discuss what is considered outside the scope of this dissertation and will not be discussed in the areas of modern ISAR research. A significant amount of research in the area of target autofocus and prediction of the motion of uncooperative ISAR targets has occurred in the last few years and this is beyond the scope of this dissertation. This dissertation will be focused on the specific case of monostatic ISAR, where the transmit and receive antennas are co-located, although some of the contributions in this dissertation can be applied to the bistatic case or multiple-input multiple-output (MIMO) measurement scenarios. Interferometric techniques have been a popular area of research for ISAR. This involves use of the interferometric combination of multiple ISAR images to increase the imaging dimension. For the latest applicable research, we will focus on recent research related to imaging techniques using monostatic ISAR of cooperative targets. Generally, this scope covers super-resolution imaging techniques, sparse apertures and imaging methods that use compressive sensing (CS) techniques, and deep learning for ISAR.

1.1.1.1 Super-Resolution ISAR Imaging

ISAR imaging is based on Fourier theory, which leads to the conclusion that spatial resolutions are limited by the received signal bandwidth and coherent processing interval (CPI). Due to the Fourier relationship between signal phase and spatial range, it can be shown that the range is inversely proportional to the signal bandwidth [4]. Similarly, cross range is inversely proportional to the CPI [5]. Super-resolution research is well established and has made other advancements in ISAR imaging possible. Here we discuss super-resolution ISAR imaging as a segue into compressive sensing (CS) techniques. The original direct Fourier inversion methods for focusing scatterer Doppler histories resulted in resolution limitations in ISAR imaging. Super-resolution techniques for ISAR imaging can be traced back to work by Ralph Schmidt in 1986 [6]. Here it was proposed that the backscattered signal from a collection of point scatterers could be separated into signal and noise subspaces. Schmidt showed that the signal and noise subspaces are orthogonal and scattering center locations can be parametrically estimated by exploiting this orthogonal relationship. This technique is referred to as “super-resolution” imaging because it results in much higher resolution over standard inverse Fourier focusing techniques, which are limited by the number of measurements. This was extended to the three-dimensional case and eventually led to three-dimensional ISAR measurements of a fir tree presented by Fortuny and Sieber in 1999 [7]. Many techniques have been developed to move past the Fourier resolution limitation. These can be grouped into two main categories: *point source* and *distributed-source* techniques [8].

Point-source techniques operate under the assumption that the target can be modeled as a collection of individual point scatterers, and these techniques seek to estimate their amplitude and position. This assumption is valid for targets that have a limited number of major scattering centers but is not effective in cases where the target is very distributed with complex scattering mechanisms. Additionally, point-source techniques generally require *a priori* knowledge of the number of scattering centers. Point-source super-resolution techniques include MUSIC [9], ESPRIT [10], CLEAN [11], RELAX [12], and bandwidth extrapolation techniques [13].

Distributed-source techniques assume that the spatial scene is a continuous function sampled on a regular grid and filtered by a point spread function (PSF). Distributed-source techniques include deconvolution and spectral estimation. Deconvolution techniques seek to invert the PSF and estimate the high-resolution target reflectivity function and include minimum mean-squared error (MMSE) [14] and singular value decomposition (SVD) [15]. Spectral estimation techniques seek to estimate the parameters of multiple sinusoids that correspond to single scatterers and include Capon's minimum variance method (MVM) [16], the amplitude and phase estimation of a sinusoid (APES) [17], and super-spatially variant apodization (SSVA) [18].

In addition to these methods, compressive sensing (CS) has been a very popular area of research in multi-dimensional radar imaging. CS depends on the fact that the spatial ISAR image is a sparse representation of the measured ISAR data in the Fourier domain. The Fourier transform satisfies the restrictive isometry property (RIP) [19] and serves as a basis for the signal representation [8]. Major contributions to the application of CS to radar imaging include [19] and [20]. The application of CS to ISAR imaging is straight-forward, but a significant amount of recent research exists over a variety of topics. Many of these topics are applying CS to more specific radar imaging applications. In [21], Kang et al apply CS techniques to bistatic ISAR imaging, while simultaneously performing translational and rotational motion compensation, and bistatic distortion compensation. Other recent research involves improvements in optimization algorithms [22] [23], waveform design and optimization [24] [25], and application to specific radar systems. Comparison of CS with other super-resolution imaging techniques concludes that CS can exceed the performance of super-resolution techniques in most applications [8].

1.1.2 Clutter Suppression and Target Detection in Radar Applications

Most clutter suppression research for radar is focused on efficient target detection in the presence of heterogeneous clutter. As opposed to imaging, these applications are generally concerned with target detection. Target detection algorithms use estimated clutter statistics to determine when a target is present. The suppression of clutter can be more difficult than noise because noise generally has a Gaussian distribution, where clutter does not. Target detection in sea clutter is a particularly difficult problem due to the nature of scattering from ocean waves. A significant amount of research has been concentrated on modeling ocean clutter in different sea states.

In 2013, Jean-François Degurse et al discuss the need for representative clutter data with no target present in using maximum likelihood estimation methods. In this case, the known target information is removed from the covariance matrix using the APES algorithm, which also removes some of the clutter, resulting in degraded clutter suppression. Two new algorithms are proposed that use deterministic-aided space-time adaptive processing (STAP) to overcome this limitation. It is shown that this is an improvement over the current methods in detection and clutter rejection [26].

X. Zhang et al propose methods for improving high frequency surface wave radar (HFSWR), which is a method for ocean environment monitoring, target detection, and target tracking over the horizon. The challenge in this application is overcoming non-homogeneous ionospheric clutter. A new algorithm is proposed based on correlation between target and clutter in the measured data. This also involves a strategy for training data selection and demonstrates improved detection of weak targets in nonhomogeneous ionospheric clutter [27].

In 2016, Zaimbashi investigates target detection in clutter using clutter whitening and an adaptive clutter detector that estimates clutter parameters from the sample covariance matrix. Subspace-based and covariance matrix-based detectors are investigated for a mono-static radar system. Simulations show that the subspace-based detector generally outperforms the sample covariance matrix detector [28].

In 2017, Sai Guo et al investigate the feasibility of applying a deep learning approach to sea clutter suppression and target detection in an inhomogeneous oceanic environment. Deep convolutional auto-encoders are used to learn and filter sea clutter and detect the target. The use of deep learning allows the removal of complex clutter patterns and does not require estimation of the clutter covariance matrix. Clutter suppression performance is demonstrated with simulated and measured data [29]. This group continues to research deep convolutional techniques for radar applications [30].

In 2018, Ling Zhang et al use region-based convolutional neural networks (R-CNN) to separate target and clutter is HFSWR using target and clutter features. Field experimental results show that the Faster R-CNN based method can automatically detect the clutter and interference with decent performance and classify them with high accuracy [31].

In 2019, Jun Liu et al address the problem of target detection in multiple-input, multiple output (MIMO) radar when the clutter covariance matrix is unknown. By exploiting the Toeplitz or persymmetric structure of the clutter covariance matrix, adaptive detectors are employed that do not require training data. Analytical expressions for the probability of false alarm and detection probability are derived for the proposed detector that takes the persymmetry into account. Numerical examples are provided to show that the proposed detectors outperform the conventional counterparts [32].

1.1.3 Research in Foliage and Vegetation Clutter

Some recent research has been dedicated specifically to vegetation clutter and clutter in windblown environments. See references [33] [34] [35] for research into clutter in windblown environments. These are generally focused on measuring the second-order RCS statistics and characteristics of the radar return from windblown grass and forestation.

In 2017, Paula Gómez-Pérez et al use S-Band and C-Band radar measurements to characterize the attenuations provided by vegetation environments [36]. The paper measures forest attenuation from different types trees and quantifies degradation of target detection over a range of frequencies.

Alessio Izzo et al present a multi-model approach for constant false alarm ratio (CFAR) detection of vehicles through foliage in foliage penetrating SAR images. This paper discusses the challenges of target detection in foliage due to non-target scatterers such as branches, trunks, and other foliage structures and that clutter modeling has been identified as a viable solution to mitigate tree and trunk detections. Physical and statistical models are combined, and performance is improved by considering both models simultaneously [37].

Raghu Raj et al present a novel hybrid computational electromagnetic (CEM) modeling framework for simulating the backscatter from forest clutter when sensed by UHF and VHF radars [38]. The approach uses a combination of physical optics and geometric optics to achieve superior fidelity in calculating the backscatter.

1.1.4 Deep Learning for ISAR and Radar Imaging

Deep learning techniques are being investigated for ISAR imaging due to the increased popularity of deep learning and two-dimensional convolution neural networks for machine vision. Both raw and processed ISAR measurement data can be considered two-dimensional complex-valued images, therefore the application of convolutional networks to the field of ISAR imaging is a natural progression. Wei and Chen [39] explore the use of deep learning for solving electromagnetic inverse problems. Although this is not a direct connection to ISAR imaging, it does represent a new line of applicable research and is novel in that deep learning is used to solve the complex inverse problem, not just recognition of features within processed images.

Most of the current research into deep learning techniques for radar imaging involves deep learning of pre-processed SAR or ISAR images. In other words, established ISAR imaging techniques are used to produce ISAR images, and deep learning is used for image interpretation including target recognition and classification in the image domain.

In 2009, Vicen Bueno et al study the use of conventional neural networks (CNNs) for sea clutter reduction and target enhancement in marine radar systems [40]. Experiments show that the use of non-linear neural networks shows promising results in clutter reduction.

In 2018, Carlos Bentes et al develop a convolutional neural network for maritime target detection and classification in TerraSAR-X high-resolution images. Presented results indicate that CNNs are efficient models to perform maritime target classification in SAR images, and the combination of different input resolutions in the CNN model improves its ability to derive features, increasing the overall classification score [41].

Albert Huizing et al improve the interpretation of CNN target classification by demonstrating, through the visualization of a saliency map, that a CNN can achieve a high classification score by using the similarity of the clutter in the SAR images in the training and test set. The saliency map is computed from the trained CNN with the Gradient-weighted Class Activation Mapping (Grad-CAM) technique. This paper also shows that by first segmenting the SAR image in target, shadow and clutter regions, and then only providing the target region of the SAR image to the CNN, the problem of clutter-influenced target classification can be mitigated at the expense of a small reduction in classification accuracy [42].

Feng Xu et al apply deep learning to automatic target recognition (ATR) in SAR images and demonstrate performance with measured data [43].

In 2018, Tiep H. Vu et al propose a Simultaneous Decomposition and Classification Network (SDCN) to alleviate noise inferences and enhance classification accuracy in classification of buried and obscured targets in ultra-wideband (UWB) ground-penetration SAR images. Current methods do not accurately represent nonlinear interactions and large training sets. The proposed method employs two jointly trained sub networks that perform denoising and classification. It is demonstrated that the joint method of denoising and classification is an improvement over other deep learning techniques [44].

Shi-Hao Yu et al propose a convolutional autoencoder that is applied to improve the performance on the half space radar high resolution range profile (HRRP) target recognition. This method is an improvement over conventional autoencoders and deep-belief networks. Performance with conventional methods results in a small improvement in accuracy [45].

Changyu Hu et al propose an ISAR imaging method that uses convolutional neural networks. This method involves using the Fourier transform of two-dimensional measurements as the input layer and the method is compared to range-doppler processing and compressive sensing imaging methods. The simulation results show good performance compared to other methods when using 25% of the measurements [46] [47].

Bin Xue et al, propose a new deep-learning-based ISAR object detection method called Deep ISAR Object Detection (DIOD). This paper states that one major problem is the lack of available annotated training data. This is mitigated with a weakly semi-supervised training method. The proposed method is testing using two real-world ISAR data sets and the proposed method outperforms existing state-of-the-art methods with higher accuracy and a shorter execution time [48].

In 2019, Sirui Tian et al discusses object classification in SAR imaging. This paper states that insufficient labeled training data is a major problem when applying deep learning to SAR object classification and proposes a multiscale deep learning network that learns features at multiple scales and combines them together to generate feature vectors for object classification. In addition, background clutter is suppressed by using an improved Lee Sigma (ILS) filter when computing the network cost function. MSTAR data sets demonstrate that the model can adaptively learn features from raw SAR data [49].

Wilmanski et al investigate the use of deep learning for classification of organic clutter contamination in outdoor RCS measurements [50]. Deep learning networks are used to identify and remove unwanted organic clutter sources. The paper states that such techniques require enormous training datasets. Data augmentation is used due to the low number of physical measurements to be used for training, but the lack of representative training data is a limitation to network performance.

Meiyan Pan et al propose a novel approach for marine target detection using deep convolutional networks to extract sea clutter and target features [51]. The established object detection network known as Faster Region-based Convolutional Neural Network (Faster R-CNN) is used to detect targets in sea clutter with promising results.

Guanqing Li et al propose a new method for the detection of small boats in the presence of sea clutter using a time-frequency analysis and DenseNet [52]. Detection of small boats in sea clutter is challenging due to the overlap of target and clutter in the time and frequency domains. Measured data is used to validate the method and classification accuracy is improved over other classification networks.

In 2020, Huilin Mu et al apply deep learning to the ground moving target imaging (GMTIm) with SAR data in the presence of strong background clutter. Different from conventional imaging methods, the proposed method is directly trained to learn an implicit imaging model of multiple moving targets. Using simulations and experiments, it is shown that the proposed method achieves significant improvement over existing state-of-the-art GMTIm methods in terms of imaging quality and efficiency [53].

One common underlying theme that is stated in most of the listed articles is that available representative training data is required to train deep learning networks to solve complex problems. In many cases, training data is simulated due to lack of real-world data. In other cases, training sets are extended by rotating and translating available data. Application of deep learning techniques to complex radar imaging problems requires access to a significant amount of training data. However, in some cases, only a limited number of measurements are available. This dissertation will present a novel method for generating unlimited representative samples of ISAR clutter imagery of moving vegetation. With an unlimited number of training samples, deep learning networks can be used for classification, target detection, and other complex radar imaging tasks.

1.2 PROPOSED CLUTTER MODEL, ANALYSIS, AND SIMULATION

1.2.1 ISAR Clutter Model

A second-order multiscale model for ISAR clutter equivalent current projection is proposed. The proposed second-order model includes multiscale horizontal and vertical correlations across the ISAR clutter image. These correlations, estimated at each scale, provide an indication of the correlation between directionally oriented pixels. The clutter equivalent current projection is proportional to the tangential components of the local scattered field on the imaging plane. Therefore, each image pixel contains contributions of scattered energy from the entire clutter volume. It is hypothesized that the multiscale statistical characteristics of these image pixels are related to scattering phenomenon in the vegetation volume. Scattering from leaves and smaller areas within the clutter volume will be associated with directional ISAR image pixel correlations at a finer scale. However, scattering from larger branches will be associated with directional ISAR image pixel correlations from lower resolutions. This multiscale directional correlation allows for additional discrimination of clutter structure and increased fidelity of simulation.

1.2.2 Multiscale Analysis of ISAR Clutter

A multiscale analysis method for ISAR clutter is proposed where multiscale model parameters are estimated. The intended application is the analysis and simulation of vegetation clutter, where physical properties result in multiscale statistical characteristics of the equivalent current projection. The motion of small leaves may result in correlated equivalent currents at a finer resolution, whereas larger structures such as trunks and branches may result in equivalent current correlations at lower resolutions. The proposed method is computationally efficient and uses wavelet coefficient statistics to estimate the directional correlations and covariances of clutter ISAR image pixels, without requiring the calculation of the entire sample covariance matrix.

The proposed multiscale analysis method models the clutter equivalent current projection as multiple image samples over time, where pixels are modeled as multivariate random variables. Figure 1 illustrates how ISAR imaging Is used to estimate a target equivalent surface current density, and the stochastic characteristics of the image samples are analyzed using the proposed multiscale analysis method.

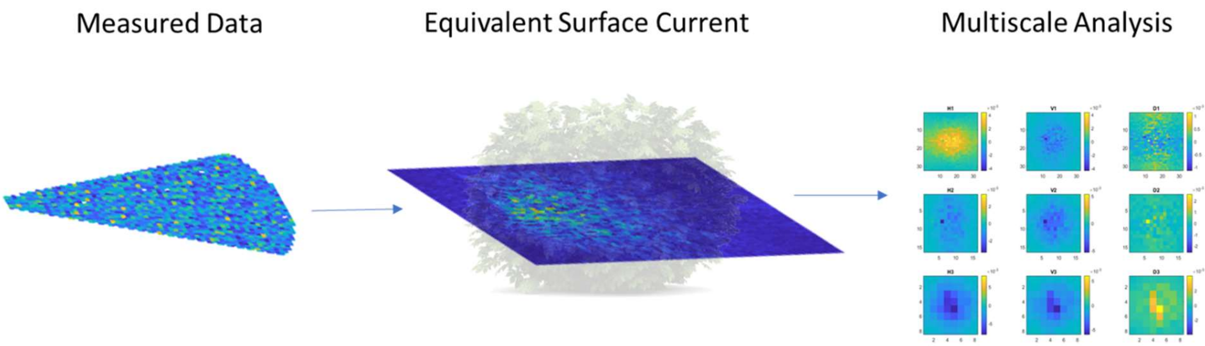

Figure 1: Multiscale Analysis of ISAR Clutter

1.2.3 Simulation of ISAR Clutter

Two methods are proposed for using multiscale characteristics to estimate the multiscale clutter model and simulate additional samples of data. The simulation methods are based on the hypothesis that the ISAR clutter equivalent current image can be modeled as the application of a two-dimensional directional correlating filter to uncorrelated random data. This expands on the work by Fung and Tjuatja and in [54], where scattering from a rough surface is modeled by parameterization of the surface roughness in a similar manner.

Two types of correlating filters are proposed and evaluated in this dissertation. Both are considered an attractive alternative to a full-covariance representation of the equivalent current because the proposed methods utilize multiscale characteristics estimated from the proposed analysis method, and therefore calculation of the full sample covariance matrix is not required. The dimensional reduction of the covariance matrix is considered a special case of this application and is based on the hypothesis that correlation between image pixels occurs over a finite range at some scale due to the physical structures in vegetation, and generally decreases over pixel distance. An example is that we may not expect the equivalent current projection related to individual leaf motion in one area of a tree to be correlated with individual leaf motion on the other side of the tree. However, equivalent currents from those areas may be correlated at some lower resolution scale due to all leaves moving together on a moving branch.

1.3 DISSERTATION ORGANIZATION AND APPROACH

A brief description of the major dissertation chapters is provided below.

1. Introduction

The dissertation topic is introduced, the problem and approach are presented, and the proposed contributions in the dissertation are summarized. The latest research in topics related to this dissertation are described and referenced.

2. Background Material

Electromagnetic Scattering and Equivalent Sources

Background material related to volume scattering of electromagnetic fields is reviewed, including far zone approximations. The concepts of equivalent volume and surface sources are presented. This background material explains how scattered fields from a three-dimensional volume can be represented by an equivalent surface current density.

ISAR Imaging of the 2D Projected Equivalent Current

An introduction to ISAR imaging theory and processing is provided. The Fourier-like relationship between the measured ISAR data in the k-space domain and surface equivalent current is explained.

Measurement Setup and Calibration of Physical Measurements

Measurement setup and calibration for physical measurements is described. Physical measurements used throughout the dissertation are described.

Multiscale Analysis

A brief introduction to multiscale analysis of complex stochastic systems is provided.

Image Similarity Measures

Image similarity measures are discussed. The measures are used to quantify image differences in the validation of model and simulation methods.

3. Multiscale Modeling and Analysis of ISAR Clutter

The multiscale clutter model is described and validated. Model parameters are estimated by a proposed multiscale analysis method.

4. Numerical Simulation of ISAR Clutter

Two methods for simulating additional samples are presented and validated using simulated data.

5. Applications for Multiscale Analysis and Simulation of ISAR Clutter

Multiscale analysis is performed on global ocean currents and measured ISAR data. The hypothesized relationship between clutter scattering phenomenon and multiscale model parameters is discussed. These hypotheses are tested using physical measurements of three plants, which are chosen for their range of scattering properties. Clutter simulations methods are evaluated by using generated training data to improve deep network prediction accuracy in two deep learning ISAR applications.

2 BACKGROUND MATERIAL

2.1 ELECTROMAGNETIC SCATTERING AND EQUIVALENT SOURCES

2.1.1 Electromagnetic Scattering

Equivalent currents are induced in a target upon illumination by a plane wave, resulting in a scattered electromagnetic field. The scattered electric field is found by three-dimensional (3D) convolution of the equivalent current density with the free-space Green's function, as shown in equation (1), where $\boldsymbol{r}$ is the vector to the observation point, $\boldsymbol{r}'$ is a vector to a point in the target volume, and the 3D free-space Green's function is given in equation (2). Figure 2 demonstrates the geometry of the problem [2].

$$\boldsymbol{E}(\boldsymbol{r}) = \iiint \boldsymbol{J}(\boldsymbol{r}')G_0(\boldsymbol{r}-\boldsymbol{r}')d\boldsymbol{r}' \tag{1}$$

$$G_0(\boldsymbol{r}-\boldsymbol{r}') = \frac{e^{-jk|\boldsymbol{r}-\boldsymbol{r}'|}}{4\pi|\boldsymbol{r}-\boldsymbol{r}'|} \tag{2}$$

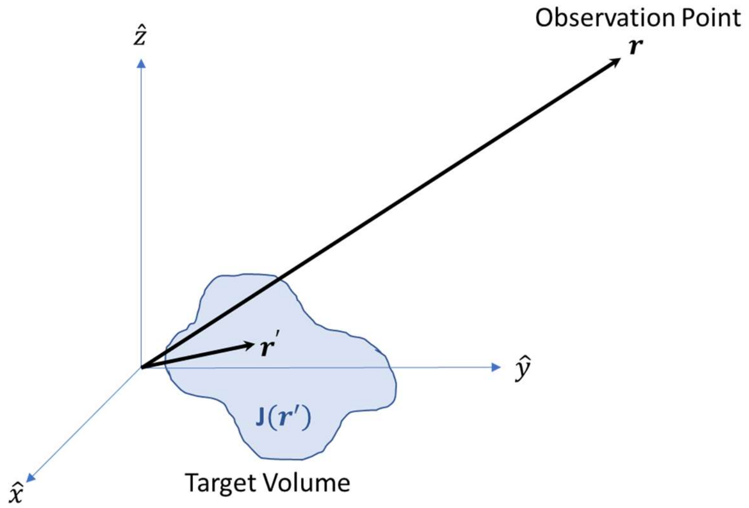

Figure 2: Observation and Target Geometry

The integral in equation (1) can be difficult to evaluate because of the $|\boldsymbol{r}-\boldsymbol{r}'|$ terms in the Green's function. If the observation point is very far compared to the size of the target volume ($r \gg r'$), we can derive an approximation that simplifies equation (1).

2.1.2 Scattered Field in the Far Zone

Under the far-field condition of $r \gg r'$, we can approximate the $|\boldsymbol{r} - \boldsymbol{r}'|$ distance as that given in equation (3). The geometry of this approximation is shown in Figure 3.

$$|\boldsymbol{r} - \boldsymbol{r}'| \approx r - \hat{\boldsymbol{r}} \cdot \boldsymbol{r}' = r\left(1 - \hat{\boldsymbol{r}} \cdot \frac{\boldsymbol{r}'}{r}\right) \tag{3}$$

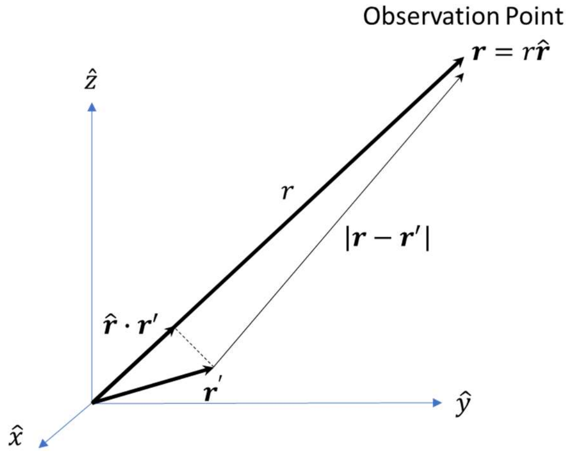

Figure 3: Far-Field Approximation Geometry

Using the approximation in equation (3), the 3D Green's function can be written as in equations (4) and (5), where $O\left(\frac{1}{r^2}\right)$ contains $1/r^2$ terms.

$$\hat{G}_0(\boldsymbol{r}, \boldsymbol{r}') = \frac{e^{-jkr}}{4\pi r} \frac{e^{jk\hat{\boldsymbol{r}}\cdot\boldsymbol{r}'}}{1 - \hat{\boldsymbol{r}} \cdot \frac{\boldsymbol{r}'}{r}} \tag{4}$$

$$\hat{G}_0(\boldsymbol{r}, \boldsymbol{r}') \approx \frac{e^{-jkr}}{4\pi r} e^{jk\hat{\boldsymbol{r}}\cdot\boldsymbol{r}'} + O\left(\frac{1}{r^2}\right) \tag{5}$$

Under the far field assumption and large r, the $1/r^2$ terms will be very small compared to the $1/r$ terms and can be dropped. Therefore, we arrive at the far-field free-space Green's function, equation (6), where $\boldsymbol{k_r} = k\hat{\boldsymbol{r}}$ is the wave vector. The far-field Green's function contains an amplitude term based only on the observation distance, and a phase term in the exponential that is based only on the component of $\boldsymbol{r}'$ in the observation direction of $\hat{\boldsymbol{r}}$.

$$\hat{G}_0(\boldsymbol{r}, \boldsymbol{r}') \approx \frac{e^{-jkr}}{4\pi r} e^{j\boldsymbol{k_r}\cdot\boldsymbol{r}'} \tag{6}$$

Applying the far-field Green's function to equation (1), results in equation (7). It is important to note that now the integral occurs only over $\boldsymbol{r'}$ target volume locations and is independent of the observation distance. Removing the amplitude term, we can simplify equation (7) to equation (8), where we now specify the measured backscattered field $\overline{\boldsymbol{E}}(\boldsymbol{k_r})$ over observation parameters in $\boldsymbol{k_r}$. Inspection of equation (8) shows that it takes a similar form as the Fourier transform.

$$\boldsymbol{E}(\boldsymbol{r}) = \frac{e^{-jkr}}{4\pi r} \iiint \boldsymbol{J}(\boldsymbol{r'}) e^{j\boldsymbol{k_r}\cdot\boldsymbol{r'}} d\boldsymbol{r'} \tag{7}$$

$$\overline{\boldsymbol{E}}(\boldsymbol{k_r}) = \iiint \boldsymbol{J}(\boldsymbol{r'}) e^{j\boldsymbol{k_r}\cdot\boldsymbol{r'}} d\boldsymbol{r'} \tag{8}$$

Equation (8) involves three-dimensional integration of a continuous equivalent current function, $\boldsymbol{J}(\boldsymbol{r'})$. One method for calculating $\overline{\boldsymbol{E}}(\boldsymbol{k_r})$ is through discretization. If we assume $\boldsymbol{J}(\boldsymbol{r'})$ contains a discrete number of volume cells, and observations are made over a range of discrete locations and frequencies, then equation (8) becomes a linear system, with $\boldsymbol{r'}$ and $\boldsymbol{k_r}$ given in cartesian coordinates, where r_x, r_y, r_z are the coordinates to a 3D target volume cell. Figure 4 and Figure 5 show the geometry of $\boldsymbol{r'}$ and $\boldsymbol{k_r}$ [1].

$$\boldsymbol{r'} = r_x\hat{x} + r_y\hat{y} + r_z\hat{z} \tag{9}$$

$$\boldsymbol{k_r} = k_x\hat{x} + k_y\hat{y} + k_z\hat{z} \tag{10}$$

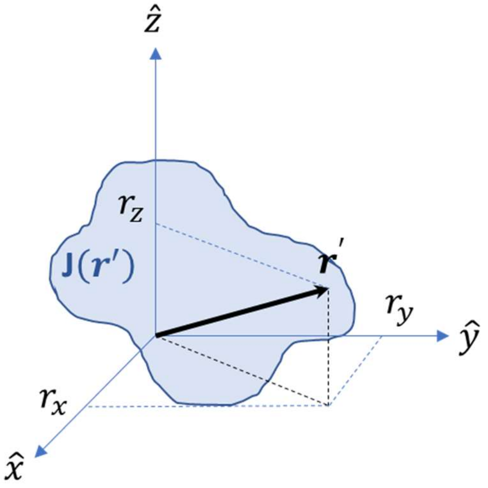

Figure 4: Target Geometry

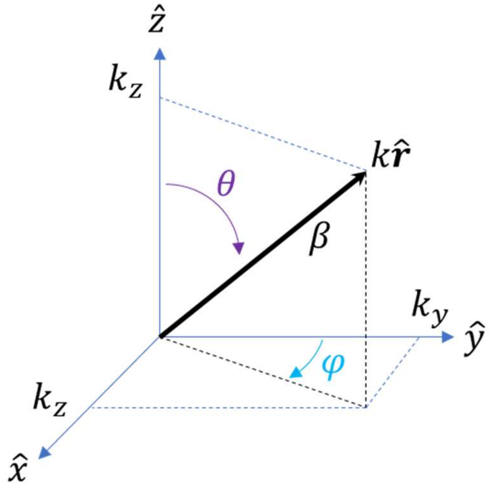

Figure 5: Mapping from observation parameters to k-space components

In Figure 5, $\boldsymbol{k_r}$ is the k-space wave vector, whose coordinates represent the wave number k in the direction of the observation vector, $\hat{\boldsymbol{r}}$. The k-space components are specified in cartesian coordinates in equation (10), with components given in equations (11) through (14) that depend on observation parameters. Since we have discretized the problem, the observation parameters of f, φ, and θ will be discrete values representing a discrete number of observations.

$$k_x = \beta \sin\theta \sin\varphi \tag{11}$$

$$k_y = \beta \sin\theta \cos\varphi \tag{12}$$

$$k_z = \beta \cos\theta \tag{13}$$

$$\beta = \frac{2\pi f}{c} \tag{14}$$

Three-dimensional ISAR imaging involves estimating $\boldsymbol{J}(\boldsymbol{r'})$ at discrete locations using discrete observations. This linear system can be solved by many different methods including the inverse Fourier transform, compressive sensing, and subspace techniques, depending on the assumptions made about the target.

2.1.3 Equivalent Sources

The field radiated from a known current density is unique. However, given an observed field, the current density is not unique, and we are free to form an equivalent current density that produces the same observed field. Using Huygens's Surface Equivalence Principle, we can write the observed far electric field as a function of the surface current density over a defined surface. This surface current density is proportional to the tangential components of the radiated fields on the chosen surface [2].

$$\boldsymbol{E}(\boldsymbol{r}) = \frac{e^{-jkr}}{4\pi r} \iiint \boldsymbol{J}(\boldsymbol{r'}) e^{j\boldsymbol{k_r}\cdot\boldsymbol{r'}} d\boldsymbol{r'} = \frac{e^{-jkr}}{4\pi r} \iint \boldsymbol{J_s}(\boldsymbol{r'}) e^{j\boldsymbol{k_r}\cdot\boldsymbol{r'}} dS' \tag{15}$$

2.2 ISAR IMAGING

Inverse Synthetic Aperture Radar (ISAR) is an active remote sensing technique used to form an image of the concentrated target scattering in two or three spatial dimensions. Like Synthetic Aperture Radar (SAR), the technique takes advantage of relative motion between the measurement platform and target to synthesize a larger aperture than is possible with any instantaneous measurements. The main difference between ISAR and SAR is that SAR generally involves a moving measurement platform and a stationary target. ISAR, on the other hand, generally involves a stationary measurement system and an uncooperative moving target with rotational and translational motion. In this case, rotational and translational motion must be estimated, and this has been a significant area of research. ISAR has the benefit of having a convenient measurement geometry in a lab setting. This involves a stationary measurement system including antennas, and controlled aspect angle, such as a rotating platform. Therefore, a controlled lab environment can present a very controlled measurement environment where imaging techniques can be explored with the elimination of complicating measurement issues.

The required relative motion between measurement platform and target is needed to produce a change in phase for concentrations of scattering centers at each aspect angle. This phase change is then focused into target spatial locations through ISAR processing and back-projection. In addition to rotational motion, this phase discrimination can be accomplished through variations in measurement frequency. Coherent stepped-frequency measurements over a defined bandwidth are used to measure target phase response over frequency. The down-range resolution of the ISAR image is related to the bandwidth of measurement frequencies. In addition to variations in frequency, the known rotation of a target can provide a predictable result from concentrated scattering areas on the target.

For additional reading on ISAR imaging background, see [1].

2.2.1 Two-Dimensional ISAR Imaging

Three-dimensional ISAR imaging requires discrete measurements over frequency, azimuth, and elevation angles (f, φ, and θ), which can be cumbersome and computationally expensive. Two-dimensional (2D) ISAR imaging in spatial planes parallel to the cartesian axes involves measuring observations over only two of the three observation parameters. This imaging plane can be interpreted as the planar projection of the equivalent volume current density. It is important to note that we are not imaging a *slice* of the equivalent volume current, but we are imaging the tangential components of the radiated field intersecting the chosen plane. This imaging plane is the equivalent surface current density described in equation (15), and accounts for all scattering mechanisms in the target volume. Therefore, with 2D ISAR imaging, we can image the two-dimensional equivalent currents in the chosen plane, which correspond to the tangential components of the scattered field from the target volume at that plane.

We can form a 2D image of the equivalent current density projected onto a two-dimensional plane. The chosen plane impacts our choice of observation parameters. For instance, if we chose the xy imaging plane at $z = 0$, we are only concerned with the k_x and k_y components of $\boldsymbol{k_r}$. Therefore, we are free to choose the observation parameter θ as a constant and measure observations over f and φ. As stated previously, we can arrange this linear system into matrix equations, where observations over f and φ, and discrete values of $\boldsymbol{J_s}$ are vectorized. If we have N total observations and we are solving for the equivalent current M discrete locations on the imaging plane, then the problem can be written as a linear system as in equation (16), where $\boldsymbol{e}$ is a vector of N observations over observation parameters $\boldsymbol{k}_{r_1}$ to $\boldsymbol{k}_{r_N}$, $\boldsymbol{z}$ is a vector of 2D coordinates on the imaging plane, and $\boldsymbol{G}$ is the N x M matrix of complex exponentials, related to the phase component of the far-field Green's function, and contains the mapping from discrete surface current density to the observed electric field.

$$\boldsymbol{e} = \boldsymbol{G}\mathbf{z} \tag{16}$$

The components of $\boldsymbol{e}$, $\boldsymbol{G}$, and $\boldsymbol{z}$, take the form shown in equations (17) through (19).

$$\boldsymbol{e} = \begin{bmatrix} \boldsymbol{E}(\boldsymbol{k}_{r_1}) \\ \vdots \\ \boldsymbol{E}(\boldsymbol{k}_{r_N}) \end{bmatrix} \tag{17}$$

$$\boldsymbol{G} = \begin{bmatrix} e^{j\boldsymbol{k}_{r_1}\cdot \boldsymbol{r}'_1} & \cdots & e^{j\boldsymbol{k}_{r_1}\cdot \boldsymbol{r}'_M} \\ \vdots & \ddots & \vdots \\ e^{j\boldsymbol{k}_{r_N}\cdot \boldsymbol{r}'_1} & \cdots & e^{j\boldsymbol{k}_{r_N}\cdot \boldsymbol{r}'_M} \end{bmatrix} \tag{18}$$

$$\boldsymbol{z} = \begin{bmatrix} \boldsymbol{J}(\boldsymbol{r}'_1) \\ \vdots \\ \boldsymbol{J}(\boldsymbol{r}'_M) \end{bmatrix} \tag{19}$$

Equation (16) can be solved by inversion techniques, including the inverse DFT, to find an equivalent current distribution that produces the electric field measured at the observation points. Once $\boldsymbol{z}$ is found, the elements of $\boldsymbol{z}$ can be mapped back to the 2D imaging plane, resulting in a 2D image of the target equivalent current projection.

2.2.2 Complex ISAR Image and Clutter Equivalent Current

ISAR imaging in a two-dimensional plane near the target volume can be considered a projection of the target equivalent current. The scattering background material shows that a volume of dielectric discontinuities will scatter an incident plane wave, resulting in a total scattered field as shown in Figure 6.

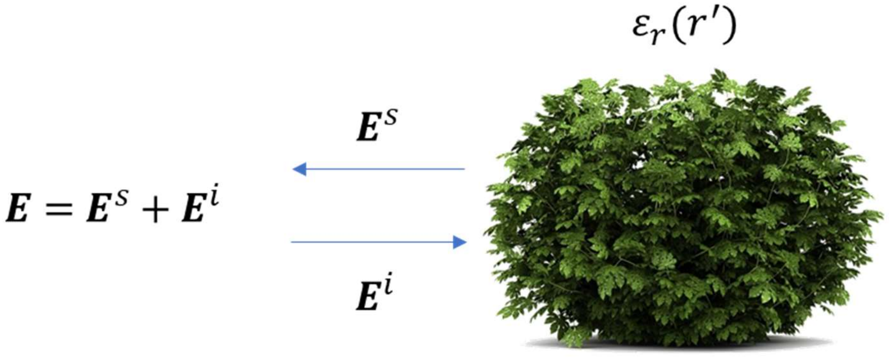

Figure 6: Total Scattered Field from a Volume of Dielectric Discontinuities

The total scattered field from a specific target volume is unique, however a target volume is not unique given a measured total scattered field and we are free to define the target equivalent current volume that would produce the measured field. The equivalent current density $\boldsymbol{J}(\boldsymbol{r}')$ is a volume current density that will radiate a field equivalent to the total scattered field (Figure 7).

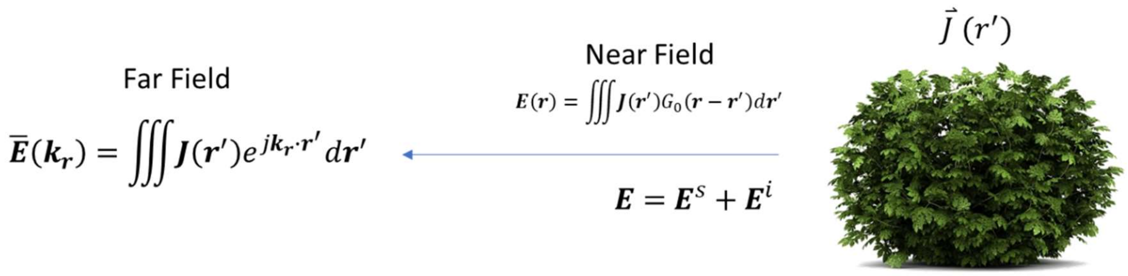

Figure 7: Equivalent Volume Currents

Using Huygens's Surface Equivalence Principle, a two-dimensional plane of equivalent current sources can be chosen that will result in an equivalent total scattered field. These surface equivalent currents $\boldsymbol{J_s}(\boldsymbol{r}')$ are proportional to the tangential components of the total scattered field at the surface boundary. Applying the far-field Green's function, we arrive at equation (8), where the far scattered field is the 2D convolution of the surface current density and the far field Green's function as shown in Figure 8.

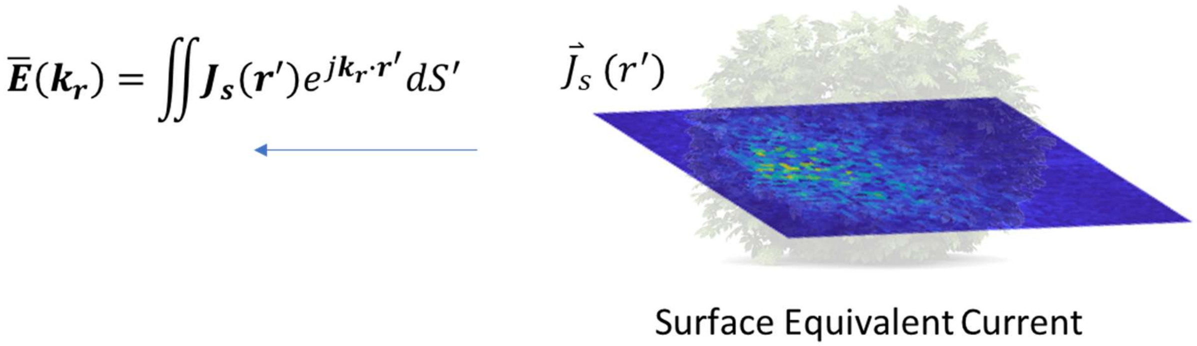

Figure 8: Surface Equivalent Current Density

If the surface current density is discretized, then we can form a linear system that relates the measured scattered field in k-space to the equivalent surface current densities (Figure 9).

2.2.3 Relationship to Fourier Transform

Examination of equation (16) shows the Fourier-like nature of the relationship between equivalent current and the measured field. Matrix $\boldsymbol{G}$ can be interpreted as a 2D discrete Fourier transform in k-space. Therefore, if the measured data is reformatted into the k-space domain using a rectangular grid of k_x and k_y components, the equivalent current can be estimated using the inverse discrete Fourier transform of the measured k-space data. Figure 9 summarizes the Fourier relationship between the measured in the k-space domain and the estimated equivalent current.

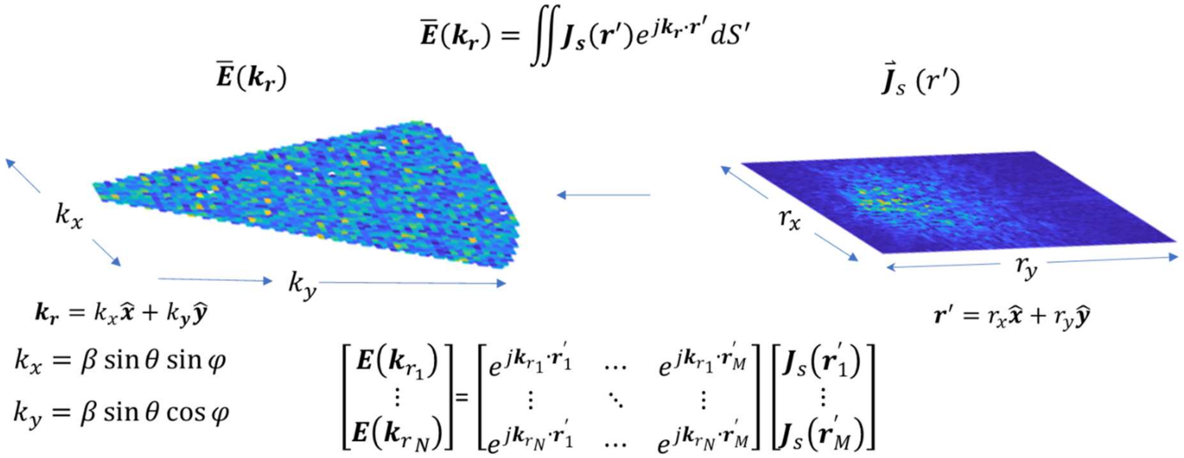

Figure 9: Linear System Relating Far Scattered Field to Surface Current Density

2.3 ISAR MEASUREMENT SETUP AND CALIBRATION

2.3.1 ISAR Measurement Setup

The backscattered field from a target is measured using the setup shown in Figure 10. A network analyzer is used to measure the S21 network parameter over a frequency range. This is a stepped frequency measurement, where the network analyzer sends a stimulus signal at a specific frequency and compares the return signal to the stimulus signal to calculate the complex S21 parameter. This S21 calculation for the desired frequency is implemented as an average S21 parameter over the stepped frequency dwell time. The S21 measurement is calibrated at the indicated calibration point, resulting in a unity magnitude and zero phase response over frequency when port 1 and port 2 are connected at the calibration reference plane. Therefore, S21 measurement data recorded by the network analyzer provides the round-trip magnitude and phase of the network analyzer stimulus relative to the calibration plane. Target rotation over a range of azimuth angles is accomplished with a turntable.

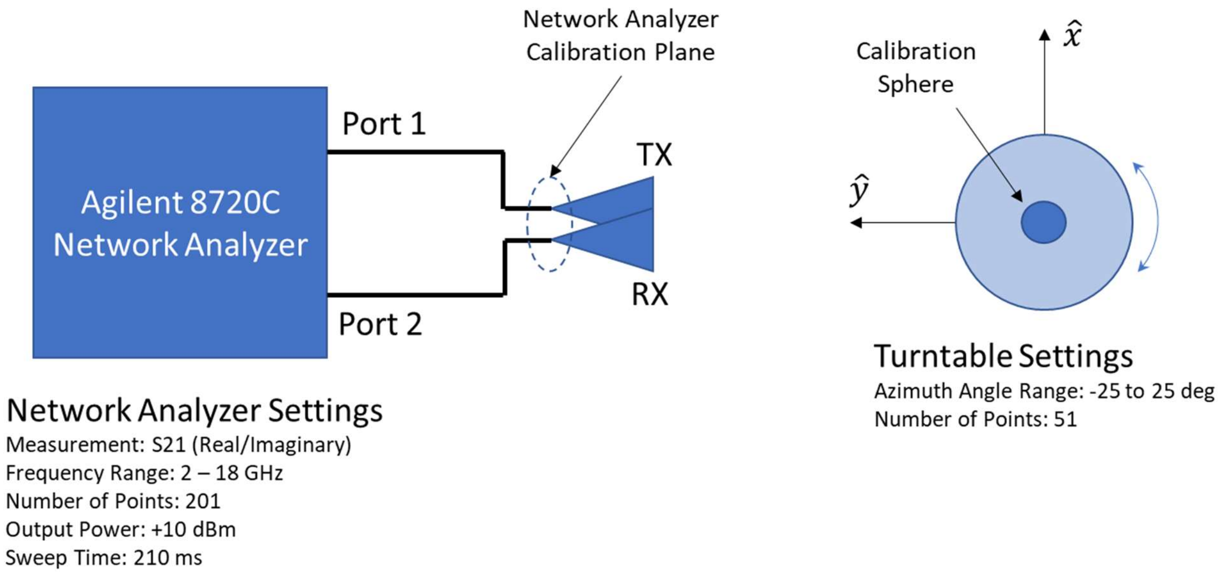

Turntable Settings
Azimuth Angle Range: -25 to 25 deg
Number of Points: 51

Network Analyzer Settings
Measurement: S21 (Real/Imaginary)
Frequency Range: 2 – 18 GHz
Number of Points: 201
Output Power: +10 dBm
Sweep Time: 210 ms

Figure 10: ISAR Measurement Setup

ISAR measurement calibration is performed using a conductive sphere placed in the center of target rotation and measured over the desired frequency range. The theoretical Mie scattering from the sphere is used to calibrate the measured S21 data over frequency. This results in a gain and phase correction factor over frequency that is applied to all measurement data and defines the zero-phase center of the measurement at the center of target rotation.

To reduce the impact of reflections from non-target items such as the turntable, background subtraction is performed on all measurements. This is accomplished by making measurements of the setup without a target and over the desired frequency and azimuth ranges. This provides the backscattered field from the measurement setup which can be subtracted from the measurements with a target present. This will reduce the magnitude of reflections from non-target elements in the measurement setup, but reflections related to interactions between the target and setup will still be present.

2.3.2 Sphere Calibration

The calibration procedure starts with S21 measurements of the target area with a conducting sphere (in this case a 1" steel sphere). Figure 11 below shows plots for the Fourier transform of the measured S21 over frequency. After applying the Fourier transform, the horizontal axis becomes time or propagation distance, which is related to phase, and is measured on the y-axis as in Figure 10. The blue plot represents the measurement of the background with the sphere present. The sphere is located at the blue peak around point 266. In the case of Figure 11, the antennas are on the right side of the plot, around the large peak at point 350. The red plot is the background measurement of the setup, which consists of everything but the sphere in this case.

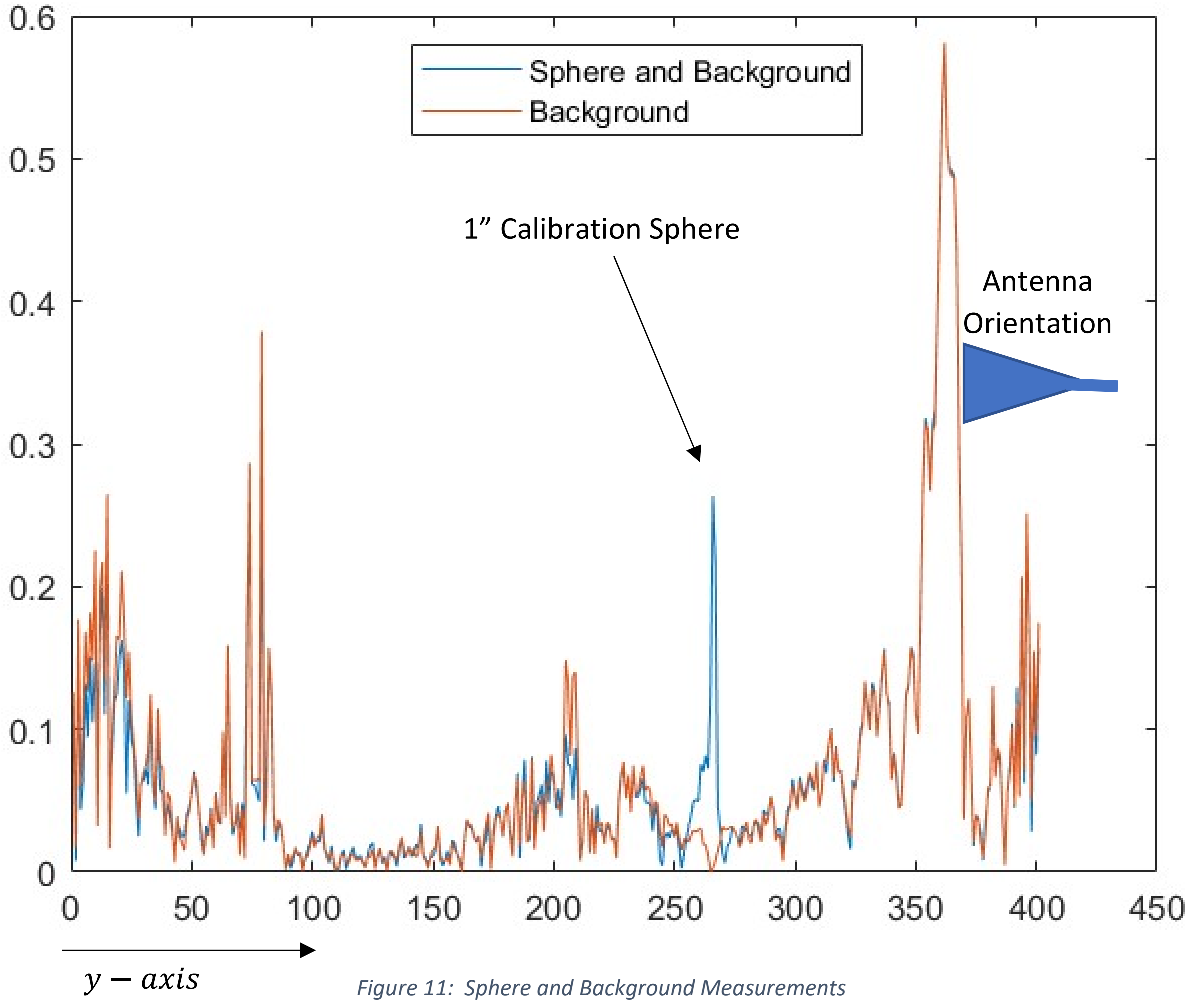

Figure 11: Sphere and Background Measurements

The total backscattered signal can be considered a linear combination of target and background if the interactions are neglected. Therefore, we can subtract the background measurement and reduce the interference in the measurement. Figure 12 below shows the comparison of the original target data (red) and the target after background subtraction (blue). Figure 13 shows the Fourier transform of the sphere data after background subtraction. Although most of the interference between the sphere and the antenna has been reduced significantly, there is still some interference beyond (to the left of) the sphere peak. This can be reduced by time-gating the sphere measurement, which essentially windows the data in the time (or distance) domain.

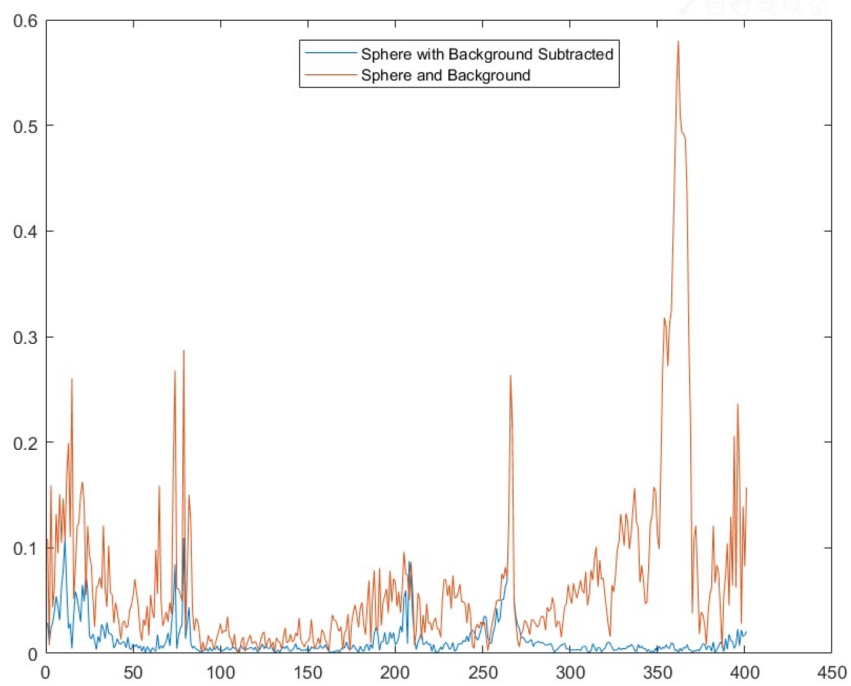

Figure 12: Comparison of FFT of Sphere Data Before and After Background Subtraction

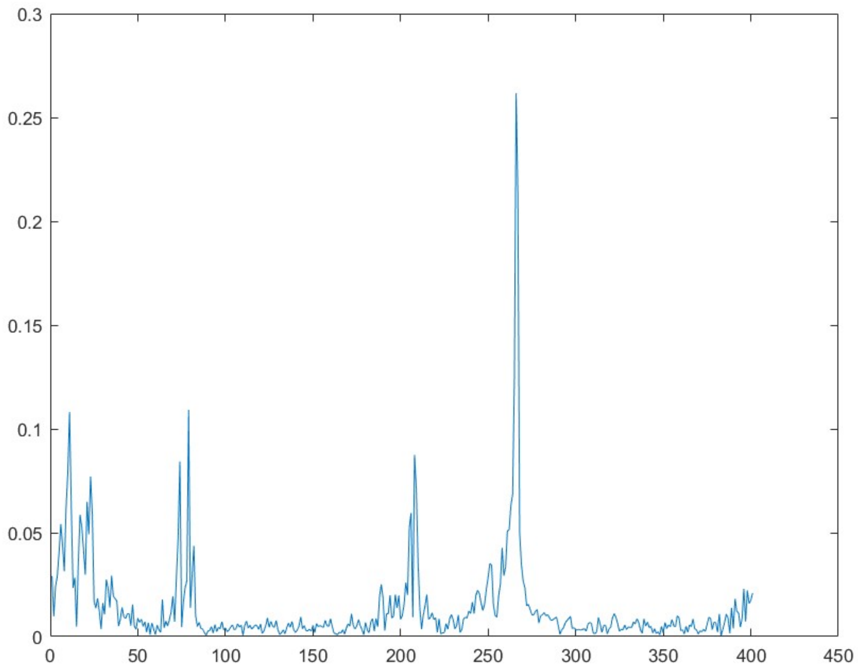

Figure 13: FFT of Sphere Data after Background Subtraction

With the isolated sphere measurement at the center of the turntable, we can now calculate the correction factor over frequency as in equation (26), where $a(f)$ is the complex correction factor, $s(f)$ is the measured sphere data, and $Mie(f)$ is the theoretical Mie scattering from a 1" conducting sphere.

$$a(f) = \frac{Mie(f)}{s(f)} \tag{20}$$

The purpose of the correction factor is to account for signal losses and phase offsets in the measurement setup and to set the zero-phase center of the measurement at the location of the sphere. This correction factor can then be applied to all subsequent measurements using equation (21), where $d(f)$ is uncalibrated measurement data over frequency, $a(f)$ is the calculated correction factor from equation (26), and $d_c(f)$ is the resulting calibrated data. The correction factor is calculated at one azimuth for the sphere but is applied at every target aspect angle.

$$d_c(f) = a(f) \cdot d(f) \tag{21}$$

2.3.3 Calibration Verification

To verify the calibration process, additional S21 measurements are taken of the 1" sphere, background is subtracted, and the calibration factor is applied. The Fourier transform of the resulting calibrated data is shown below in Figure 14, where the calibrated sphere measurement agrees well with the theoretical Mie scattering response of a 1" sphere located at the zero-phase reference plane.

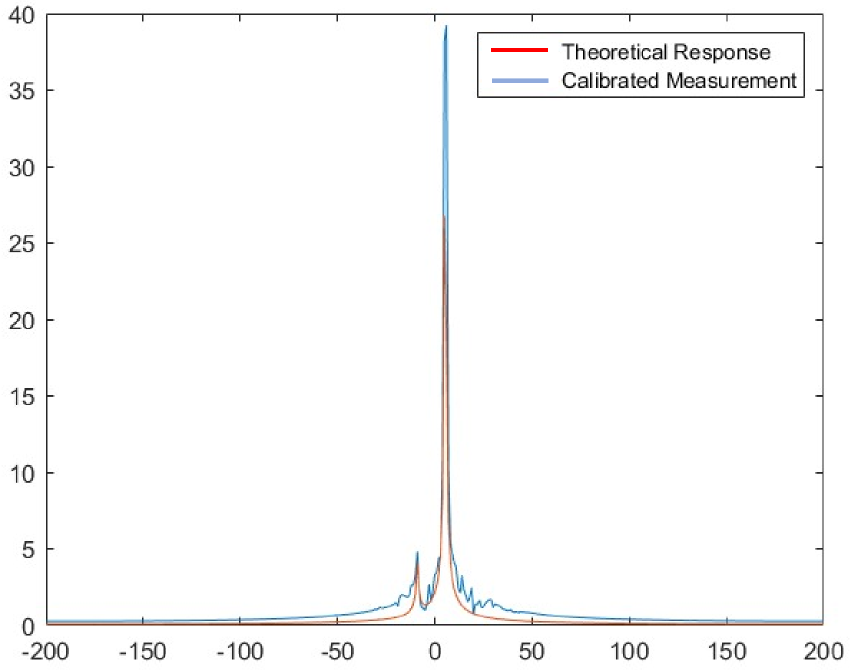

Figure 14: Comparison of Theoretical Sphere Response to Calibrated Sphere Response

2.3.4 ISAR Measurement Test Articles

Physical measurements used in the course of this research consists of ISAR imaging of different species of plants in the presence of wind. The plants were chosen to have a variety of physical characteristics that result in a range of scattering modes. In this dissertation, plants are referred to as Plant A, Plant B, etc. and wind is described as "no wind", "light wind", or "medium wind". Wind speeds are not quantified but are consistent across measurement scenarios.

Figure 15: Plant Species A - E

Each measurement scenario consists of 2D ISAR image samples of a plant in the presence of wind. The ISAR data for each plant and wind speed is structured into 100 image samples where each image pixel represents a complex-valued resolution cell on this projected xy image plane.

The data for each measurement scenario is structured as a 3D matrix of size 64x64x100, where each of the 100 image samples is a 64x64 complex-valued image.

2.4 MULTISCALE ANALYSIS OF COMPLEX STOCHASTIC SYSTEMS

Interactions within and between complex stochastic systems can be highly complex. Due to this complexity, process models are often used to estimate the magnitude and directionality of interactions. However, these models are based on simplifications of our understanding of these complex systems and are imperfect. The increased availability of data allows the determination of complex multiscale relationships if appropriate statistical methods are applied [55].

A significant amount of research has been performed in the field of multiscale analysis of geophysical systems. Multiscale interactions have recently received extensive attention in the literature and have been proposed as a mechanism for the triggering of extreme events [56] [57] [58] and patterns formation [59] [60]. Examples of this increasing interest for multiscale and cross-scale interactions can be found in ecology [61] [62] [63] [64] [58] [59] [65] [66] and climate dynamics [67] [68] [69] and also in fields other than geosciences such as network and econometrics.

Considerably less attention has been devoted to the analysis of couplings and feedbacks taking place at different temporal scales and across them [70] [69], to the development of ad hoc statistics able to capture the evolution in time of such couplings [71] [72] and to the investigation of the spectral features of systems displaying strong connectivity across interannual, seasonal and subseasonal [73].

Casagrande et al use multiscale analysis to uncover couplings and interactions between complex geophysical systems including the relationship between air temperature and soil moisture. Here a ‘local coupling’ metric is introduced to describe the relationship between the data over multiple scales. This local coupling metric, the wavelet cross-correlation, is explored for identifying and assessing linear and intermittent interactions across different temporal scales in geophysical systems. What is particularly appealing in this measure is its ability to decompose linear correlations in scale and time, preserving simultaneously the total correlation of the system [74].

Although Casagrande et al use this multiscale approach to find coupling between different related sets of data, the general multiscale wavelet decomposition approach is valid for determining local couplings in single processes as well [55].

2.4.1 Multiscale Wavelet Analysis

There are several multiscale analysis methods, but wavelets are well established and commonly used. Multiscale analysis using wavelets has been shown to be an effective tool for the analysis of complex geophysical processes and other examples of correlated spatial data [55]. Souare uses this approach in the analysis of SAR imagery in [75], and A. Lucrecio explores ISAR imaging using wavelet transforms in [76].

The approach of this dissertation is to decompose each ISAR image sample into directional wavelet components and characterize the second-order characteristics of these components at each scale. Due to the diversity of foliage structure, a multiscale approach will allow an additional discriminator between physical structures and characteristics of the clutter. Leaves might show spatial correlation at high-resolution scales, but little correlation at lower resolutions. Branches and larger structures may show spatial correlation at lower resolutions.

2.5 IMAGE SIMILARITY MEASURES

2.5.1 Similarity Measures Introduction and History

Similarity measures are used to quantitatively describe differences between two images. The definition of an image can be very broad here and can relate to two-dimensional channel RGB photos as well as 2D complex ISAR images. The following section will define an image as an arrangement of values in two or more dimensions, and more specifically, a 2D spatial arrangement and one or more channel depths. In addition, we are also concerned about the stochastic properties of time-varying images. Our goal is to create additional ISAR clutter samples for the purpose the convolutional neural network training. We need a quantitative measure to gauge the effectiveness of different techniques in building our clutter model. This section will describe techniques used in comparing the similarity of static images and images representing stochastic processes.

Multitemporal SAR imaging is a related application to ISAR image samples. In 2007, Inglada and Mercier compare several methods for measuring the similarity of multitemporal SAR images [77]. Differences in SAR images can be used to detect geographical changes and the focus of their work is comparing SAR images from only two instances in time. Although SAR images contain positive pixel intensity values, Inglada and Mercier describe similarity measures that can also apply to images containing complex values. These techniques are related to the distribution of pixels in a small area of the image, but the general concept of KL divergence can be used to statistical differences in time as well.

Inglada and Mercier briefly describe previous methods to detect changes in SAR images. In radar images, the basic standard detector is the ratio of local means [78]. Although this type of detection is robust to speckle noise, which is often found in SAR images, it is limited to first-order statistics and is not very discriminatory. A classical model for SAR intensity introduced by Ulaby et al. assumes the image texture is a zero mean multiplicative process. This means that changes occurring that preserve the mean value will not be detected by techniques involving only mean values [79]. Bujor et al. described a method involving the use of higher-order statistics for change detection in SAR images [80]. This work concluded that mean ratios were useful for step changes and higher-order log-cumulants were used for more subtle progressive changes in consecutive multitemporal images. Inglada and Mercier concluded that comparing local probability density functions (PDFs) in the neighborhood of homologous pixels is useful for change detection. However, this requires that the pdfs be known, which precludes the direct use of histogram methods. Inglada and Mercier propose several approaches for change estimation using only a small number of samples for local statistics estimation, up to fourth order [77].

2.5.2 Image Similarity Measures

Information theory shows that the Kullback-Leibler (KL) divergence is a good measure for the comparison of probability density functions (PDFs). Inglada and Mercier propose a method where the PDFs are estimated and then compared using variations of the KL divergence.

2.5.2.1 Kullback-Leibler Divergence

Given PDFs of two random variables described by distributions f_X and f_Y, the KL divergence is defined below in equation (22). The statistical description of this measure can be thought of as the information in x that is used for the discrimination between x and y. It can also be understood as the entropy of P_X relative to P_Y.

$$K(Y|X) = \int log \frac{f_X(x)}{f_Y(x)} f_X(x) dx \tag{22}$$

The KL divergence will vanish as the two distributions become equal. Equation (22) is not a symmetric measure, but a symmetric version can be formed using equation (23) below.

$$D(X|Y) = D(Y|X) = K(Y|X) + K(X|Y) \tag{23}$$

2.5.2.2 Correlation Matrix Similarity Measure

In some multitemporal image applications, we have a need for characterizing the temporal behavior of the images over time. In many wide-sense stationary applications, where second-order statistics stay constant over time, this can include the covariance between pixels. The covariance matrix provides information related to the variance and amount of correlation between multivariate random variables.

In 2005, Herdin et al describe the correlation matrix distance between two correlation matrices, $\boldsymbol{R}_1$ and $\boldsymbol{R}_2$ as in equation *(24)*, where $\| \;\|_f$ is the Frobenius norm and $tr\{\quad\}$ is the trace function, or sum of the diagonal elements of a matrix [81].

$$d_{corr}(\boldsymbol{R}_1, \boldsymbol{R}_2) = 1 - \frac{tr\{\boldsymbol{R}_1 \boldsymbol{R}_2\}}{\|\boldsymbol{R}_1\|_f \ \|\boldsymbol{R}_2\|_f} \tag{24}$$

2.5.2.3 Multiscale Correlation Similarity Measure

In order to incorporate a multiscale similarity measure, we define a new measure based on the multiscale correlation estimates over a set of images. For any scale and/or direction, this similarity measure is the mean-squared error (MSE) of the difference estimated correlations at that scale and/or direction. This MSE is calculated as shown below in equation (25), where X_1 and X_2 are directional correlation maps (H, V, D) from image sets 1 and 2, L is the decomposition level, and N is the total number of elements in each of X_1 and X_2.

$$d^L_{X_1 X_2} = \sqrt{\frac{1}{N} \sum [X^L_1 - X^L_2]^2} \tag{25}$$

3 MULTISCALE MODELING AND ANALYSIS OF ISAR CLUTTER

The goal of this research is to develop a multiscale model for ISAR clutter, estimate model parameters from measured data, and use the parametric model to generate additional representative samples of ISAR clutter. In the typical ISAR scenario, the modeled clutter will be homogeneous, but we do not want to preclude clutter that may be non-homogeneous. The ISAR measurements used this research are of individual plants and are not homogeneous.

3.1 MULTISCALE CLUTTER MODEL ORDER

The proposed multiscale model contains multiscale statistics up to second-order. The projected equivalent current image benefits from the central limit theorem, where each image pixel consists of contributions from the entire clutter volume, and although the pixel statistics are not assumed to be Gaussian, it is hypothesized that a second-order model is appropriate.

The proposed second-order model consists of ISAR clutter pixel mean and variance, as well as multiscale horizontal and vertical correlations across the ISAR clutter image. These correlations, estimated at each scale, provide an indication of the correlation between spatially oriented pixels. The clutter equivalent current projection is proportional to the tangential components of the local scattered field on the imaging plane. Therefore, each image pixel contains scattered energy from every area of the clutter volume. It is hypothesized that the multiscale statistical characteristics of these image pixels are related to scattering phenomenon in the vegetation volume. Scattering from leaves and smaller areas within the clutter volume will be associated with ISAR image pixel correlations at a finer scale. However, scattering from larger branches will be associated with ISAR image pixel correlations from lower resolutions and in certain directions. This multiscale directional correlation allows for additional discrimination of clutter structure and increased fidelity of replication.

Scattering from clutter can be complex and approximations such as the point-scattering model are not effective at modeling higher-order scattering modes and interactions. However, if we approach the projection of this complicated equivalent current volume as a complete representation of all scattering from the clutter, then we can use the proposed multiscale model to simulate additional representative samples that include all scattering modes. The intent here is not to spatially image the clutter exactly, but to estimate the multiscale characteristics of the 2D equivalent current projection in order to analyze and simulate additional data that is representative of the clutter.

3.2 MODEL ORDER VALIDATION

In order to validate the use of a second-order model, image similarity characteristics will be calculated using both second- and fourth-order models. In both cases, the ISAR image pixels from measured ISAR data are used to calculate the first four moments over all samples at each image pixel. For the second-order model, only the mean and variance are used to generate additional samples. For the fourth-order model, all four moments are used in generating additional samples. In both cases, the generated samples are compared to the original data using the *KL Divergence* of the data distributions. This essentially provides a qualitative metric on how closely the distributions generated using the second- and fourth-order models compare to the original data. In order to account for a variety of scattering modes and homogeneity, analysis of plants A, B, and C in both no wind and light wind will be used. The KL divergence is specified in dB of KL divergence error ϵ, or $10 \cdot \log_{10} \epsilon$.

The tables below show results for full resolution of this data, using the entire 16 GHz frequency bandwidth and 51 degrees of aspect angle rotation, which represents the highest spatial resolution and the least amount of spatial averaging. Half-resolution was also tested and resulted in approximately 1 dB error improvement in the worst-case KL divergence, and very little change to the mean KL divergence. The results of the model-order analysis are shown below in Table 1 and Table 2.

Table 1: Model Order Analysis Results – Mean Image KL Divergence

Plant under Test	**Wind**	**Mean Image KL Divergence**	
		2nd-Order Model	**4th-Order Model**
Plant A	No Wind	-21.53	-21.90
Plant A	Light Wind	-21.75	-22.12
Plant B	No Wind	-21.51	-21.86
Plant B	Light Wind	-21.52	-21.90
Plant C	No Wind	-21.49	-21.84
Plant C	Light Wind	-21.62	-21.98

Table 2: Model Order Analysis Results – Worst Case Image KL Divergence

Plant under Test	**Wind**	**Worst Case Image KL Divergence**	
		2nd-Order Model	**4th-Order Model**
Plant A	No Wind	-13.32	-13.71
Plant A	Light Wind	-12.31	-12.97
Plant B	No Wind	-12.36	-13.36
Plant B	Light Wind	-12.97	-12.76
Plant C	No Wind	-13.22	-14.09
Plant C	Light Wind	-12.22	-12.91

The results in Table 1 and Table 2 show that there is only a few tenths of a dB difference in the KL divergence of the second- and fourth-order models. These results indicate that a second-order model is appropriate for these ISAR measurements.

3.3 ESTIMATION OF MULTISCALE MODEL PARAMETERS

3.3.1 Multiscale Notation

Wavelet coefficients will follow the notation shown below in equation (26), where A is the approximation coefficient of decomposition level L at location m. This notation is used for wavelet detail coefficients H, V, and D as well. In most cases, m will indicate row and column coordinates, such as x, y. However, for simplicity of some derivations, m may indicate a single index in a vectorized group of coefficients.

$$A_m^L \tag{26}$$

Properties of the multiscale wavelet coefficients will indicate the corresponding component as a subscript, such as in equation (27), where this parameter describes the variance of the horizonal wavelet detail coefficient at position m and decomposition level L.

$$\sigma_{H_m^L}^2 \tag{27}$$

Image samples are two-dimensional images over N samples. Image components are referred to as pixels and the statistics of pixels and multiscale components will be calculated over N samples. For instance, the mean and variance of pixel values are given in equations (28) and (29), where $\mu_I(x,y)$ and $\sigma_I^2(x,y)$ are the sample mean and variance of pixel x, y calculated over N samples of image $I(x,y,n)$.

$$\mu_I(x,y) = \sum_{n=1}^{N} \frac{I(x,y,n)}{N} \tag{28}$$

$$\sigma_I^2(x,y) = \sum_{n=1}^{N} \frac{\left(I(x,y,n) - \mu_I(x,y)\right)^2}{N} \tag{29}$$

3.3.1 Multiscale Correlation and Covariance Estimation

Directional image correlation and covariance can be estimated from the variances of the wavelet decomposition coefficients. Each wavelet coefficient can be considered a linear combination of a group of pixels from the previous decomposition level multiplied by the wavelet filter coefficients. We model pixels in each decomposition level as multivariate random variables; therefore, each wavelet coefficient can be considered a weighted sum of multivariate random variables and the total variance of the wavelet coefficient is the sum of the covariance matrix of contributing elements. By solving a linear system of equations involving unknown directional correlations and known wavelet coefficient variances, the directional correlation and covariance for each scale can be estimated.

A complete characterization of the second-order clutter projection characteristics requires estimation of the full sample covariance matrix, which gives the covariance between any two image pixels. The dimensions of the covariance matrix increase exponentially with increases in image dimension and can result in a very large matrix. In this analysis we choose to limit the correlation to a finite pixel distance at each scale, where correlation is assumed to be some decreasing function over pixel distance in horizontal and vertical directions. This multi-scale directional correlation estimate allows the characterization of correlation from small image areas at finer scales, as well as broader areas of correlation at coarser scales. Modeling directional correlation in the horizontal and vertical image directions provides an additional discriminator between scattering phenomenon in the clutter. The proposed analysis method describes estimated horizontal and vertical correlation mapping at image location x, y and decomposition level L in equations (30) and (31).

$$\rho_H^L(x,y) = \rho_{H_{x,y}}^L \tag{30}$$

$$\rho_V^L(x,y) = \rho_{V_{x,y}}^L \tag{31}$$

Equations (30) and (31) describe the estimated directional correlation in the area of the image centered at coordinate x, y. The analysis operates under the assumption that the directional correlation in the image can be modeled as the application of a parameterized two-dimensional (2D) correlating filter to random independent seed data, $I_s(x, y, n)$. Each pixel of random seed data at location x, y is modeled as an independent normally distributed random variable over N samples. The correlating filter has directional parameters of α_H and α_V over scale, which correspond to the horizontal and vertical correlation shape. For an exponential correlating function, α_H and α_V describe the directional decay of the filter. Equation (32) is an example of a 2D exponential correlating function with direction parameters α_H and α_V, where d_H, d_V are integers representing pixel offsets from filter center.

$$f(d_H, d_V) = \left[e^{-\left|\frac{d_H}{\alpha_H}\right|}\right]\left[e^{-\left|\frac{d_V}{\alpha_V}\right|}\right] = e^{-\left(\left|\frac{d_H}{\alpha_H}\right|+\left|\frac{d_V}{\alpha_V}\right|\right)} \tag{32}$$

Calculation of correlated data I_f by applying of a correlating filter to the seed data I_s is shown in equation (33). Each pixel of I_f is calculated as a weighted sum of seed pixels from I_s, where the weights are determined by the correlating filter coefficients in f_{xy}, which is defined at each xy image location.

$$I_f(x,y,n) = \sum_{d_x=-d}^{d} \sum_{d_y=-d}^{d} I_s\left(x+d_x, y+d_y, n\right) \cdot f_{xy}\left(d_x, d_y\right) \tag{33}$$

Multiscale analysis of the image allows for estimating image correlation over a range of scales. Calculation of the entire covariance matrix will provide an estimate of the correlation between any two pixels, but under the assumption that correlation occurs over a finite pixel distance, we can reduce the complexity of the analysis. Two-dimensional wavelet decomposition is used as the basis for the multiscale analysis. The directional nature of wavelet decomposition provides a direct application to the directional correlation estimation in the clutter data. Consider a 4x4 image area, with image pixels labeled according to Figure 16.

4x4 Area of Image Pixels

I_{11}	I_{12}	I_{21}	I_{22}
I_{13}	I_{14}	I_{23}	I_{24}
I_{31}	I_{32}	I_{41}	I_{42}
I_{33}	I_{34}	I_{43}	I_{44}

Figure 16: Image pixels area notation

Horizontal Wavelet Components

H_1^1	H_2^1
H_3^1	H_4^1

Figure 17: Wavelet components

Each of these pixels can be modeled as a multivariate random variable with mean, variance, and unknown correlation to the other pixels. Here we use the Debauchies 2-tap wavelet filters to decompose this image area into four components. There are many wavelets suitable for many multiscale analysis applications. Here, our intent is to simply form a weighted sum of pixels from the previous layer. This could be done manually without wavelet filters or algorithms, but wavelet tools are readily available and provide a convenient basis for analysis.

3.3.1.1 Choice of Wavelet Filter

The Debauchies 2-tap filter is chosen for this application simply because the size of filter (2x2 in this case) allows us to estimate the correlations at a finer resolution for each decomposition level. The formulations in this section can be adapted to accommodate a larger wavelet filter, but this results in estimated correlations over a larger image area, which is equivalent to results at higher levels of decomposition. A smaller wavelet filter simplifies the correlation estimation process and allows for finer resolution in the directional correlation estimations. The use of other wavelet filters with specific characteristics is identified as an area of further research.

The 2D wavelet filters are tensor products of one-dimensional approximation and detail (lowpass and highpass) filters. W_A contains lowpass elements in both directions, W_H contains highpass elements in the horizontal direction and lowpass elements in the vertical direction. Conversely, W_V contains highpass elements in the vertical direction and lowpass elements in the horizontal direction. The diagonal filter, W_D contains highpass elements in both directions.

$$W_H = \begin{bmatrix} 1 & -1 \\ 1 & -1 \end{bmatrix} \qquad W_V = \begin{bmatrix} 1 & 1 \\ -1 & -1 \end{bmatrix} \qquad W_D = \begin{bmatrix} 1 & -1 \\ -1 & 1 \end{bmatrix} \qquad W_A = \begin{bmatrix} 1 & 1 \\ 1 & 1 \end{bmatrix}$$

Filters are applied to 2x2 non-overlapping blocks of image pixels. Using the notation in Figure 16 and Figure 17, the wavelet coefficients can be described as in equation (34), where W_{H_n} is indexed according to equation (35).

$$H_m^1 = \sum_{n=1}^{4} I_{m,n} W_{H_n} \tag{34}$$

$$W_{H_n} = \begin{bmatrix} W_{H_1} & W_{H_2} \\ W_{H_3} & W_{H_4} \end{bmatrix} = \begin{bmatrix} 1 & -1 \\ 1 & -1 \end{bmatrix} \tag{35}$$

Similarly, the other directional and approximation components are found using equations (36) through (38).

$$V_m^1 = \sum_{n=1}^{4} I_{m,n} W_{V_n} \tag{36}$$

$$D_m^1 = \sum_{n=1}^{4} I_{m,n} W_{D_n} \tag{37}$$

$$A_m^1 = \sum_{n=1}^{4} I_{m,n} W_{A_n} \tag{38}$$

Each wavelet coefficient can be considered a weighted sum of image pixels or coefficients from the previous layer, where the weights are the elements of the 2D wavelet filters. The variance of a sum of dependent random variables is equal to the sum of all covariance matrix elements. For the H_1^1 coefficient, the covariance matrix of all contributing elements is given in equation (39).

$$C_{H_1^1} = \begin{bmatrix} W_{H_1}W_{H_1}\sigma_{I_{11}}^2 & \rho_{12}W_{H_1}W_{H_2}\sigma_{I_{11}}\sigma_{I_{12}} & \rho_{13}W_{H_1}W_{H_3}\sigma_{I_{11}}\sigma_{I_{13}} & \rho_{14}W_{H_1}W_{H_4}\sigma_{I_{11}}\sigma_{I_{14}} \\ \rho_{21}W_{H_2}W_{H_1}\sigma_{I_{12}}\sigma_{I_{11}} & W_{H_2}W_{H_2}\sigma_{I_{12}}^2 & \rho_{23}W_{H_2}W_{H_3}\sigma_{I_{12}}\sigma_{I_{13}} & \rho_{24}W_{H_2}W_{H_4}\sigma_{I_{12}}\sigma_{I_{14}} \\ \rho_{31}W_{H_3}W_{H_1}\sigma_{I_{13}}\sigma_{I_{11}} & \rho_{32}W_{H_3}W_{H_2}\sigma_{I_{13}}\sigma_{I_{12}} & W_{H_3}W_{H_3}\sigma_{I_{13}}^2 & \rho_{34}W_{H_3}W_{H_4}\sigma_{I_{13}}\sigma_{I_{14}} \\ \rho_{41}W_{H_4}W_{H_1}\sigma_{I_{14}}\sigma_{I_{11}} & \rho_{42}W_{H_4}W_{H_2}\sigma_{I_{14}}\sigma_{I_{12}} & \rho_{43}W_{H_4}W_{H_3}\sigma_{I_{14}}\sigma_{I_{13}} & W_{H_4}W_{H_4}\sigma_{I_{14}}^2 \end{bmatrix} \tag{39}$$

To simplify equation (39), we can map each of the 12 correlations to a general directional correlation as shown in Figure 18 and defined in equations (40) through (42). The covariance matrix can now be written as equation (43).

$$\rho_{H_{12}}, \rho_{H_{21}}, \rho_{H_{34}}, \rho_{H_{43}} = \rho_{H_1^1} \tag{40}$$

$$\rho_{H_{13}}, \rho_{H_{31}}, \rho_{H_{24}}, \rho_{H_{42}} = \rho_{V_1^1} \tag{41}$$

$$\rho_{H_{14}}, \rho_{H_{41}}, \rho_{H_{23}}, \rho_{H_{32}} = \rho_{D_1^1} \tag{42}$$

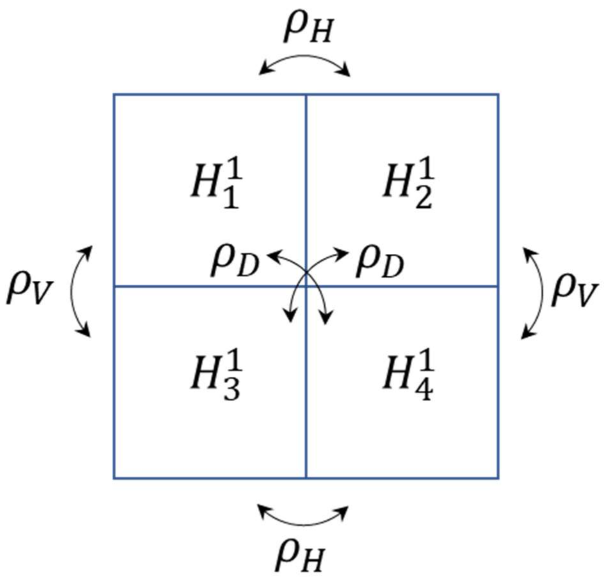

Figure 18: Correlation Mapping

$$C_{H_1^1} = \begin{bmatrix} \sigma_{I_{11}}^2 & \rho_{H_1^1}\sigma_{I_{11}}\sigma_{I_{12}} & -\rho_{V_1^1}\sigma_{I_{11}}\sigma_{I_{13}} & -\rho_{D_1^1}\sigma_{I_{11}}\sigma_{I_{14}} \\ \rho_{H_1^1}\sigma_{I_{12}}\sigma_{I_{11}} & \sigma_{I_{12}}^2 & -\rho_{D_1^1}\sigma_{I_{12}}\sigma_{I_{13}} & -\rho_{V_1^1}\sigma_{I_{12}}\sigma_{I_{14}} \\ -\rho_{V_1^1}\sigma_{I_{13}}\sigma_{I_{11}} & -\rho_{D_1^1}\sigma_{I_{13}}\sigma_{I_{12}} & \sigma_{I_{13}}^2 & \rho_{H_1^1}\sigma_{I_{13}}\sigma_{I_{14}} \\ -\rho_{D_1^1}\sigma_{I_{14}}\sigma_{I_{11}} & -\rho_{V_1^1}\sigma_{I_{14}}\sigma_{I_{12}} & \rho_{H_1^1}\sigma_{I_{14}}\sigma_{I_{13}} & \sigma_{I_{14}}^2 \end{bmatrix} \tag{43}$$

The variances from equation (43) can be estimated from sample variance of the image pixels. The directional correlations are unknowns and we can write the variance of the H_1^1 coefficient as equation (44), where $v_{A_1^1}$ through $v_{D_1^1}$ are given in equations (45) through (48).

$$\sigma_{H_1^1}^2 = \sum C_{H_1^1} = v_{A_1^1} + v_{H_1^1}\rho_{H_1^1} - v_{V_1^1}\rho_{V_1^1} - v_{D_1^1}\rho_{D_1^1} \tag{44}$$

$$v_{A_1^1} = \sigma_{11}^2 + \sigma_{12}^2 + \sigma_{13}^2 + \sigma_{14}^2 \tag{45}$$

$$v_{H_1^1} = 2\sigma_{11}\sigma_{12} + 2\sigma_{13}\sigma_{14} \tag{46}$$

$$v_{V_1^1} = 2\sigma_{11}\sigma_{13} + 2\sigma_{12}\sigma_{14} \tag{47}$$

$$v_{D_1^1} = 2\sigma_{11}\sigma_{14} + 2\sigma_{12}\sigma_{13} \tag{48}$$

Similarly, we can write an equation for the variances of the other three wavelet coefficients.

$$\sigma_{V_1^1}^2 = \sum C_{V_1^1} = v_{A_1^1} - v_{H_1^1}\rho_{H_1^1} + v_{V_1^1}\rho_{V_1^1} - v_{D_1^1}\rho_{D_1^1} \tag{49}$$

$$\sigma_{D_1^1}^2 = \sum C_{D_1^1} = v_{A_1^1} - v_{H_1^1}\rho_{H_1^1} - v_{V_1^1}\rho_{V_1^1} + v_{D_1^1}\rho_{D_1^1} \tag{50}$$

$$\sigma_{A_1^1}^2 = \sum C_{A_1^1} = v_{A_1^1} + v_{H_1^1}\rho_{H_1^1} + v_{V_1^1}\rho_{V_1^1} + v_{D_1^1}\rho_{D_1^1} \tag{51}$$

The wavelet coefficient variances are a function of known image pixel variances and unknown directional correlations. We can write equations (44) and (49) through (51) as a linear system in matrix form.

$$\boldsymbol{v} = \boldsymbol{C\rho} \tag{52}$$

$$\boldsymbol{v} = \begin{bmatrix} \sigma^2_{H_1^1} \\ \sigma^2_{V_1^1} \\ \sigma^2_{D_1^1} \\ \sigma^2_{A_1^1} \end{bmatrix} \tag{53}$$

$$\boldsymbol{C} = \begin{bmatrix} v_{A_1^1} & v_{H_1^1} & -v_{V_1^1} & -v_{D_1^1} \\ v_{A_1^1} & -v_{H_1^1} & v_{V_1^1} & -v_{D_1^1} \\ v_{A_1^1} & -v_{H_1^1} & -v_{V_1^1} & v_{D_1^1} \\ v_{A_1^1} & v_{H_1^1} & v_{V_1^1} & v_{D_1^1} \end{bmatrix} \tag{54}$$

$$\boldsymbol{\rho} = \begin{bmatrix} 1 \\ \rho_{H_1^1} \\ \rho_{V_1^1} \\ \rho_{D_1^1} \end{bmatrix} \tag{55}$$

Equation (52) can now be used to solve for the directional correlations.

$$\boldsymbol{\rho} = \boldsymbol{C}^{-1}\boldsymbol{v} \tag{56}$$

This process can be repeated for every wavelet coefficient to find the estimated directional correlation at every x, y decomposed image location at each scale. Equation (56) applies for every level and can be written more generally as equation (57), with elements defined in equations (58) through (60).

$$\boldsymbol{\rho}^L_{x,y} = {\boldsymbol{C}^L_{x,y}}^{-1}\boldsymbol{v}^L_{x,y} \tag{57}$$

$$\boldsymbol{v}^L_{x,y} = \begin{bmatrix} \sigma^2_{H^L_{x,y}} \\ \sigma^2_{V^L_{x,y}} \\ \sigma^2_{V^L_{x,y}} \\ \sigma^2_{V^L_{x,y}} \end{bmatrix} \tag{58}$$

$$\boldsymbol{C}^L_{x,y} = \begin{bmatrix} v_{A^L_{x,y}} & v_{H^L_{x,y}} & -v_{V^L_{x,y}} & -v_{D^L_{x,y}} \\ v_{A^L_{x,y}} & -v_{H^L_{x,y}} & v_{V^L_{x,y}} & -v_{D^L_{x,y}} \\ v_{A^L_{x,y}} & -v_{H^L_{x,y}} & -v_{V^L_{x,y}} & v_{D^L_{x,y}} \\ v_{A^L_{x,y}} & v_{H^L_{x,y}} & v_{V^L_{x,y}} & v_{D^L_{x,y}} \end{bmatrix} \tag{59}$$

$$\boldsymbol{\rho}^{L}_{x,y} = \begin{bmatrix} 1 \\ \rho_{H^{L}_{x,y}} \\ \rho_{V^{L}_{x,y}} \\ \rho_{D^{L}_{x,y}} \end{bmatrix} \tag{60}$$

In equation (59), the elements of $v_{A^{L}_{x,y}}$, $v_{H^{L}_{x,y}}$, $v_{V^{L}_{x,y}}$, and $v_{D^{L}_{x,y}}$ depend on the variances from the previous level, where m_1 through m_4 are elements from the previous level $L-1$ that contribute to the coefficient at x, y of the current level L. In wavelet decomposition, the approximation coefficients from level L are used as the input to the level $L+1$ decomposition. Therefore, $v_{A^{L}_{x,y}}$, $v_{H^{L}_{x,y}}$, $v_{V^{L}_{x,y}}$, and $v_{D^{L}_{x,y}}$ can be written as functions of the previous level's $A^{L-1}_{x,y}$ sample variances.

$$v_{A^{L}_{x,y}} = \sigma^2_{A^{L-1}_{m_1}} + \sigma^2_{A^{L-1}_{m_2}} + \sigma^2_{A^{L-1}_{m_3}} + \sigma^2_{A^{L-1}_{m_4}} \tag{61}$$

$$v_{H^{L}_{x,y}} = 2\sigma_{A^{L-1}_{m_1}}\sigma_{A^{L-1}_{m_2}} + 2\sigma_{A^{L-1}_{m_3}}\sigma_{A^{L-1}_{m_4}} \tag{62}$$

$$v_{V^{L}_{x,y}} = 2\sigma_{A^{L-1}_{m_1}}\sigma_{A^{L-1}_{m_3}} + 2\sigma_{A^{L-1}_{m_2}}\sigma_{A^{L-1}_{m_4}} \tag{63}$$

$$v_{D^{L}_{x,y}} = 2\sigma_{A^{L-1}_{m_1}}\sigma_{A^{L-1}_{m_4}} + 2\sigma_{A^{L-1}_{m_2}}\sigma_{A^{L-1}_{m_3}} \tag{64}$$

3.3.2 Multiscale Covariance vs Correlation

Image correlation is useful in uniform images where scattering intensity is consistent across the image and pixels represent scattering from the clutter. However, if the image is non-uniform and contains areas of very weak scattering, then the covariance is a better visualization of scattering phenomenon. Nonuniform ISAR images may contains areas where system noise is dominant and the correlation between these pixels is not relevant to the analysis. For this reason, multiscale covariance is shown in analysis of measured data. The estimated multiscale covariance is easily calculated from the estimated multiscale correlation and sample image variance.

3.4 VALIDATION OF MULTISCALE MODEL PARAMETER ESTIMATION METHOD

The proposed multiscale analysis is performed on known correlated data to validate the proposed multiscale correlation estimation method. The data is created by application of a two-dimensional exponential correlating filter, with the resulting horizontal and vertical correlations shown below in Figure 19.

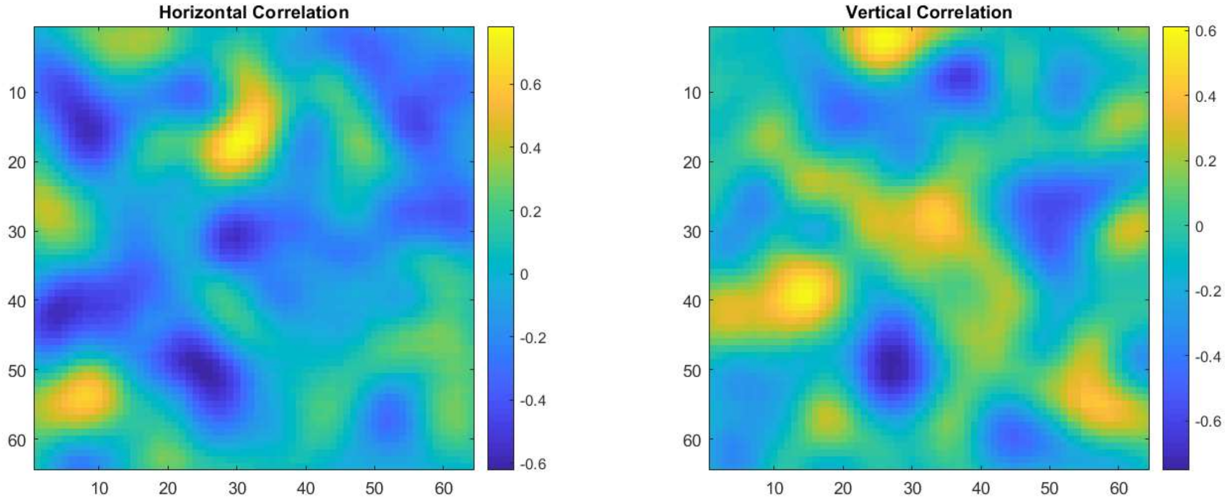
Horizontal Correlation

Vertical Correlation

Figure 19: Directional Correlation used to Create Correlated Data

The proposed multiscale analysis methods described in this chapter are then used to estimate the multiscale correlations for the known data. Three scales are analyzed and the results are shown in Figure 20, where H, V, and D refer to the horizontal, vertical, and diagonal directions respectively, and numbers 1, 2 and 3 refer to the decomposition level. The initial data is composed of 1000 samples of 64x64 images.

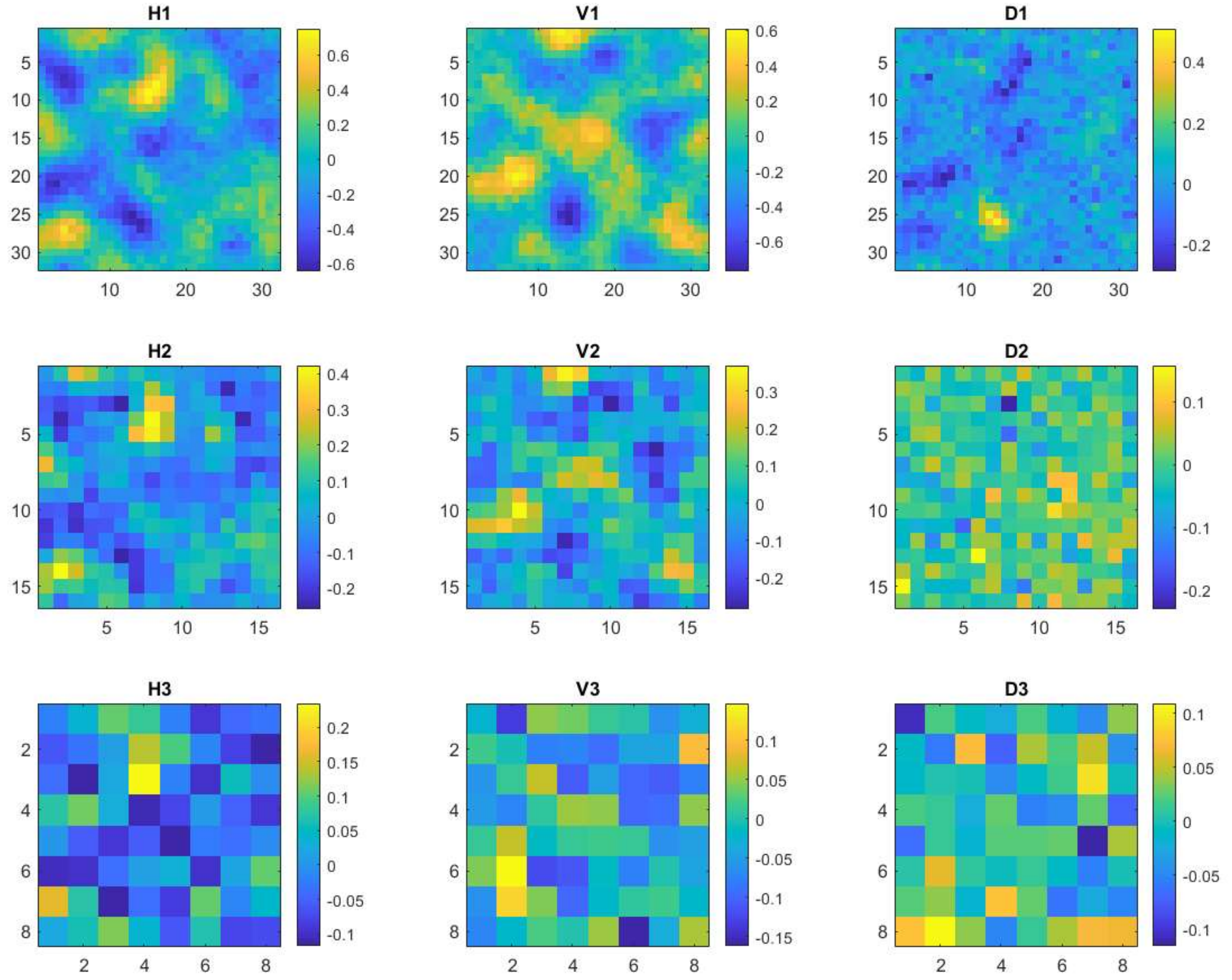

Figure 20: Estimated Directional Correlations for Simulated Data

Visual inspection of the estimated directional multiscale correlations show that they are in good agreement with the original directional correlation in Figure 19. Due to the use of an exponential filter for correlation, we would expect correlation to decrease as decomposition level increases from 1 to 3. For a more quantitative comparison, we can create correlated data with a constant correlation over the entire image. In this case, we choose a 2D exponential function as shown in equation (65), where we choose $\alpha_H, \alpha_V = 1$, and d_H and d_V are the horizontal and vertical pixel offsets.

$$f(d_H, d_V) = \left[e^{-\left|\frac{d_H}{\alpha_H}\right|}\right]\left[e^{-\left|\frac{d_V}{\alpha_V}\right|}\right] = e^{-\left(\left|\frac{d_H}{\alpha_H}\right|+\left|\frac{d_V}{\alpha_V}\right|\right)} \tag{65}$$

Applying this correlating filter to random seed data results in correlated data. We can calculate the correlation of this data based on the exponential filter coefficients. The correlation calculation is shown in equation (66), where D is the total length of the exponential filter and results in the offset correlations shown below in Table 3.

$$\rho(d) = \frac{1}{\sigma_f^2} \sum_{n=d+1}^{D-d+1} f(n+d)f(n) \tag{66}$$

$$\sigma_f^2 = \sum_{n=1}^{D} f^2(n) \tag{67}$$

$$f(d) = e^{-|d|} \tag{68}$$

Table 3: Correlation for Pixel Offsets Using Exponential Correlating filter

Pixel Offset	f(d)	Correlation
0	1	1
1	0.3679	0.6481
2	0.1353	0.3415
3	0.0498	0.1635
4	0.0183	0.0741
5	0.0067	0.0324
6	0.0025	0.0138
7	0.0009	0.0057
8	0.0003	0.0023

The multiscale analysis of data that has been correlated with the 2D exponential filter in equation (65) is shown in Figure 21.

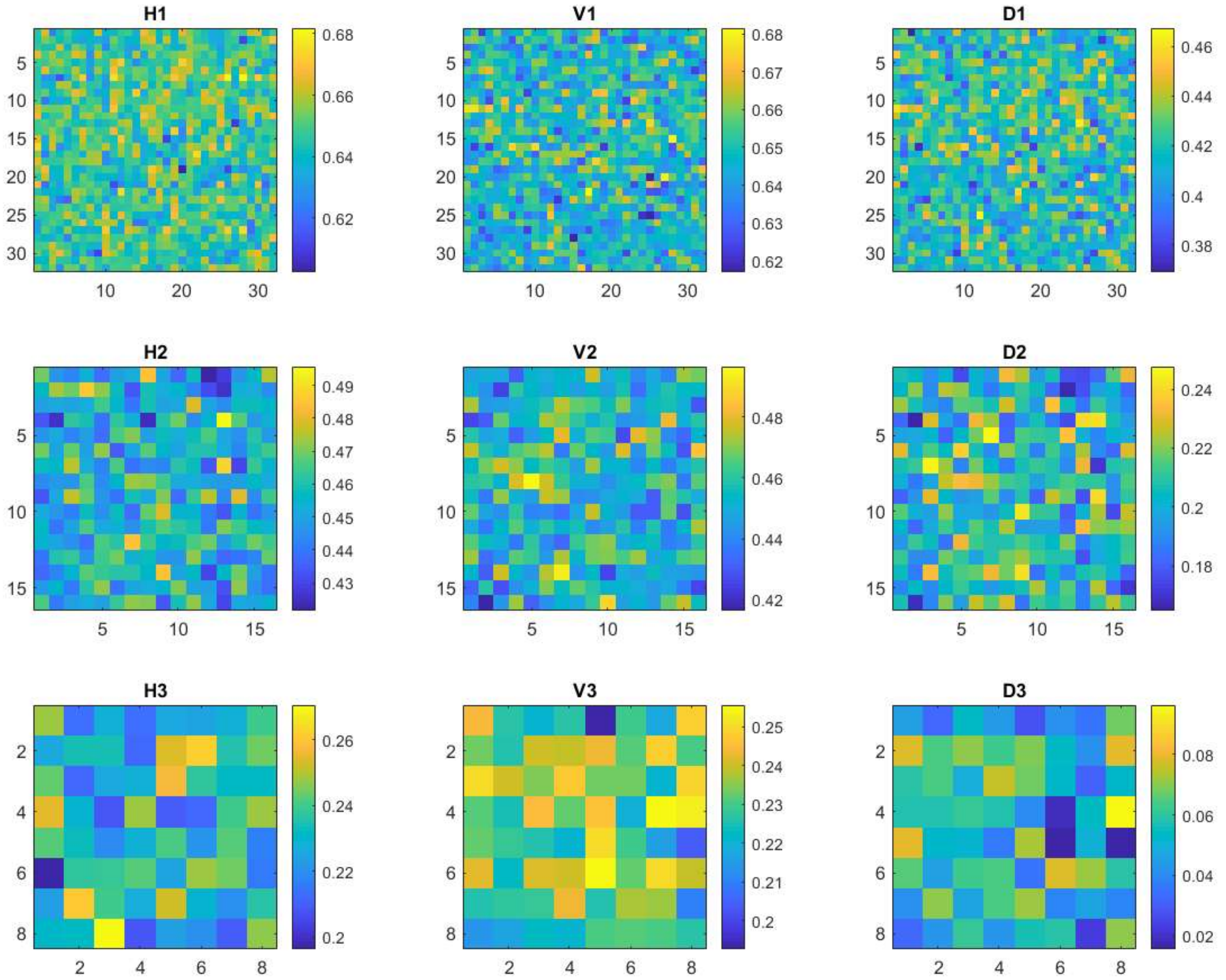

Figure 21: Multiscale Analysis of Data Correlation with Exponential Filter and Alpha of 1.0

The multiscale analysis estimates the directional correlation between groups of pixels at each scale. Referring to Figure 22, we see that the fist level of decomposition (left) equals the correlation of single-pixel offsets in the horizontal, vertical, and diagonal directions. However, in the second level of decomposition, we are estimating the correlation between the *groups* of pixels. For instance, the estimated level 2 horizontal correlation is the total correlation between the group of grey pixels and the group of red pixels. The total correlation in the case is a combination of correlations due to 1, 2, or 3 horizontal pixel offsets, and 0 or 1 vertical pixel offsets.

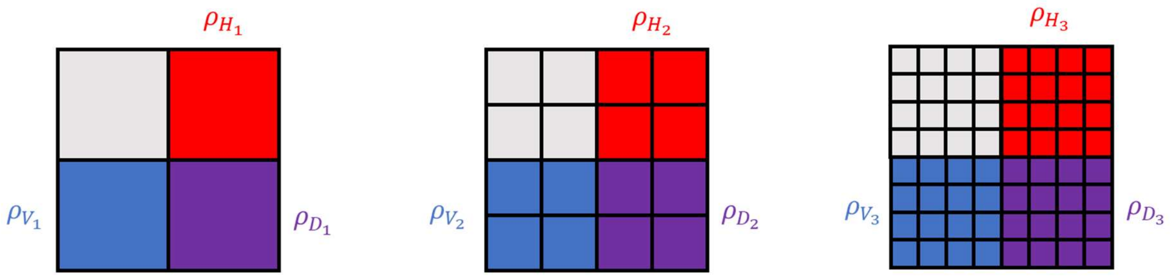

Level 1 Decomposition

Level 2 Decomposition

Level 3 Decomposition

Figure 22: Multiscale Directional Correlation

From Figure 21, we see that the multiscale analysis provides average estimated directional correlations over scale that are summarized in Table 4.

Table 4: Estimated Directional Correlations for Exponential Correlating function and Alpha of 1.0

Correlation	**H**	**V**	**D**
Level 1	0.647	0.648	0.420
Level 2	0.454	0.454	0.205
Level 3	0.232	0.232	0.054

Table 4 shows that the level decomposition provides estimated directional correlations that are consistent with the single pixel offset correlations shown in Table 3. The two-dimensional exponential filter is created from the multiplication of two one-dimensional exponential functions as in equation (65). Therefore, one would expect the single-pixel diagonal component to be the product of the single-pixel offsets in the horizontal and vertical directions. In Table 4, we see that the level 1 diagonal component is approximately equal to product of the horizontal and vertical components. In fact, for all decomposition levels in Table 4, the diagonal component is approximately the product of the horizontal and vertical components.

For the level 2 and level 3 decomposition levels, the estimated correlations are actually a mixture of different horizontal and vertical offset correlation values between pairs of pixels, and the total directional correlations represent the correlation between block groups of pixels as demonstrated in Figure 22.

The proposed method for estimation of multiscale directional correlations from samples of correlated data has been validated and agrees with the calculation of expected values.

4 NUMERICAL SIMULATION OF ISAR CLUTTER

4.1 SIMULATION OF ISAR CLUTTER USING MULTISCALE MODEL PARAMETERS

Two methods for simulating additional ISAR image samples based on the multiscale statistics are proposed. Both methods involve the concept of applying a 2D directional correlating filter to random seed data and scaling for image mean and variance. The first method uses a correlating filter with exponentially decaying magnitude, and with horizontal and vertical shape parameters that describe the directional rate of decay of the filter. These shape parameters are calculated from estimated directional correlations. The second method involves the derivation of a more arbitrary correlating function that, when applied to random seed data, will result in the desired multiscale correlations that have been estimated form the original data over multiple scales. This correlating function has parameters for each direction at each scale which define the shape of the correlating filter. Both methods define filter parameters across all image pixels, based on the estimated directional correlations from the multiscale analysis. Both methods will be compared to a more computationally complex third method that involves generating multivariate samples from the entire sample covariance matrix, which is the upper limit to correlation fidelity.

4.2 SIMULATION METHOD 1 – EXPONENTIAL CORRELATING FILTER

Upon estimation of the multiscale directional correlation we can form a correlating filter that, when applied to random seed data, will result in the desired correlation between image pixels at one or more scales. If we assume an exponential correlating filter shape, then only correlations estimated from the first level of multiscale decomposition are needed to form the exponential filter. This is because we only need the single pixel offset correlation to fully characterize the exponential decay. The goal is to form a directional exponential correlating filter that, when applied to random seed data, will result in the desired directional correlation. The random seed data is labeled $I_s(r,c)$ where r and c are the row and column indexes of the image, and each element of $I_s(r,c)$ is considered a normal random variable with zero mean and unit variance over the desired number of output image samples. We then define the correlating filter, in this case a 2D directional exponential filter, as shown in equation (69), where shape parameters α_H and α_V are found through analysis of the original data.

$$f(d_H, d_V) = \left[e^{-\left|\frac{d_H}{\alpha_H}\right|}\right]\left[e^{-\left|\frac{d_V}{\alpha_V}\right|}\right] = e^{-\left(\left|\frac{d_H}{\alpha_H}\right|+\left|\frac{d_V}{\alpha_V}\right|\right)} \tag{69}$$

4.2.1 Estimation of Exponential Correlating filter Shape Parameters

The estimated directional correlations calculated in the previous section are useful for multiscale analysis of the clutter. However, under the assumption that correlation can be modeled as the application of correlating filters to random data, the correlating filter shape parameters $\alpha_{H_{xy}}$ and $\alpha_{V_{xy}}$ are needed for generating representative image samples from random seed data. The correlating filter shape parameters can be estimated from the directional correlations found in the previous multiscale analysis section.

Consider the one-dimensional case of two correlated image pixels, I_{f_1} and I_{f_2} that are each formed as a weighted sum of independent normally distributed seed variables I_{s_1} through I_{s_8}, as shown in Figure 23.

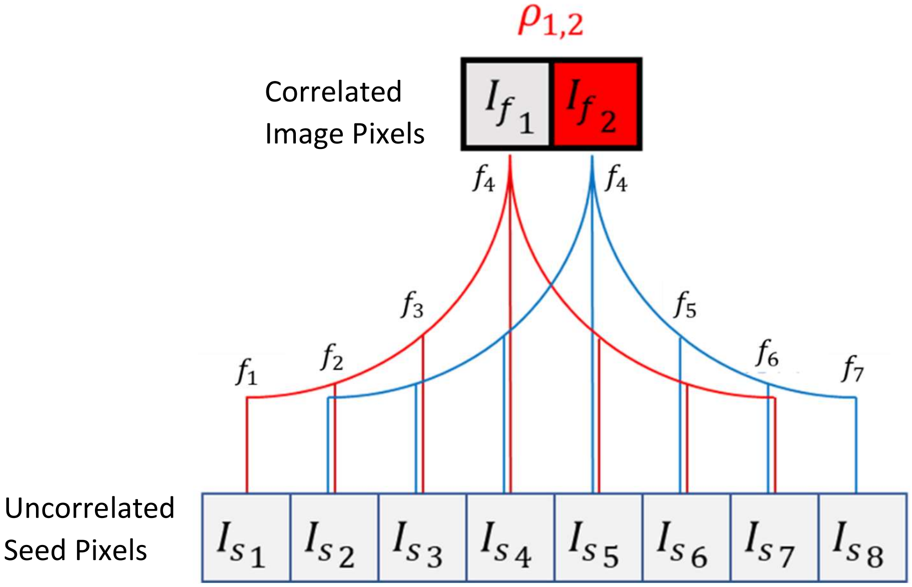

Figure 23: Image pixels modeled as weighted sums of independent seed variables

The red and blue correlating functions, f_1 and f_2, need not be the same but will be considered the same here as f. The filter is expressed as equations (70) through (72), where the index d is an integer that represents pixel distance from filter center over some finite distance $\pm d_n$.

$$f(d) \tag{70}$$

$$d \in I \tag{71}$$

$$-d_n \leq d \leq d_n \tag{72}$$

The covariance between pixels I_{f_1} and I_{f_2} is given in equation (73), and this leads to the correlation between I_{f_1} and I_{f_2} in equations (75) and (76). Since the seed pixels have been created with zero mean and unit variance, the value of $\sigma^2_{I_{s_n}}$ will be unity.

$$cov\left(I_{f_1}, I_{f_2}\right) = cov\left(\sum_{n=1}^{7} f(n) I_{s_n}, \sum_{n=2}^{8} f(n-1) I_{s_n}\right) \tag{73}$$

$$cov\left(I_{f_1}, I_{f_2}\right) = \sum_{n=2}^{7} \sigma_{I_{s_n}}^2 f(n) f(n-1) = \sum_{n=2}^{7} f(n) f(n-1) \tag{74}$$

$$\rho_{I_{f_{m1,m2}}} = \frac{cov\left(I_{f_1}, I_{f_2}\right)}{\sigma_{I_{f_1}} \sigma_{I_{f_2}}} = \frac{1}{\sigma_{I_{f_1}} \sigma_{I_{f_2}}} \sum_{n=2}^{7} f(n) f(n-1) \tag{75}$$

$$\sigma_{I_{f_1}} \sigma_{I_{f_2}} = \sum_{n=1}^{8} f^2(n) \tag{76}$$

Equations (75) and (76) can be written in more general form for an arbitrary distance between pixels given a defined correlating function with total length of D and pixel separation d, shown in equations (77) and (78).

$$\rho_{I_{f_{1,2}}}(d) = \frac{1}{\sigma_{I_{f_1}} \sigma_{I_{f_2}}} \sum_{n=d+1}^{D-d} f(n) f(n-1) \tag{77}$$

$$\sigma_{I_{f_1}} \sigma_{I_{f_2}} = \sum_{n=1}^{8} f^2(n) \tag{78}$$

Equations (77) and (78) are for the one-dimensional case, but it can be shown that with correlating filters formed from the tensor product of one-dimensional filters, equations (77) and (78) are still applicable. Therefore, from equation (77) and (78), the horizontal or vertical correlation at pixel separation distance d is equal to the sum of the two-dimensional correlating filter multiplied by a d-pixel shifted version of itself and divided by the sum of the product of the unshifted filter coefficients, where the shift occurs in the horizontal or vertical direction. The two-dimensional calculation for a DxD filter is shown in equations (79) through (81), where r and c are the row and column coordinates for the two-dimensional filter coefficients, respectively.

$$\rho_{I_{f_{1,2}}}(d_H) = \frac{1}{\sigma_{I_{f_1}} \sigma_{I_{f_2}}} \sum_{r=1}^{D} \sum_{c=d_H+1}^{D-d_H} f(r, c+d_H) f(r, c) \tag{79}$$

$$\rho_{I_{f_{1,2}}}(d_V) = \frac{1}{\sigma_{I_{f_1}}\sigma_{I_{f_2}}} \sum_{c=1}^{D} \sum_{r=d_V+1}^{D-d_V} f(r+d_V,c)f(r,c) \tag{80}$$

$$\sigma_{I_{f_1}}\sigma_{I_{f_2}} = \sum_{r=1}^{D}\sum_{c=1}^{D} f^2(r,c) \tag{81}$$

This is a simple calculation when the filter is known but the inverse problem of finding filter shape parameters from the correlation is not straight forward. Curve fitting techniques can be used to estimate the function that maps correlation to filter shape parameters, and the inverse of that function can be used to find filter shape parameters that provide a desired correlation.

For example, with a one-dimensional exponential correlating function such as equation (82), we can find the relationship between correlation and α. This is done by evaluating equation (82) over a range of exponential decay parameters, in this case α.

$$f(\alpha,d) = e^{-\left|\frac{d}{\alpha}\right|} \tag{82}$$

Figure 24 shows the correlation calculation for the single-pixel offset ($d = 1$) of an exponential function with decay parameter α.

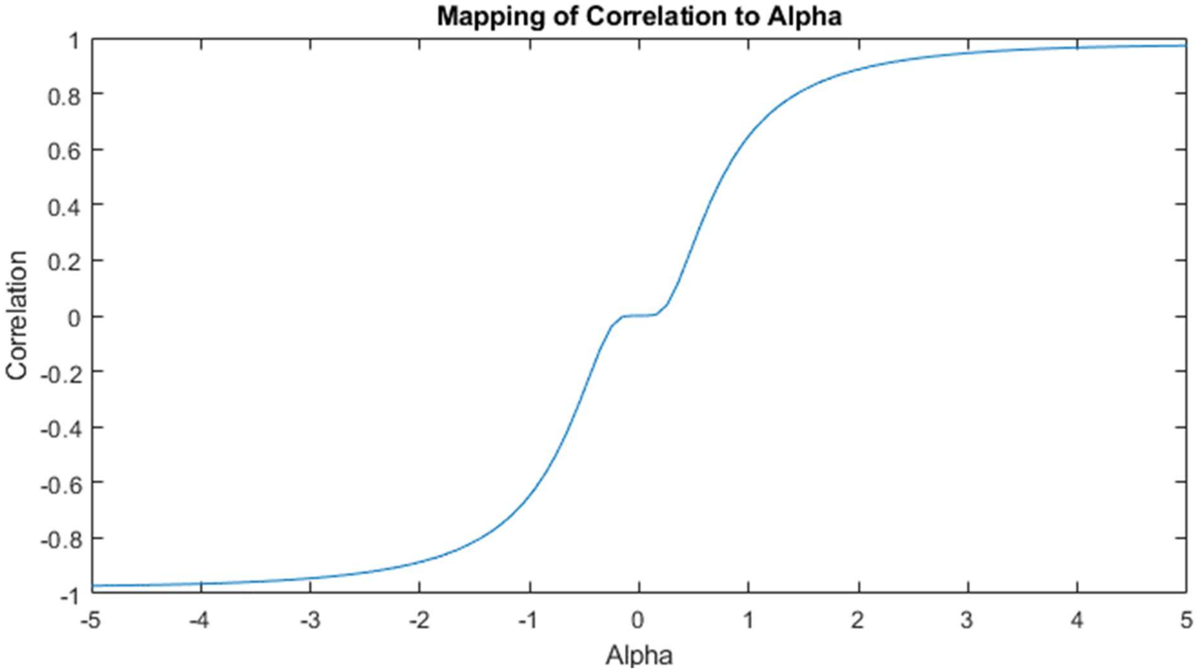

Figure 24: Mapping of Exponential Decay Parameter to Correlation

Once this is calculated for a chosen correlating function form, the inverse can be used to find the correlating filter decay parameter from the desired correlation. The correlating filter can then be applied to random seed data, resulting in the desired correlation between pixels.

4.2.2 Validation of Method 1 Shape Parameter Estimation

We can validate this process by correlating data with a two dimensional exponential filter with arbitrary shape parameters across the image, performing multiscale analysis to find the estimated directional correlations from the first decomposition level, then using the inverse curve fitting method above to estimate the shape parameters from the directional correlations. These should match the original shape parameters that were used to correlate the data.

The true directional image decay parameters are shown below, along with the estimated correlation. This estimated correlation is then used to estimate the decay parameters. Estimated decay parameters can then be compared to the known decay parameters used in generating the data to evaluate the estimation accuracy.

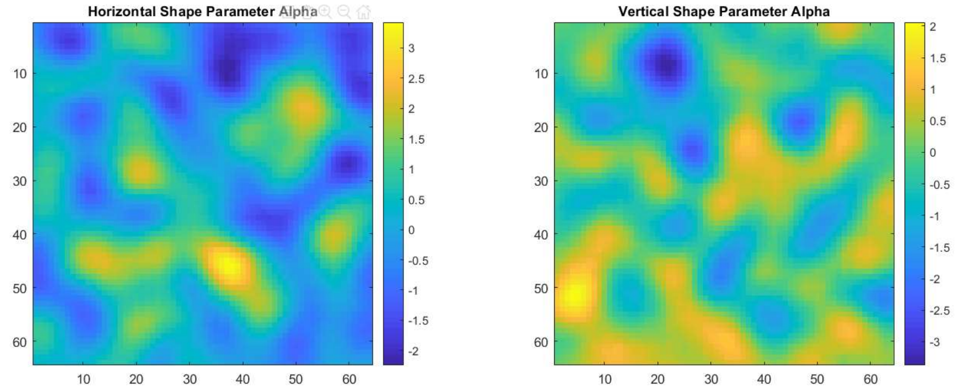
Horizontal Shape Parameter Alpha

Vertical Shape Parameter Alpha

Figure 25: Actual Shape Parameters used to Correlate Data

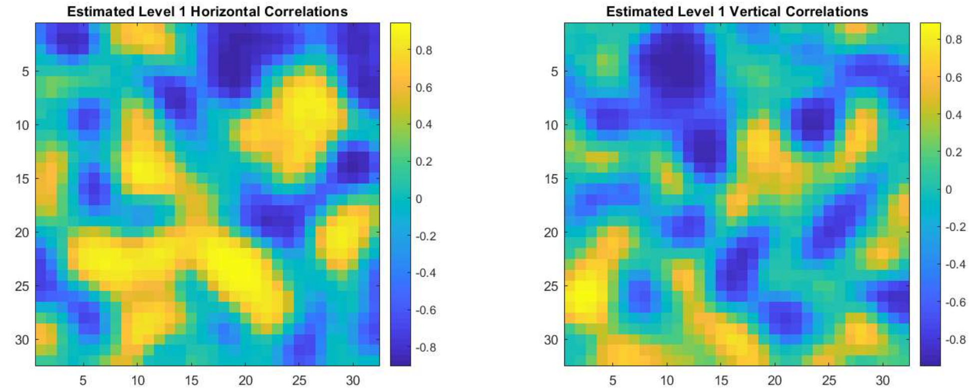
Estimated Level 1 Horizontal Correlations

Estimated Level 1 Vertical Correlations

Figure 26: Estimated Directional Correlation from Level 1 Multiscale Analysis

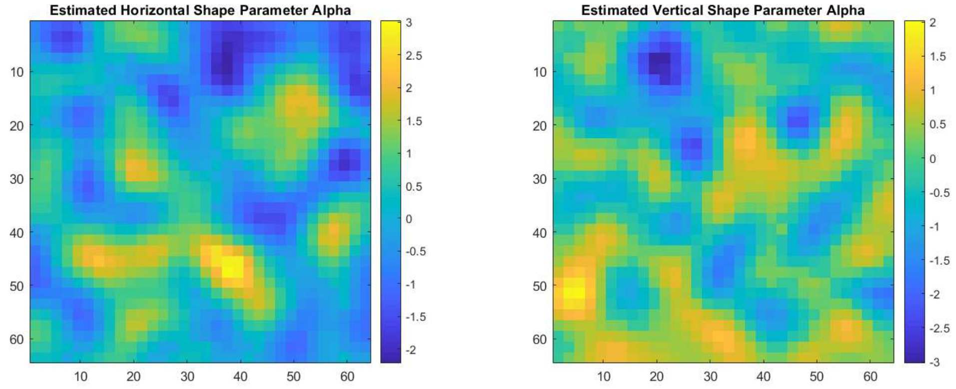
Estimated Horizontal Shape Parameter Alpha

Estimated Vertical Shape Parameter Alpha

Figure 27: Estimated Horizontal and Vertical Shape Parameters

Examination of Figure 25 through Figure 27 shows that the final estimated exponential decay parameters are in good visual agreement with the actual exponential decay parameters that were used to generate the simulated data.

4.2.3 Application of Two-Dimensional Exponential Correlating filter

Once the parametric correlating filter coefficients have been determined, the correlating filter is then applied to each of N images of the seed data in I_s according to equation (83), resulting in $I_c(r,c,n)$, which contains N images of size r x c with the desired correlation.

$$I_c(r,c,n) = \sum_{d_r=-d}^{d} \sum_{d_c=-d}^{d} I_s(r+d_r, c+d_c, n) \cdot f_{rc}(d_r, d_c) \tag{83}$$

The data in I_c can then be scaled for desired mean and variance (μ_f and σ_f^2) to obtain the final scaled output data, where $\sigma_c^2(r,c)$ is the sample variance of I_c over N images samples at pixel (r,c).

4.2.4 Negative Correlation

As presented, formulations for the exponential correlating filter will result only in positive correlation. However, negative correlation can certainly be present in correlated data so it must be accounted for. Since we are dealing with multiscale correlation, the ability to have positive or negative correlation at any one decomposition level is desirable. One method for achieving negative exponential correlation is shown in Figure 28. The signs of filter coefficients are chosen so that the correlation due to the product of the modified filter with its 1- 2- and 4-pixel shift results in approximately the negative correlation of the same pixel offsets with the original filter. This allows for the shifted product of the most significant filter coefficients to result in negative correlation at the 2^{n-1} pixel offset from decomposition level n. Negative correlation in the curve of Figure 24 was created in this manner. The symmetry of this curve demonstrates that negative correlations can be effectively represented this way.

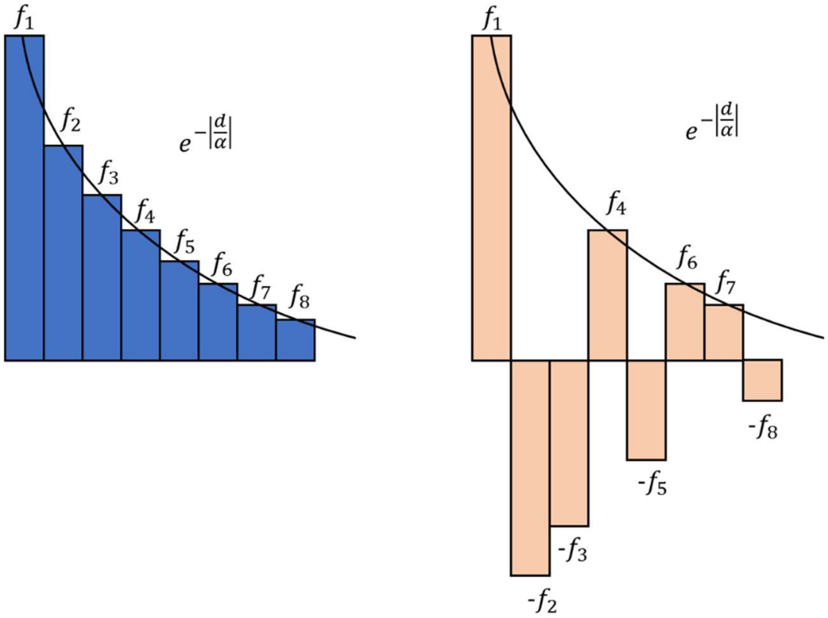

Figure 28: Negative Correlation

4.3 Simulation Method 2 – Non-Exponential Correlating filter

Not all correlated data can be accurately estimated by an exponential correlating filter. Use of an exponential filter means that correlations will always decay over distance. With scattering from vegetation, however, correlation in the image will depend on the physical structure and correlation can be much different at different scales. For instance, large branches may result in a high amount of correlation at low resolution scales, but correlation at higher resolutions might be smaller or even negative due to the motion of leaves. It is beneficial to have some additional flexibility in defining the correlating filter shape so that we can account for a wider range of multiscale correlations. Here we propose Method 2, where we define a correlating filter whose unidirectional shape is defined by three parameters. This filter is built according to Figure 29. The design of this filter is intended to provide some control over correlation over three levels of wavelet decomposition. The estimated correlations form the first decomposition level will be mostly impacted by the blue portions below, since the first decomposition level find correlations between adjacent pixels. The estimated correlations form the second decomposition level will be mostly impacted by the red portions below, since the second decomposition level find correlations between adjacent pairs of pixels, and so on. In the final step, we make the filter symmetric around the center value of 1 for the zero offset.

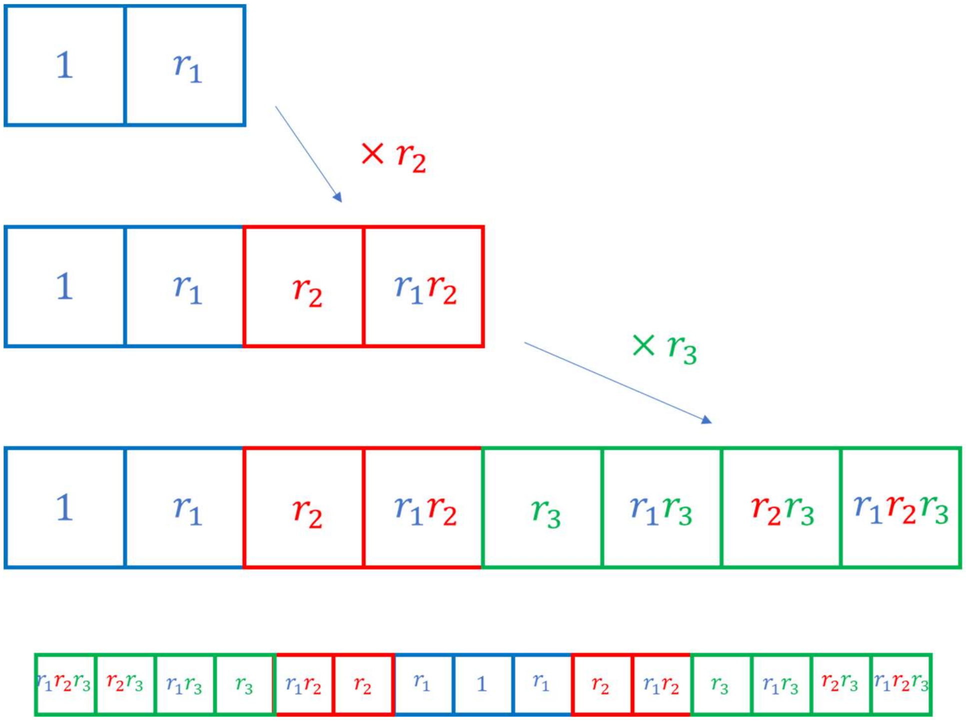

Figure 29: Formation of Correlating function from Three Shape Parameters

Examining equation (66), we know that the correlation of two pixels is calculated as the sum of the product of the overlapping sections of the correlating filter coefficients that were used to correlate the data. Equations (84) and (85) show the single-pixel offset correlation due to filter f, where f_n is the nth coefficient of filter f.

$$\rho_{1,2} = \frac{1}{\sigma_{I_{f_1}}\sigma_{I_{f_2}}} \sum_{n=d+1}^{D-d} f_n f_{n+d} \tag{84}$$

$$\sigma_{I_{f_1}}\sigma_{I_{f_2}} = \sum_{n=1}^{D} f_n^2 \tag{85}$$

This is useful for finding the correlation between two pixels, but we are also interested modeling the correlation between *groups* of pixels, such as the multiscale correlations. Consider Figure 30, where we are calculating correlation image pixels I_{f_m} from independent random seed variables I_{s_m}, using the four 7-element correlating functions. Here, we see I_{f_1} is a function of seed variables I_{s_1} through I_{s_7}, with filter coefficients f_n, with n an integer from 1 to 7. For simplicity, we will assume the correlating filters all have the same coefficients.

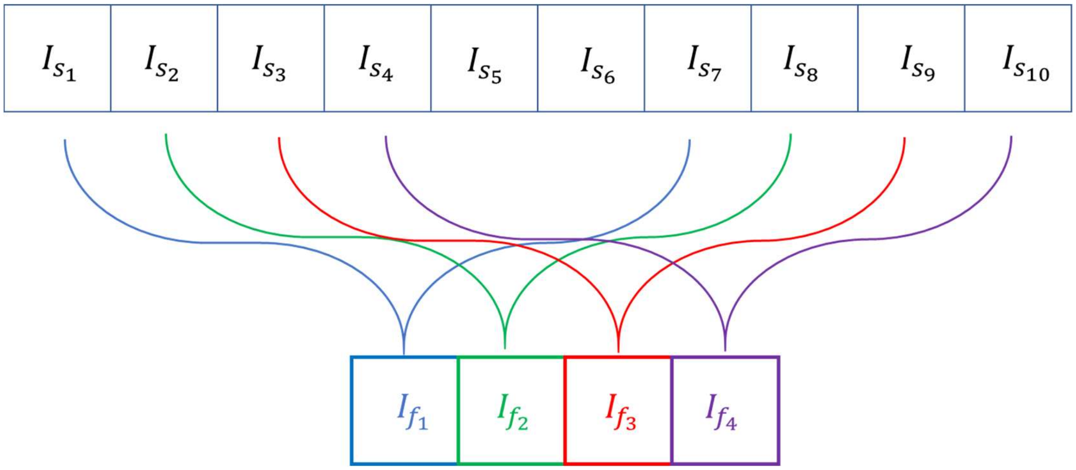

Figure 30: Pixel Group Correlation Example

Since the random seed variables are independent, the correlation between elements of I_{f_m} will depend on the common elements of I_{s_m}. For instance, I_{f_1} and I_{f_3} will be correlated due to both being composed of common seed elements I_{s_3} through I_{s_7}. For any two pixels in I_{f_m} we know the correlation is calculated as in equation (66). However, if we are decomposing the elements of I_{f_m} and want to find the correlation between two groups of pixels, such as in Figure 31, we treat the groups as a sum. This is shown in equation (86) and (87).

$$I_{f_{12}} = I_{f_1} + I_{f_2} = \sum_{n=1}^{7} f_n \, I_{s_n} + \sum_{n=2}^{8} f_{n-1} \, I_{s_n} \tag{86}$$

$$I_{f_{34}} = I_{f_3} + I_{f_4} = \sum_{n=3}^{9} f_{n-2} \, I_{s_n} + \sum_{n=4}^{10} f_{n-3} \, I_{s_n} \tag{87}$$

Grouping by overlapping elements of I_{s_n}, we can write these as equations (88) and (90) with variances given in equations (89) and (91).

$$I_{f_{12}} = f_1 I_{s_1} + f_7 I_{s_8} + \sum_{n=2}^{7} I_{s_n} \left(f_n f_{n-1} \right) \tag{88}$$

$$\sigma_{I_{f_{12}}}^2 = \sum_{n=d+1}^{D-d} f_n f_{n+d} \tag{89}$$

$$I_{f_{34}} = f_1 I_{s_3} + f_7 I_{s_{10}} + \sum_{n=4}^{9} I_{s_n} \left(f_{n-2} f_{n-3} \right) \tag{90}$$

$$\sigma_{I_{f_{34}}}^2 = \sum_{n=d+1}^{D-d} f_n f_{n+d} \tag{91}$$

$$\sigma_{I_{f_{12}}} \sigma_{I_{f_{34}}} = \sum_{n=d+1}^{D-d} f_n f_{n+d} \tag{92}$$

Gathering common I_{s_n} terms with $\sigma_{I_{s_n}}^2 = 1$, the correlation between these groups of pixels is shown in equation (94). Non-overlapping elements of I_{s_n} will not contribute to correlation.

$$\rho_{12,34} = \frac{1}{\sigma_{\mathrm{I}_{\mathrm{f}_{12}}} \sigma_{\mathrm{I}_{\mathrm{f}_{34}}}} \sum \mathrm{I}_{\mathrm{f}_{12}} \cdot \mathrm{I}_{\mathrm{f}_{34}} \tag{93}$$

$$\rho_{12,34} = \frac{1}{\sigma_{\mathrm{I}_{\mathrm{f}_{12}}} \sigma_{\mathrm{I}_{\mathrm{f}_{34}}}} \left\{ f_1 (f_2 + f_3) + \left[\sum_{n=1}^{4} (f_n + f_{n+1}) \, (f_{n+2} + f_{n+3}) \right] + (f_5 + f_6) f_7 \right\} \tag{94}$$

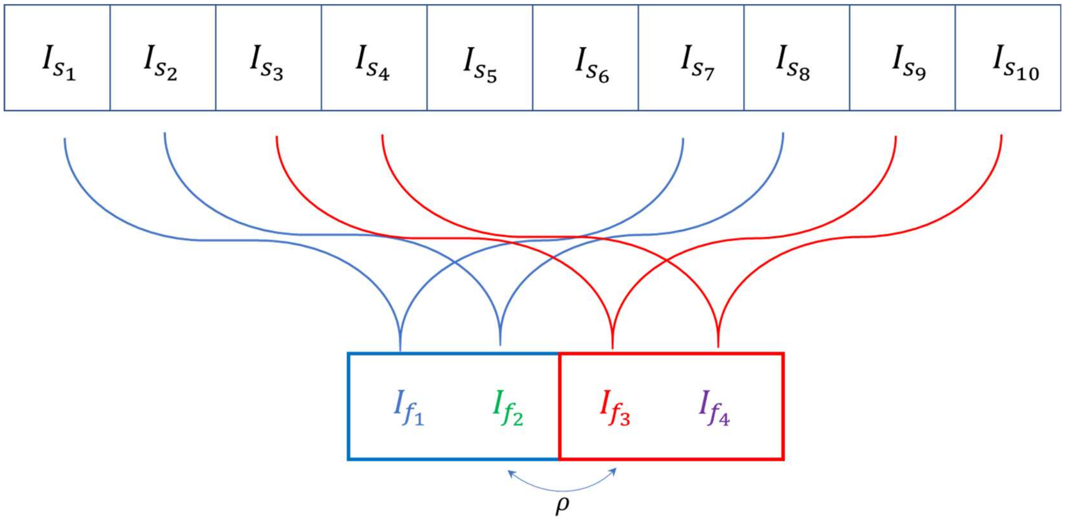

Figure 31: Correlation Example Between Groups of Pixels

In the same manner, we can show the correlation between two adjacent groups of four pixels.

$$\begin{aligned}\rho_{1234,5678} = \frac{1}{\sigma_{I_{f_{1234}}}\sigma_{I_{f_{5678}}}} [& f_1(f_2+f_3+f_4+f_5) + (f_1+f_2)(f_3+f_4+f_5+f_6) \\ & + (f_1+f_2+f_3)(f_4+f_5+f_6+f_7) + (f_1+f_2+f_3+f_4)(f_5+f_6+f_7) \\ & + (f_2+f_3+f_4+f_5)(f_6+f_7) + (f_3+f_4+f_5+f_6)f_7]\end{aligned} \tag{95}$$

$$\sigma_{I_{f_{1234}}}\sigma_{I_{f_{5678}}} = f_1(f_2+f_3) + \left[\sum_{n=1}^{4}(f_n+f_{n+1})(f_{n+2}+f_{n+3})\right] + (f_5+f_6)f_7 \tag{96}$$

In our multiscale analysis using wavelet decomposition, we are essentially looking at correlation between adjacent pixels in the level 1 decomposition, correlation between two groups of four pixels in the level 2 decomposition, and so on. Although equations (94) and (95) are for the one-dimensional case, the same theory can be applied, albeit with more complicated equations.

Using our arbitrary correlating function from Figure 29 along with equation (94), we can calculate the expected correlations due to correlating parameters r_1, r_2, r_3 for a desired direction. However, this is a nonlinear equation and finding r_1, r_2, r_3 from the desired correlations $\rho_{1,2}$, $\rho_{12,34}$, and $\rho_{1234,5678}$ can be achieved using nonlinear solvers. In our application, the filter shape parameters can be found from the estimated directional multiscale correlations. It should be noted here that not all desired correlation combinations can be mapped to a set of r_1, r_2, r_3 parameters. Care must be taken to bound the parameters so that the solver does not diverge. The nonlinear solution here is one example and solver options were not evaluated in the scope of this dissertation.

4.3.1 Estimation of Correlating Filter Shape Parameters

The nonlinear inverse problem can be solved by many methods. For simplicity, we use a gradient descent algorithm to adjust the shape parameters until the calculated correlation converges to the desired correlations. An example result is shown below in Figure 32, where we perform the gradient descent over 100 iterations. In this case, we are trying to find correlating filter shape parameters that will converge to a level 1 correlation of 0.3, a level 2 correlation of -0.25, and a level 3 correlation of 0.2. Initial shape parameter values are arbitrarily chosen to be one-half of the desired correlation values.

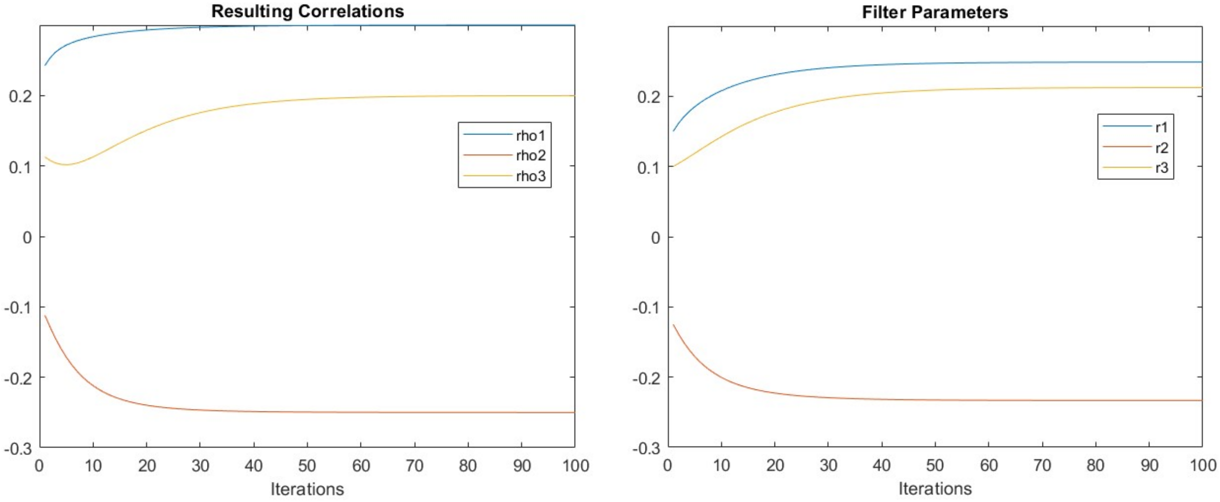

Figure 32: Gradient Descent Solution of Filter Parameters

Figure 32 shows convergence of the correlations to the desired values of $\rho_1 = 0.3$, $\rho_2 = -0.2$, and $\rho_3 = 0.1$. This multiscale correlation was achieved using the correlating filter shape parameters of $r_1 = 0.248$, $r_2 = -0.233$, and $r_3 = 0.212$. The resulting correlating filter is shown below in Figure 33.

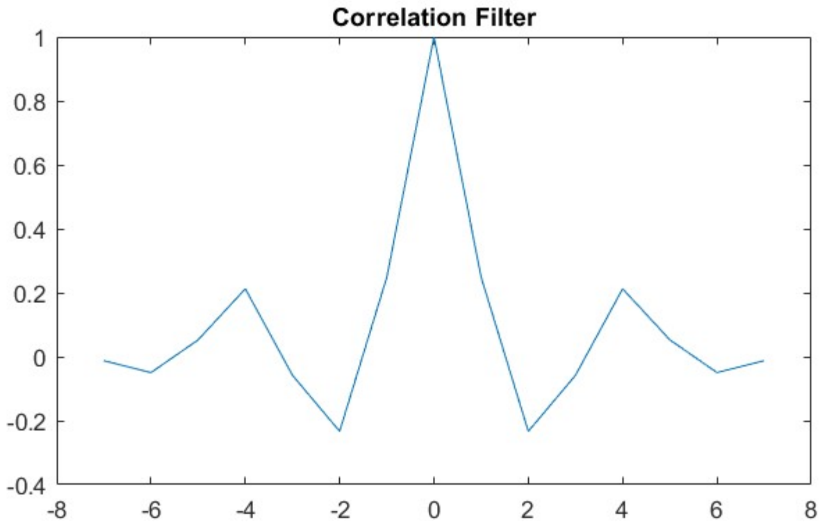

Figure 33: Calculated Correlating filter for Desired Correlation

4.3.2 Validation of Method 2 Shape Parameter Estimation

This proposed simulation method can be validated by forming correlating data using a non-exponential correlating filter with arbitrary shape parameters, performing multiscale analysis to find the estimated multiscale directional correlations, then using the method above to estimate the shape parameters from the directional correlations.

The arbitrary original r1, r2, and r3 horizontal and vertical correlating filter shape parameters used to create the correlated data are shown below in Figure 34.

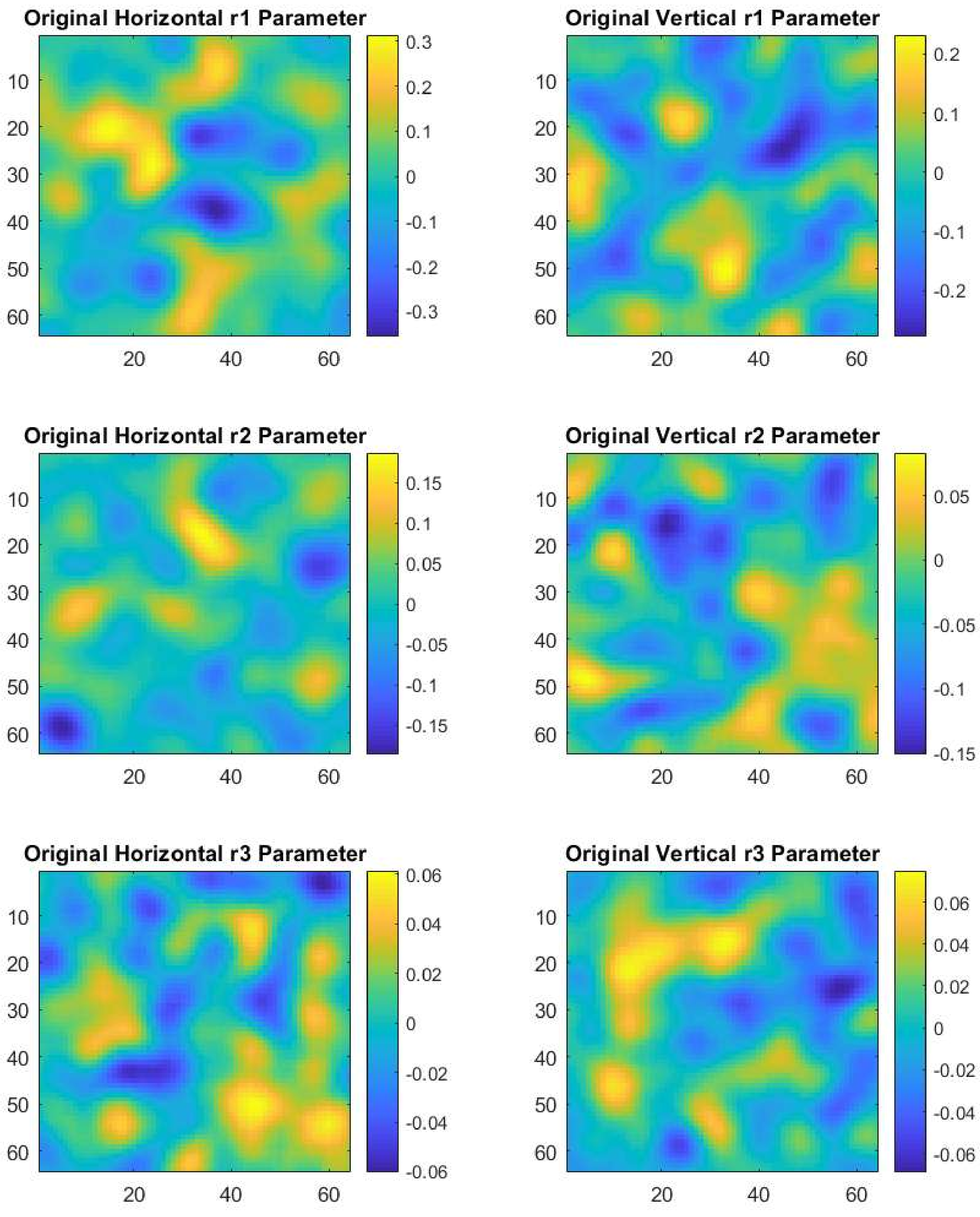

Figure 34: Actual Shape Parameters used to Correlate Data

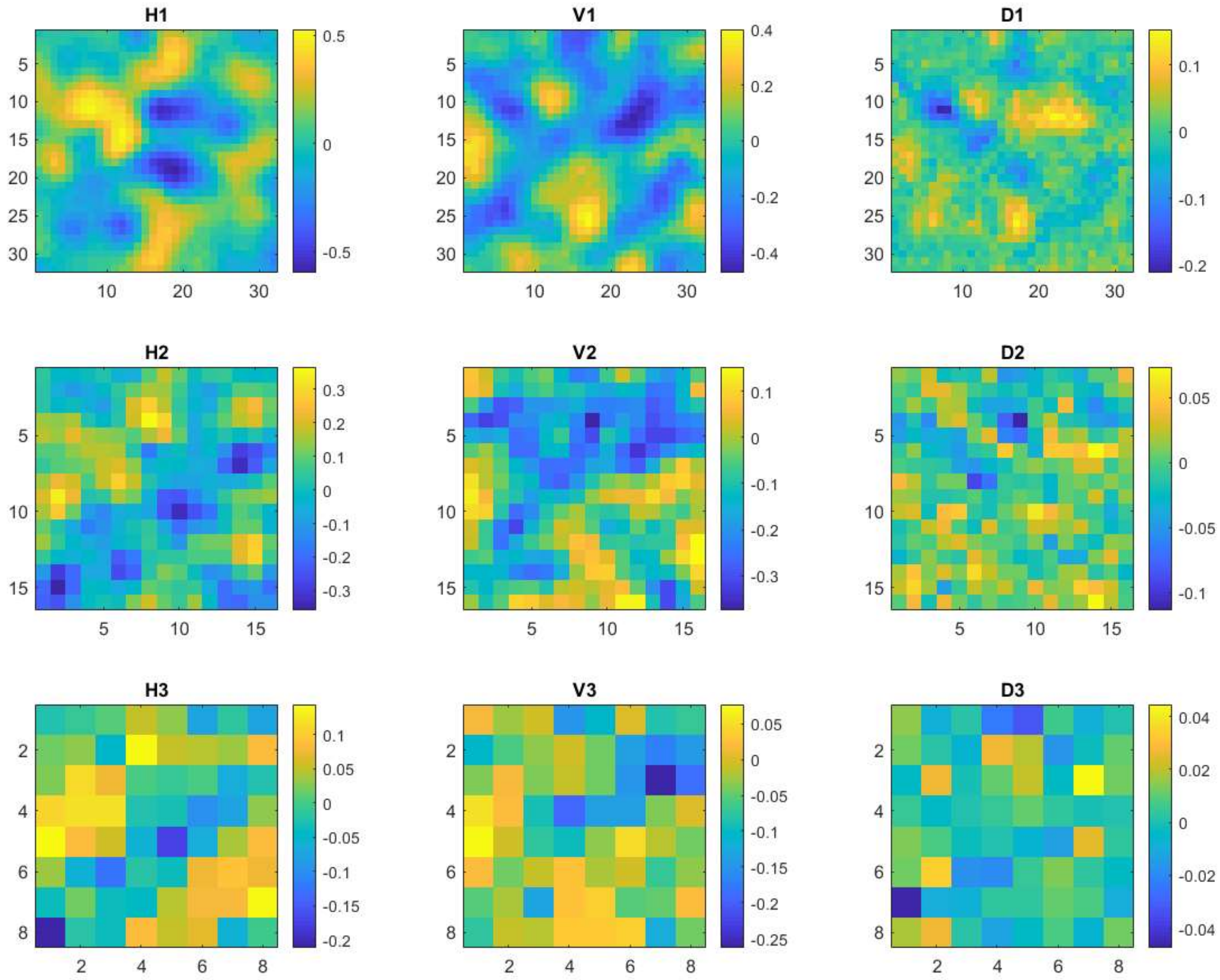

Figure 35: Estimated Directional Correlation from Multiscale Analysis

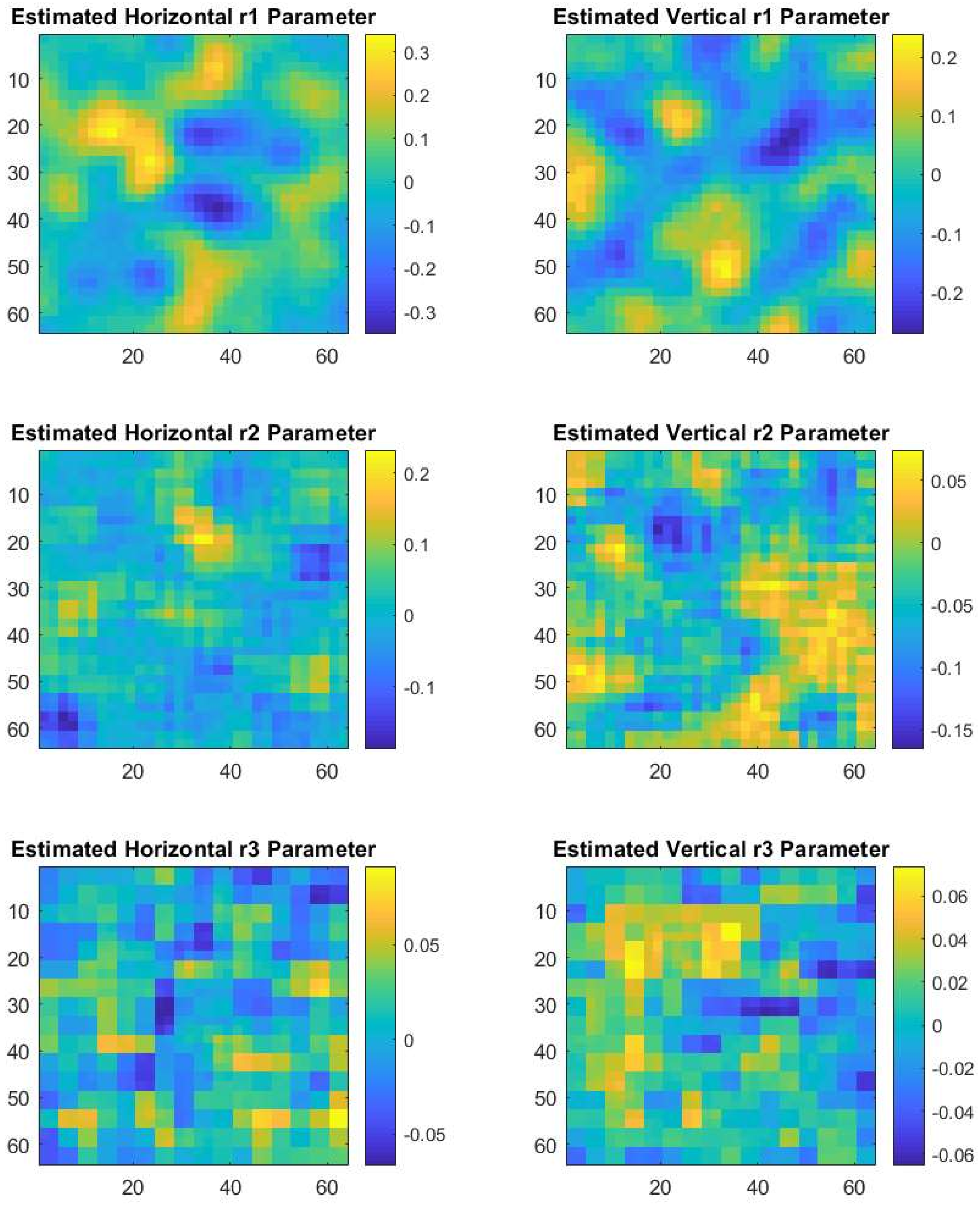

Figure 36: Estimated Horizontal and Vertical Shape Parameters

Examination of Figure 34 through Figure 36 shows that estimated shape parameters are in good agreement at level 1 decomposition, but diverge somewhat from the actual parameters as the decomposition level increases. However, the goal is not to estimate the exact correlating filter shape parameters themselves, but to recreate the correlation in the original data. If we use the estimated correlating filter shape parameters in Figure 36 to generate additional data and perform multiscale analysis on that data, we can get a good comparison of the method's ability to generate additional representative samples. This comparison is shown below for each correlation direction.

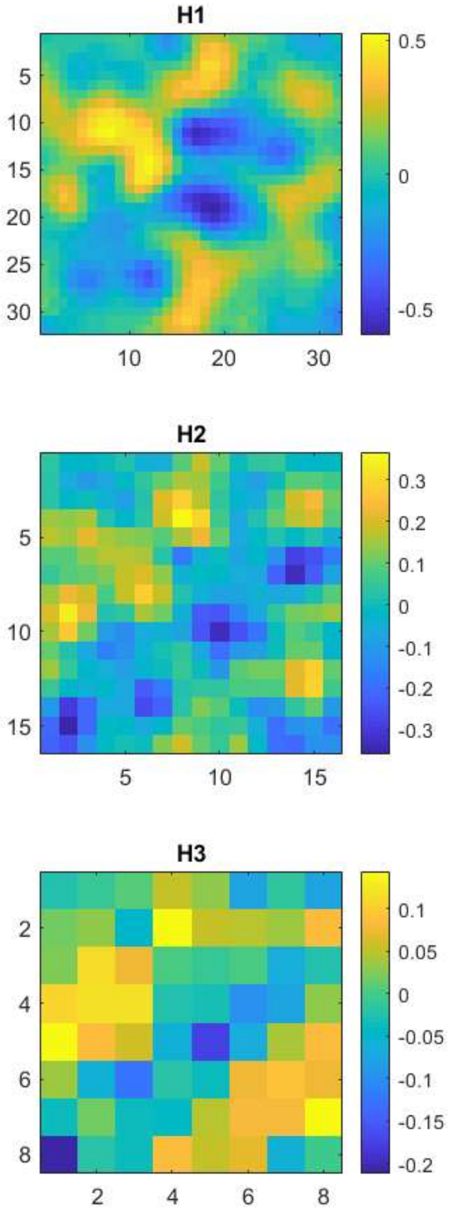

Figure 37: Horizontal Correlations from Original Data

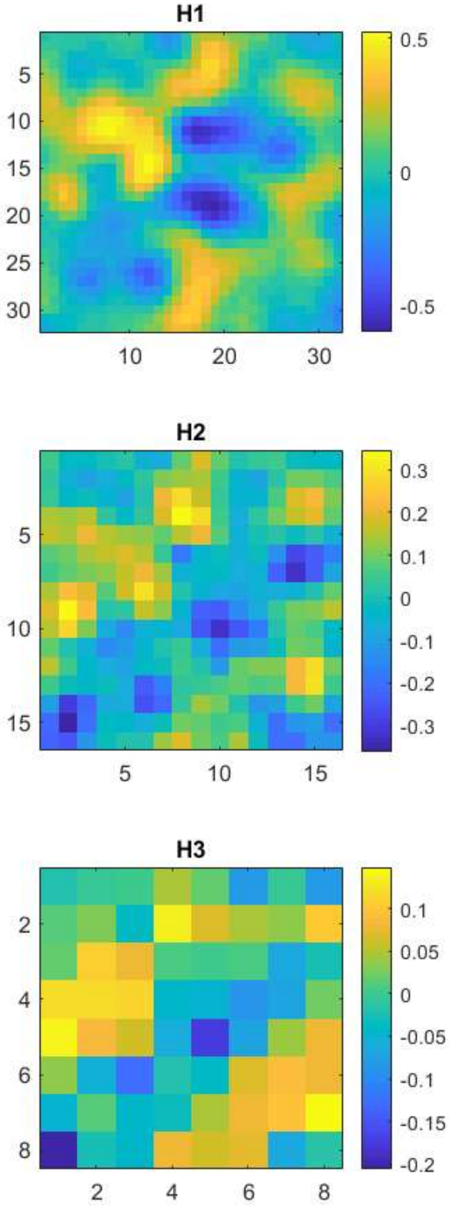

Figure 38: Horizontal Correlations from Simulated Data

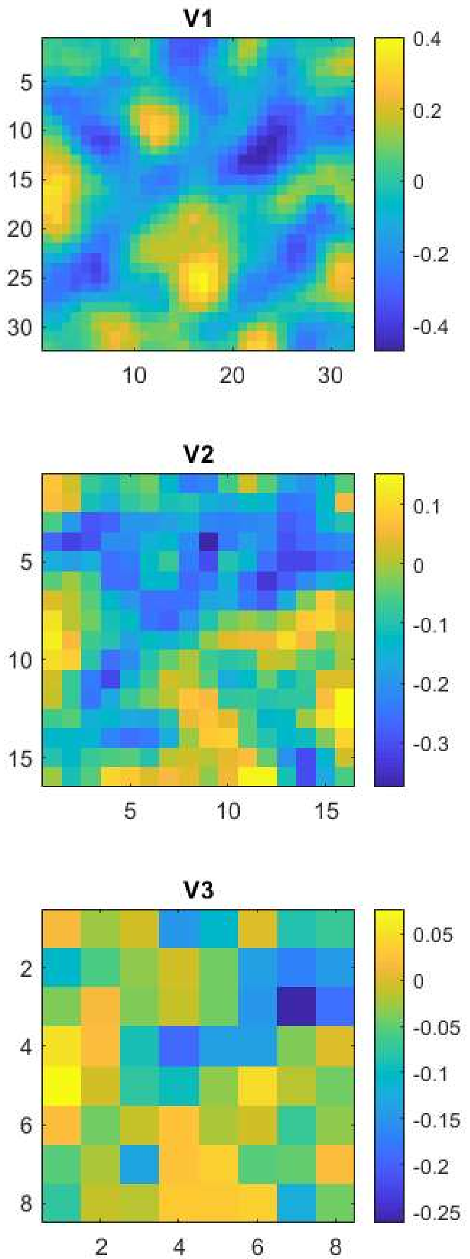

Figure 39: Vertical Correlations from Original Data

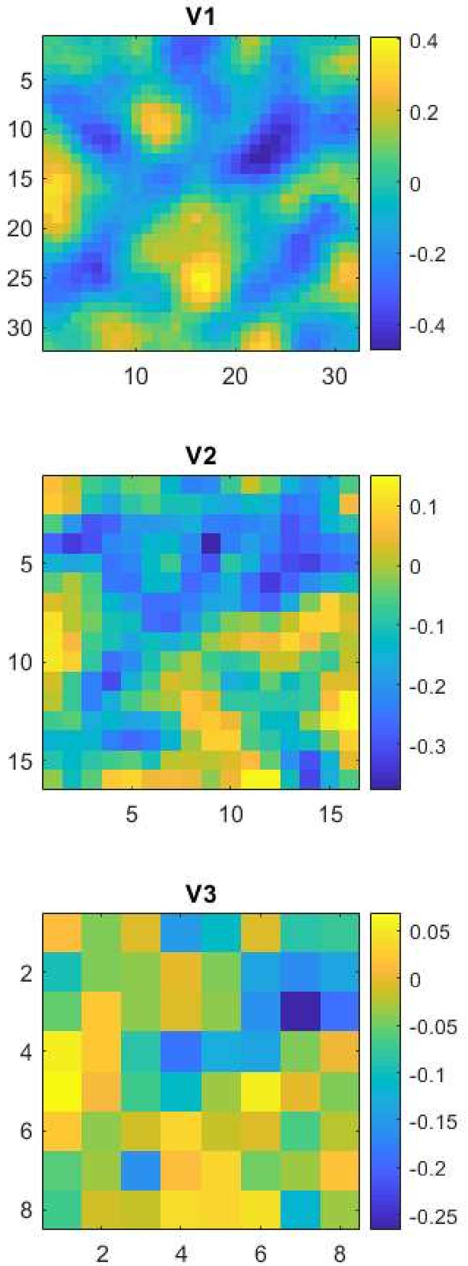

Figure 40: Vertical Correlations from Simulated Data

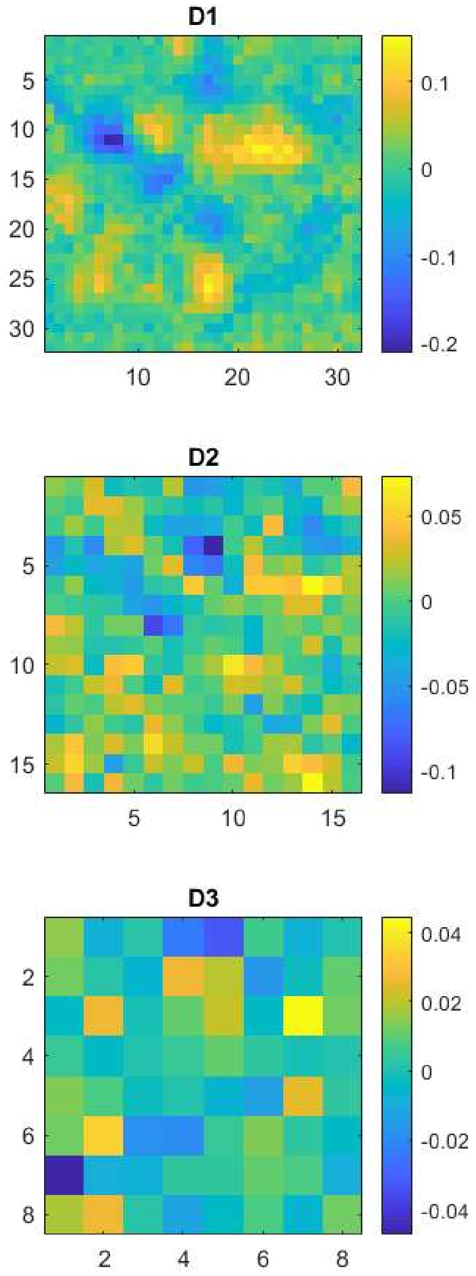

Figure 41: Diagonal Correlations from Original Data

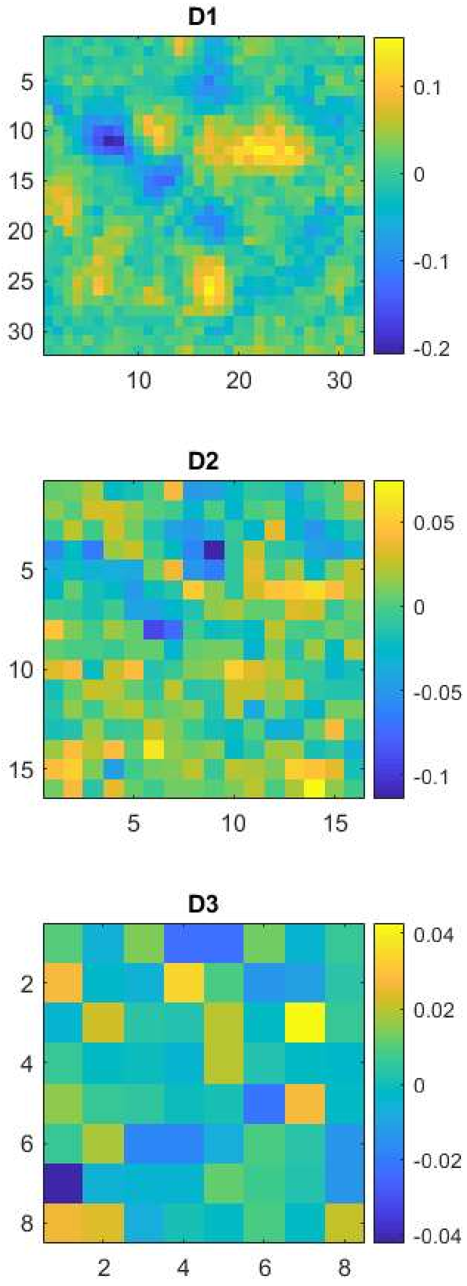

Figure 42: Diagonal Correlations from Generated Data

Examination of Figure 37 through Figure 42 shows that although the estimated shape parameters in Figure 36 differ from the original shape parameters, the data generated from the estimated shape parameters results in a multiscale correlation estimate that is visually very close to the estimated correlations of the original data. This indicates that the correlating filter coefficients are not unique to the desired correlations and we only need to find one correlating filter solution that provides the desired multiscale correlations.

Although this visual agreement is a good indication of the accuracy of the method, we need a more qualitative analysis to gauge the effectiveness of each method in generating data. This is addressed with image similarity measures.

4.4 EXPERIMENTAL VALIDATION OF ISAR CLUTTER SIMULATION METHODS

The similarity measures described above will be used to evaluate the two data simulation methods. The KL divergence method will compare distributions. In our application of sets of multiple images, this measure can be used to compare the distribution over samples at each pixel, as well as the distribution of image pixels in a local area of each image. Distributions will be estimated by the histogram of the pixels, using the same binning values for each comparison.

4.4.1 Simulation of General Correlated Data

Correlated data is generated using both proposed methods and compared to the original data and other methods. Both data simulation methods are used to generate additional samples and similarity measures are used to evaluate the data simulation methods. Multivariate data simulation using the entire sample covariance matrix is used as a baseline for comparison and this is referred to as *full covariance baseline data* in the following metrics. Table 5 Summarizes the data used for comparison.

Table 5: Description of Dataset Names in Similarity Metrics

Dataset Name	**Data Description**
Original Data	The original data to be simulated
Baseline Full Covariance Data	New Data simulated using the full covariance matrix and multivariate generation methods
Method 1 Data	New Data simulated using method 1 above
Method 2 Data	New Data simulated using method 2 above

Summaries of the similarity measures for simulated and measured data are provided below, and plots of the pixel-based similarities and associated histograms can be found in Appendix B and Appendix C for simulated and measured data, respectively.

4.4.1.1 Summary of Similarity Measures for General Correlated Data

Simulated data using both methods was created using both an exponential correlating filter and a non-exponential correlating filter. Multiscale analysis is performed on both simulated data sets to estimate the directional multiscale correlation of each data set. Multiscale correlation similarity measures are calculated to quantitatively show the simulation accuracy of each method. In the similarity measures below, lower numbers indicate more similar correlation data. Correlation similarity measures are calculated for level 1 only, and for all three decomposition levels.

Table 6: Multiscale Correlation Similarity Results Summary for Simulated Data

	Additional Samples Using Full Covariance		**Additional Samples Using Method 1**		**Additional Samples Using Method 2**	
	Average Level 1 Correlation Similarity	Average Level 1-3 Correlation Similarity	Average Level 1 Correlation Similarity	Average Level 1-3 Correlation Similarity	Average Level 1 Correlation Similarity	Average Level 1-3 Correlation Similarity
Data Generated with Exponential Correlating function	0.0154	0.0157	0.0172	0.0201	0.0172	0.0170
Data Generated with Non-Exponential Correlating function	0.0106	0.0137	0.0111	**0.1151**	0.0152	0.0167

Method 2 Has Better Ability to Produce Desired Level 2 and 3 Correlations

Table 7: Covariance Matrix Similarity Summary for Simulated Data

	Additional Samples Using Method 1	**Additional Samples Using Method 2**
Original Data with Exponential Correlating function	0.7531	0.7534
Original Data with Non-Exponential Correlating function	0.5058	0.3747

Method 2 Covariance Matrix is more Similar to Original Covariance Matrix

Table 8: Mean KL Divergence of Full Covariance Data by Pixel and 8x8 Image Area

Full Covariance Data	**Mean KL Divergence by Pixel**		**Mean KL Divergence By 8x8 Image Area**	
Data Set	Real	Imaginary	Real	Imaginary
Data Generated with Exponential Correlating function	0.0017	0.0017	3.53E-06	3.35E-06
Data Generated with Non-Exponential Correlating function	0.0016	0.0016	3.80E-06	3.81E-06

Table 9: Mean KL Divergence of Method 1 by Pixel and 8x8 Image Area

Method 1	**Mean KL Divergence by Pixel**		**Mean KL Divergence By 8x8 Image Area**	
Data Set	Real	Imaginary	Real	Imaginary
Data Generated with Exponential Correlating function	0.0013	0.0013	2.89E-05	2.75E-05
Data Generated with Non-Exponential Correlating function	0.0013	0.0013	2.96E-05	2.80E-05

Table 10: Mean KL Divergence of Method 2 by Pixel and 8x8 Image Area

Method 2	**Mean KL Divergence by Pixel**		**Mean KL Divergence By 8x8 Image Area**	
Data Set	Real	Imaginary	Real	Imaginary
Data Generated with Exponential Correlating function	0.0013	0.0013	2.89E-05	2.67E-05
Data Generated with Non-Exponential Correlating function	0.0013	0.0013	3.02E-05	2.92E-05

Both Methods Have an Order of Magnitude Less Similarity to Original Distribution as Compared to Data Simulated with Full Covariance Matrix

4.4.2 Simulation of Physical ISAR Measurements

The data under analysis is two-dimensional ISAR measurements of Plants D and E in the presence of two speeds of forced air from one direction to simulate wind. Refer to the background material for more information on physical measurements. Wind speed was not measured but is characterized as light wind and medium wind. The light wind resulted in small deflection of the leaves, whereas the medium wind resulted in significant deflection of branches and leaves. Photos of the two plants are shown below in Figure 43 and Figure 44. These plants were chosen for their difference in structure for comparison. Plant D has many smaller leaves on many smaller branches. Plant E has fewer large leaves on a few larger stalks.

Figure 43: Plant Species D

Figure 44: Plant Species E

Each measurement scenario consists of 2D samples of a plant in the presence of wind. The ISAR data for each plant and wind speed is structured into 100 samples of the clutter equivalent current. Each image pixel represents a complex-valued resolution cell on this projected xy image plane. The data for each measurement scenario is structured as a 3D matrix of size 64x64x100, where each of the 100 image samples is a 64x64 complex-valued 2D image.

4.4.2.1 Summary of Similarity Measures for Physical ISAR Measurements

Simulation methods 1 and 2 were used to simulate additional samples of data and these are compared to the samples of original data. In the similarity measures below, lower numbers indicate more similar data.

Table 11: Multiscale Correlation Similarity Results Summary for Simulated Data

	Additional Samples Using Full Covariance		**Additional Samples Using Method 1**		**Additional Samples Using Method 2**	
	Average Level 1 Correlation Similarity to Original Data	Average Level 1-3 Correlation Similarity to Original Data	Average Level 1 Correlation Similarity to Original Data	Average Level 1-3 Correlation Similarity to Original Data	Average Level 1 Correlation Similarity to Original Data	Average Level 1-3 Correlation Similarity to Original Data
Plant D, Light Wind	0.0465	0.0456	0.0591	**0.2000**	0.0599	0.0668
Plant D, Medium Wind	0.0476	0.0479	0.0590	**0.2051**	0.0590	0.0733
Plant E, Light Wind	0.0453	0.0473	0.0638	**0.2137**	0.0657	0.0769
Plant E, Medium Wind	0.0467	0.0472	0.0598	**0.1907**	0.0592	0.0635

Method 1 Has Inferior Ability to Produce Desired Level 2 and 3 Correlations

Table 12: Correlation Matrix Similarity for Measured Data

Similarity of Generated Data Sample Covariance Matrix to Original Data Sample Covariance Matrix		
	Method 1	**Method 2**
Plant D, Light Wind	0.9745	0.9711
Plant D, Medium Wind	0.9744	0.9719
Plant E, Light Wind	0.9761	0.9705
Plant E, Medium Wind	0.9738	0.9704

Method 2 Covariance Matrix is Slightly Closer to Original than Method 1 Covariance Matrix

Table 13: Mean KL Divergence of Full Covariance Data by Pixel and 8x8 Image Area

Full Covariance Data	**Mean KL Divergence by Pixel**		**Mean KL Divergence By 8x8 Image Area**	
Data Set	Real	Imaginary	Real	Imaginary
Plant D, Light Wind	0.0144	0.0147	3.03E-04	2.86E-04
Plant D, Medium Wind	0.0151	0.0149	2.94E-04	2.89E-04
Plant E, Light Wind	0.0151	0.0151	2.83E-04	2.97E-04
Plant E, Medium Wind	0.0155	0.0158	2.81E-04	2.89E-04

Table 14: Mean KL Divergence of Method 1 Data by Pixel and 8x8 Image Area

Method 1	**Mean KL Divergence by Pixel**		**Mean KL Divergence By 8x8 Image Area**	
Data Set	Real	Imaginary	Real	Imaginary
Plant D, Light Wind	0.0145	0.0142	3.03E-04	2.84E-04
Plant D, Medium Wind	0.0146	0.0145	2.92E-04	2.96E-04
Plant E, Light Wind	0.0146	0.0146	2.96E-04	3.08E-04
Plant E, Medium Wind	0.0142	0.0143	2.86E-04	2.83E-04

Table 15: Mean KL Divergence of Method 2 Data by Pixel and 8x8 Image Area

Method 2	**Mean KL Divergence by Pixel**		**Mean KL Divergence By 8x8 Image Area**	
Data Set	Real	Imaginary	Real	Imaginary
Plant D, Light Wind	1.45E-02	1.44E-02	2.75E-04	2.87E-04
Plant D, Medium Wind	0.0147	0.0143	2.91E-04	2.87E-04
Plant E, Light Wind	0.0146	0.0145	2.96E-04	3.15E-04
Plant E, Medium Wind	0.0144	0.0142	2.84E-04	2.72E-04

For Measured Data, All Methods Performed Similarly

4.4.3 Similarity Measure Analysis and Conclusions

From the similarity measure analysis, it can be concluded that Method 2 is much better for simulating desired correlations in decomposition levels beyond level 1. This is expected since Method 1 data was simulated using correlating filter shape parameters derived from level 1 estimated correlations. Since method 1 uses an exponential correlating filter, it will not be able to accurately produce level 2 and 3 correlations that are not exponential in nature.

For simulated data, both proposed methods provided an order of magnitude lower distribution similarity over data simulated using the full covariance matrix. However, for measured data, all three methods provided similar measures of distribution similarity.

For simulating data that has an exponential correlation shape, Method 1 is appropriate. However, for more complex data, Method 2 is needed to achieve a variable range of correlation values at higher decomposition levels. Analysis of the measured plant data indicates that, although the data does decay over distance, it was not exactly exponential. These results show that for the ISAR measurements of moving plants, Method 2 is a better option over the simple exponential correlating filter. Similarity measures give a good quantitative comparison, but it can be beneficial to compare methods in a real application. Example applications for analysis and simulation are provided in the next section.

5 APPLICATIONS FOR MULTISCALE ANALYSIS AND SIMULATION

5.1 MULTISCALE ANALYSIS OF SCATTERING PHENOMENON IN VEGETATION CLUTTER

5.1.1 Multiscale Analysis Hypotheses

A significant hypothesis of this dissertation is that multiscale correlation and covariance are related to physical structure and scattering phenomenon in the clutter. Consider the case of a single point scatterer with a small amount of motion. Given that the point source is infinitely small, it will only occupy one imaging cell at one time. With a small amount of motion, it will likely remain in that single imaging cell, causing a small variance in the amplitude and/or phase. However, as motion increases, the point scatterer will split time between two adjacent pixels. Since it will be in only one or the other of the adjacent pixels, the amplitudes of the two pixels will have a negative correlation. One will have increased amplitude when the point source is in that pixel and the other will have decreased amplitude. As the scatterer moves into the other imaging cell, the opposite is true. As scatterer motion increases further, involving additional cells, there will be negative correlation amongst a group of imaging cells. Now consider an extended scatterer that occupies a group of imaging cells. As the extended scatterer motion increases, groups of pixels will change together, based on the physical structure of the clutter, and other adjacent pixels will have the opposite relationship as motion increases. Therefore, we hypothesize that as motion increases, the amount of correlation at each scale will generally decrease but may be correlated at some scale depending on the physical characteristics of the clutter. Additionally, as we increase the decomposition level and reduce the correlation resolution, we are effectively estimating the correlation between larger and larger groups of raw image pixels. Therefore, we can hypothesize that for a given clutter structure, estimated correlation will become more negative with higher levels of decomposition.

Summary of Hypotheses for Vegetation Clutter

1. Image pixel variance will increase with motion and leaf size
2. Correlation will generally decrease with pixel distance
3. Correlation will generally decrease as decomposition level increases
4. Correlation will decrease with increased clutter motion

5.1.1.1 Relating Multiscale Statistics and Scattering Processes

Using the proposed multiscale analysis method, we can estimate the directional covariances at chosen decomposition levels for the six measurement scenarios. We choose three levels of decomposition for this analysis, which will result in estimated directional covariance (horizontal, vertical, and diagonal) for each decomposition level. With a starting image size of 64x64 pixels, the first level of decomposition will provide 32x32 directional covariance estimates. Level 2 decomposition will provide 16x16 directional covariance estimates, and so on. Full multiscale correlation and covariance data for the six measurement scenarios is shown in Appendix A. Multiscale covariance analysis will be presented in two different ways. First, all directional components and scales will be shown for each plant. Additionally, all six measurements scenarios will be shown together for each multiscale component.

5.1.1.2 A Note on Correlation vs Covariance

Much of the multiscale analysis formulations are focused on estimating multiscale correlations. However, this can be deceptive when viewing the full correlation maps over the entire ISAR image area. Figure 45 below shows the level 1 estimated horizontal correlation (left) and covariance (right) for a plant. The correlation map shows a very large area of correlation on the far left, but the plant does not exist in this spatial area and may be deceptive due to the very low backscatter return from that spatial area. The covariance map (right) appears to be more value-added in determining scattering characteristics from the plant volume. For this reason, the estimated covariance data will be shown instead of the correlation.

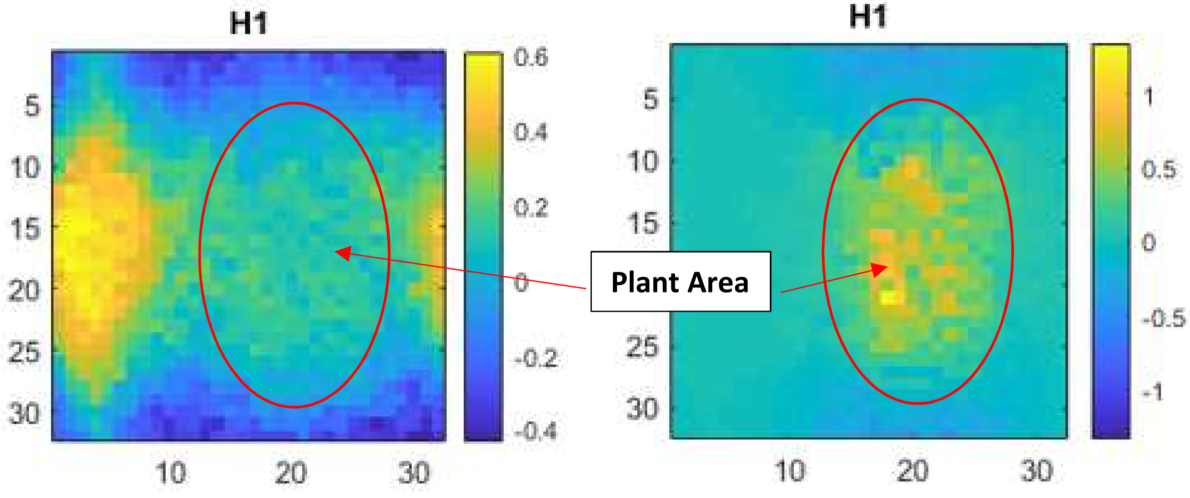

Figure 45: Correlation vs Covariance

5.1.1.3 Measurement Subjects for Hypothesis Testing

In order to test these hypotheses, multiscale analysis was carried out on three different plants in the presence of forced air. Photos of the plants are shown below in Figure 46 and were chosen based on have a wide variety of physical characteristics. Plant A has very large extended scatterers, large spacing between leaves, and significant leaf motion. Plant B has medium-sized scatterers, smaller spacing, and smaller leaf motion. Plant C has small, dense scatterers with a small amount of leaf motion.


Plant A **Plant B** **Plant C**

Figure 46: Plants used for ISAR Measurements

2D ISAR Measurements were recorded according to the measurement and calibration method previously described and the proposed multiscale analysis was performed to provide estimated covariance over three decomposition levels for each plant, in cases with no wind and with light wind. This results in six measurement scenarios (three plants, two wind speeds). The ISAR image samples for each plant and wind speed are structured into 100 samples of the 2D clutter equivalent current. Each image pixel represents a complex-valued resolution cell on this projected xy image plane. The data for each measurement scenario is structured as a 3D matrix of size 64x64x100, where each of the 100 image samples is a 64x64 complex-valued 2D image.

5.1.2 Testing Hypothesis 1 – Variance Increases with Motion and Leaf Size

The mean ISAR image, mean k-space image, and pixel variance are calculated for each of the six measurement scenarios and are shown in Figure 47 through Figure 49. The main point here is that the clutter is not uniform. The sample mean and variance vary across the image due to the physical structure of the plants. The average pixel variance for each scenario is summarized below in Table 16.

Table 16: Summary of ISAR Image Variance over Six Measurement Scenarios

Mean Sample Variance	Plant A	Plant B	Plant C
No Wind	0.0044	0.0043	0.0042
Light Wind	1.6979	1.1305	0.3215

Table 16 indicates that hypothesis 1 is correct and variance increases with leaf size and motion. Inspection of the sample mean ISAR image shows that Plant A has very localized scattering due to the two large cane stems, as well some lighter scattering from the large leaves. Plant B shows more distributed scattering but with some non-uniform structure present. Plant C shows distributed scattering and an increased amount of energy outside the physical bounds of the plant, indicating a significant amount of higher-order scattering present.

As expected, the variance decreases from Plant A to B to C as the size of the leaves decreases. Larger leaves serve as a moment arm and allow for a larger amount of displacement, which translates to increased image pixel variance. Variance was similar in all plants with no wind present, which indicates the variance may be related to system measurement noise but may also result from small amounts of motion due to ambient air.

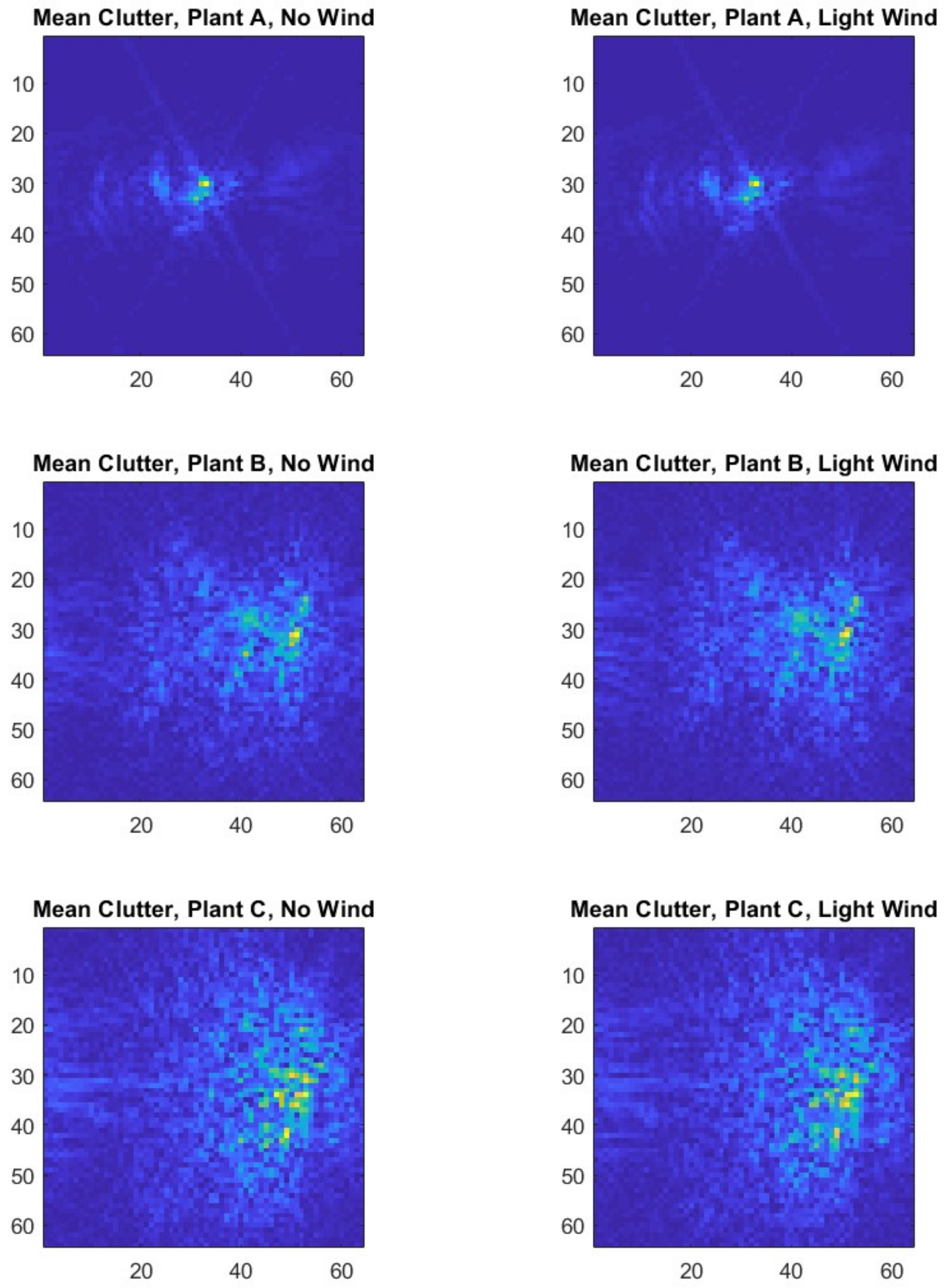

Figure 47: Sample Mean for Six Measurement Scenarios

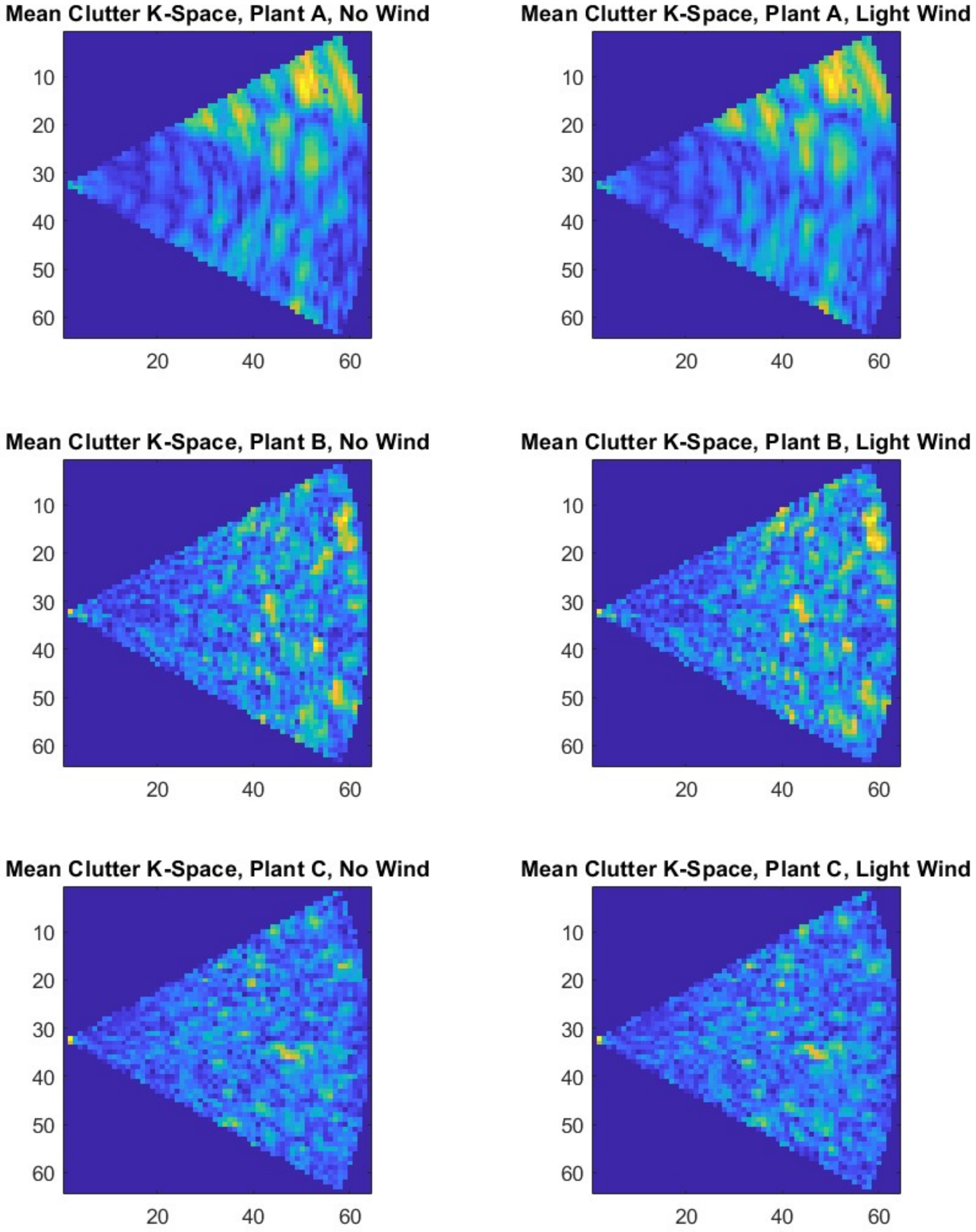

Mean Clutter K-Space, Plant A, No Wind

Mean Clutter K-Space, Plant A, Light Wind

Mean Clutter K-Space, Plant B, No Wind

Mean Clutter K-Space, Plant B, Light Wind

Mean Clutter K-Space, Plant C, No Wind

Mean Clutter K-Space, Plant C, Light Wind

Figure 48: Sample Mean K-Space Image

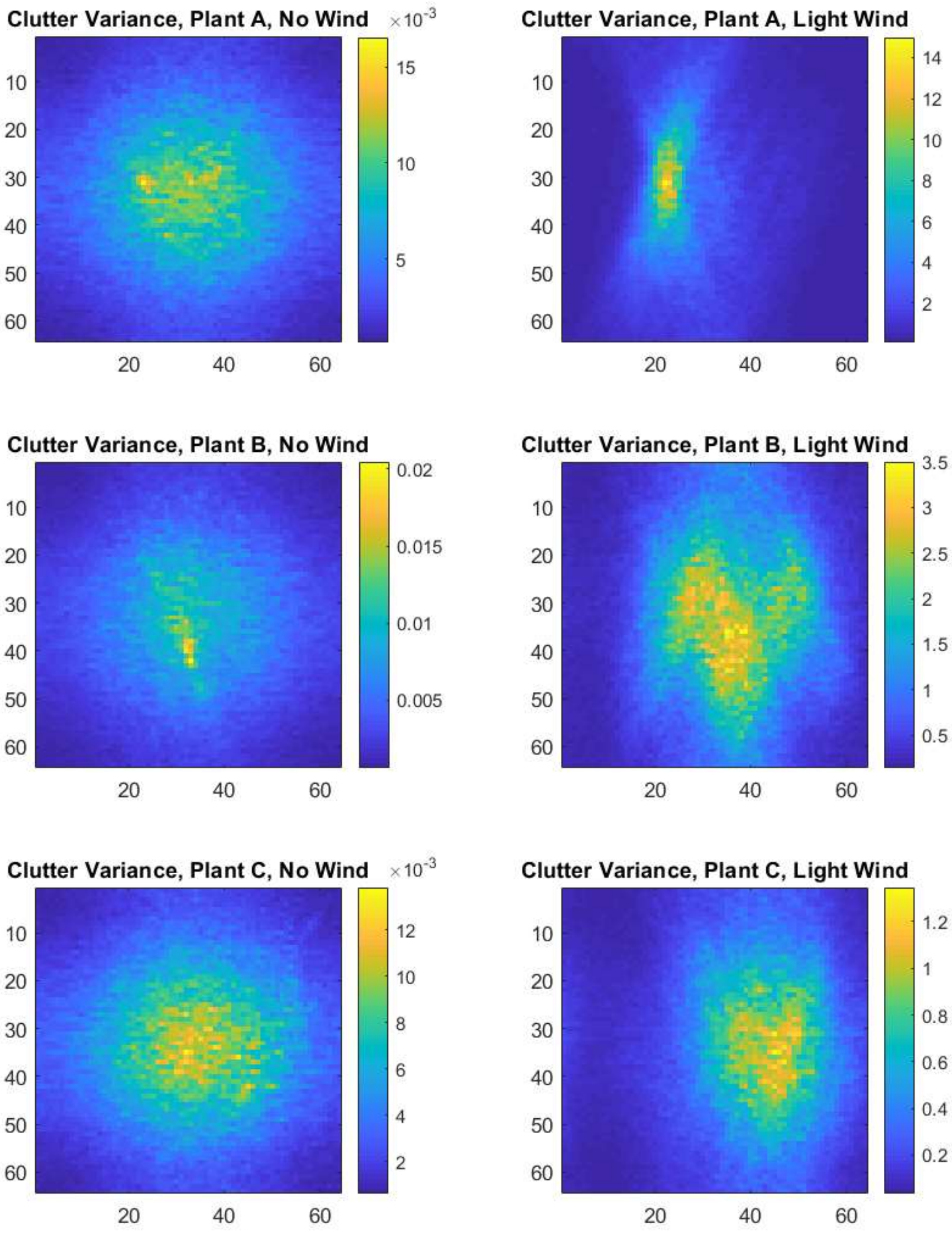
Clutter Variance, Plant A, No Wind

Clutter Variance, Plant A, Light Wind

Clutter Variance, Plant B, No Wind

Clutter Variance, Plant B, Light Wind

Clutter Variance, Plant C, No Wind

Clutter Variance, Plant C, Light Wind

Figure 49: Sample Variance

5.1.3 Testing Hypothesis 2 – Correlation Decreases with Pixel Separation

We introduce the *mean 2D correlating function*, which indicates the mean relative spatial correlation over all image pixels. This is formed by simply rearranging the contents of the sample covariance matrix to retain the spatial relationships for neighboring pixels and provides insight into the directional and spatial nature of correlation in image samples. The magnitude of the mean 2D correlating function for the three plants with no wind is shown in Figure 50 and with light wind Figure 51. Horizontal and vertical plots through the origin are shown to help visualize the shape of the directional correlation.

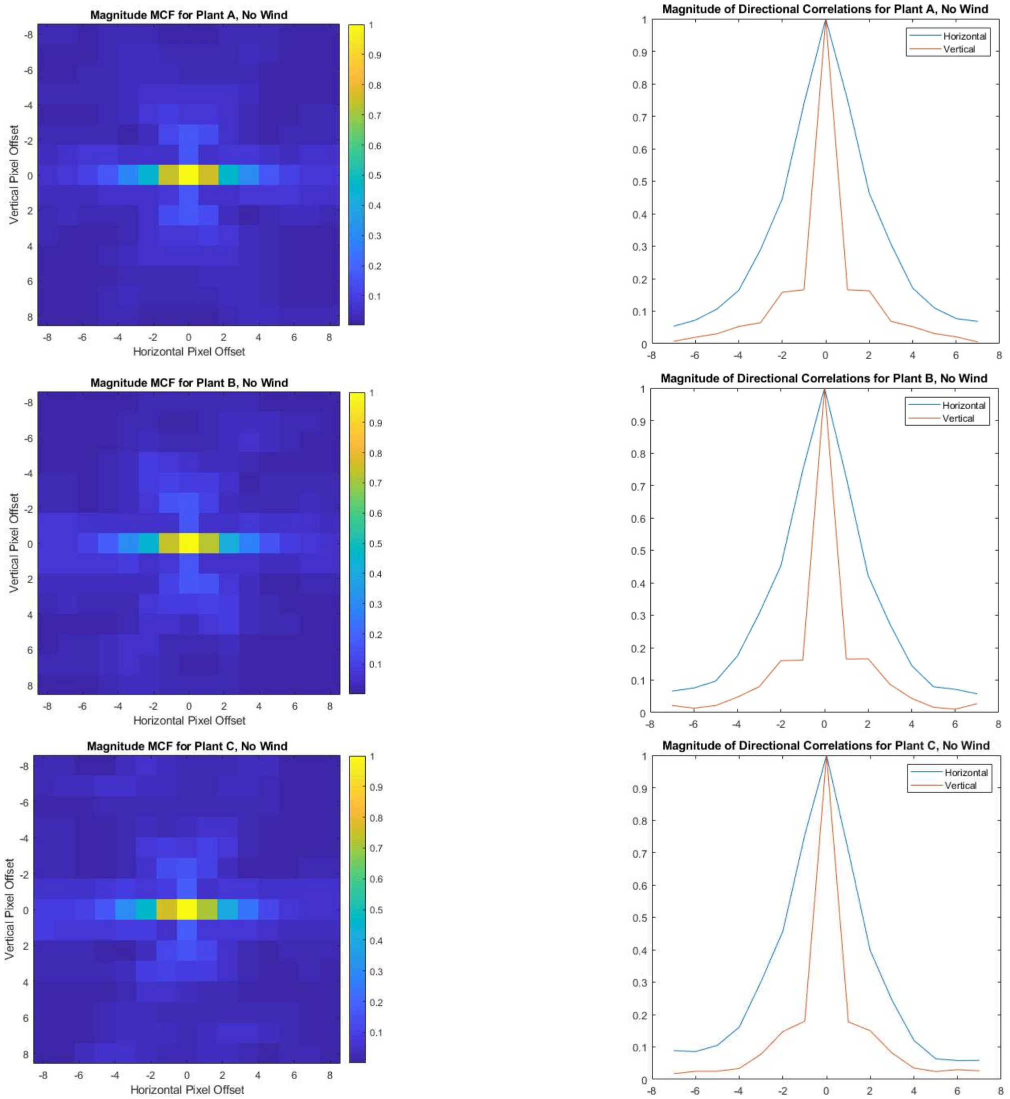

Figure 50: Mean Correlating function Magnitude of Three Plants with No Wind

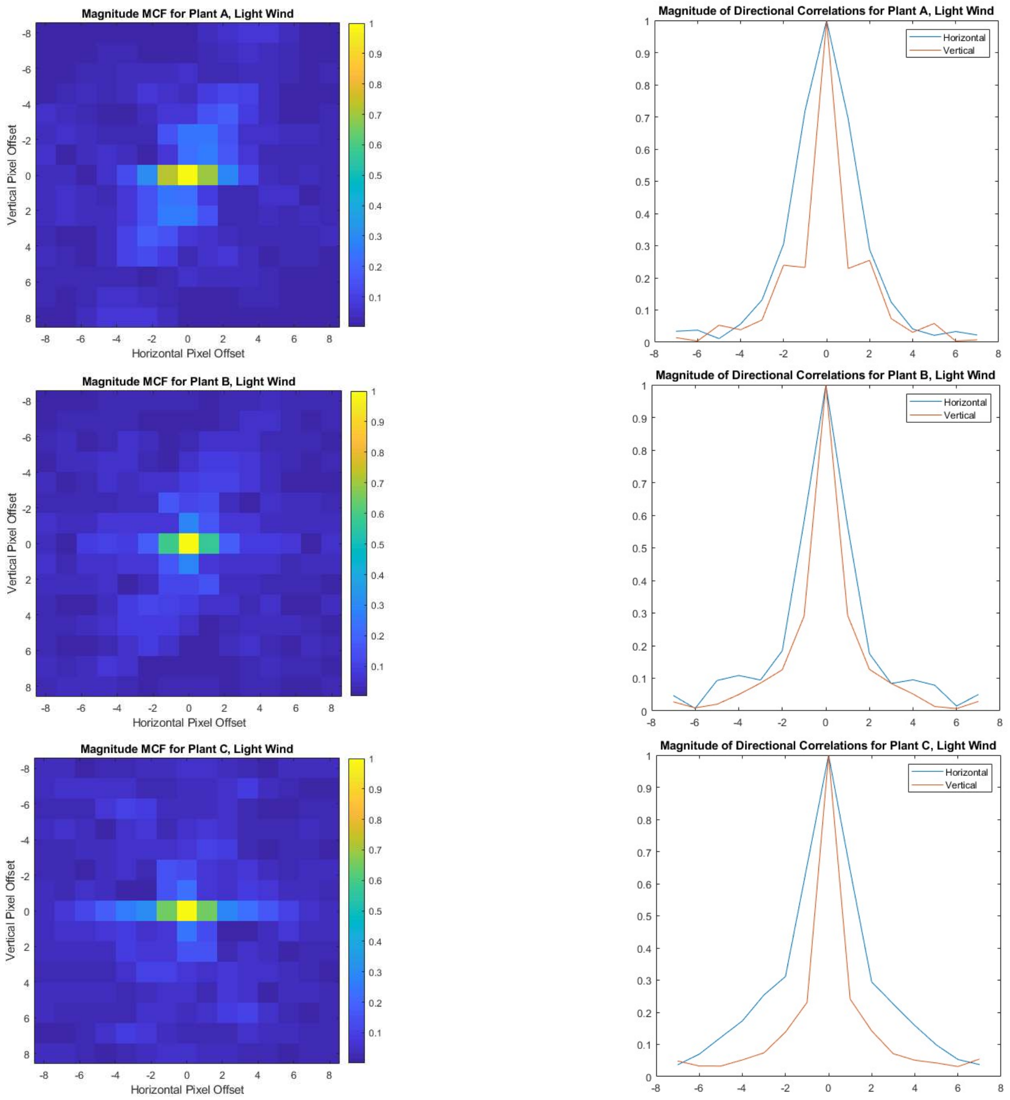

Figure 51: Mean Correlating function Magnitude of Three Plants with Light Wind

Inspection of Figure 50 and Figure 51 shows that hypothesis 2 is correct for these measurement scenarios and the correlation generally decreases with pixel distance. Our approach for clutter simulation is to find a parameterized correlating filter that can be applied to random data that will result in the desired directional correlation. The plots in Figure 50 and Figure 51 indicate that the exponential function is worth exploration for simulating the correlation in plant ISAR measurements. However, this conclusion is based on raw image pixel correlations. A multiscale analysis is important in analyzing the stochastic properties of complex systems over different scales.

5.1.4 Testing Hypothesis 3 - Correlation Decreases as Decomposition Level Increases

The mean correlation over scale is plotted in Figure 52 for the cases of no wind, and in Figure 53 for the cases of light wind. The plots verify that in all cases, the correlation does decrease as the decomposition increases from Level 1 to Level 3.

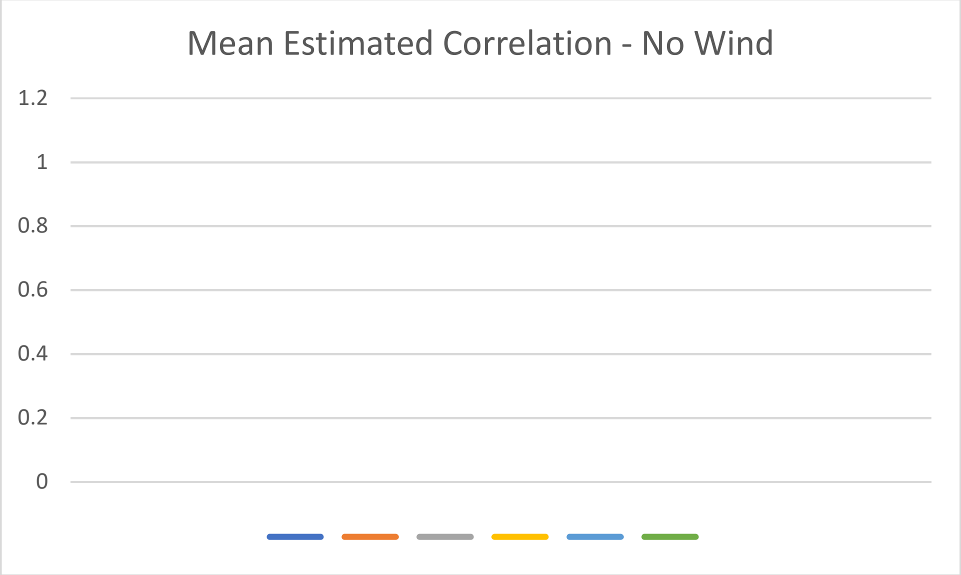

Figure 52: Mean Correlation by Decomposition Level for No Wind

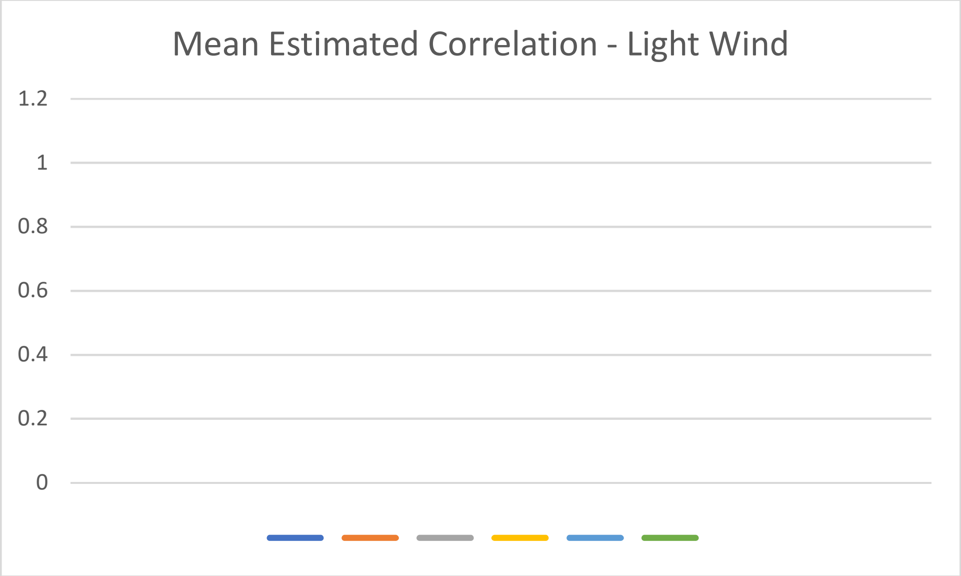

Figure 53: Mean Correlation by Decomposition Level for Light Wind

5.1.5 Testing Hypothesis 4 - Correlation Decreases with Increased Clutter Motion

Mean Correlation is plotted below by decomposition level for no wind and light wind in Figure 54 through Figure 56. Examination of the plots shows that for level 1 decomposition, the hypothesis appears generally true for this data set, especially for the horizontal component. However, this falls apart in levels 2 and 3. Further investigation reveals that Plant C, which shows increased correlation with increased motion, is a dense plant and in the presence of motion, the entire plant moves together. This demonstrates one benefit of the multiscale analysis. At the level 1 decomposition, the scattering phenomenon is dominated by the very small leaves. At level 2, correlation is determined by groups of leaves moving together. Therefore, we can conclude that the correlation will depend on the structure of the plant and generalizations about correlation as related to wind speed may not represent reality.

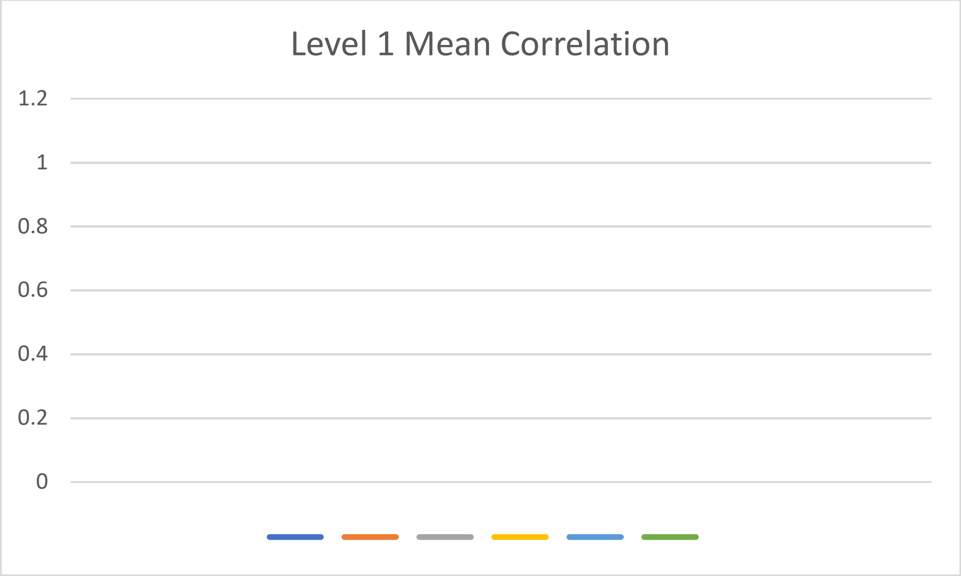

Figure 54: Level 1 Mean Correlation

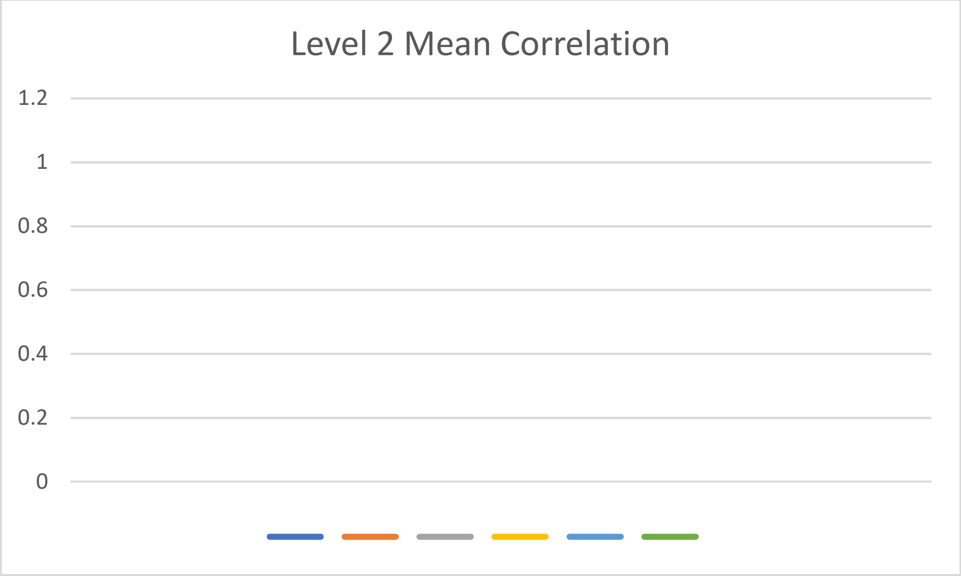

Figure 55: Level 2 Mean Correlation

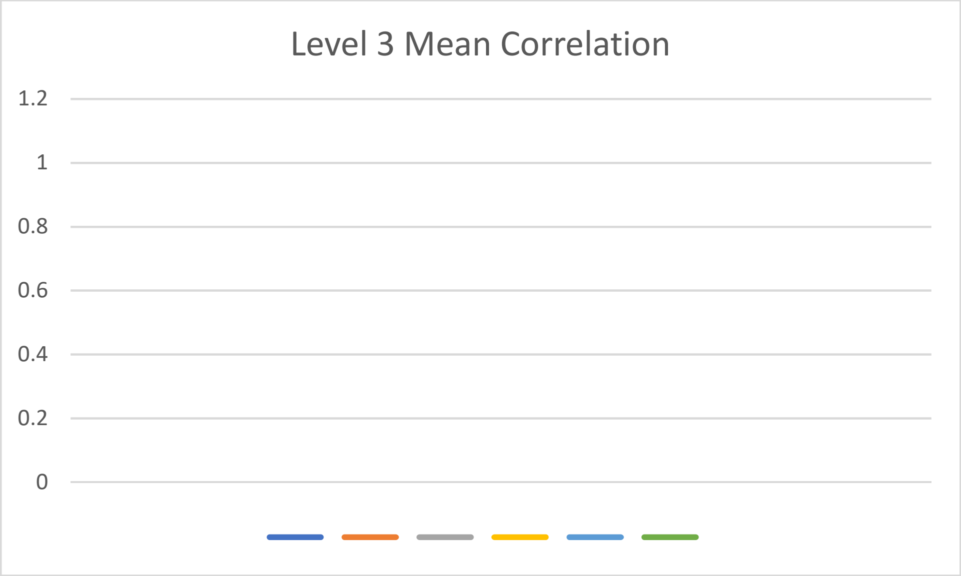

Figure 56: Level 3 Mean Correlation

5.2 MULTISCALE ANALYSIS OF GLOBAL OCEAN CURRENT DATA

For additional demonstration of the multiscale analysis technique, the proposed method will be applied to the analysis of global ocean current data [82]. Although this data is created from a variety of sensors and is not related to ISAR imaging, the analysis of this data shows that the proposed multiscale analysis method has value in other fields with complex stochastic data.

Some amount of correlation is expected in global ocean current data due to the continuous nature of currents at some scale. However, the proposed multiscale analysis can show varying directional correlations at different scales, indicating broader relationships in currents between ocean areas. Properties of the data used in this analysis are shown below in Table 17.

Table 17: Ocean Current Data Properties

DOI	10.5067/OSCAR-03D01
Short Name	OSCAR_L4_OC_third-deg
Description	OSCAR (Ocean Surface Current Analysis Real-time) contains near-surface ocean current estimates, derived using quasi-linear and steady flow momentum equations. The horizontal velocity is directly estimated from sea surface height, surface vector wind and sea surface temperature. These data were collected from the various satellites and in situ instruments. The model formulation combines geostrophic, Ekman and Stommel shear dynamics, and a complementary term from the surface buoyancy gradient. Data are on a 1/3-degree grid with a 5-day resolution. OSCAR is generated by Earth Space Research (ESR)
Coverage	Global
Latitude Range	-66 to 66 deg
Longitude Range	-180 to 180 deg
Date Range	2019
Temporal Resolution	5 Day
Spatial Resolution	0.33 deg
Data Format	Zonal and Meridional Flow Velocities
Data Size	72 Samples of 480 x 1200-pixel Images for Zonal and Meridional Data

The mean magnitude of ocean current velocity from the 72 samples in 2019 is shown below in Figure 57.

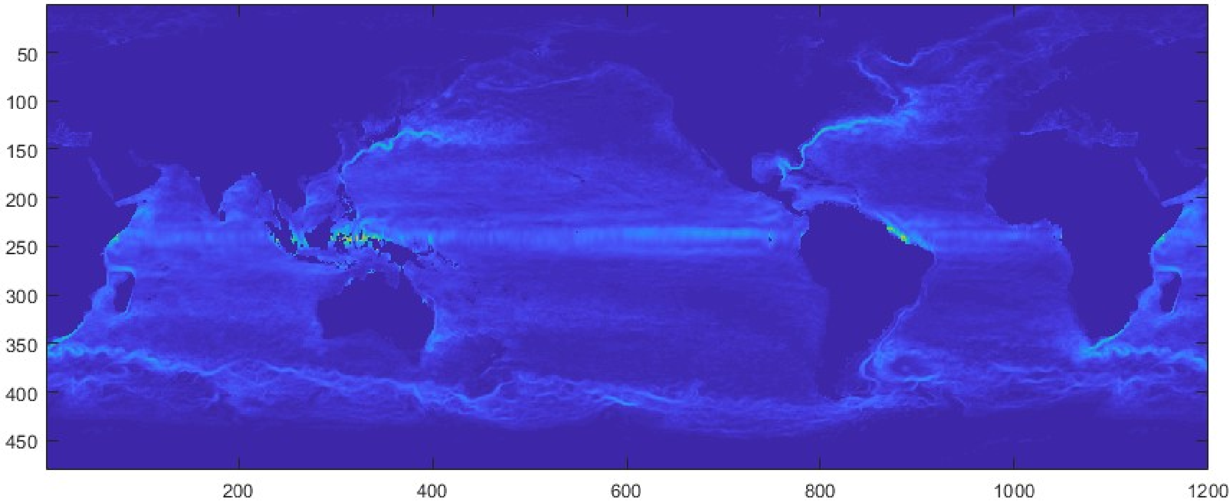

Figure 57: Mean Ocean Current Velocity Magnitude

In order to be compatible with our analysis method, the data is formatted into complex data, with the zonal flow velocity as the real component and the meridional flow velocity as the complex component. The formatted data results in 72 samples of complex 480 x 1200 data. Multiscale analysis is performed over four levels of decomposition to estimate the multiscale correlations. The results of the analysis are shown below in Figure 58 through Figure 60, where dark blue areas of the image are land and not analyzed.

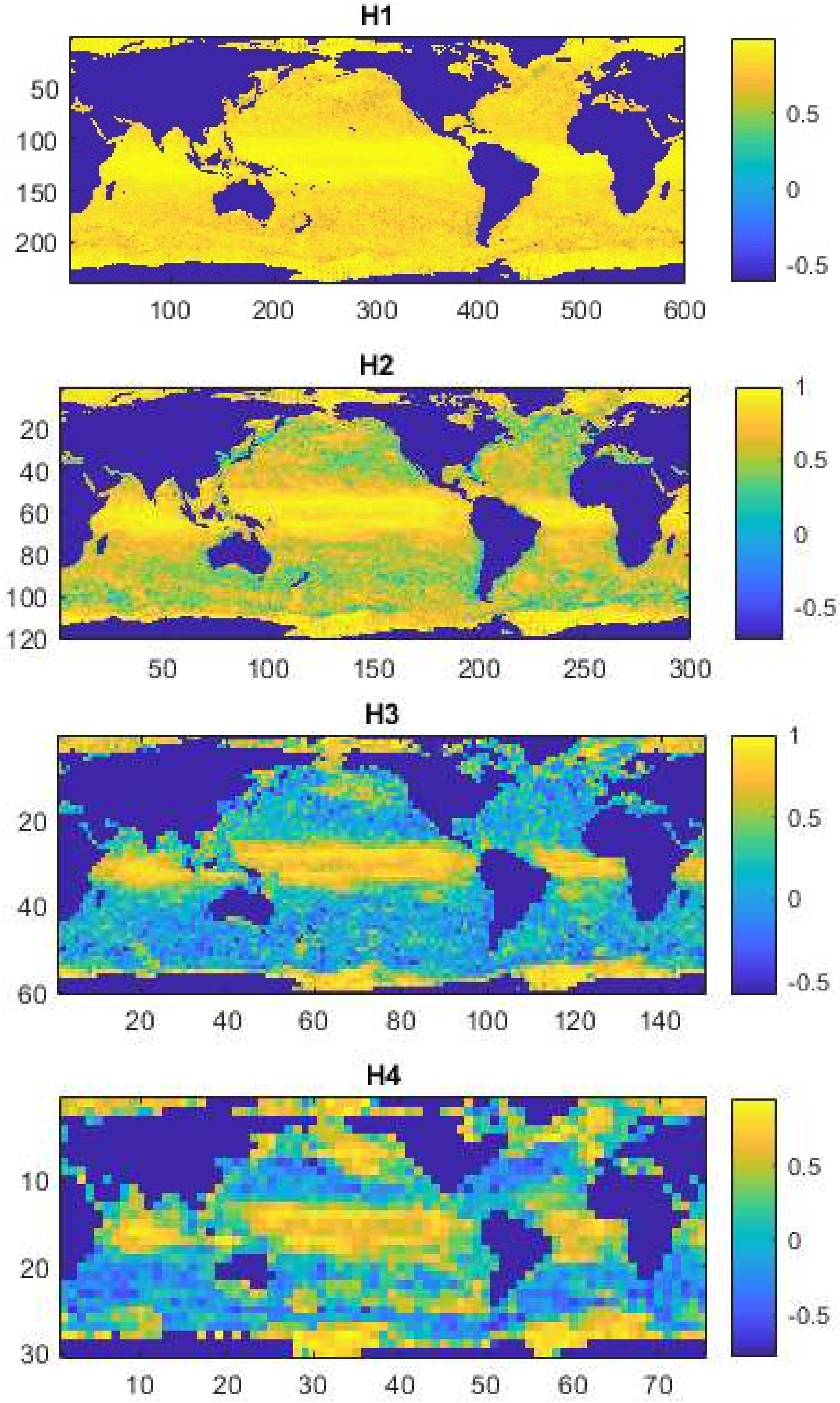

Figure 58: Horizontal Component of Ocean Current Multiscale Analysis for Decomposition Levels 1 - 4

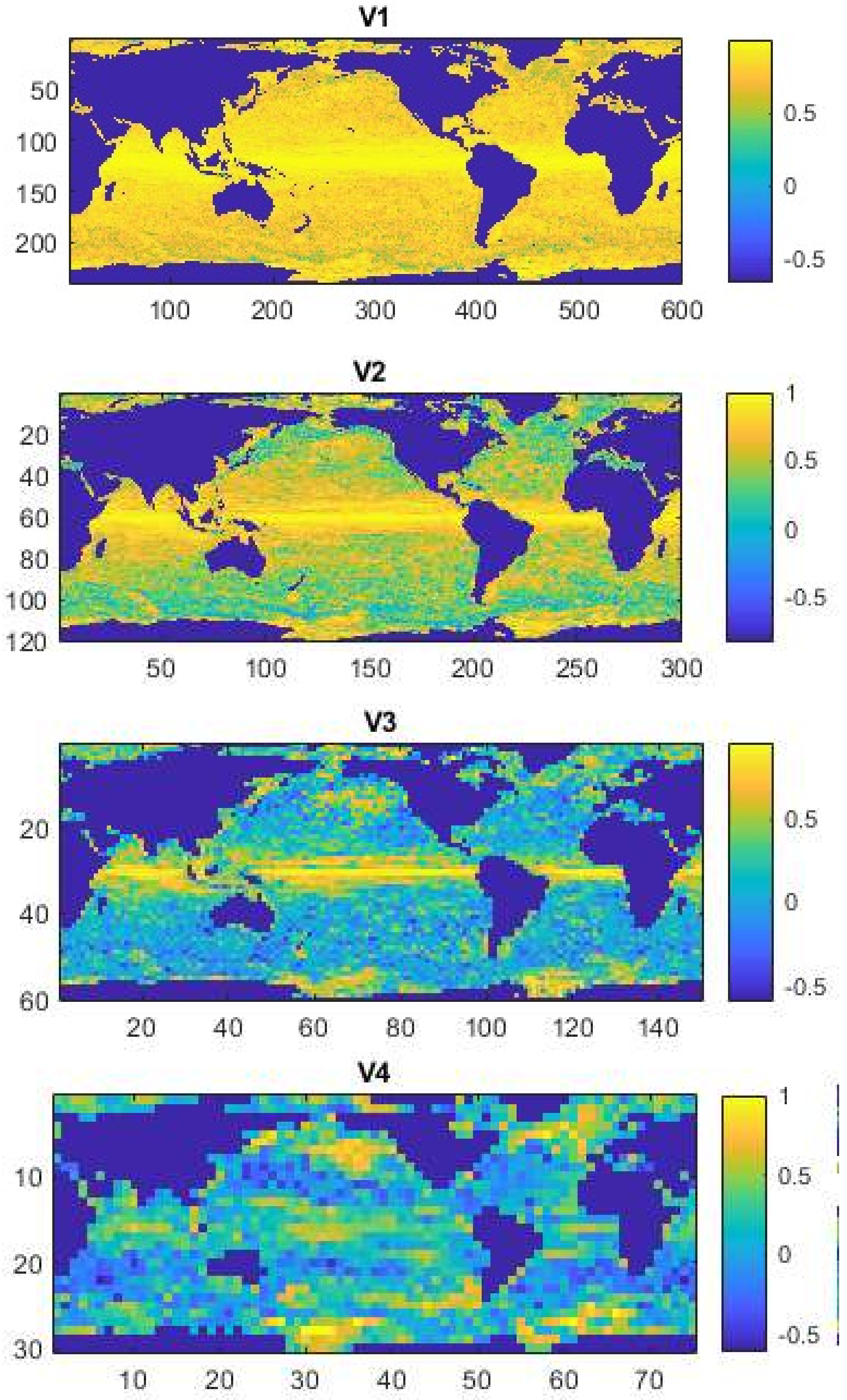

Figure 59: Vertical Component of Ocean Current Multiscale Analysis for Decomposition Levels 1 - 4

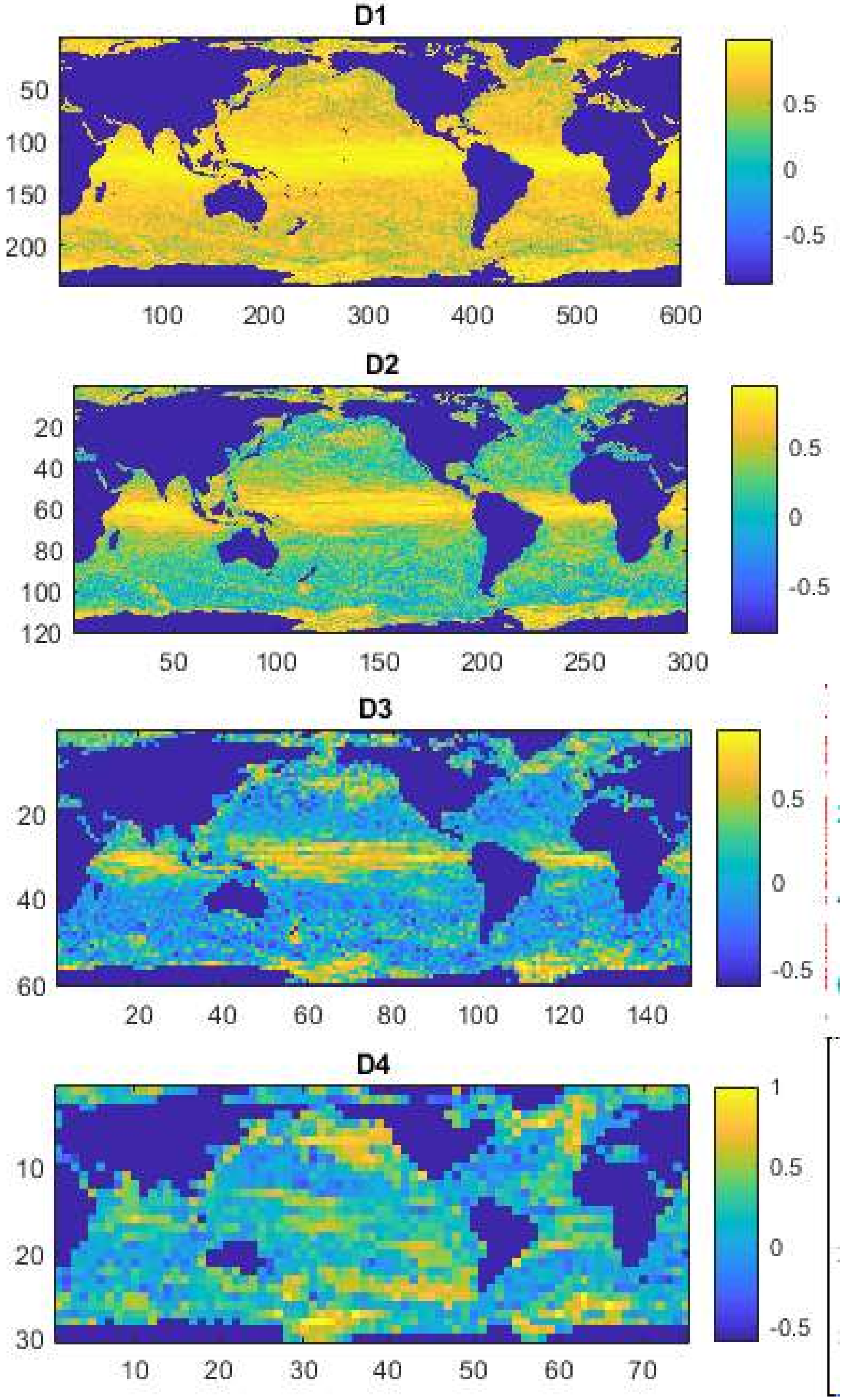

Figure 60: Diagonal Component of Ocean Current Multiscale Analysis for Decomposition Levels 1-4

As expected, multiscale analysis of the ocean currents shows that current velocities are globally very correlated at the level 1 decomposition and highest resolution. However, as the decomposition level increases, we see continued correlation concentrated at the equator and decreasing correlation in other areas. As the decomposition level increases further, the directional correlations show concentrated areas of correlation in other areas. This example shows that the proposed multiscale analysis has value in other fields where directional spatial correlation is of interest.

5.3 DEEP LEARNING CONVOLUTIONAL NETWORK APPLICATIONS FOR ISAR CLUTTER

5.3.1 Introduction

Deep learning is an expanding area of research for solving complex problems. The combination of non-linear activation functions with convolutional layers allows for deep learning networks to learn very complicated non-linear processes. However, training these networks to learn the appropriate convolutional kernels and weights usually requires many training samples. In some cases, physical measurements, and therefore training samples, may be limited [83] [84].

One contribution of this dissertation is methods for generating additional representative samples of ISAR clutter data for the purpose of training deep learning networks for classification and other tasks related to clutter mitigation. The deep learning applications are not necessarily intended to be a novel aspect of this dissertation, although some do have merit, are relatively unexplored applications, and warrant further research. In order to prove the value of this contribution, this chapter will present example deep learning applications and show how the additional generated samples can improve training accuracy and prediction performance. In almost all current deep learning research related to ISAR, the availability of representative training samples is significant factor in training.

5.3.2 Deep Learning Application 1 – Clutter Classification

Clutter from vegetation and other moving structures can have stochastic properties related to the physical characteristics of the clutter. Furthermore, clutter removal methods may require identification or classification of the clutter. This example application involves the classification of clutter. Deep learning convolutional networks are extremely powerful tools in classification problems and if properly trained, can learn very subtle discriminators. The convolutional nature of these deep learning networks results in the ability to find consistent spatially oriented patterns in the input data, especially mean data. For this reason, a very simple and small network can be used to learn to classify data due to the mean of training samples.

Vegetation and other types of clutter can often be uniform, depending on many factors. Uniform clutter is more likely to have zero mean backscatter due to the application of the Central Limit Theorem. Therefore, it is important when dealing with deep learning for clutter classification to assume the worst case of a zero-mean image. The same argument can be made for image variance, which can also be a realistic attribute of uniform clutter and the case of unit variance should be considered. For clutter modeled as second order, this leaves correlation as a final discriminator in convolutional networks. Correlation between pixels can be learned by a network’s convolution filters or kernels, but learning the correlation requires more training than learning to discriminate due to data means.

In consideration of the above points, our classification examples will assume data with zero mean and/or unit variance, and correlation that is specific to each clutter class. This presents a more difficult problem than classes with different and specific means. Having a more difficult problem underscores the importance of additional, representative training samples and allows us to evaluate the effectiveness of the data generation methods in the context of convolutional networks.

5.3.2.1 Classification Network Architecture

For demonstration of this application, a simple convolutional network will be used. As stated above, the intent here is not to design a novel network, but to demonstrate how additional representative sample, generated form a limited number of measurements, can improve performance in deep learning applications.

We choose a network with an input layer, three convolution layers separate by batch normalization; ReLu activation; and pooling, with a fully connected layer and softmax layer at the end for classification. A diagram of the network architecture is shown below in Figure 61.

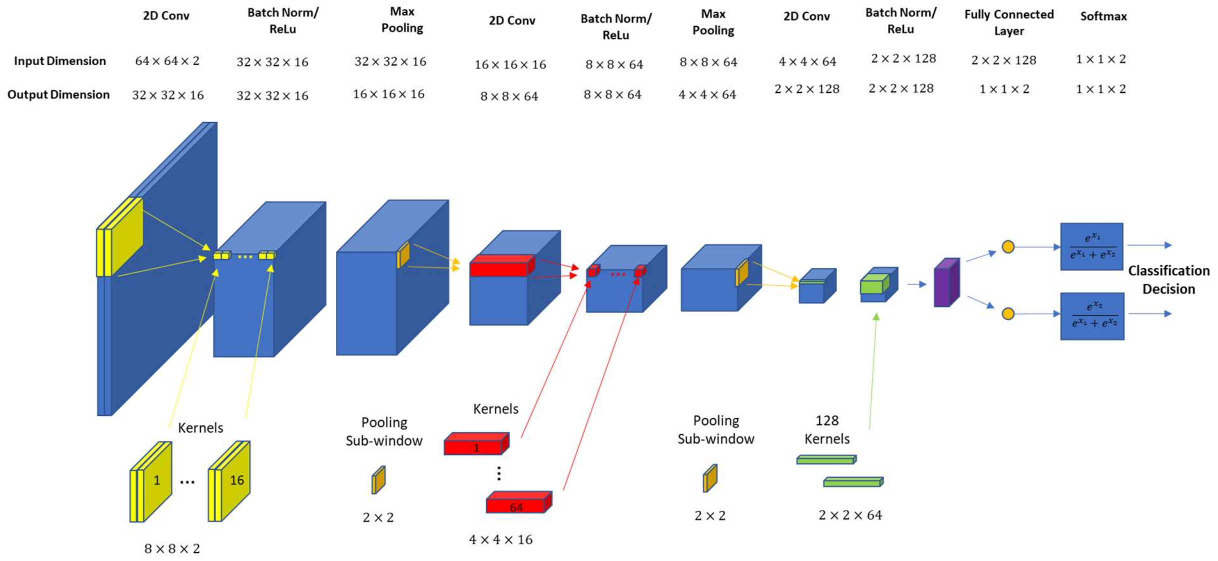

	2D Conv	Batch Norm/ ReLu	Max Pooling	2D Conv	Batch Norm/ ReLu	Max Pooling	2D Conv	Batch Norm/ ReLu	Fully Connected Layer	Softmax
Input Dimension	$64 \times 64 \times 2$	$32 \times 32 \times 16$	$32 \times 32 \times 16$	$16 \times 16 \times 16$	$8 \times 8 \times 64$	$8 \times 8 \times 64$	$4 \times 4 \times 64$	$2 \times 2 \times 128$	$2 \times 2 \times 128$	$1 \times 1 \times 2$
Output Dimension	$32 \times 32 \times 16$	$32 \times 32 \times 16$	$16 \times 16 \times 16$	$8 \times 8 \times 64$	$8 \times 8 \times 64$	$4 \times 4 \times 64$	$2 \times 2 \times 128$	$2 \times 2 \times 128$	$1 \times 1 \times 2$	$1 \times 1 \times 2$

Figure 61: Classification CNN Architecture

This network layer details are shown below in Table 18.

Table 18: Convolutional Network Layer Details

	NAME	TYPE	ACTIVATIONS	LEARNABLES
1	imageinput 64x64x2 images with 'zerocenter' normalization	Image Input	64×64×2	-
2	Conv1 16 8x8x2 convolutions with stride [2 2] and padding 'same'	Convolution	32×32×16	Weights 8×8×2×16 Bias 1×1×16
3	batchnorm_1 Batch normalization with 16 channels	Batch Normalization	32×32×16	Offset 1×1×16 Scale 1×1×16
4	Relu1 ReLU	ReLU	32×32×16	-
5	maxpool_1 2x2 max pooling with stride [2 2] and padding [0 0 0 0]	Max Pooling	16×16×16	-
6	Conv2 64 4x4x16 convolutions with stride [2 2] and padding 'same'	Convolution	8×8×64	Weights 4×4×16×64 Bias 1×1×64
7	batchnorm_2 Batch normalization with 64 channels	Batch Normalization	8×8×64	Offset 1×1×64 Scale 1×1×64
8	Relu2 ReLU	ReLU	8×8×64	-
9	maxpool_2 2x2 max pooling with stride [2 2] and padding [0 0 0 0]	Max Pooling	4×4×64	-
10	Conv3 128 2x2x64 convolutions with stride [2 2] and padding 'same'	Convolution	2×2×128	Weights 2×2×64×128 Bias 1×1×128
11	batchnorm_3 Batch normalization with 128 channels	Batch Normalization	2×2×128	Offset 1×1×128 Scale 1×1×128
12	Relu3 ReLU	ReLU	2×2×128	-
13	fc 2 fully connected layer	Fully Connected	1×1×2	Weights 2×512 Bias 2×1
14	Soft softmax	Softmax	1×1×2	-
15	classoutput crossentropyex with classes '2' and '4'	Classification Output	-	-

5.3.2.2 Input Data Format

The image input layer accommodates two layers, which correspond to the real and imaginary components of the input images. Some work has been done on creating convolutional networks that can accommodate complex data, but as of the writing of this dissertation, the most prevalent tools require real input data. This is driven by the fact that most convolutional networks are applied to problems involving visible color or greyscale images. However, using real and imaginary components of the ISAR image as inputs works well. This arrangement allows for phase information to be learned in the kernels of the first convolutional layer.

5.3.2.3 Training Data Formation

For this application, we choose a simple classification problem using modified measurement data from two plants in the presence of light and medium wind. The data under analysis is two-dimensional ISAR measurements of two species of plants in the presence of two speeds of forced air from one direction to simulate wind. Wind speed was not measured but is characterized as light wind and medium wind. The light wind resulted in small deflection of the leaves, whereas the medium wind resulted in significant deflection of branches and leaves. Photos of the two plants are shown below in Figure 62 and Figure 63. These plants were chosen for their difference in structure for comparison. Plant A has many smaller leaves on many smaller branches. Plant B has fewer large leaves on a few larger stalks.


Figure 62: Plant Species A


Figure 63: Plant Species B

Each measurement scenario consists of 2D samples of a plant in the presence of wind. The ISAR data for each plant and wind speed is structured into 100 samples of the clutter equivalent current. Each image pixel represents a complex-valued resolution cell on this projected xy image plane. The data for each measurement scenario is structured as a 3D matrix of size 64x64x100, where each of the 100 image samples is a 64x64 complex-valued 2D image.

5.3.3 Sample Mean

The sample mean over 100 samples for the four measurement scenarios is shown below in Figure 64.

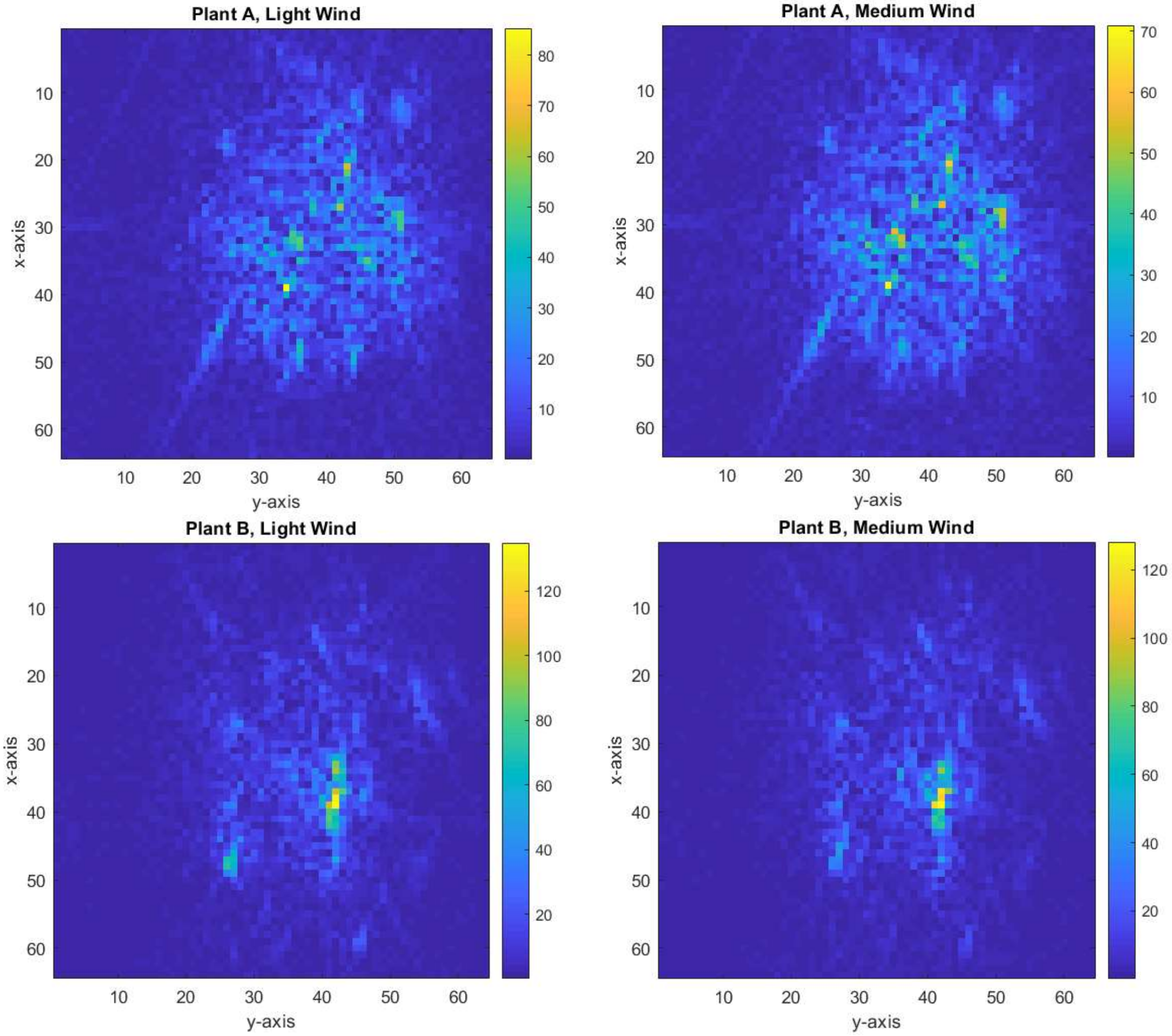

Figure 64: Sample Mean for ISAR Measurements

These images are projections of the volume equivalent current onto the xy plane, or from a "top" view of the plant. The sample means are indicative of the plant type, with Plant A showing more distributed concentrated areas of lower intensity equivalent currents consistent with many leaves and branches, and Plant B showing more concentrated areas of stronger equivalent currents consistent with fewer larger leaves and branches. The sample means for each plant species are similar for the two wind speeds, but there are some differences due to constant deflection from directional forced air.

5.3.4 Sample Variance

The sample variance over 100 samples for the four measurement scenarios is shown below in Figure 65.

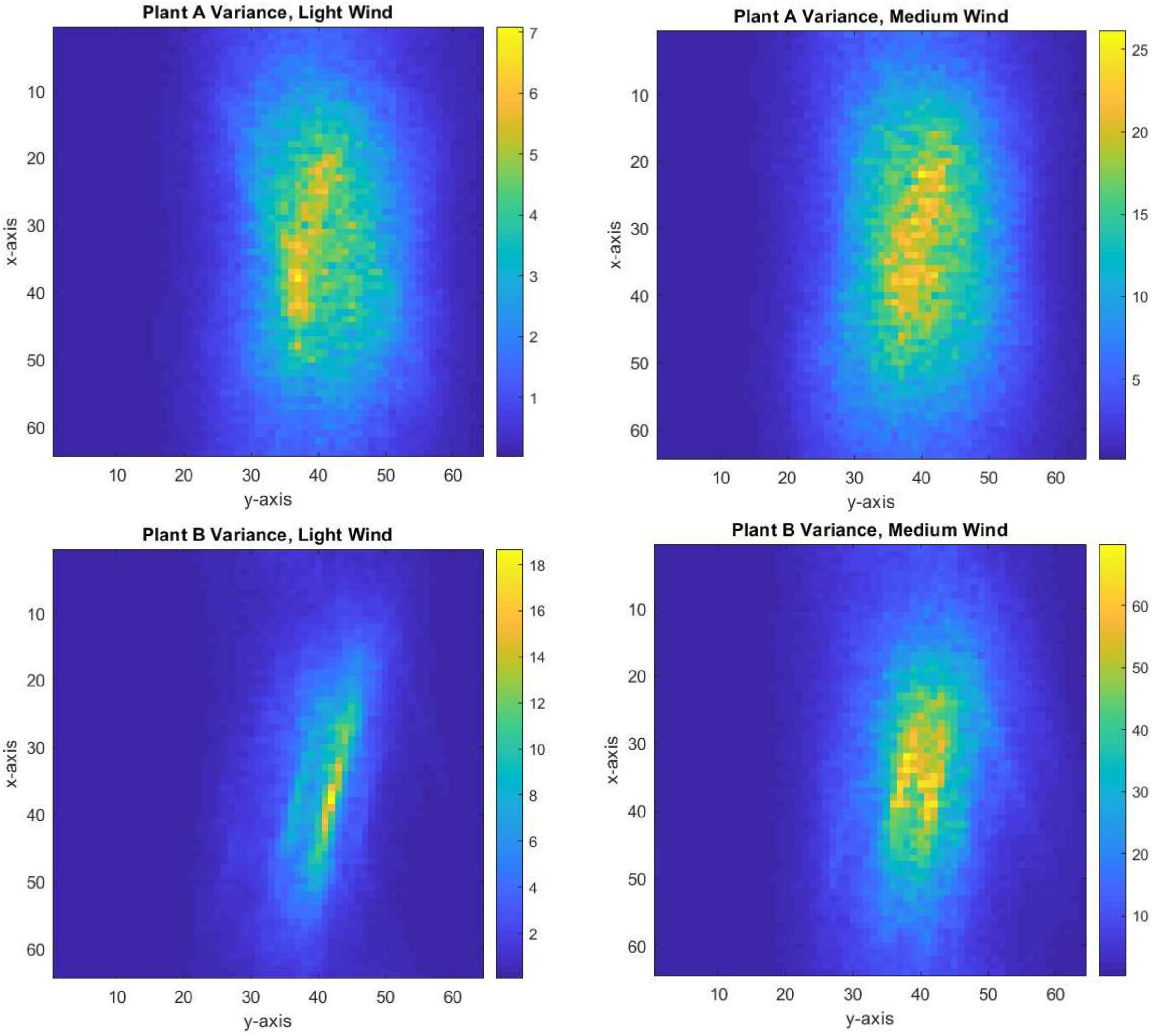

Figure 65: Sample Variance for ISAR Measurements

Multiscale analysis of measured data demonstrates that estimated correlations are more plant specific. A network should easily be able to classify by plant even in the presence of multiple wind speeds, but a more challenging problem is to classify by both plant and wind speed. In this case, the network will need to learn subtle features of the correlation. This is a difficult task and will help form a distinction between data generation methods. The goal is to classify input images as one of four classes, Plant A with light wind, Plant A with medium wind, Plant B with light wind, or Plant B with medium wind. Starting with 100 samples of measured data from each class, we apply the data generation techniques from Chapter 4 to generate many more representative samples. We then arrange these additional samples into training data by normalizing for zero mean and unit variance and dividing the data into training and validation sets.

5.3.4.1 Training Strategy

Due to the use of a second order model with limited correlation lags, the original measured data will be different from the simulated data in very specific ways. In training the network on the new generated data, the intent is for the network to learn features in the simulated data that exist in the original measured data. If the simulated data is very close, with the same features, then training on only the new simulated data is appropriate. However, as the difference between the original and simulated data increases, training on only the simulated data will cause it to learn features that may not exist in the original data. Therefore, we can add the original data into the training and validation data to help ensure that the network is not too specific and only learning features of the new simulated data. In these examples, 10% of the training data will be from original measured data, and 90% will be from the new simulated data.

When training networks on limited amounts of data, the specific training is highly dependent on random seeding of weights. On limited data sets, this can result in a large degree of variation in the prediction accuracy of the network. In this case, we will train the network multiple times and record the average prediction accuracy.

5.3.4.2 Training and Prediction Accuracy

The figures of merit in these examples will be training and prediction accuracy. Training accuracy demonstrates that there are enough samples to learn discriminators in the data. The use of separate validation data ensures that the network is not over trained and memorizing the data rather than learning features.

Prediction accuracy will be calculated by performing a final classification prediction on the original measured data by the trained network. This method allows prediction accuracy to be a good measure of the quality of our generated samples as related to improving the performance of the network. Both data generation methods and data generated from the complete covariance matrix method will be evaluated. This allows us to verify that the similarity measures are a good indicator of deep learning network performance when using training data from that method.

In this application, we will train networks with increasing numbers of generated samples and show training and prediction accuracy as a function of training samples. This will demonstrate that the novel contributions presented in this dissertation are valid for improving network prediction accuracy in these example applications.

5.3.5 Results for Zero-Mean Measured Clutter Classification

Table 19: Zero-Mean Classification Example Properties

Number of Classes	4
Input Data	100 ISAR image samples from each of Plant A, B in light and medium wind
Input Data Processing	Normalized for zero-mean
Data Generation Methods	Full Covariance, Method 1 Exponential Correlating function, Method 2 General Correlating function
Training Data Size Range	100 to 1000 Samples
Validation Data Size Range	100 to 1000 Samples
Training Data Composition	90% New Generated Data 10% Original Measured Data

5.3.6 Network Prediction Accuracies on Zero-Mean Clutter Measured Data

Table 20: Network Prediction Accuracy for Zero-Mean Classification

	Network Trained with 100 Training Samples	Network Trained with 250 Training Samples	Network Trained with 500 Training Samples	Network Trained with 1000 Training Samples
Data Generation Method 1 – Exponential Correlating function	69.8%	92.1%	93.8%	95.3%
Data Generation Method 2 – General Correlating function	76.4%	92.6%	94.3%	96.8%
Data Generation Method 3 – Full Covariance Multivariate	88.6%	97.9%	99.3%	98.8%
Original Measured Data (100 samples)	83.3%			

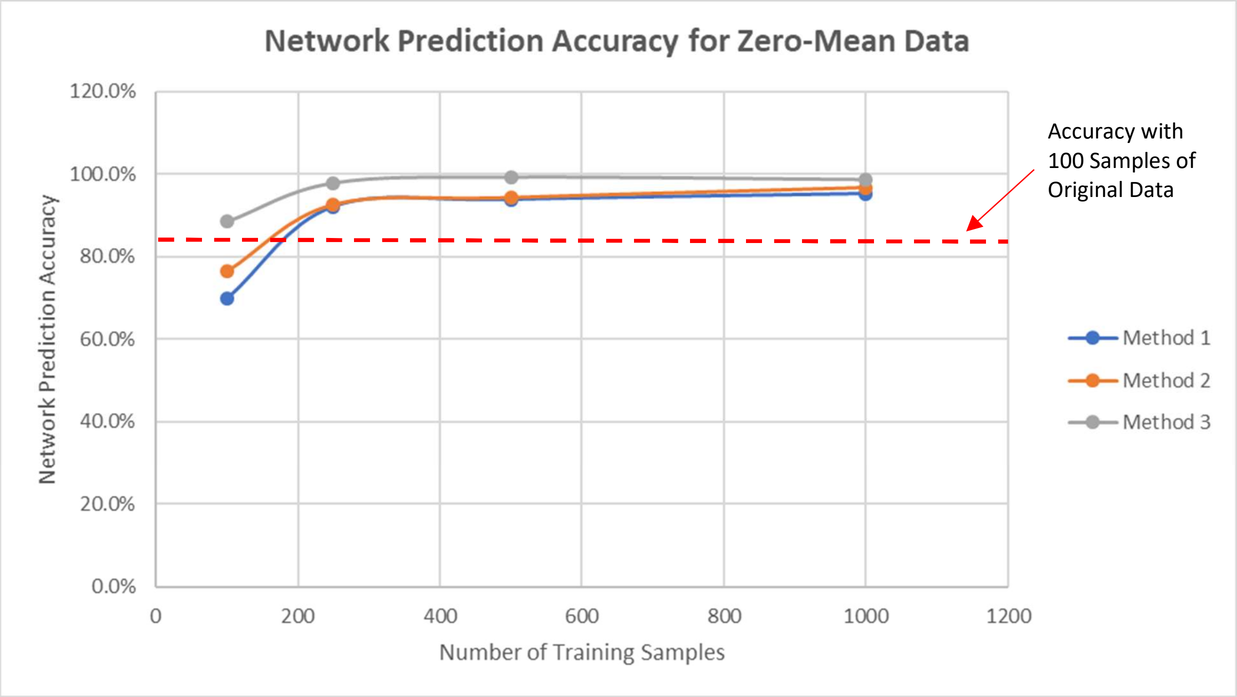

Figure 66: Network Prediction Accuracy for Zero-Mean Data

Method 2 Performs Slightly Better than Method 1 and Both Are an Improvement Over Training with the Original Data

5.3.7 Results for Zero-Mean, Unit Variance Measured Clutter Classification

Table 21: Zero-Mean, Unit Variance Classification Example Properties

Number of Classes	4
Input Data	100 ISAR image samples from each of Plant A, B in light and medium wind
Input Data Processing	Normalized for zero-mean, unit variance at each pixel
Data Generation Methods	Full Covariance, Method 1 Exponential Correlating function, Method 2 General Correlating function
Training Data Size Range	100 to 1000 Samples
Validation Data Size Range	100 to 1000 Samples
Training Data Composition	90% New Generated Data 10% Original Measured Data

5.3.7.1 Network Prediction Accuracies on Zero-Mean, Unit-Variance Measured Data

Table 22: Network Prediction Accuracy for Zero Mean, Unit Variance Classification

	Network Trained with 100 Training Samples	Network Trained with 250 Training Samples	Network Trained with 500 Training Samples	Network Trained with 1000 Training Samples
Data Generation Method 1 – Exponential Correlating function	28.8%	63.1%	85.5%	90.5%
Data Generation Method 2 – General Correlating function	42.0%	74.3%	89.5%	93.5%
Data Generation Method 3 – Full Covariance Multivariate	78.3%	96.5%	97.5%	97.5%
Original Measured Data (100 samples)	68.6%			

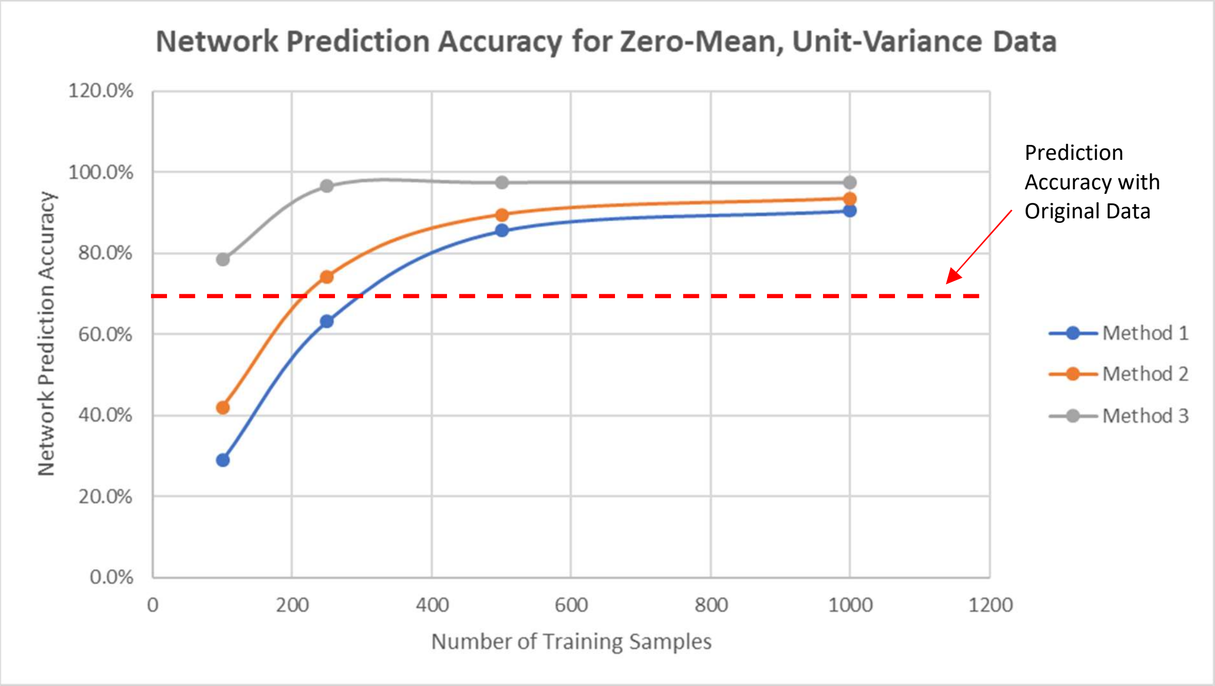

Figure 67: Network Prediction Accuracy for Zero-Mean, Unit-Variance Data

Method 2 Performs Better than Method 1 and Both Are an Improvement Over Training with the Original Data when using 500 or More Training Samples

5.3.7.2 Results Analysis

These results indicate that in this classification example, network prediction accuracy is improved when the network is trained on additional samples using each of all three generation methods. Using the full covariance method results in the largest increase in accuracy, and this is expected since it should be the closest representation of the original data.

Network prediction accuracy for the zero-mean data was higher that prediction accuracy for the zero-mean, unit-variance data. This is expected due to the additional features provided by the non-normalized variance. Additionally, for the non-normalized variance case, data generation methods 1 and 2 have similar network prediction accuracy values. This indicates that the network is utilizing some variance features instead of correlation features, and the variance for both data generation methods is similar. For the zero-mean, unit variance case, the network prediction accuracy differs more for the three data generation methods. In this case, the main discriminator should be correlation, and the results are expected, where prediction accuracy increases with data generation methods with more accurate representation of correlation.

5.3.8 Deep Learning Application 2 –Target Location

In this application, we are using the convolutional network to learn the location of a target on a grid of possible spatial locations in the 2D image place. This application will demonstrate the effectiveness of each data generation method, along with some control data sets. This application will initially use a constant complex-valued target, followed a stochastic zero-mean target that changes every sample. The case of locating a zero-mean uncorrelated stochastic target in zero-mean correlated stochastic clutter is a very difficult problem for standard imaging techniques. Using a stochastic target forces the network to learn variance and correlation features in the clutter, thereby allowing us to evaluate the quality of the data replication.

5.3.8.1 Target Location Network Architecture

The network architecture for this application will be similar to the previous application but with minor adjustments. The network architecture is shown below in Table 23. In this application, the number of learnable kernels in the first convolution layer is increased to 64. This allows the network to learn more input image-layer features, which improves performance of the network in this application.

Table 23: Convolutional Network Layer Details

	NAME	TYPE	ACTIVATIONS	LEARNABLES
1	imageinput 64x64x2 images with 'zerocenter' normalization	Image Input	64×64×2	-
2	Conv1 64 8x8x2 convolutions with stride [2 2] and padding 'same'	Convolution	32×32×64	Weights 8×8×2×64 Bias 1×1×64
3	batchnorm_1 Batch normalization with 64 channels	Batch Normalization	32×32×64	Offset 1×1×64 Scale 1×1×64
4	Relu1 ReLU	ReLU	32×32×64	-
5	maxpool_1 2x2 max pooling with stride [2 2] and padding [0 0 0 0]	Max Pooling	16×16×64	-
6	Conv2 16 4x4x64 convolutions with stride [2 2] and padding 'same'	Convolution	8×8×16	Weights 4×4×64×16 Bias 1×1×16
7	batchnorm_2 Batch normalization with 16 channels	Batch Normalization	8×8×16	Offset 1×1×16 Scale 1×1×16
8	Relu2 ReLU	ReLU	8×8×16	-
9	maxpool_2 2x2 max pooling with stride [2 2] and padding [0 0 0 0]	Max Pooling	4×4×16	-
10	Conv3 16 2x2x16 convolutions with stride [2 2] and padding 'same'	Convolution	2×2×16	Weights 2×2×16×16 Bias 1×1×16
11	batchnorm_3 Batch normalization with 16 channels	Batch Normalization	2×2×16	Offset 1×1×16 Scale 1×1×16
12	Relu3 ReLU	ReLU	2×2×16	-
13	fc 25 fully connected layer	Fully Connected	1×1×25	Weights 25×64 Bias 25×1
14	Soft softmax	Softmax	1×1×25	-
15	classoutput crossentropyex	Classification Output	-	-

We choose a 5x5 target location grid for this application, resulting in 25 total classes. Each class represents a potential target location, as shown in Figure 68.

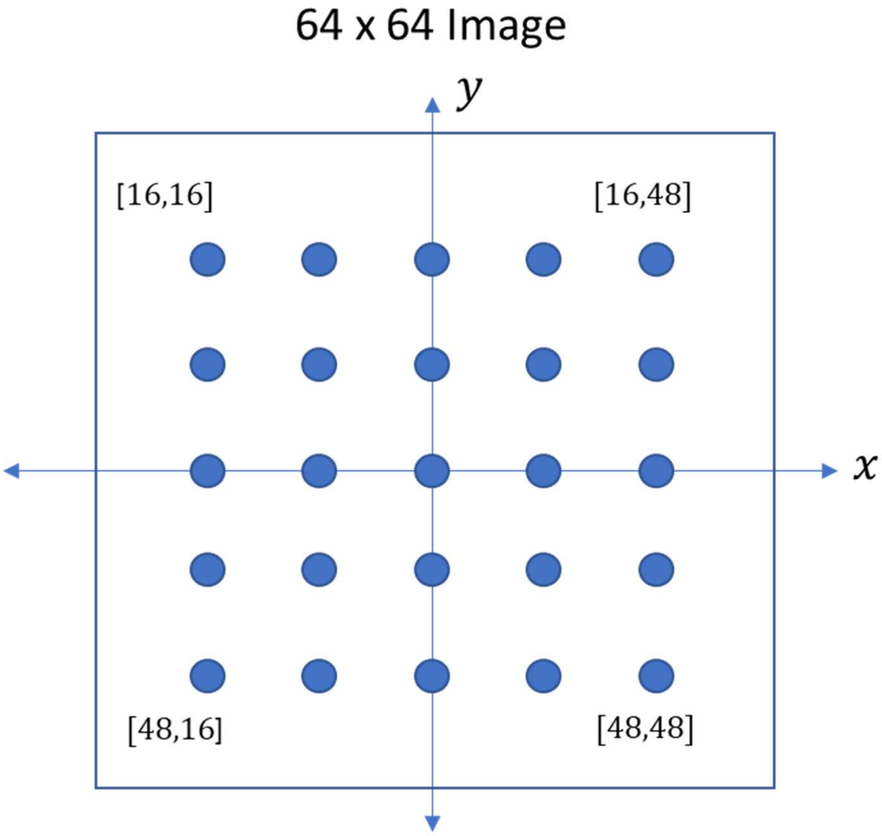

Figure 68: Target Location Grid

5.3.8.2 Training Data Formation

For this application we use simulated clutter data so data correlation can be controlled. This clutter data is created using data generation method two, where we apply a correlating function to random seed data. The estimated multiscale correlation of the simulated data is shown in Figure 69.

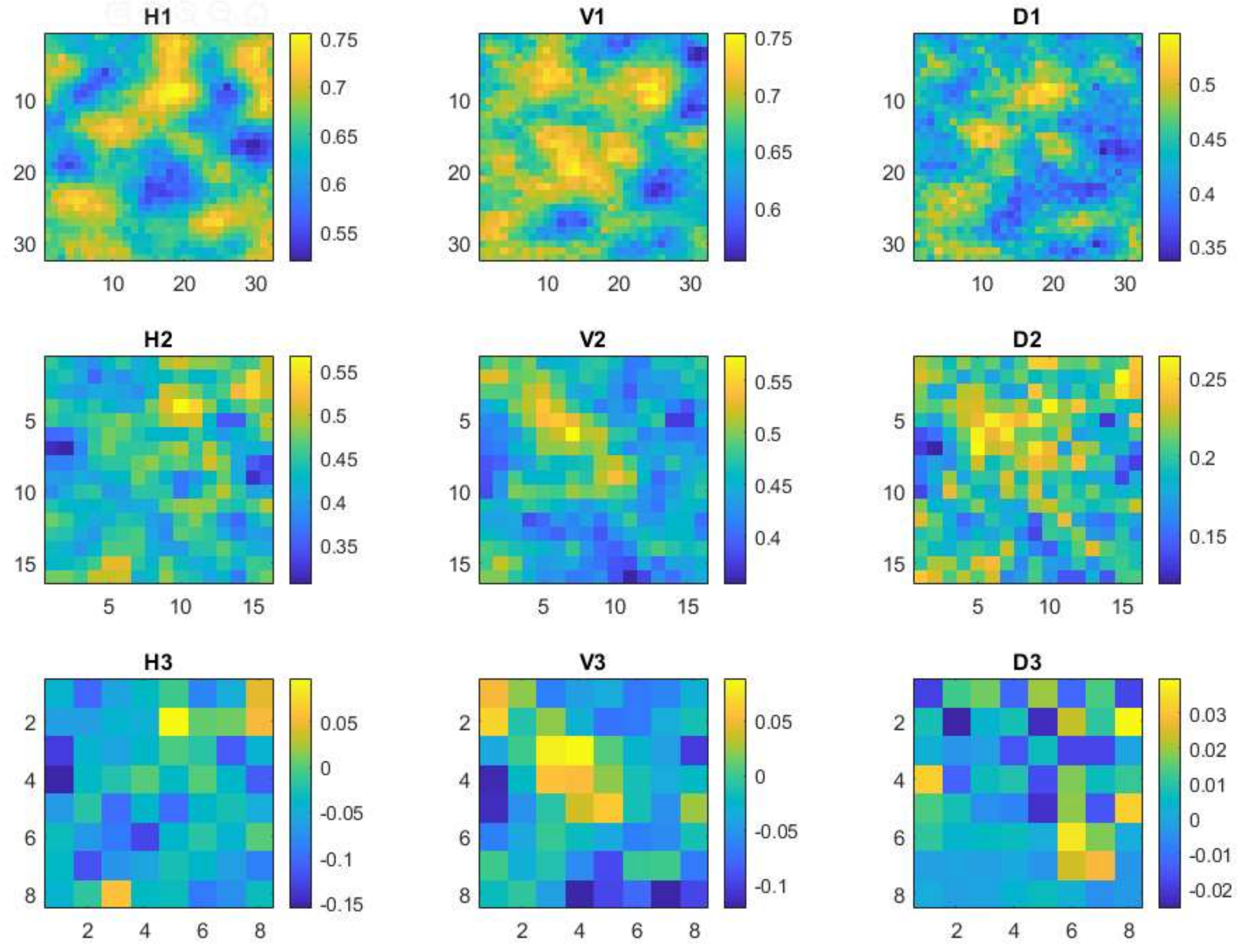

Figure 69: Estimated Multiscale Correlations of Simulated Clutter Data for Target Location Application

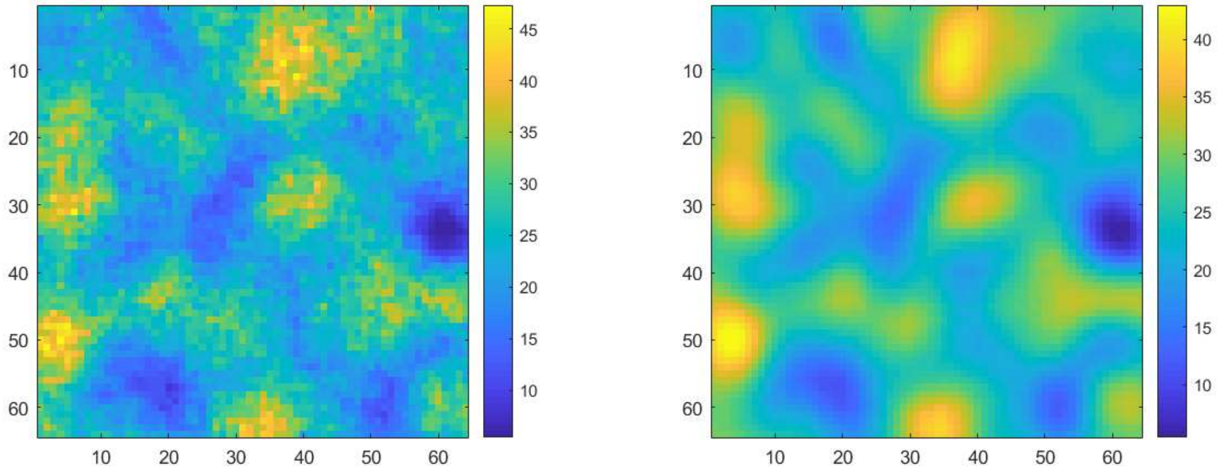

Figure 70: Variance of Simulated Clutter over 100 samples (left) and 1000 samples (right)

The target is defined as a near uncorrelated 8x8 group of pixels centered at one of the potential target locations. For each data generation method, the simulated target is added to the generated clutter at the potential target locations to create the training data, and the target power is varied relative to the clutter power over a range of SNR values. The training data sets are summarized below.

1. **Original Data**
   1000 total samples of simulated data are generated. 100 of these samples are used for the data simulation methods below and the full set of 1000 samples is used for evaluating network prediction accuracy. In addition, network training is performed on 100 samples of the original simulated data to demonstrate that training accuracy suffers from lack of samples.

2. **Method 1 Data**
   Original data is simulated using Method 1, where a directional exponential filter is applied to random seed data. 5000 total samples are generated from analysis of 100 samples of the original data. This is divided into 2500 training samples and 2500 validation samples.

3. **Method 2 Data**
   Original data is simulated using Method 2, where a directional non-exponential correlating filter is applied to random seed data. 5000 total samples are generated from analysis of 100 samples of the original data. This is divided into 2500 training samples and 2500 validation samples.

4. **Full Covariance Data**
   Original data is simulated using the entire sample covariance matrix. 5000 total samples are generated from analysis of 100 samples of the original data. This is divided into 2500 training samples and 2500 validation samples.

5. **Uncorrelated Variance Data**
   This data is created from the sample variance of the original data, and all pixels are uncorrelated. This is a control data set that allows us to evaluate whether the network is learning variance features or correlation features in the data. 5000 total samples are generated from the variance of 100 samples of the original data. This is divided into 2500 training samples and 2500 validation samples.

5.3.8.3 Constant Target

The arbitrary constant target consists of an 8 x 8 grid of constant complex values. For this simulation, the real and imaginary components of the target are shown below in Figure 71.

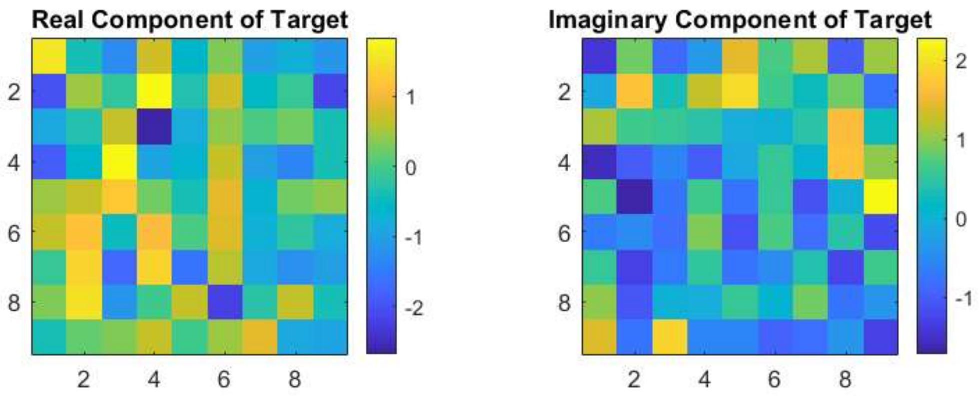

Figure 71: Fixed Target for Location Application

The target amplitude is adjusted to achieve a desired signal-to-clutter ratio.

5.3.8.4 Stochastic Target

The stochastic target is modeled as an 8 x 8 image, where pixels are uncorrelated second-order random variables with defined variance across the 8 x 8 image. The target image changes for every training sample. The target image variance is chosen to result in a desired signal to clutter power ratio. An example training image of the clutter with added target is shown below in Figure 72, where the target is location in position 1 of 25 and has a relative power that is -1.7 dB relative to clutter power (left), a target power that is equal to the clutter power (middle), and a target power that is 1.75 dB relative to the clutter power (right).

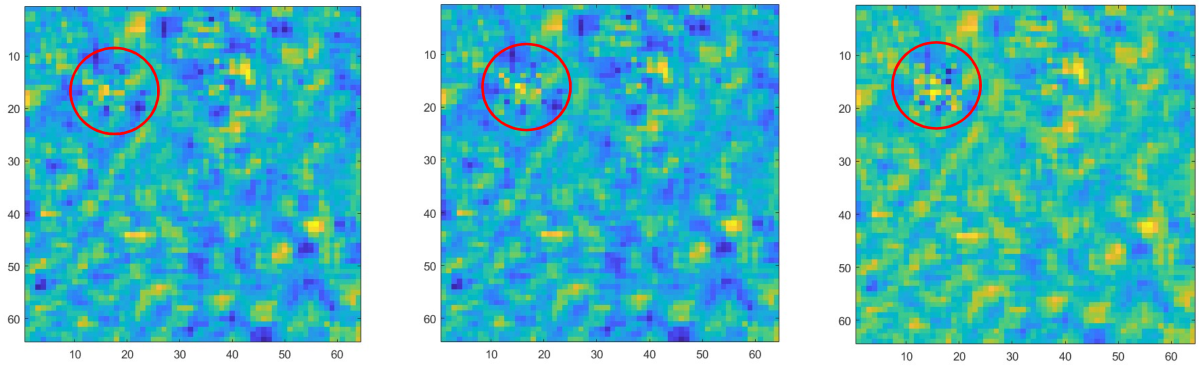

Figure 72: Example Training Image (Real Component) with Target Power from -1.7 dB (left) to +1.75dB relative to Clutter Power

5.3.8.5 Training Strategy

The goal for this example is to show how network prediction accuracy is dependent on the quality of the correlation estimate in the generated data. Pure variance data will provide less features to learn than the data generation method 1. The data generation method 2 has a higher-order estimate of the directional correlations and will provide more features than method 1. In this way we can use network prediction accuracy to quantify the quality of each data generation method within the context of the deep learning application.

5.3.9 Results for Constant Target Location Application

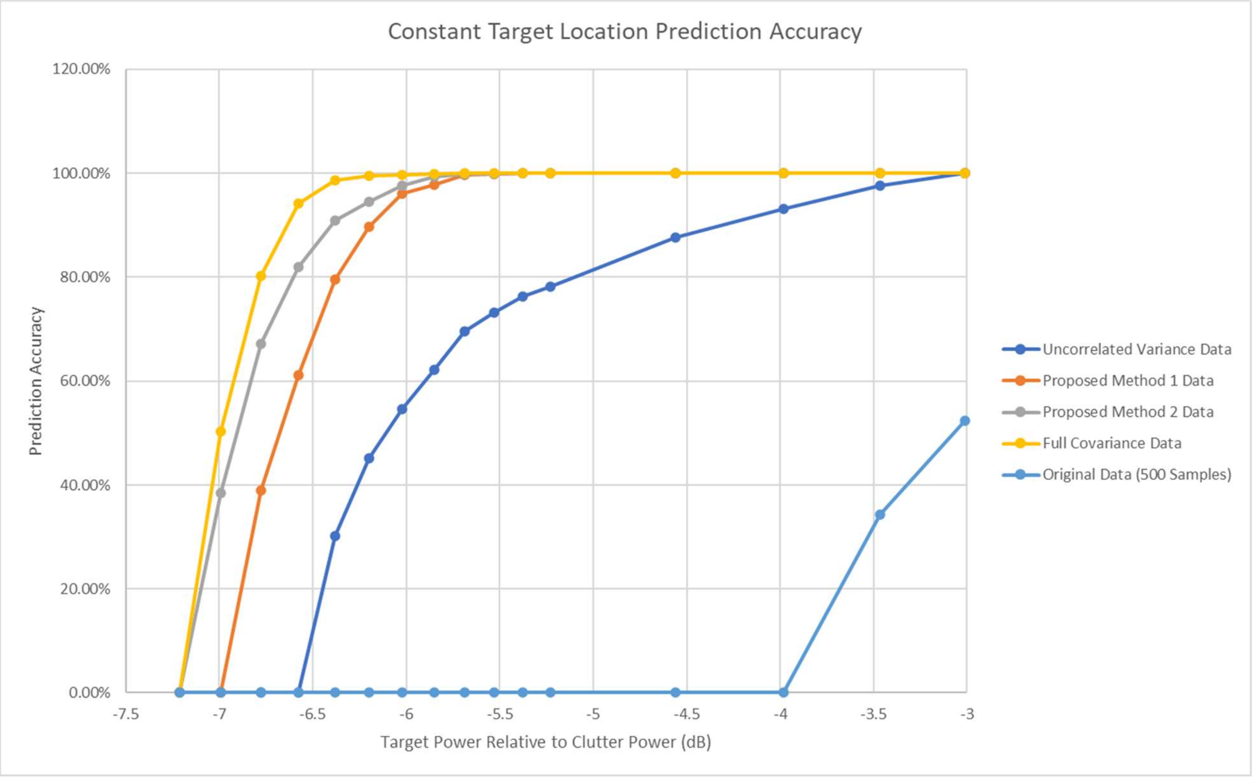

Figure 73: Constant Target Location Prediction Accuracy

Method 1 and 2 Able to Locate Target in Much Higher Target-to-Clutter Ratio than When Using Original Data. Variance Control Data Shows Variance Features are Being Used for Target Location, but Correlation Features are More Effective.

5.3.9.1 Constant Target Location Results Analysis

Figure 73 shows that target location prediction accuracy is significantly increased by training the network on additional generated samples. A ~3 dB target sensitivity improvement is achieved using the proposed data generation methods over the use of 500 samples of the original data. The proposed correlation estimation methods perform better than the variance data, indicating that the network is improving performance by learning correlation features in the data.

5.3.9.2 Results for Stochastic Target Location Application

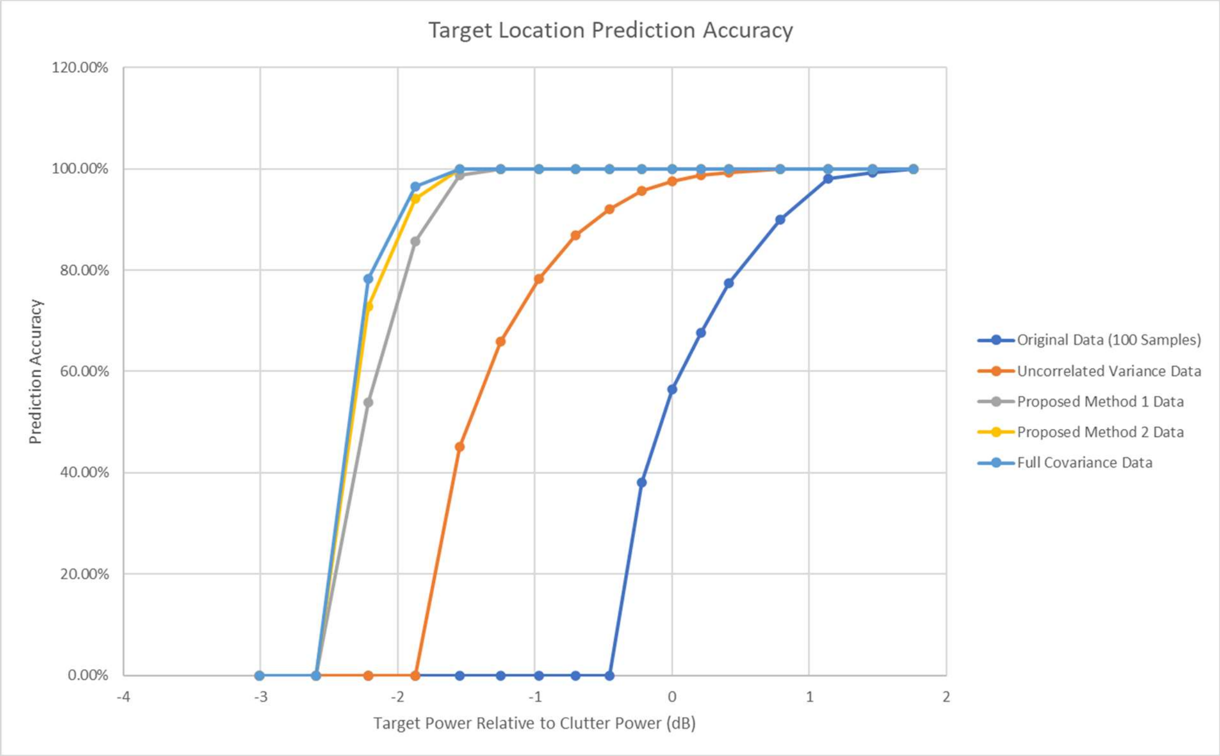

Figure 74: Stochastic Target Location Prediction Accuracy

Locating a Stochastic Target is a More Difficult Application. Method 1 and 2 Able to Locate Target in Much Higher Target-to-Clutter Ratio than When Using Original Data. Variance Control Data Shows Variance Features are Being Used for Target Location, but Correlation Features are More Effective.

5.3.9.3 Stochastic Target Location Results Analysis

Figure 74 shows the network prediction accuracy for a network trained with the five data sets described above. The original 100 samples of data resulted in the lowest network prediction accuracy, which is expected given the smaller training size. The uncorrelated variance data was the next-best performer and predictable performed worse than the training sets with correlated data, as image power (or variance) provides the only discriminating features. The correlated data sets performed best and have similar performance, with network prediction accuracy slightly increasing as the correlation estimate fidelity increases from method 1 to method 2 to full covariance data.

This application demonstrates that the data generation methods proposed in this dissertation result in a consistently higher target location prediction accuracy over the 100 samples of original data and an uncorrelated second-order model of the data. In addition, both methods perform similarly to the idea case of the full covariance data set.

6 CONCLUSIONS

This dissertation has proposed a second-order multiscale model, a multiscale analysis method, and simulation methods for ISAR clutter images. Significant conclusions are listed below, and additional details can be found in the body of the dissertation.

6.1 MULTISCALE ISAR CLUTTER MODEL

The ISAR clutter model order is validated using statistical distributions of physical ISAR measurements and demonstrates that a second-order model is appropriate for the ISAR image of the projected equivalent current. A fourth-order model results in a KL divergence error improvement of less than 1 dB. This is a small improvement but comes at a cost of increased computational and model complexity.

6.2 MULTISCALE ISAR CLUTTER ANALYSIS

The multiscale analysis method allows for accurate estimation of multiscale ISAR clutter model parameters without requiring the calculation of the full sample covariance matrix, although it operates under the assumption that at each scale, correlation decreases with pixel separation. This assumption is deemed appropriate for the physical ISAR measurements of plants used in this research but may not apply to more general correlated data. An example comparison of actual directional correlation to estimated directional correlation is shown below.

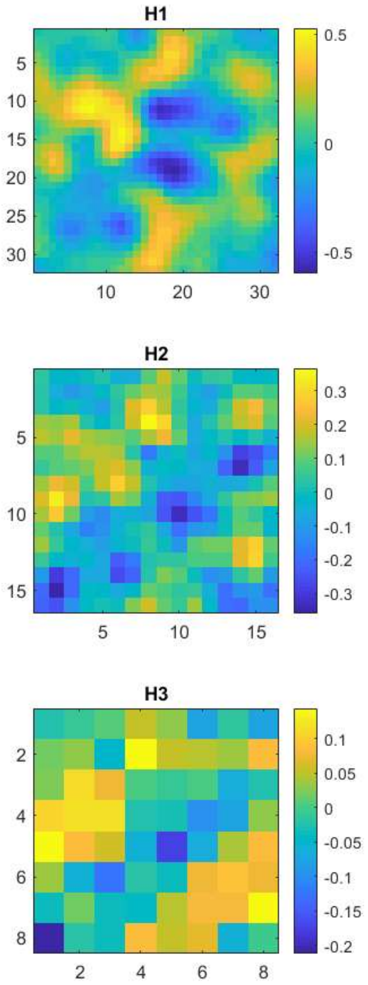

Figure 75: Actual Horizontal Correlation over Scale

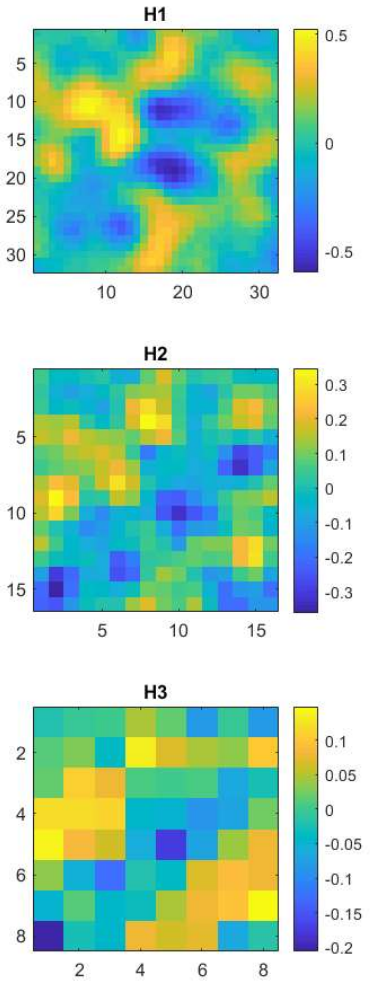

Figure 76: Estimated Horizontal Correlation over Scale

Figure 75 and Figure 76 show how estimated multiscale model parameters match the known data under analysis. In addition, the multiscale analysis has shown to have some merit in the analysis of additional data types, especially spatially correlated geophysical processes. Figure 77 below shows an example of the application of the proposed multiscale analysis to global ocean current velocities. This level 3 multiscale correlation in the zonal flow direction shows areas of correlated ocean currents that aren’t obvious at the original image scale.

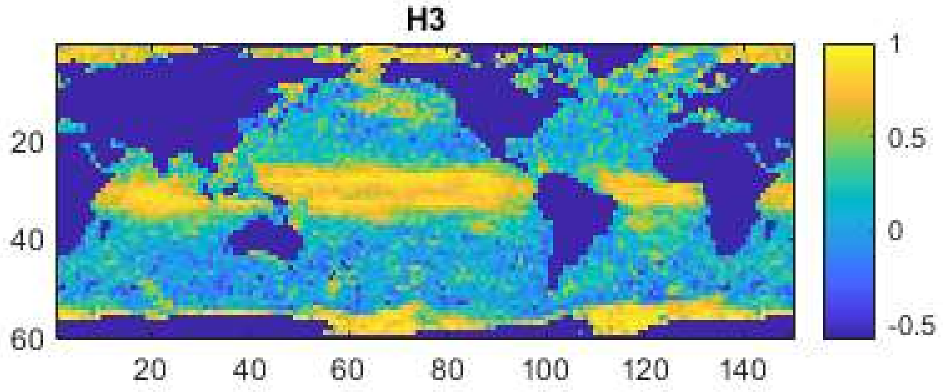

Figure 77: Level 3 Horizontal Correlation of Ocean Current Velocity

6.3 SIMULATION OF ISAR CLUTTER

Two data simulation methods are proposed, where directional correlating filters are applied to random seed data to generate simulated representative samples of ISAR clutter images. These contributions provide the first methods for multiscale modeling, analyzing, and simulation of the projected equivalent current in moving vegetation. Deep learning is the main intended application for these generated samples as deep convolutional networks require many representative training samples to learn the appropriate convolutional kernels and weights. Deep learning is a powerful tool for solving complex problems including the location and classification of targets embedded in strong clutter. Having the ability to generate additional representative samples that improve network performance is a significant contribution in the upcoming field of deep learning. One example of deep learning prediction accuracy improvement is shown below in Figure 78.

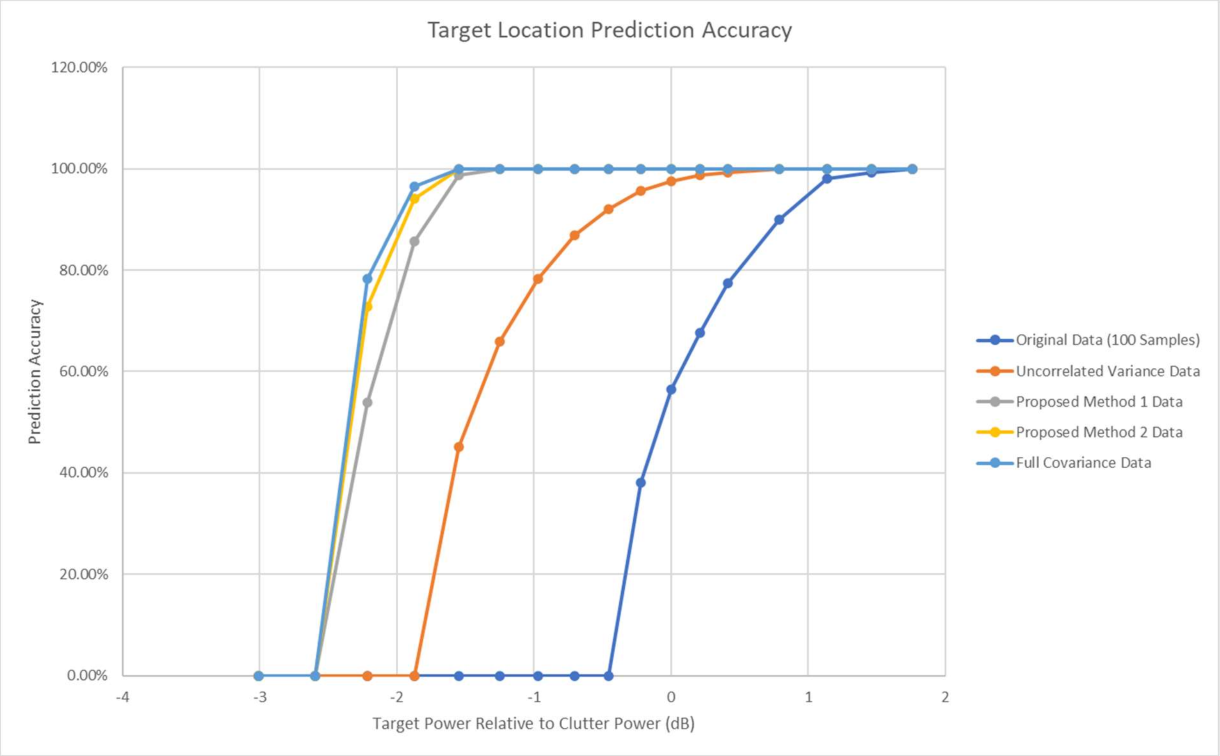

Figure 78: Deep Learning Prediction Accuracy Improvement

Figure 78 shows that the two proposed simulation methods (yellow and grey) perform close to the idea case (light blue) of using the full covariance matrix for generating additional data. In addition, they perform much better than the test case of uncorrelated data (orange) and 100 the original available data that was modeled and analyzed (dark blue). We can conclude that for convolution networks trained to recognize correlation features, the proposed modeling, analysis, and simulation methods are able to provide additional training samples that improve prediction accuracy.

6.4 RELATIONSHIP OF MULTISCALE ANALYSIS TO SCATTERING AND CLUTTER STRUCTURE

Estimated model parameters have been shown to provide an indication of scattering phenomenon in ISAR clutter. Four hypotheses relating the multiscale model parameters to scattering phenomenon have been proposed and tested. These hypotheses are listed below with their associated conclusions.

Table 24: Multiscale Analysis Hypothesis Testing Results

Hypothesis	**Conclusion**
Image pixel variance will increase with motion and leaf size	Verified with Measured Data
Correlation will generally decrease with pixel distance	Verified with Measured Data
Correlation will generally decrease as decomposition level increases	Verified with Measured Data
Correlation will decrease with increased clutter motion	Not Verified Depends on clutter structure

Table 24 shows that scattering phenomenon and clutter structure are related to the proposed multiscale analysis. Therefore, the proposed analysis method can provide discriminating clutter features that can be used for clutter identification and characterization. In addition, this provides more features for deep learning applications to learn and use for clutter mitigation in ISAR imaging.

7 BIBLIOGRAPHY

[1] B. Borden and M. Cheney, Fundamentals of Radar Imaging, Philadelphia, PA: Society of Industrial and Applied Mathematics, 2009.

[2] C. Balanis, Advanced Engineering Electromagnetics, John Wiley & Sons, Inc., 1989.

[3] P. Yi, H. Xiaotao, C. Fan and P. Lei, "Vegetation clutter modeling using ultra high frequency LFMCW radar," in *IEEE National Radar Conference - Proceedings*, 2015.

[4] X. Zhu, W. Hu and B. Guo, "A review of super-resolution inverse synthetic aperture radar imaging algorithms," in *2017 7th IEEE International Conference on Electronics Information and Emergency Communication (ICEIEC)*, Macau, 2017.

[5] M. Martorella and V. Chen, Inverse Synthetic Aperture Radar Imaging: Principles, Algorithms, and Applications, [Online]: Institution of Engineering and Technology, 2014.

[6] R. Schmidt, "Multiple Emitter Location and Signal Parameter Estimation," *IEEE Transactions on Antennas and Propagation,* pp. 276-280, 1986.

[7] A. J. Sieber and J. Fortuny, "Three-dimensional synthetic aperture radar imaging of a fir tree: first results," *IEEE Transactions on Geoscience and Remote Sensing,* pp. 1006-1014, March 1999.

[8] E. Giusti, D. Cataldo, A. Bacci, S. Tomei and M. Martorella, "ISAR Image Resolution Enhancement: Compressive Sensing Versus State-of-the-Art Super-Resolution Techniques," *IEEE Transactions on Aerospace and Electronic Systems,* vol. 54, no. 4, pp. 1983-1997, Aug. 2018.

[9] J. Odendaal, E. Barnard and C. Pistorius, "Two-dimensional superresolution radar imaging using the MUSIC algorithm," *IEEE Trans. Antennas Propagation,* vol. 42, no. 10, pp. 1386-1391, Oct. 1994.

[10] T. Kailath and R. Roy, "ESPRIT-estimation of signal parameters via rotational invariance techniques," *IEEE Transactions om Acoustic and Speech Signal Processing,* vol. 37, no. 7, pp. 984-995, 1989.

[11] B. Steinberg and J. Tsao, "Reduction of sidelobe and speckle artifacts in microwave imaging: The CLEAN technique," *IEEE Transactions on Antennas and Propagation,* vol. 36, no. 4, pp. 543-556, 1988.

[12] J. Li and Z. S. Liu, "Implementation of the RELAX algorithm," *IEEE Transactions on Aerospace and Electronics Systems,* vol. 34, no. 2, p. 657–664, 1998.

[13] T. G. Moore, B. W. Zuerndorfer and E. C. Burt, "Enhanced imagery using spectral-estimation-based techniques," *Lincoln Laboratory Journal,* vol. 10, no. 2, 1997.

[14] K. Gerlach and S. D. Blunt, "Adaptive pulse compression via MMSE estimation," *IEEE Transactions on Aerospace Electronics Systems,* vol. 42, no. 2, pp. 572-584, April 2006.

[15] R. O. Lane, "Bayesian super-resolution with application to radar target recognition," PhD Dissertation, Department of Electronics and Electrical Engineering, Univeristy of London, Feb 2008.

[16] J. Capon, "High-resolution frequency-wavenumber spectrum analysis," *Proceedings of the IEEE,* vol. 57, no. 8, pp. 1408-1418, 1969.

[17] P. Stoica and J. Li, "An adaptive filtering approach to spectral estimation and SAR imaging," *IEEE Transactions on Signal Processing,* vol. 44, no. 6, pp. 1469-1484, June 1996.

[18] M. Kosek and H. Stankwitz, "Super-resolution for SAR/ISAR RCS measurement using spatially invariant apodization," *Proceedings of the 17th Annual Meeting and Symposium of the Antenna Measurement Techniques Association,* Nov. 1995.

[19] L. Zhang, "Resolution Enhancement for Inverse Synthetic Aperture Radar Imaging Under Low SNR via Improved Compressive Sensing," *IEEE Transactions on Geoscience and Remote Sensing,* vol. 48, no. 10, pp. 3824-3838, Oct. 2010.

[20] L. Zhang, Z. Qiao, M. Xing, Y. Li and Z. Bao, "High-Resolution ISAR Imaging With Sparse Stepped-Frequency Waveforms," *IEEE Transactions on Geoscience and Remote Sensing,* vol. 49, no. 11, pp. 4630-4651, Nov. 2011.

[21] M. Kang, S. Lee, K. Kim and J. Bae, "Bistatic ISAR Imaging and Scaling of Highly Maneuvering Target With Complex Motion via Compressive Sensing," *IEEE Transactions on Aerospace and Electronic Systems,* vol. 54, no. 6, pp. 2809-2826, Dec. 2018.

[22] J. Rong, Y. Wang and T. Han, "Iterative Optimization-Based ISAR Imaging With Sparse Aperture and Its Application in Interferometric ISAR Imaging," *IEEE Sensors Journal,* vol. 19, no. 19, pp. 8681-8693, Oct.1, 2019.

[23] Y. Gu, C. Pei, X. Wang, R. Chen and S. Tao, "Full polarisation ISAR imaging based on joint sparse Bayesian compressive sensing," *The Journal of Engineering,* vol. 2019, no. 20, pp. 6947-6950, Oct. 2019.

[24] S. Wei, L. Zhang, H. Ma and H. Liu, "Sparse Frequency Waveform Optimization for High-Resolution ISAR Imaging," *IEEE Transactions on Geoscience and Remote Sensing,* vol. 58, no. 1, pp. 546-566, Jan. 2020.

[25] J. Chen, L. Xu, X. Pan, P. Zheng and S. Xiao, "High-Resolution ISAR Imaging With Sparse Aperture VFM Waveforms Under Low SNR Condition," *IEEE Access,* vol. 7, pp. 110651-110659, 2019.

[26] J. F. Degurse, L. Savy, S. Marcos and J.-P. Molinie, "Deterministic Aided STAP for Target Detection in Heterogeneous Situations," *International Journal of Antennas and Propagation,* 2013.

[27] X. Zhang, Q. Yang and W. Deng, "Weak Target Detection within the Nonhomogeneous Ionospheric Clutter Background of HFSWR Based on STAP," *International Journal of Antennas and Propagation,* 2013.

[28] A. Zaimbashi, "Target detection in clutter background: Null or whiten the clutter," in *24th Iranian Conference on Electrical Engineering*, Shiraz, 2016.

[29] S. Guo, Q. Zhang, Y. Shao and W. Chen, "Sea Clutter and Target Detection with Deep Neural Networks," in *2nd International Conference on Artificial Intelligence and Engineering Applications*, 2017.

[30] Q. Zhang, Y. Shao, S. Guo, L. Sun and W. Chen, "A Novel Method for Sea Clutter Suppression and Target Detection via Deep Convolutional Autoencoder," *International Journal of Signal Processing,* vol. 2, pp. 35-40, 2017.

[31] L. Zhang, W. You, Q. Wu and S. Qi, "Deep Learning-Based Automatic Clutter/Interference Detection for HFSWR," *Remote Sensing,* 2018.

[32] J. Liu, J. Han, Z.-J. Zhang and J. Li, "Target Detection Exploiting Covariance Matrix Structures in MIMO Radar," *Signal Processing,* vol. 154, 2018.

[33] P. Lombardo and J. B. Billingsley, "A new model for the Doppler spectrum of windblown radar ground clutter," in *Proceedings of the 1999 IEEE Radar Conference*, Waltham, MA, 1999.

[34] J. R. Franz and J. K. Jao, "UHF windblown clutter measurements and modeling," in *2006 IEEE Conference on Radar*, Verona, NY, 2006.

[35] Y. Goncharenko, G. Farquharson, V. Gorobets, V. Gutnik and Y. Tsarin, "Adaptive Moving Target Indication in a Windblown Environment," *IEEE Transactions on Aerospace and Electronic Systems,* vol. 50, no. 4, pp. 2989-2997, 2014.

[36] P. Gómez-Pérez, M. Crego-García and I. Cuiñas, "Quantifying the degradation on radar detection range through vegetation clutter," in *2017 IEEE International Symposium on Antennas and Propagation & USNC/URSI National Radio Science Meeting*, San Diego, CA, 2017.

[37] A. Izzo, M. Liguori, C. Clemente, C. Galdi, M. D. Bisceglie and J. J. Soraghan, "Multimodel CFAR Detection in Foliage Penetrating SAR Images," *IEEE Transactions on Aerospace and Electronic Systems, vol. 53, no. 4,* vol. 53, no. 4, pp. 1769-1780, August 2017.

[38] R. G. Raj, M. Kluskens, D. Zolnick, S. T. Chun and J. Brozena, "An efficient hybrid CEM approach to modeling backscatter of forest clutter," in *2017 IEEE International Symposium on Antennas and Propagation & USNC/URSI National Radio Science Meeting*, San Diego, CA, 2017.

[39] X. Chen and Z. Wei, "Deep-Learning Schemes for Full-Wave Nonlinear Inverse Scattering Problems," *IEEE Transactions on Geoscience and Remote Sensing,* pp. 1849-1860, 2019.

[40] R. l. Vicen-Bueno, R. Carrasco-Alvarez, M. Rosa-Zurera and J. C. Nieto-Borge, "Sea Clutter Reduction and Target Enhancement by Neural Networks in a Marine Radar System," *Sensors,* vol. 9, pp. 1913-1936, 2009.

[41] C. Bentes, D. Velotto and B. Tings, "Ship Classification in TerraSAR-X Images With Convolutional Neural Networks," *IEEE Journal of Oceanic Engineering,* vol. 43, no. 1, pp. 258-266, Jan. 2018.

[42] A. Huizing and M. Heiligers, "On the importance of visual explanation and segmentation for SAR ATR using deep learning," in *2018 IEEE Radar Conference (RadarConf18)*, Oklahoma City, OK, 2018.

[43] F. Xu, H. Wang, Q. Song, W. Ao, Y. Shi and Y. Qian, "Intelligent Ship Recongnition from Synthetic Aperture Radar Images," in *IGARSS 2018 - 2018 IEEE International Geoscience and Remote Sensing Symposium*, Valencia, 2018.

[44] T. H. Vu, L. Nguyen, T. Guo and V. Monga, "Deep network for simultaneous decomposition and classification in UWB-SAR imagery," in *2018 IEEE Radar Conference*, Oklahoma City, OK, 2018.

[45] Y. Xie and S. Yu, "Application of a Convolutional Autoencoder to Half Space Radar Hrrp Recognition," in *2018 International Conference on Wavelet Analysis and Pattern Recognition (ICWAPR)*, Chengdu, 2018.

[46] C. Hu, L. Wang and O. Loffeld, "A Novel Inverse Synthetic Aperture Radar Imaging Method Using Convolutional Neural Networks," in *5th International Workshop on Compressed Sensing applied to Radar, Multimodal Sensing, and Imaging (CoSeRa)*, 2018.

[47] C. Hu, L. Wang, Z. Li, L. Sun and O. Loffeld, "Inverse synthetic aperture radar imaging using complex-value deep neural network," *The Journal of Engineering,* vol. 2019, no. 20, pp. 7096-7099, Oct. 2019.

[48] N. Tong and B. Xue, "DIOD: Fast and Efficient Weakly Semi-Supervised Deep Complex ISAR Object Detection," *EEE Transactions on Cybernetics,* vol. 49, no. 11, pp. 3991-4003, Nov. 2019.

[49] S. Tian, C. Wang and H. Zhang, "SAR Object Classification with a Multi-Scale Convolutional Auto-Encoder," in *2019 SAR in Big Data Era (BIGSARDATA)*, Beijing, China, 2019.

[50] M. Wilmanski, G. Dester, M. Hawks and R. Smith, "Deep Learning for Organic Clutter Detection in Radar Cross Section Data," in *2019 International Conference on Electromagnetics in Advanced Applications (ICEAA)*, Grenada, Spain, 2019.

[51] M. Pan, J. Chen, S. Wang and Z. Dong, "A Novel Approach for Marine Small Target Detection Based on Deep Learning," in *2019 IEEE 4th International Conference on Signal and Image Processing*, 2019.

[52] G. Li, Z. Song and Q. Fu, "Small Boat Detection via Time-Frequency Analysis and DenseNet," in *2019 IEEE 4th International Conference on Signal and Image Processing*, 2019.

[53] H. Mu, Y. Zhang, C. Ding, Y. Jiang, M. H. Er and A. C. Kot, "DeepImaging: A Ground Moving Target Imaging Based on CNN for SAR-GMTI System," *IEEE Geoscience and Remote Sensing Letters,* pp. 1-5, 2020.

[54] A. K. Fung and S. Tjuatja, "Advanced Models for Backscattering from Rough Surfaces," in *Managing Technologically Driven Organizations: The Human Side of Innovation and Change, IEMC 2003 Proceedings*, Boston, 2003.

[55] E. Casagrande, B. Mueller, D. G. Miralles, D. Entekhabi and A. Molini, "Wavelet correlations to reveal multiscale coupling in geophysical systems," *Journal of Geophysical Research: Atmospheres,* vol. 120, pp. 7555-7572, 2015.

[56] D. Miralles, T. Holmes, R. d. Jeu and J. H. Gash, "Global land-surface evaporation estimated from satellite-based observations," *Hydrology and Earth System Sciences Discussions,* vol. 15, pp. 453-459, October 2010.

[57] D. Peters, R. Pielke, B. Bestelmeyer and C. Allen, "Cross-Scale Interactions, Nonlinearities, and Forecasting Catastrophic Events," *Proceedings of the National Academy of Sciences,* vol. 101, no. 42, pp. 15130-15135, 2004.

[58] K. Raffa, B. Aukema, B. Bentz and A. Carroll, "Cross-Scale Drivers of Natural Disturbances Prone to Anthropogenic Amplification: The Dynamics of Bark Beetle Eruptions," *BioScience,* vol. 58, no. 6, pp. 501-517, June 2008.

[59] T. Scanlon, K. Caylor, S. Levin and I. Rodriguez-Iturbe, "Positive feedbacks promote power-law clustering of Kalahari vegetation," *Nature,* vol. 449, no. 7159, pp. 209-212, 2007.

[60] V. Guttal and C. Jayaprakash, "Spatial variance and spatial skewness: Leading indicators of regime shifts in spatial ecological systems," *Theoretical Ecology,* vol. 2, no. 1, pp. 3-12, 2008.

[61] C. Allen and C. S. Holling, Cross-scale Structure and Scale Breaks in Ecosystems and Other Complex Systems, New York: Columbia University Press, 2002, p. 2013.

[62] M. A. Moritz, M. E. Morais, L. A. Summerell and J. M. Carlson, "Wildfires, complexity, and highly optimized tolerance," *Proceedings of the National Academy of Sciences,* vol. 102, no. 50, pp. 17912-17917, 2006.

[63] D. W. Cash, W. N. Adger, F. Berkes and P. Garden, "Scale and Cross-Scale Dynamics: Governance and Information in Multilevel World," *ECOLOGY AND SOCIETY,* vol. 11, no. 2, p. 8, 2006.

[64] D. P. C. Peters, B. Bestelmeyer and M. G. Turner, "Cross-scale interactions and changing pattern-process relationships: Consequences for system dynamics," *Ecosystems,* vol. 10, no. 5, pp. 790-796, 2007.

[65] S. F. Thrush, J. E. Hewitt, A. M. Lohrer and L. Chiaroni, "When small changes matter: The role of cross-scale interactions between habitat and ecological connectivity in recovery," *Ecological Applications,* vol. 23, no. 1, pp. 226-238, 2013.

[66] E. E. Werner, C. J. Davis, D. Skelly and R. A. Relyea, "Cross-Scale Interactions and the Distribution-Abundance Relationship," *PLoS ONE,* vol. 9, no. 5, 2014.

[67] N. J. Holbrook, J. Li, M. Collins and E. D. Lorenzo, "Decadal Climate Variability and Cross-Scale Interactions: ICCL 2013 Expert Assessment Workshop," *Bulletin of the American Meteorological Society,* vol. 95, pp. ES155-ES158, 2014.

[68] D. P. C. Peters, R. A. P. Sr., B. Bestelmeyer and C. D. Allen, "Chapter: Spatial Nonlinearities: Cascading Effects in the Earth System," in *Terrestrial Ecosystems in a Changing World*, Berlin, Germany, Springer, 2007, pp. 165-174.

[69] A. Molini, G. G. Katul and A. Porporato, "Causality across rainfall time scales revealed by continuous wavelet transforms," *Journal of Geophysical Research Atmospheres ,* vol. 115, 2010.

[70] M. Dhamala, G. Rangarajan and M. Ding, "Analyzing Information Flow in Brain Networks with Nonparametric Granger Causality," *NeuroImage,* vol. 41, no. 2, pp. 354-362, 2008.

[71] M. Lungarella, A. Pitti and Y. Kuniyoshi, "Information Transfer at multiple scales," *Physical Review E,* vol. 76, no. 5, 2007.

[72] P. Guttorp and D. B. Percival, "Wavelet Analysis of Covariance With Application to Atmospheric Time Series," *Journal of Geophysical Research D: Atmospheres,* pp. 14941-14962, 2000.

[73] C. Torrence and G. P. Compo, "A Practical Guide to Wavelet Analysis," *Bulletin of the American Meteorological Society,* vol. 79, no. 1, pp. 61-78, 1997.

[74] I. Daubechies and C. Heil, "Ten Lectures on Wavelets," *Computers in Physics,* vol. 6, no. 6, p. 697, 1992.

[75] M. Souare, "SAR Image Analysis in Wavelets Domain," Case Western Reserve University, August 2014.

[76] A. Lucrecio, "ISAR imaging using Fourier and wavelet transforms," Institutional Archive of the Naval Postgraduate School, Monterey, CA, 2007.

[77] J. Inglada and G. Mercier, "A New Statistical Similarity Measure for Change Detection in Multitemporal SAR IMages and Its Extension to Multiscale Change Analysis," *IEEE Transactions on Geoscience and Remote Sensing,* pp. Vol. 45, No. 5, pp 1432 - 1445, 2007.

[78] E. J. M. Rignot and J. Zyl, "Change Detection Techniques for ERS-1 SAR Data," *IEEE Transactions on Geoscience and Remote Sensing,* pp. vol. 31, no. 4, pp. 896 - 906, 1993.

[79] F. T. Ulaby, F. Kouyae, B. Brisco and T. H. L. Williams, "Textural Information in SAR Images," *Transactions on Geoscience and Remote Sensing,* pp. vol. GRS-24, no. 2, pp. 235 - 245, 1986.

[80] F. Trouvé, E. Valet, E. Nicolas, J. M. Rudant and J. Bujor, "Application of Log-Cumulants to the Detection of Spatiotemporal Discontinuities in Multitemporal SAR images," *IEEE*

Transactions on Geoscience and Remote Sensing, pp. vol. 42, no. 10, pp. 2073 - 2084, 2004.

[81] M. Herdin, N. Czink, H. Ozcelik and E. Bonek, "Correlation matrix distance, a meaningful measure for evaluation of non-stationary MIMO channels," in *Vehicular Technology Conference*, 2005.

[82] ESR, "OSCAR third degree resolution ocean surface currents," PO.DAAC https://doi.org/10.5067/OSCAR-03D01, CA, USA, 2009.

[83] X. He, N. Tng and X. Hu, "Automatic Recognition of ISAR Images based on Deep Learning," in *CIE International Conference on Radar*, 2016.

[84] S. Xaied, A. Toumi and A. Khenchaf, "Target Classification using Convolutional Deep Learning and Auto-Encoder Models," in *4th International Conference on Advanced Technologies for Signal and Image Processing (ATSIP)*, 2018.

[85] M. Iwamoto and K. Suwa, "A two-dimensional bandwidth extrapolation technique for polarimetric synthetic aperture radar images," *IEEE Transactions on Geoscience and Remote Sensing,* pp. 45-54, 2007.

[86] X. He, N. Tong and X. Hu, "Automatic recognition of ISAR images based on deep learning," in *2016 CIE International Conference on Radar (RADAR)*, Guangzhou, 2016.

[87] R. M. Narayanan and X. Xu, "Enhanced resolution in SAR/ISAR imaging using iterative sidelobe apodization," *IEEE Transactions on Image Processing,* vol. 14, no. 4, pp. 537-547, April 2005.

[88] I. J. Gupta, "High resolution radar imaging using 2-D linear prediction," *IEEE Transactions on Antennas and Propagation,* vol. 42, no. I, pp. 31-37, 1994.

[89] S. Tjuatja and J. Mitchell, "ISAR Imaging in the Presence of Quasi-Random Multiplicative Noise Using Convolutional Deep Learning," in *IGARSS 2019 - 2019 IEEE International Geoscience and Remote Sensing Symposium*, Yokohama, Japan, 2019.

[90] S. Huang, J. Qian, Y. Wang, X. Yang and L. Yang, "ISAR Maneuvering Target Imaging Based on Convolutional Neural Network," in *IGARSS 2019 - 2019 IEEE International Geoscience and Remote Sensing Symposium*, Yokohama, Japan, 2019.

[91] N. Tong and B. Xue, "Real-World ISAR Object Recognition and Relation Discovery Using Deep Relation Graph Learning," *IEEE Access,* vol. 7, pp. 43906-43914, 2019.

[92] S. L. Borison, S. B. Bowling and K. M. Cuomo, "Super-resolution methods doe wideband radar," *Lincoln Laboratory Journal,* vol. 5, no. 3, pp. 441-461, 1992.

[93] E. Pottier and J. S. Lee, Polarimetric Radar Imaging: From Basics to Applications, Boca Raton: CRC Press, 2009.

[94] A. Quinquis, E. Radoi and F. Totir, "Some Radar Imagery Results Using Superresolution Techniques," *IEEE Transactions on Antennas and Propagation,* vol. 52, no. 5, pp. 1230-1244, May 2004.

[95] I. Jouny, F. Garber, R. Moses and E. Walton, "Applications of the Bispectrum in Radar Signature Analysis and Target Identification," *Automatic Object Recognition,* vol. 1471, pp. 142-153, September 1991.

[96] X. Chen, "Subspace-based optimization method for inverse scattering problems with an inhomogeneous background medium," *Inverse Problems,* vol. 26, 2010.

[97] X. Chen, "Signal-subspace method approach to intensity-only electromagnetic inverse scattering problem," *Journal of the Optical Society of America,* vol. 25, pp. 2018-2024, 2008.

[98] X. Chen, "MUSIC imaging applied to total internal reflection tomography," *Journal of the Optical Society of America,* vol. 25, pp. 357-364, 2008.

[99] A. Fannjiang, "Compressive inverse scattering II. multi-shot SISO measurements with born scatterers," *Inverse Problems,* vol. 26, 2010.

[100] Z. Wang and S. Abeysekera, "Performance of Correlation-Based Frequency Estimation Methods in the Presence of Multiplicative Noise," *IEEE Transactions on Vehicular Technology,* vol. 55, no. 4, pp. 1281-1290, July 2006.

[101] Y. S. Yoon and M. Amin, "High-Resolution Through-the-Wall Radar Imaging Using Beamspace MUSIC," *IEEE Transactions on Antennas and Propagation,* vol. 56, no. 6, pp. 1763-1774, 2008.

[102] Y. Zhu, Y. Su and W. Yu, "An ISAR Imaging Method Based on MIMO Technique," *IEEE Transactions on Geoscience and Remote Sensing,* vol. 147, no. 2, pp. 139-148, 2000.

[103] W. Qiu, Z. Hongzhong, J. Zhou and Q. Fu, "High-Resolution Fully Polarimetric ISAR Imaging Based on Compressive Sensing," *IEEE Trans. On Geoscience and Remote Sensing,* vol. 52, no. 10, pp. 6119-6131, October 2014.

[104] X. Gu and Y. Zhang, "Effectiveness and uniqueness conditions for 2-D MUSIC algorithm used in ISAR imaging," in *2nd Asian-Pacific Conference on Synthetic Aperture Radar*, 2009.

[105] S. Gunnala, L. Camacho and S. Tjuatja, "Target detection above rough surfaces in microwave imaging using Compressive Sampling," in *2010 IEEE International Geoscience and Remote Sensing Symposium*, 2010.

[106] L. v. Kempen and H. Sahli, "Signal processing techniques for clutter parameters estimation and clutter removal in GPR data for landmine detection," in *Proceedings of the 11th IEEE Signal Processing Workshop on Statistical Signal Processing*, Singapore, 2001.

[107] E. A. Marengo, "Quasi-Born approximation scattering and inverse scattering of multiple scattering targets," *IET Radar, Sonar & Navigation,* vol. 11, no. 8, pp. 1276-1284, 2017.

[108] K. Sarabandi, "Electromagnetic Scattering from Slightly Rough Surfaces with Inhomogeneous Dielectric Profiles," *IEEE Transactions on Antennas and Propagation,* vol. 45, no. 9, pp. 1419-1430, 1997.

[109] F. Lin, R. C. Qiu, J. P. Browning and M. C. Wicks, "Target detection with function of covariance matrices under clutter environment," in *IET International Conference on Radar Systems (Radar 2012)*, Glasgow, UK, 2012.

[110] H. S. Kim, "Dissertation: Adaptive Target Detection in Radar Imaging," University of Michigan, 2001.

[111] J. Metcalf, S. D. Blunt and B. Himed, "A machine learning approach to cognitive radar detection," in *2015 IEEE Radar Conference (RadarCon)*, Arlington, VA, 2015.

[112] L. Ma, J. Wu, J. Zhang, Z. Wu, G. Jeon, Y. Zhang and T. Wu, "Research on Sea Clutter Reflectivity Using Deep Learning Model in Industry 4.0," *IEEE Transactions on Industrial Informatics,* 2019.

[113] W. Huang, X. Liu and E. W. Gill, "OceanWind andWave Measurements Using X-Band Marine Radar: A Comprehensive Review," *Remote Sensing,* vol. 9, no. 1261, pp. 1-39, 2017.

APPENDIX A: MULTISCALE ANALYSIS OF MEASURED ISAR CLUTTER

In the following figures, the labels A0, A1, B0, B1, C0, C1 represent the following measurement scenarios:

A0 – Plant A, No Wind
A1 – Plant A, Light Wind
B0 – Plant B, No Wind
B1 – Plant B, Light Wind
C0 – Plant C, No Wind
C1 – Plant C, Light Wind

Histograms show the distribution of covariance over each covariance map.

MULTISCALE COMPONENTS BY PLANT

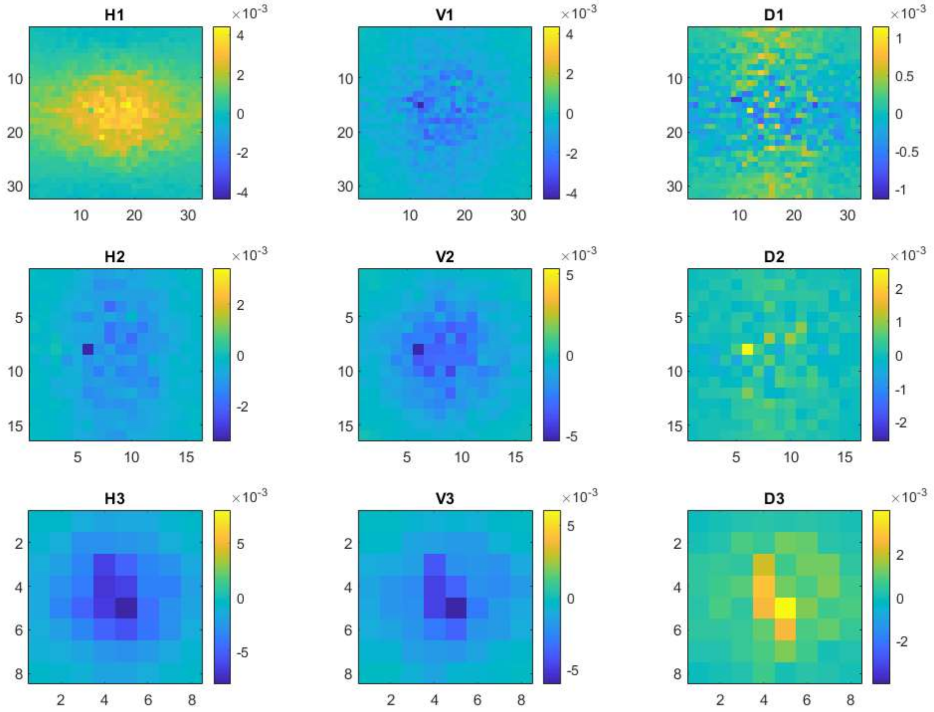

Figure 79: Multiscale Covariance for Plant A, No Wind

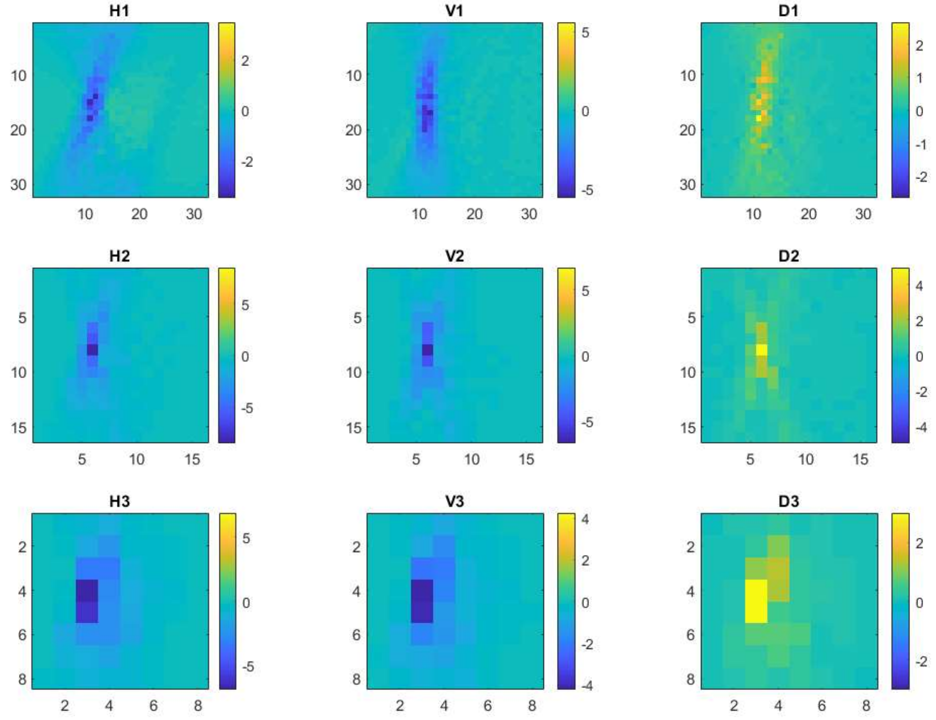

Figure 80: Multiscale Covariance for Plant A, Light Wind

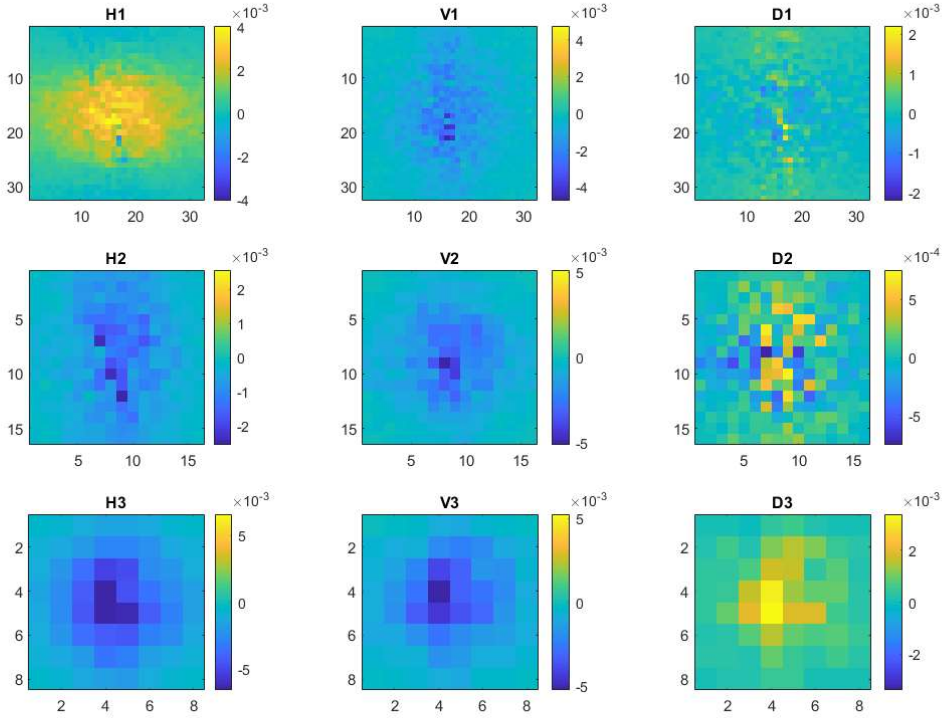

Figure 81: Multiscale Covariance for Plant B, No Wind

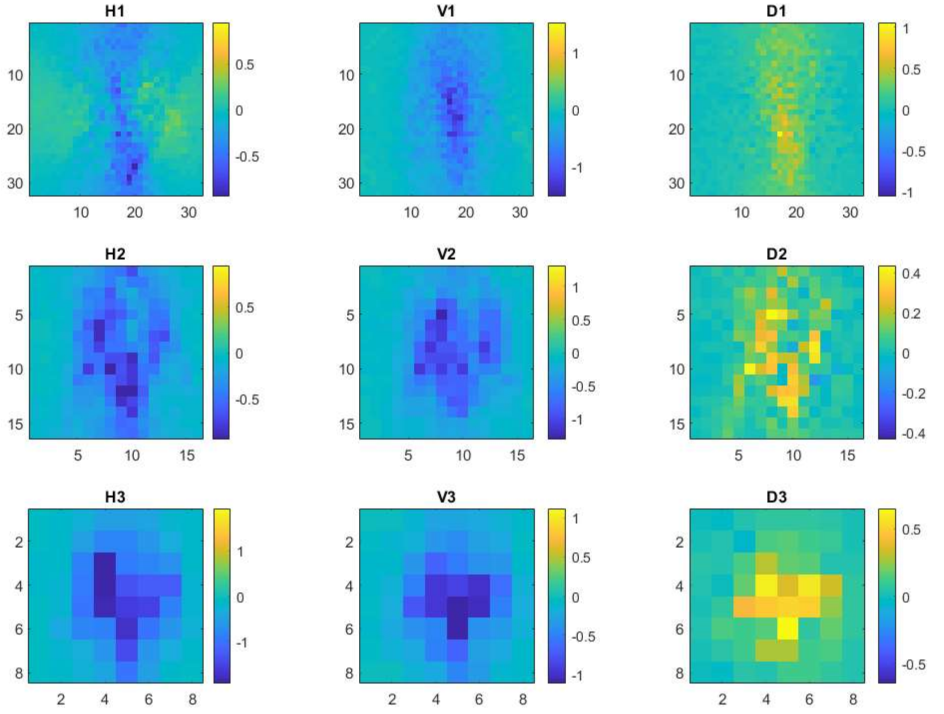

Figure 82: Multiscale Covariance for Plant B, Light Wind

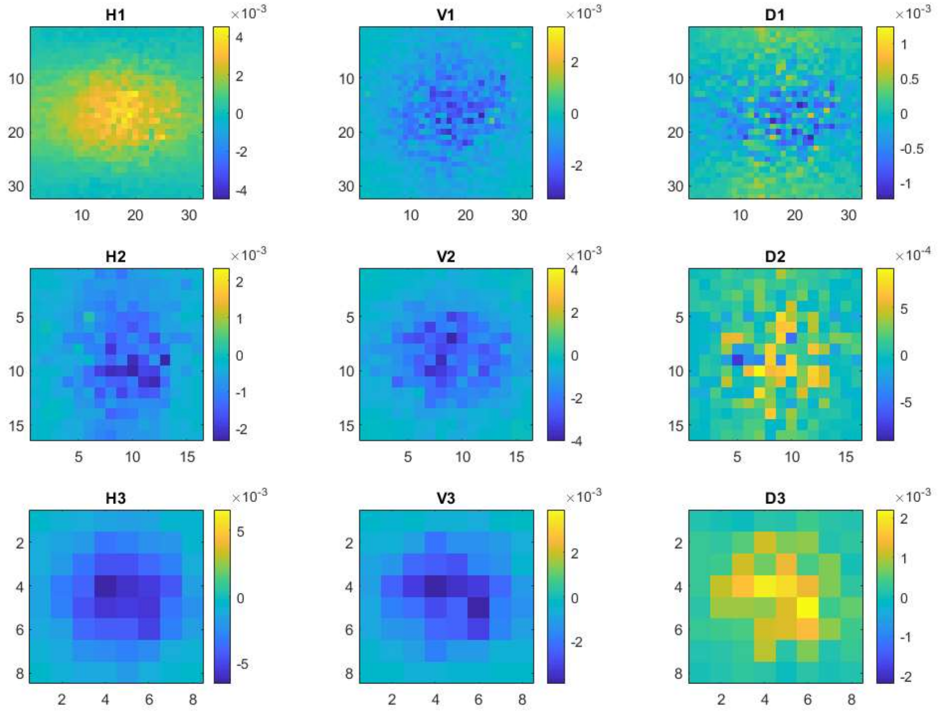

Figure 83: Multiscale Covariance for Plant C, No Wind

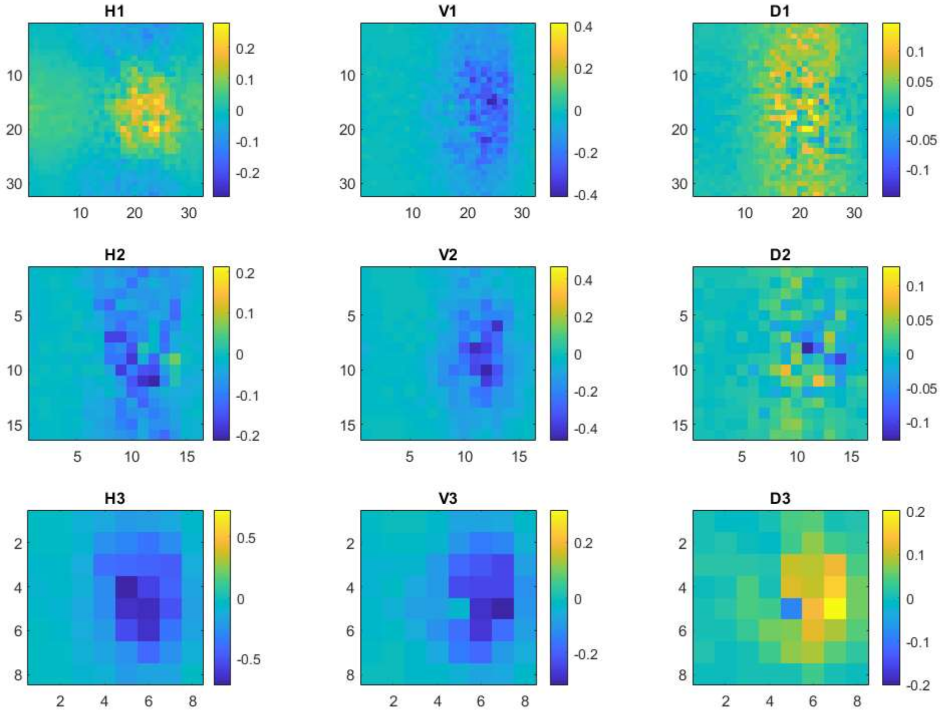

Figure 84: Multiscale Covariance for Plant C, Light Wind

MULTISCALE ANALYSIS BY COMPONENT AND LEVEL WITH HISTOGRAMS

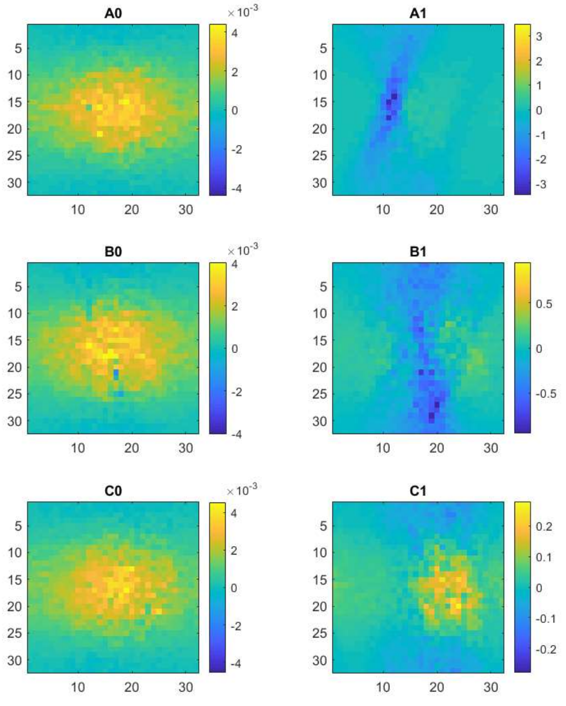

Figure 85: Level 1 Horizontal Component for Six Measurement Scenarios

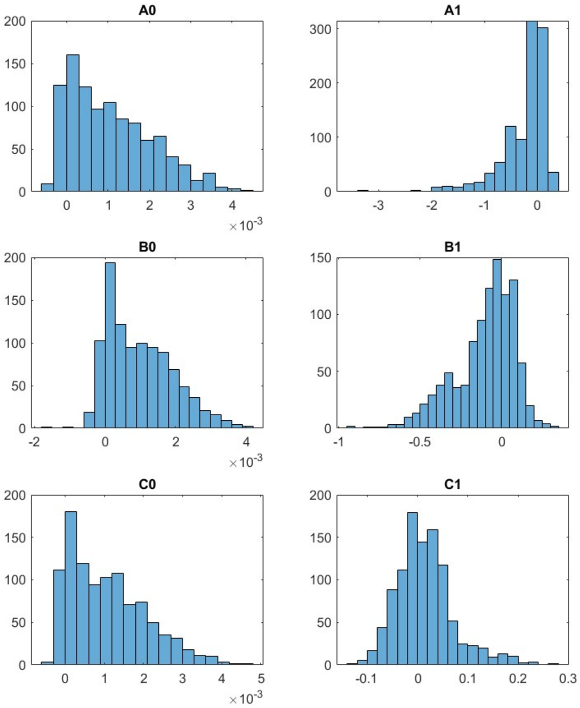

Figure 86: Level 1 Horizontal Component Histograms

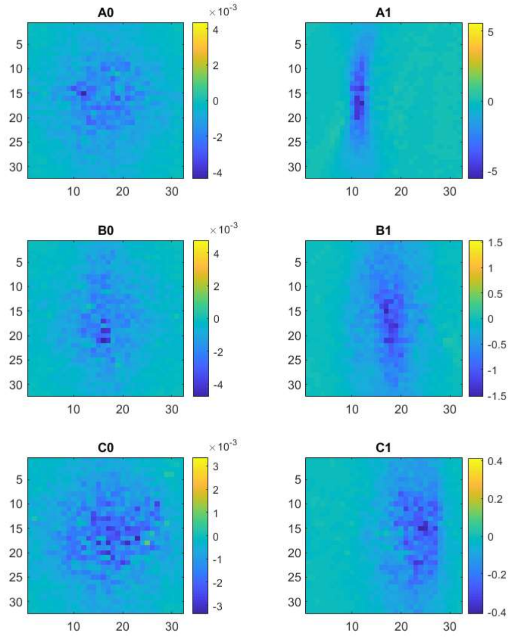

Figure 87: Level 1 Vertical Component for Six Measurement Scenarios

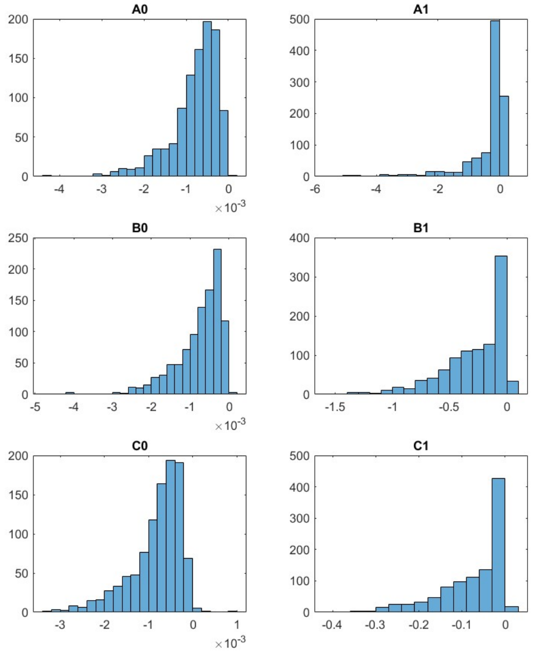

Figure 88: Level 1 Vertical Component Histograms

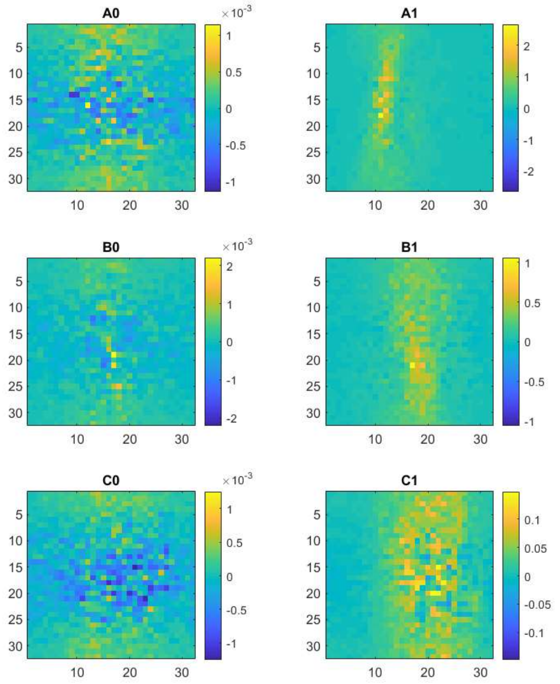

Figure 89: Level 1 Diagonal Component for Six Measurement Scenarios

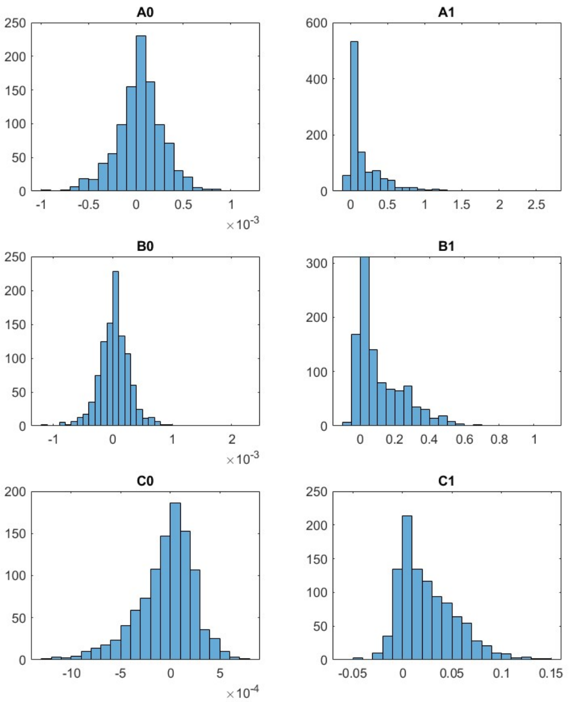

Figure 90 Level 1 Diagonal Component Histograms

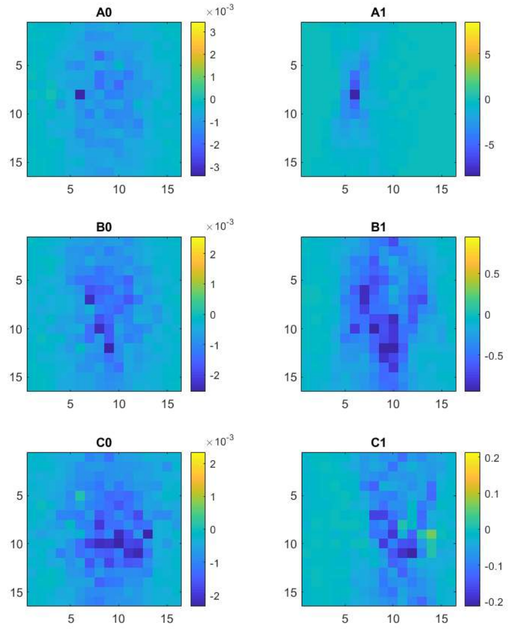

Figure 91: Level 2 Horizontal Component for Six Measurement Scenarios

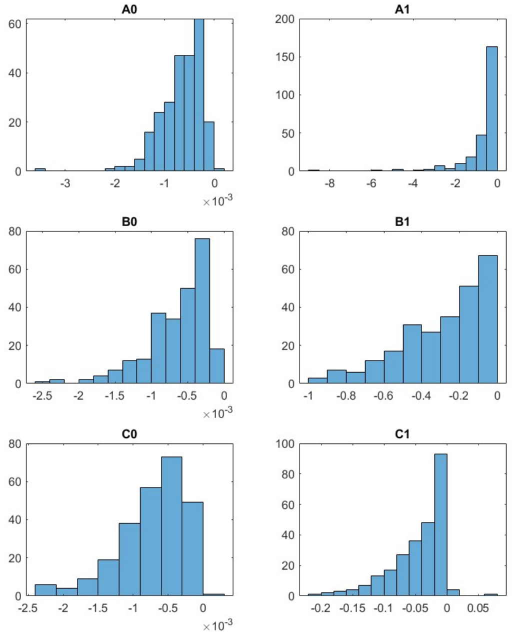

Figure 92: Level 2 Horizontal Component Histograms

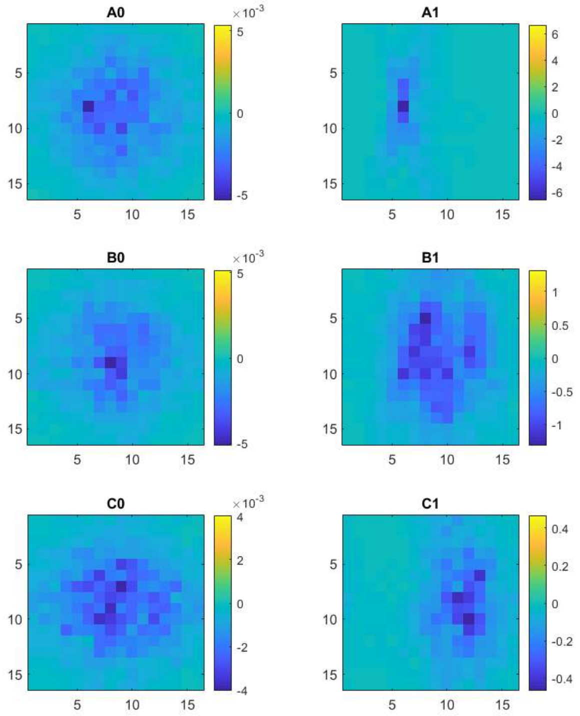

Figure 93: Level 2 Vertical Component for Six Measurement Scenarios

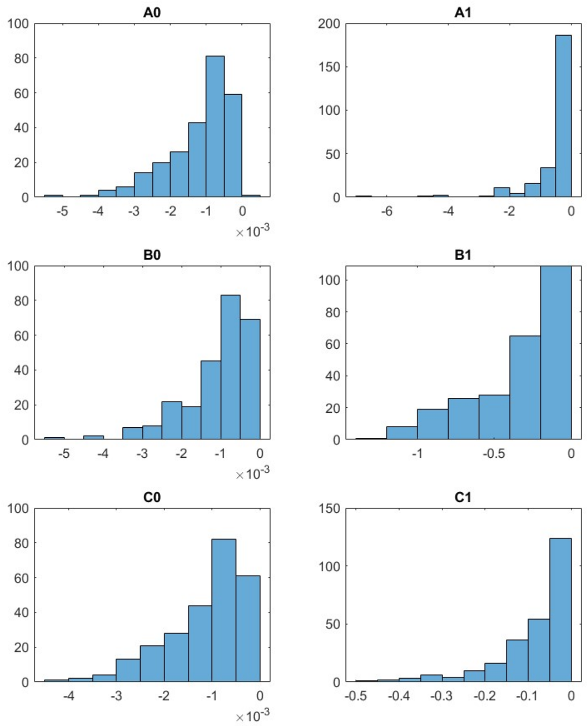

Figure 94: Level 2 Vertical Component Histograms

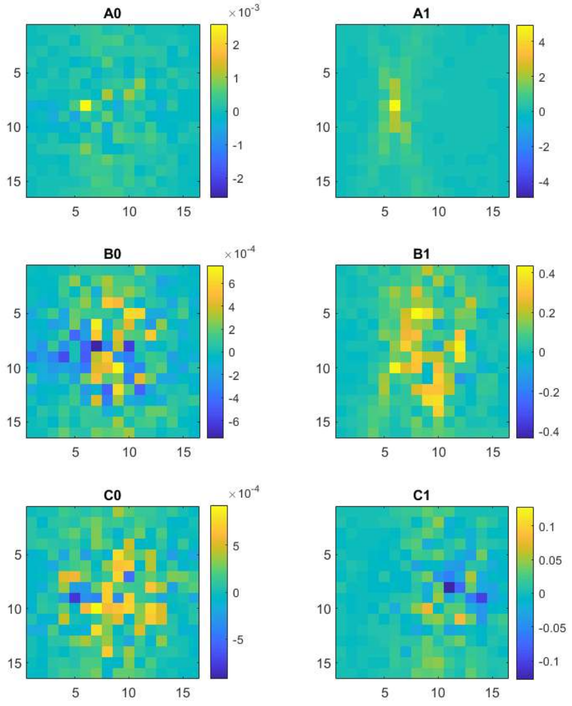

Figure 95: Level 2 Diagonal Component for Six Measurement Scenarios

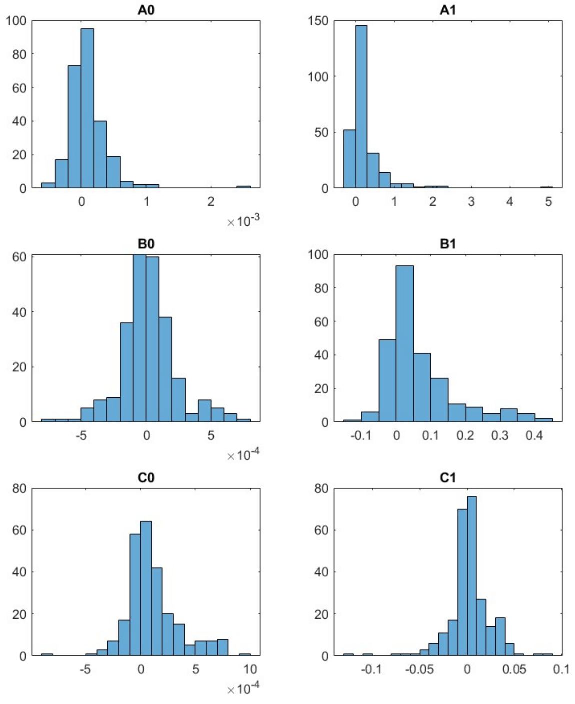

Figure 96: Level 2 Diagonal Component Histograms

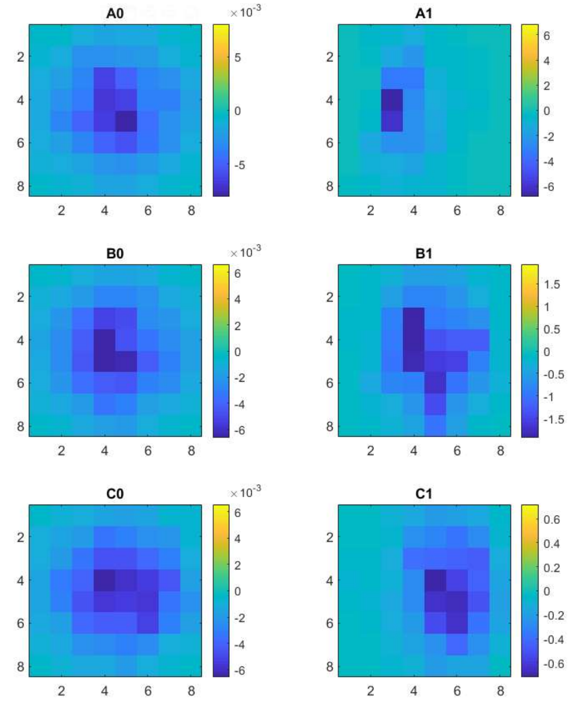

Figure 97: Level 3 Horizontal Component for Six Measurement Scenarios

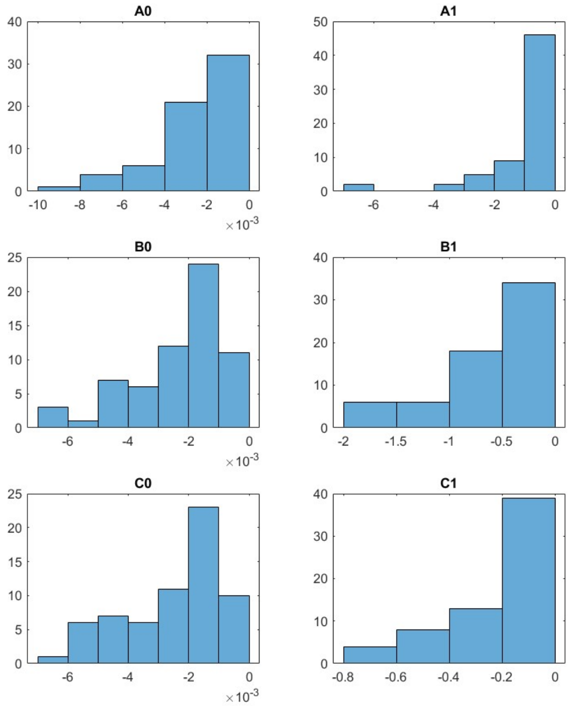

Figure 98: Level 3 Horizontal Component Histograms

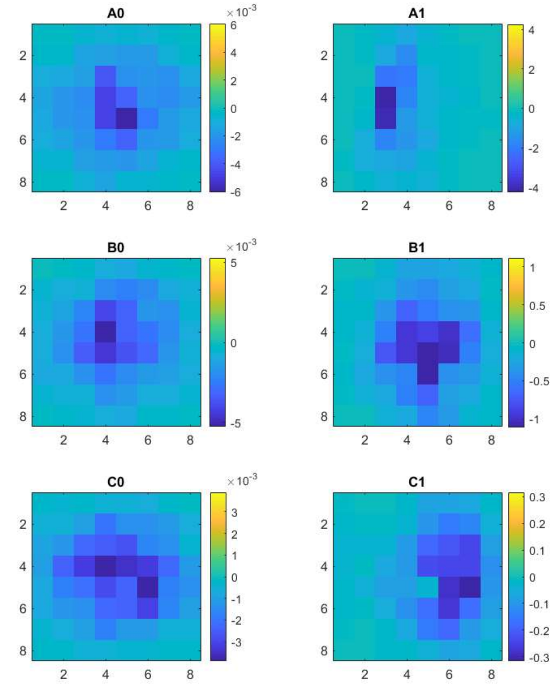

Figure 99: Level 3 Vertical Component for Six Measurement Scenarios

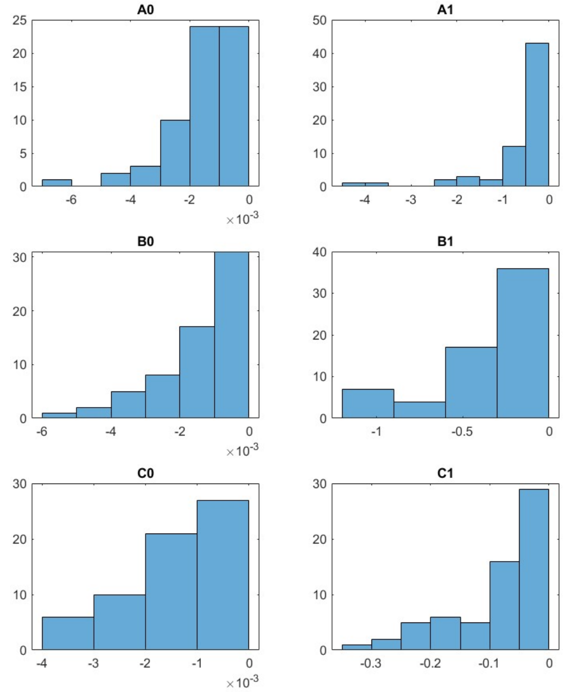

Figure 100: Level 3 Vertical Component Histograms

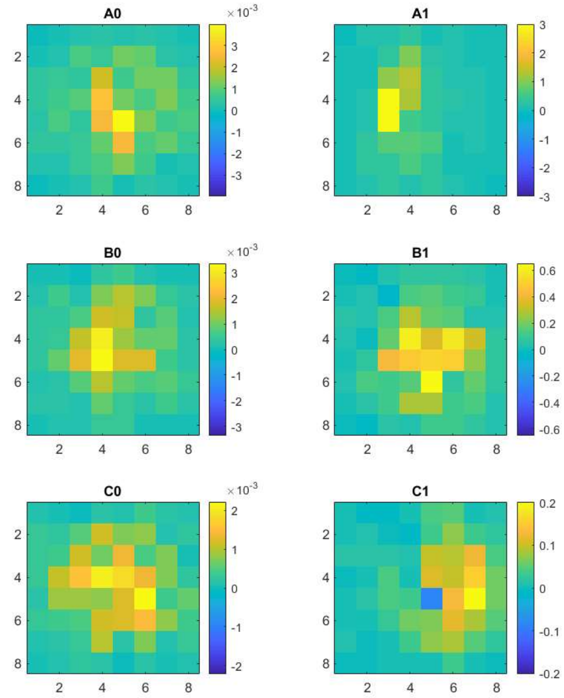

Figure 101: Level 3 Diagonal Component for Six Measurement Scenarios

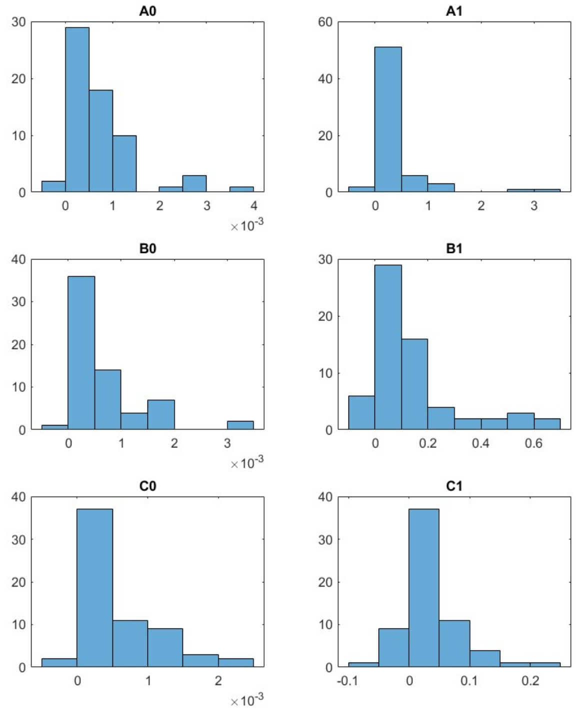

Figure 102: Level 3 Diagonal Component Histograms

APPENDIX B: SIMILARITY PLOTS AND HISTOGRAMS FOR GENERATED SAMPLES OF SIMULATED DATA

SAMPLES OF SIMULATED DATA GENERATED WITH EXPONENTIAL CORRELATING FUNCTION

Estimated Multiscale Directional Correlation Maps

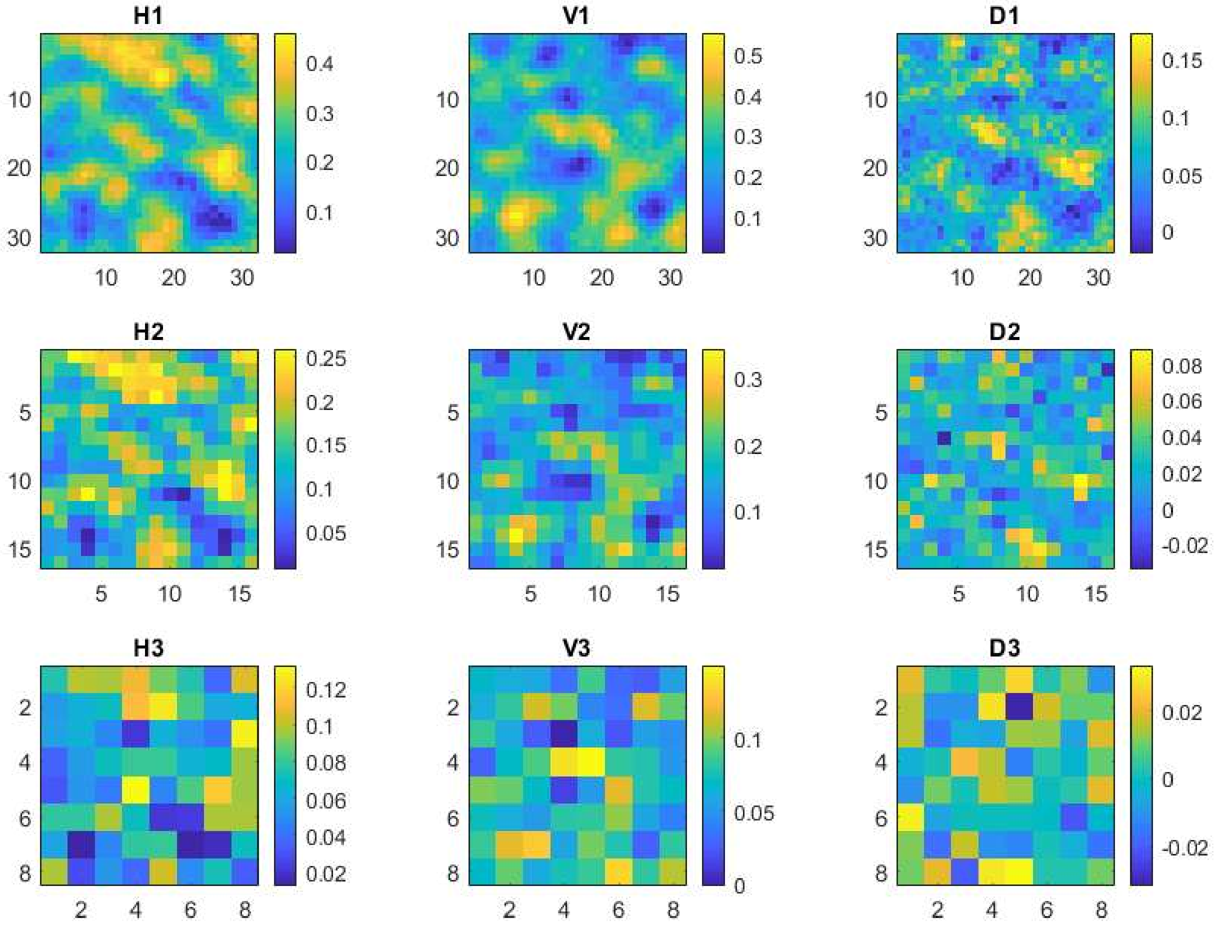

Figure 103: Estimated Multiscale Correlations of Original Data (1000 Samples)

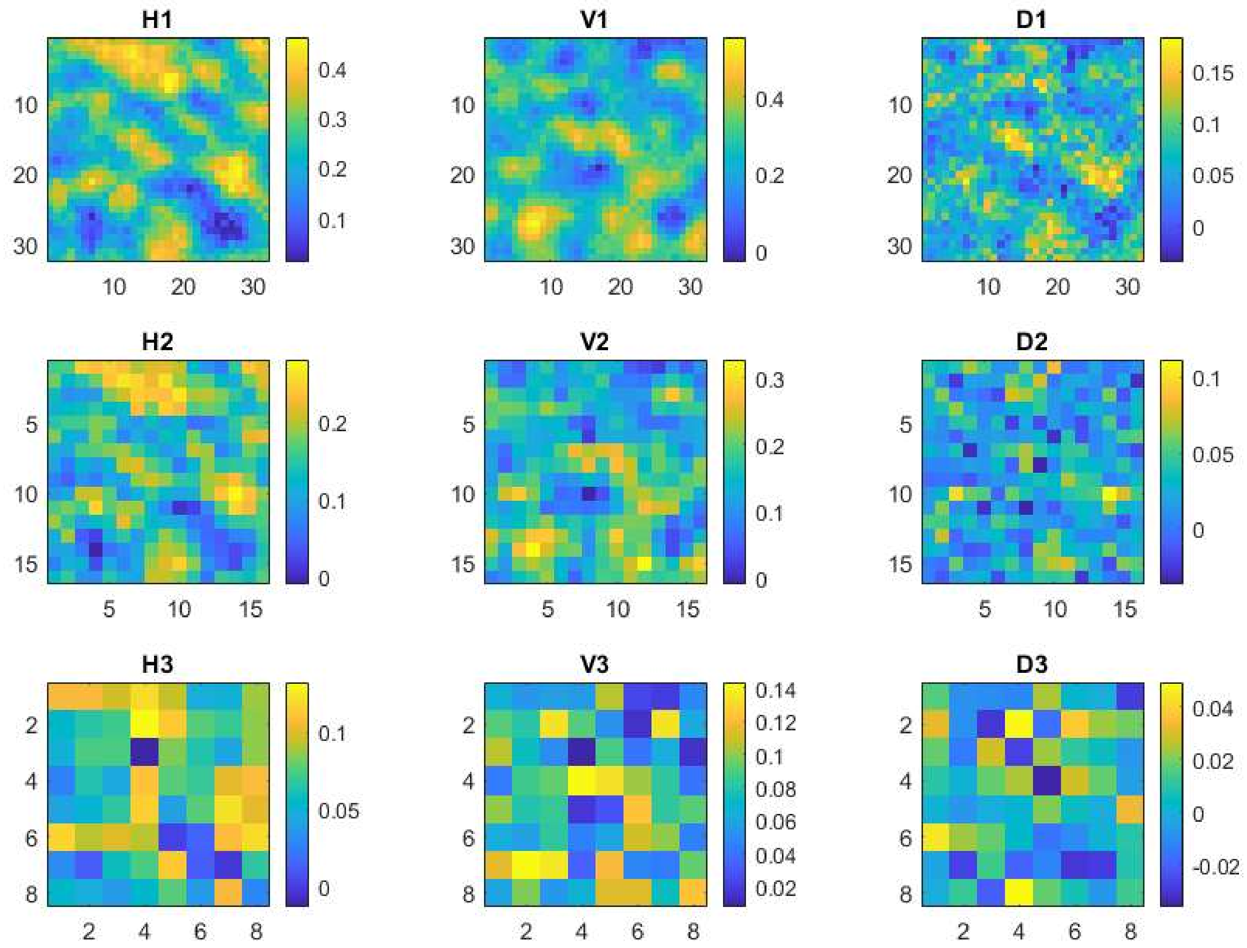

Figure 104: Estimated Multiscale Correlations of Baseline Full Covariance Data (1000 Samples)

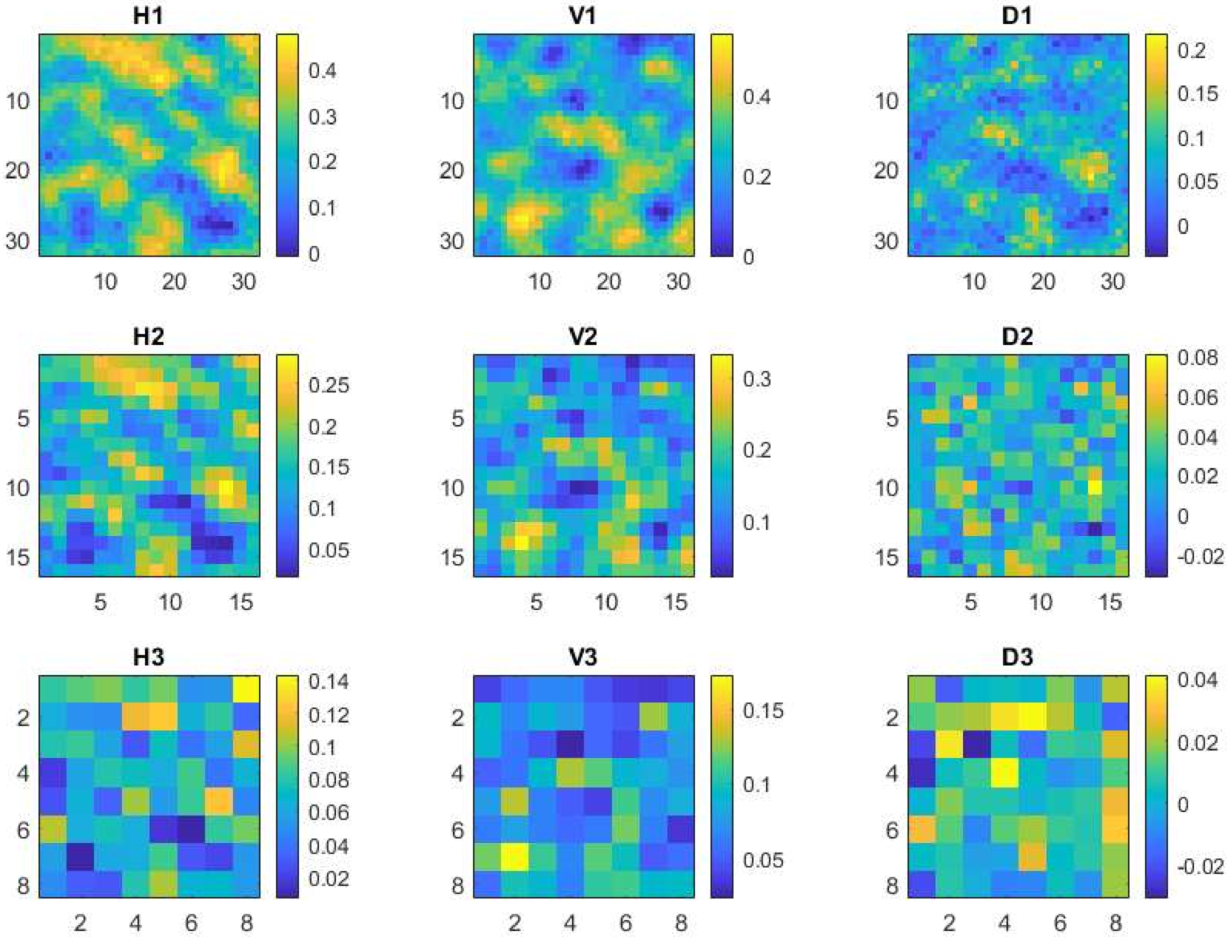

Figure 105: Estimated Multiscale Correlations of Method 1 Data (1000 Samples)

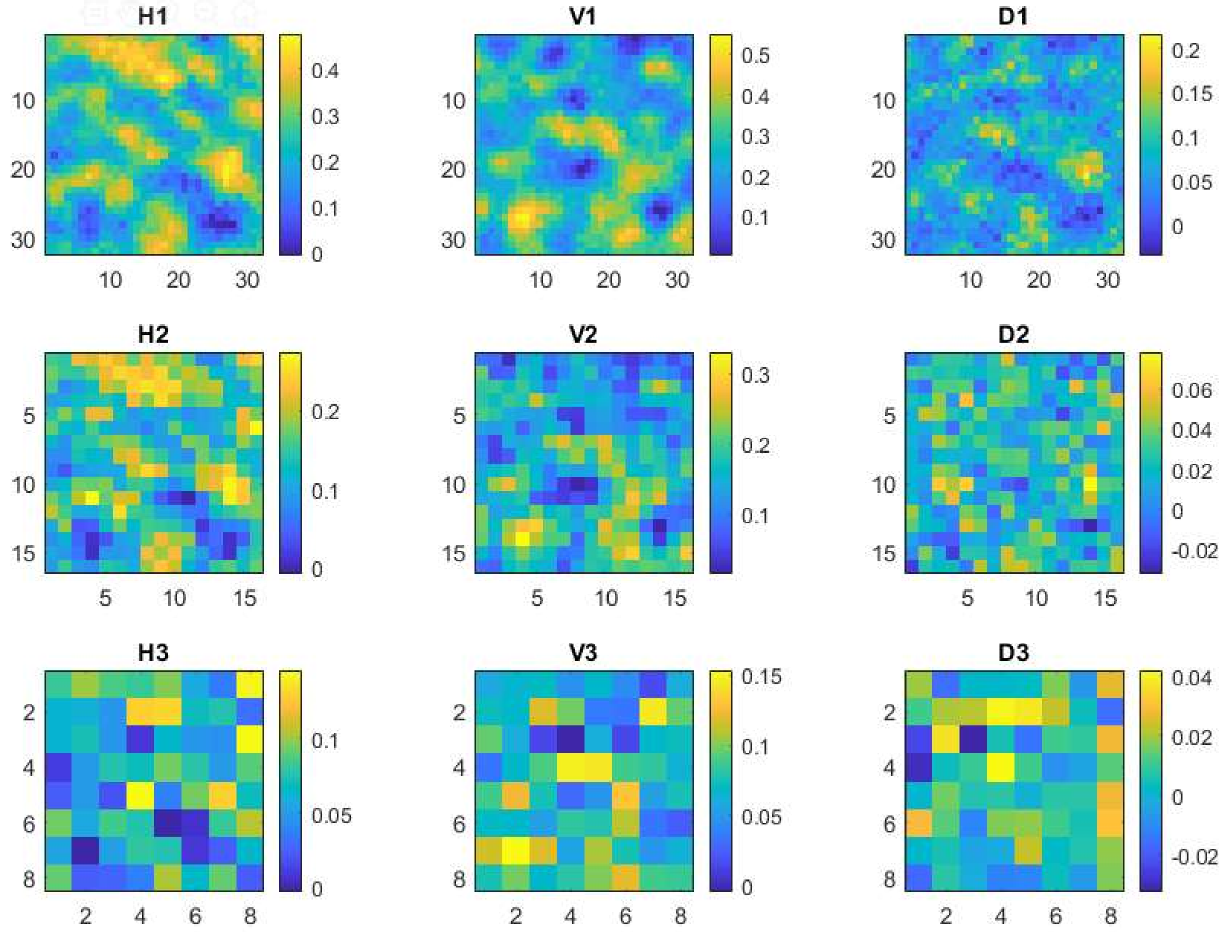

Figure 106: Estimated Multiscale Correlations of Method 2 Data (1000 Samples)

KL Divergence by Pixel and Image Area

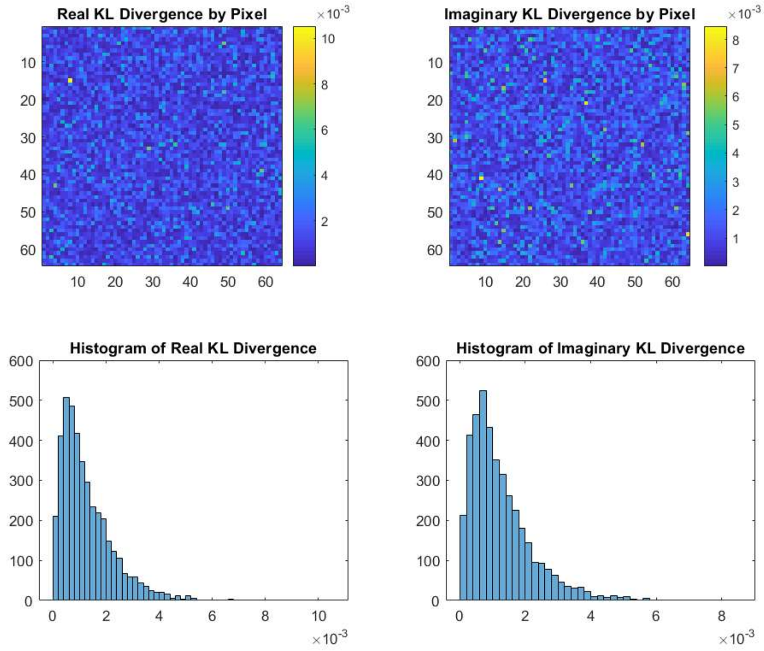

Figure 107: KL Divergence per Pixel for Full Covariance Baseline Data and Simulated Data (1000 Samples)

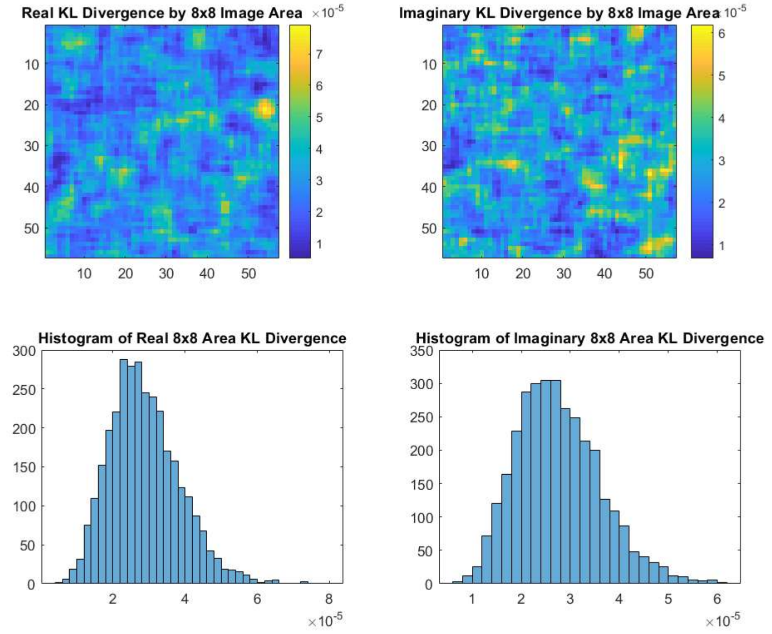

Figure 108: KL Divergence over 8x8 Image Area for Full Covariance Baseline Data and Simulated Data (1000 Samples)

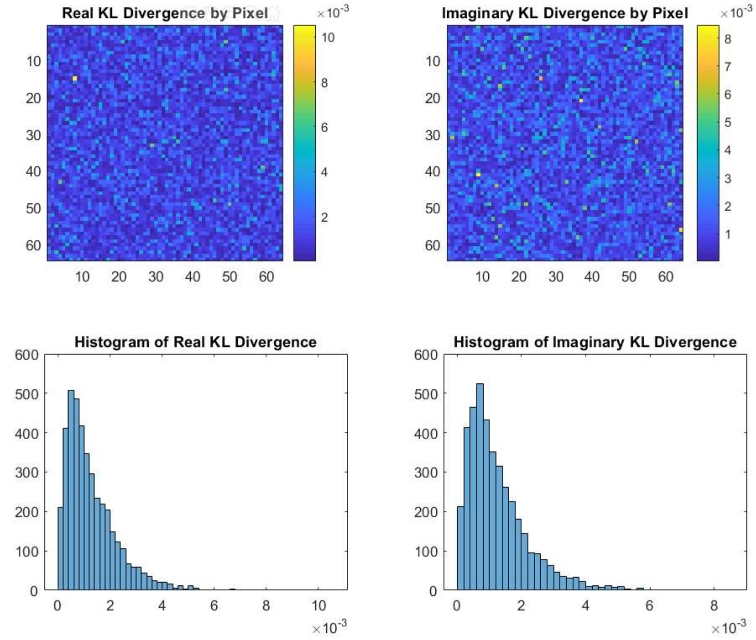

Figure 109: KL Divergence per Pixel for Data Generation Method 1 and Simulated Data (1000 Samples)

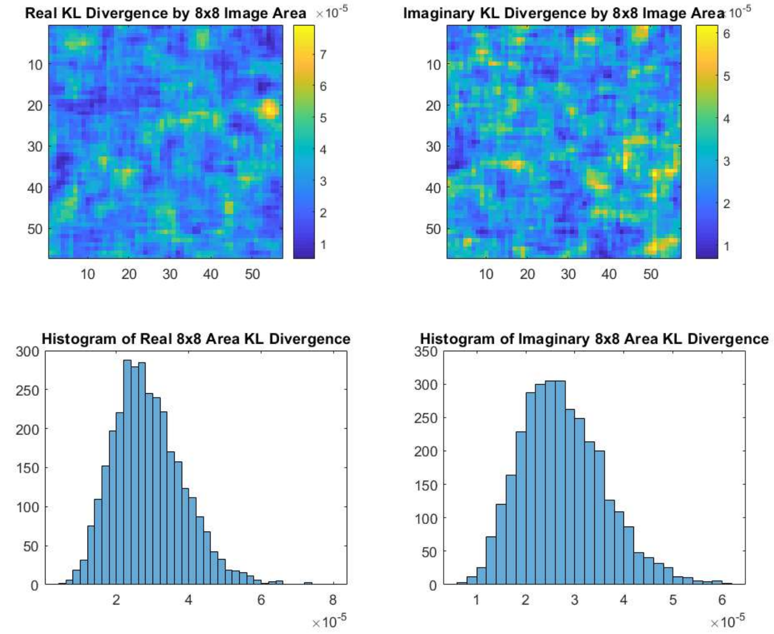

Figure 110: KL Divergence over 8x8 Image Area for Data Generation Method 1 and Simulated Data (1000 Samples)

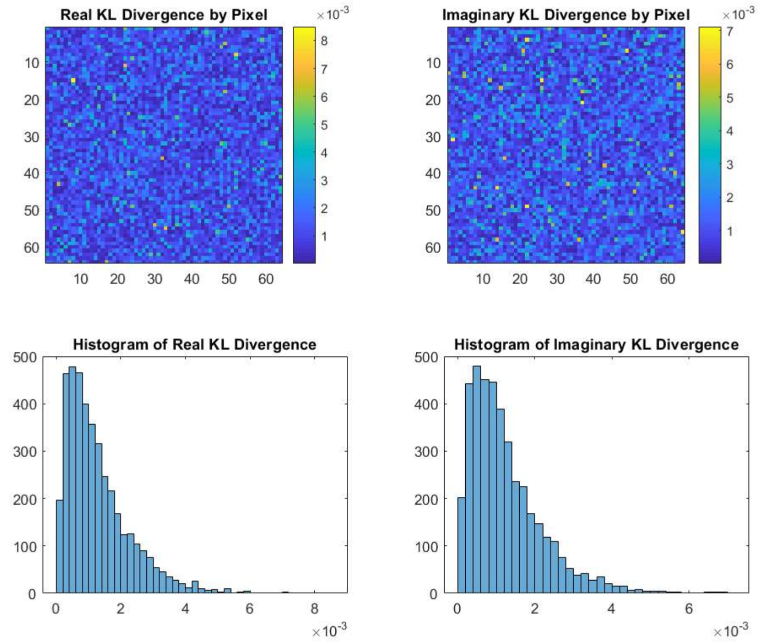

Figure 111: KL Divergence per Pixel for Data Generation Method 2 and Simulated Data (1000 Samples)

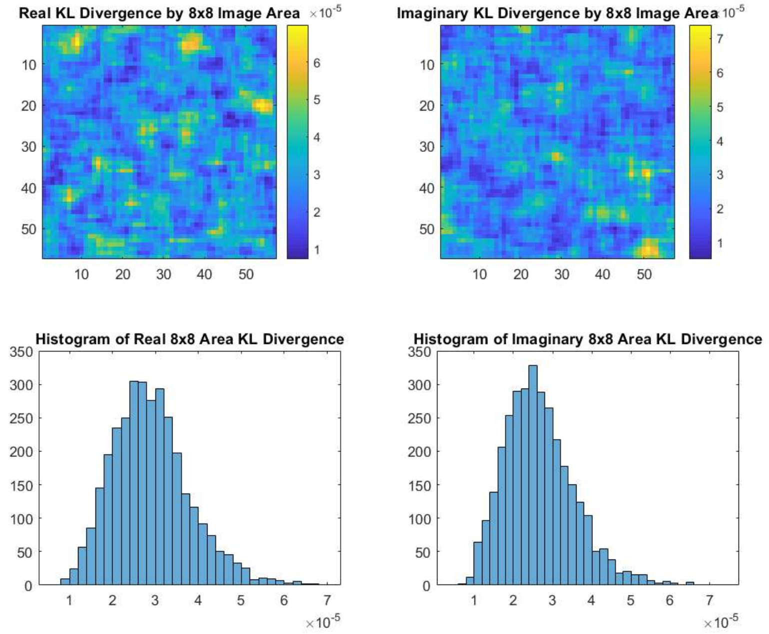

Figure 112: KL Divergence over 8x8 Image Area for Data Generation Method 2 and Simulated Data (1000 Samples)

SIMILARITY METRICS BETWEEN SAMPLES OF SIMULATED DATA WITH EXPONENTIAL CORRELATING FUNCTION AND GENERATED SAMPLES

Correlation Matrix Similarity to Original Data

Table 25: Correlation Matrix Similarity for Baseline Full Covariance Data and Original Data (1000 Samples)

Baseline Full Covariance Data	Method 1 Data	Method 2 Data
0.2437	0.7531	0.7534

Multiscale Directional Correlation Similarity to Original Data

Table 26: MSE of Estimated Multiscale Directional Correlations (1000 Samples from Simulated Data)

MSE between Original Data and Generation Methods	Baseline Full Covariance Data	Method 1 Data	Method 2 Data
RH1	1.49%	1.57%	1.57%
RV1	1.51%	1.48%	1.48%
RD1	1.61%	2.10%	2.10%
RH2	1.38%	2.25%	1.48%
RV2	1.52%	2.13%	1.41%
RD2	1.45%	2.37%	2.27%
RH3	1.85%	1.89%	1.45%
RV3	1.81%	2.05%	1.33%
RD3	1.51%	2.21%	2.22%

SAMPLES OF SIMULATED DATA GENERATED WITH NON-EXPONENTIAL CORRELATING FUNCTION

Estimated Multiscale Directional Correlation Maps

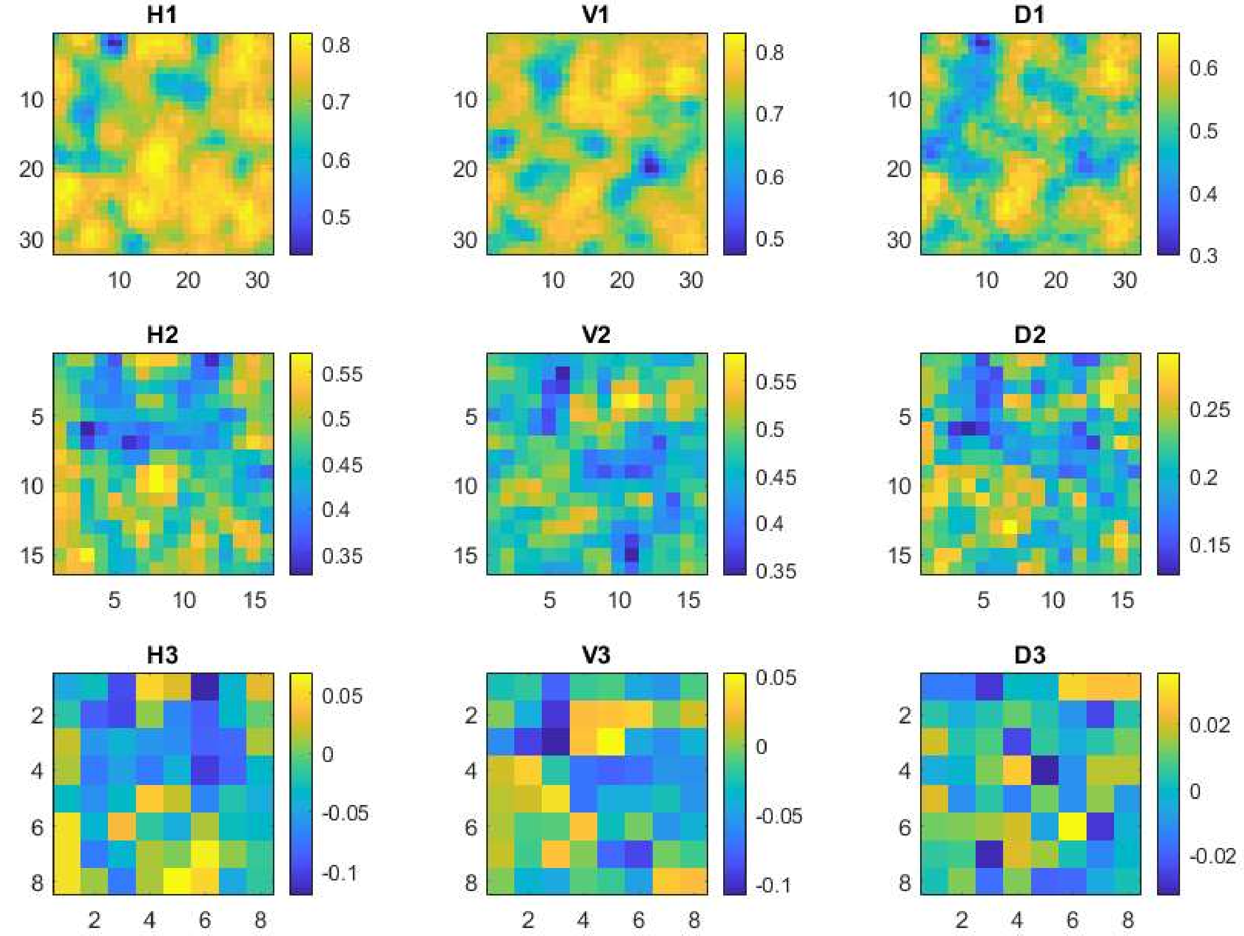

Figure 113: Estimated Multiscale Correlations of Original Data (100 Samples)

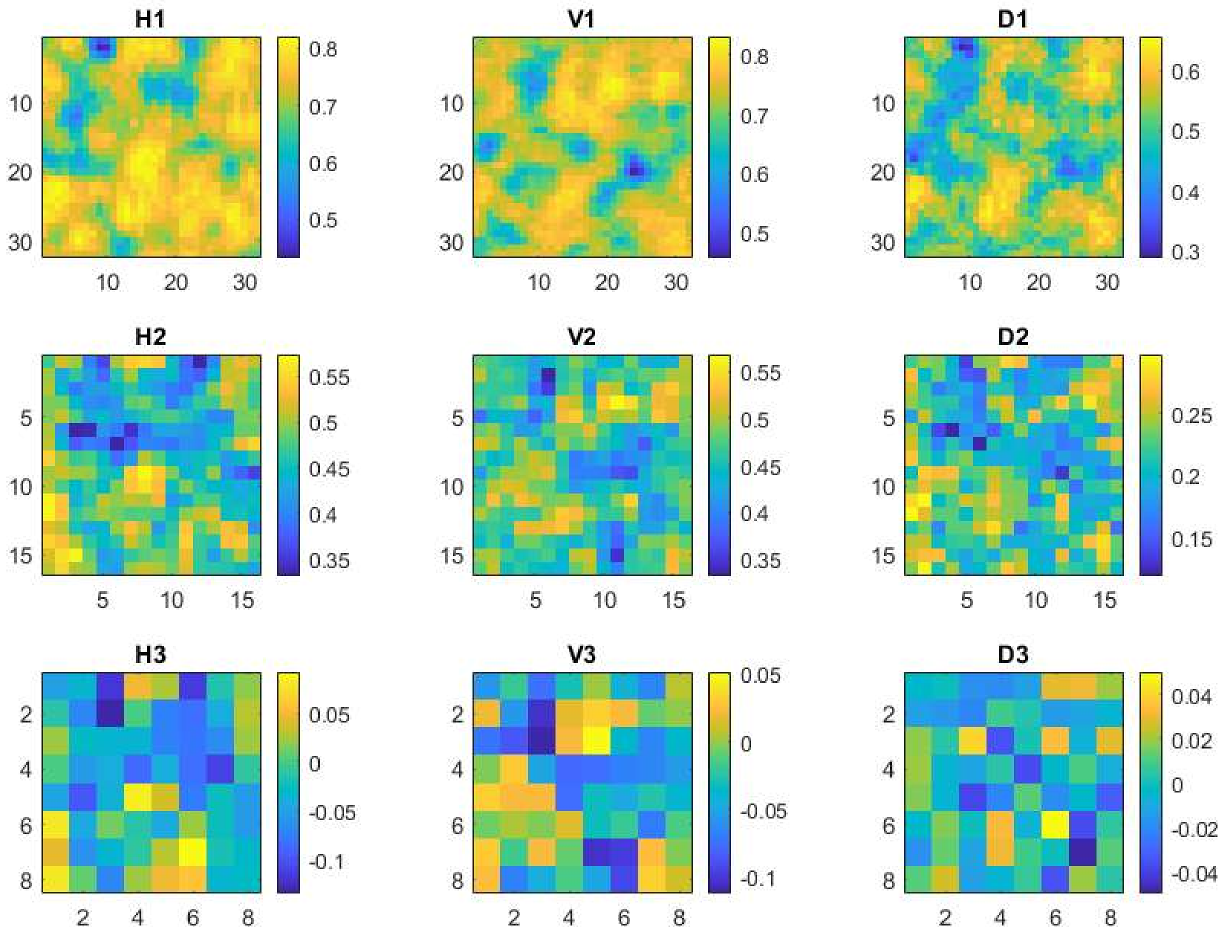

Figure 114: Estimated Multiscale Correlations of Full Covariance Baseline Data (100 Samples)

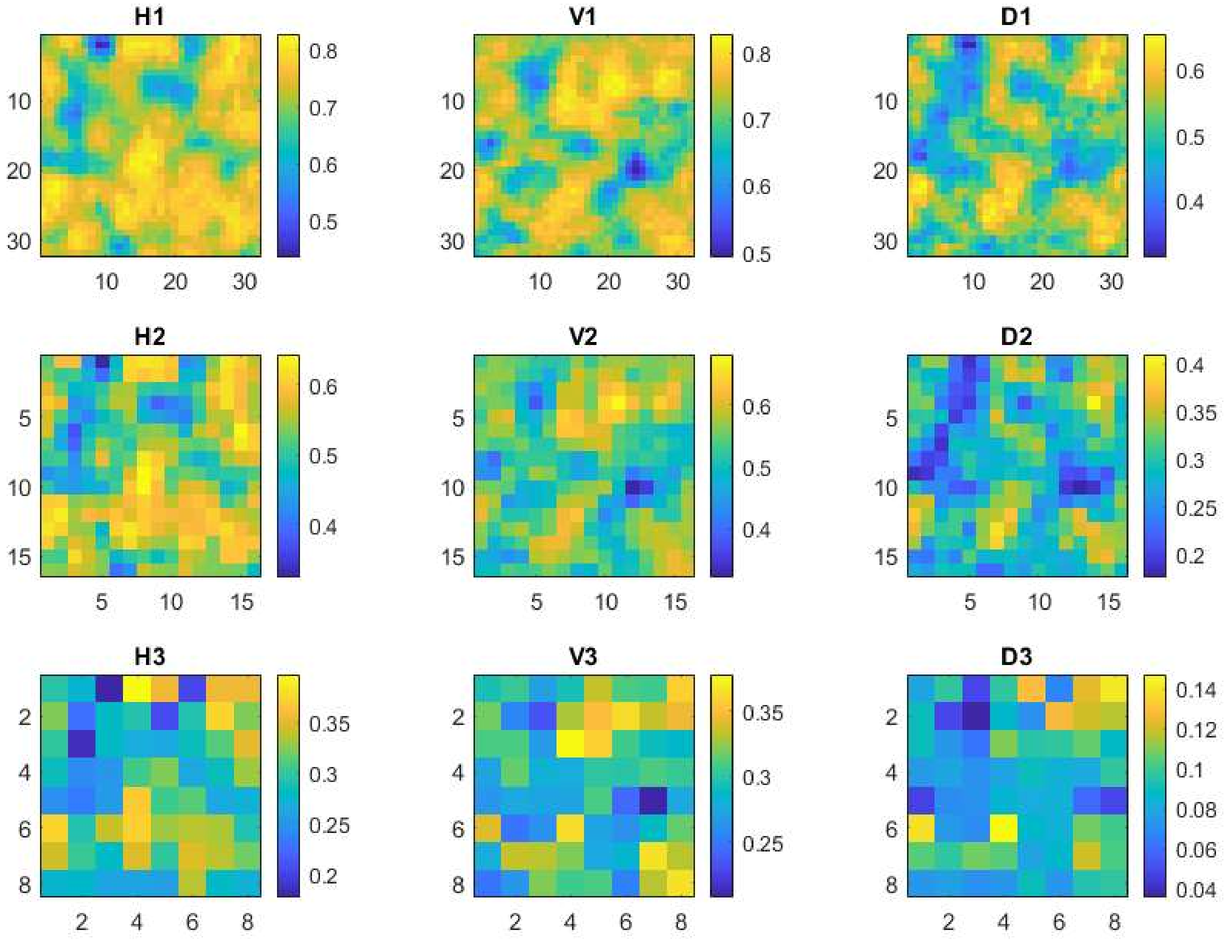

Figure 115: Estimated Multiscale Correlations of Method 1 Data (100 Samples)

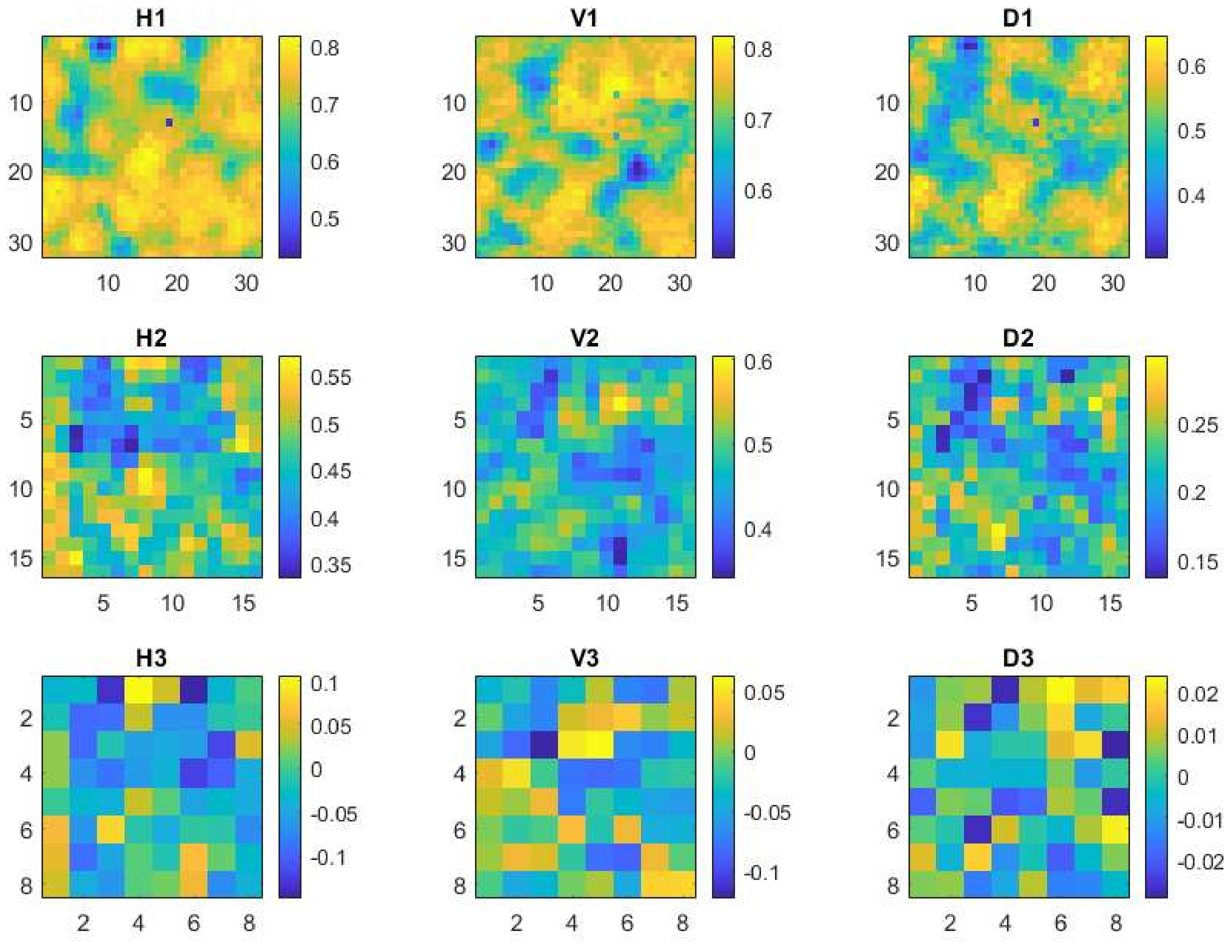

Figure 116: Estimated Multiscale Correlations of Method 2 Data (100 Samples)

KL Divergence by Pixel and Image Area

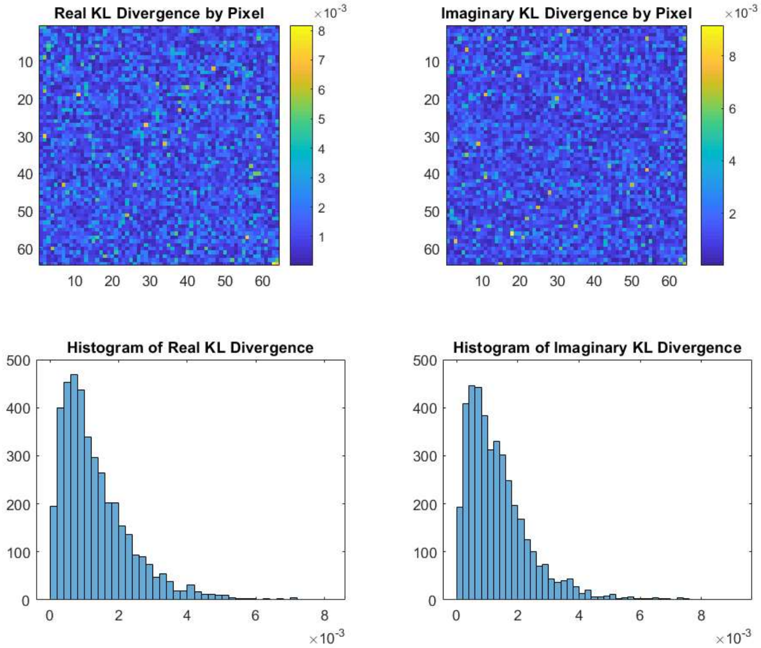

Figure 117: KL Divergence per Pixel between Full Covariance Baseline Data and Original Data

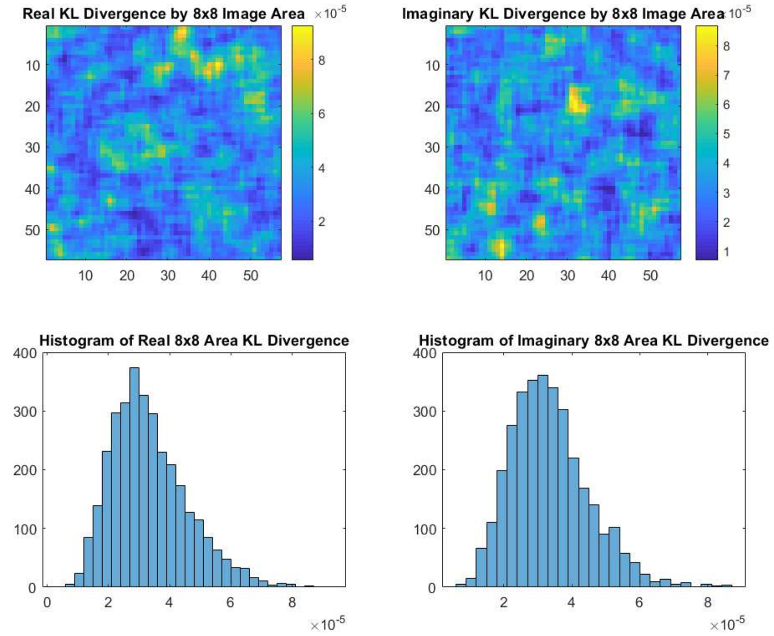

Figure 118: KL Divergence over 8x8 Image Area between Full Covariance Baseline Data and Original Data

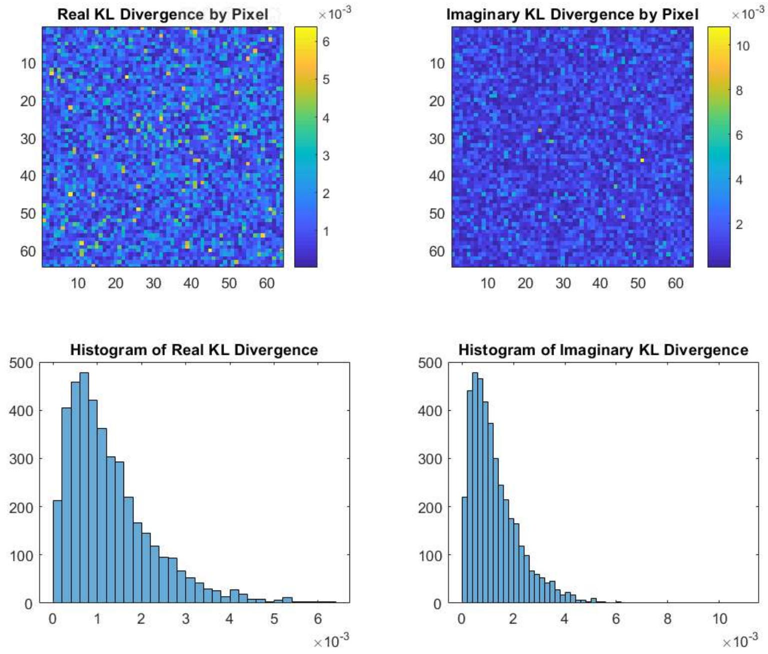

Figure 119: KL Divergence per Pixel between Method 1 Data and Original Data

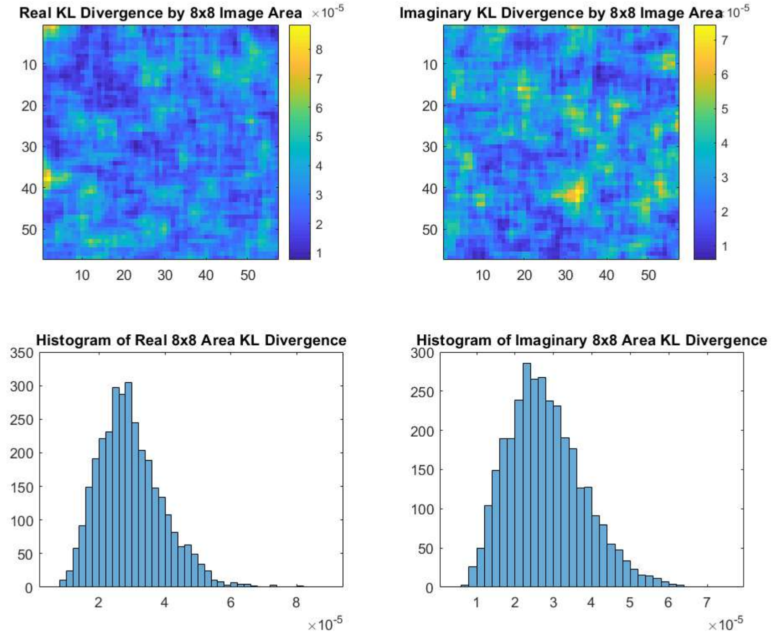

Figure 120: KL Divergence over 8x8 Image Area between Method 1 Data and Original Data

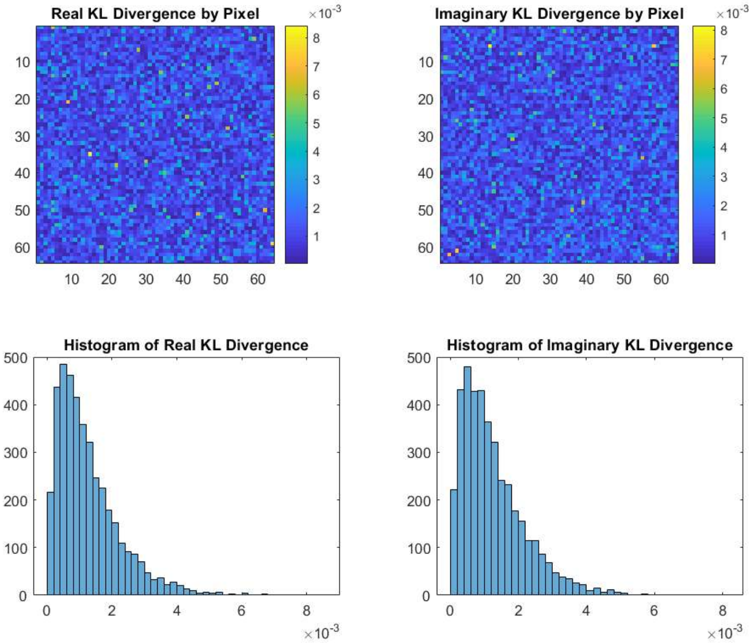

Figure 121: KL Divergence per Pixel between Method 2 Data and Original Data

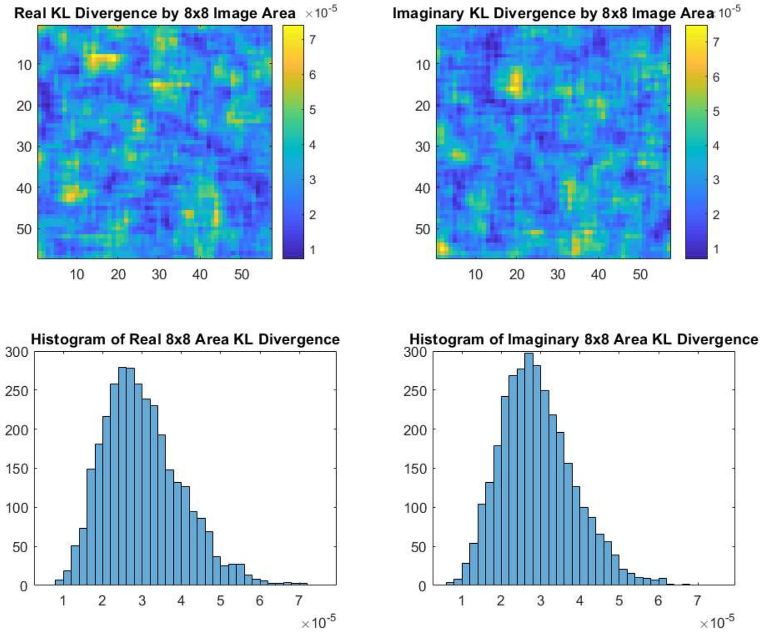

Figure 122: KL Divergence over 8x8 Image Area between Method 2 Data and Original Data

SIMILARITY METRICS BETWEEN SAMPLES OF SIMULATED DATA WITH NON-EXPONENTIAL CORRELATING FUNCTION AND GENERATED SAMPLES

Qualitative metrics from the similarity measures are summarized here to compare the proposed methods to the ideal baseline method that uses the full covariance matrix.

Correlation Matrix Similarity to Original Data

Table 27: Correlation Matrix Similarity for Baseline Full Covariance Data and Original Data (100 Samples)

Baseline Full Covariance Data	Method 1 Data	Method 2 Data
0.1457	0.5058	0.3747

Multiscale Directional Correlation Similarity to Original Data

Table 28: MSE of Estimated Multiscale Directional Correlations (100 Samples from Simulated Data)

MSE between Original Data and Generation Methods	Baseline Full Covariance Data	Method 1 Data	Method 2 Data
RH1	0.91%	0.92%	1.43%
RV1	0.94%	0.95%	1.26%
RD1	1.34%	1.45%	1.88%
RH2	1.41%	8.69%	1.37%
RV2	1.29%	8.79%	1.28%
RD2	1.65%	8.43%	1.92%
RH3	1.69%	32.51%	2.21%
RV3	1.51%	32.67%	1.57%
RD3	1.59%	9.15%	2.12%

APPENDIX C: SIMILARITY PLOTS FOR GENERATED SAMPLES OF MEASURED DATA

SIMULATION OF MEASURED DATA – PLANT D, LIGHT WIND

Estimated Multiscale Directional Correlation Maps

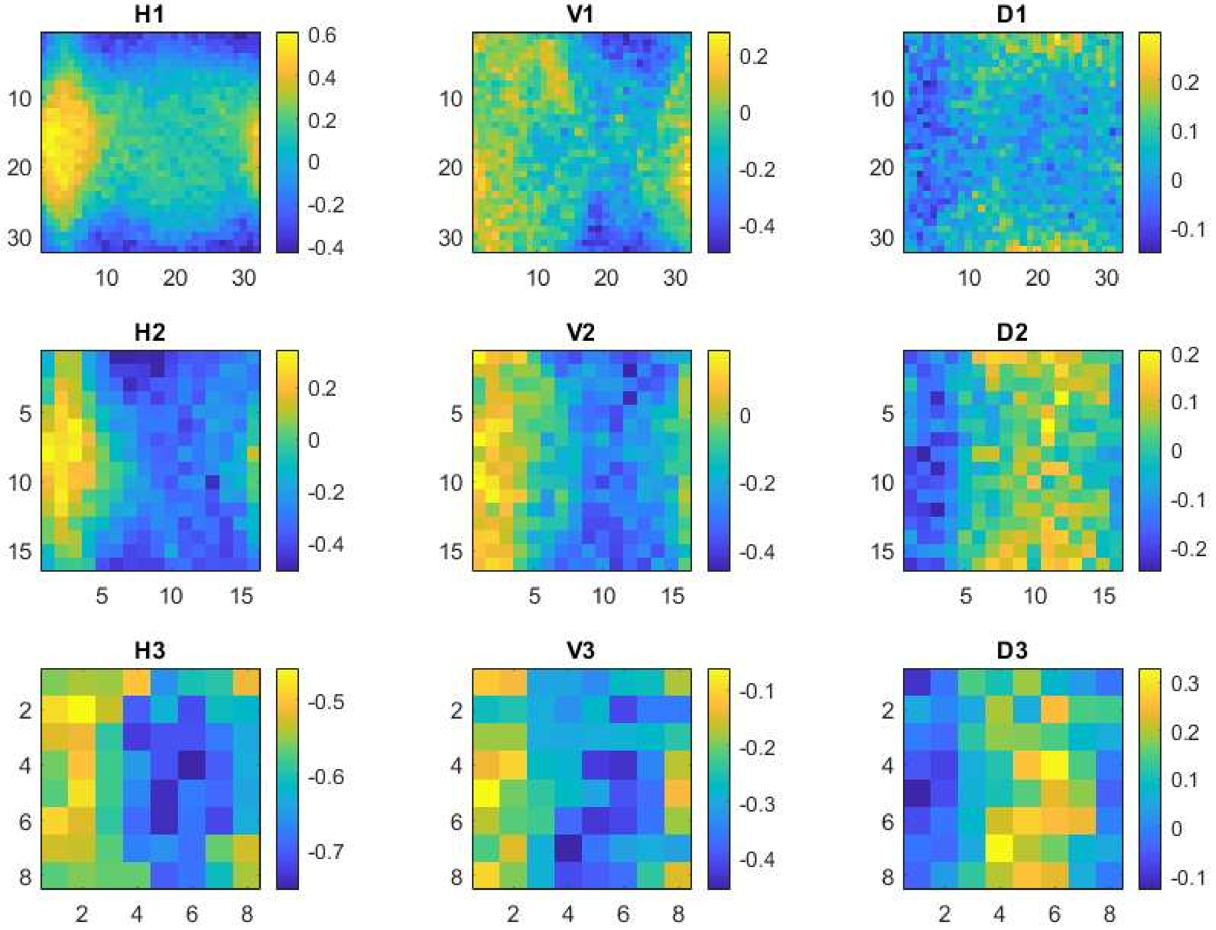

Figure 123: Estimated Multiscale Correlations of Measured Data - Plant D, Light Wind

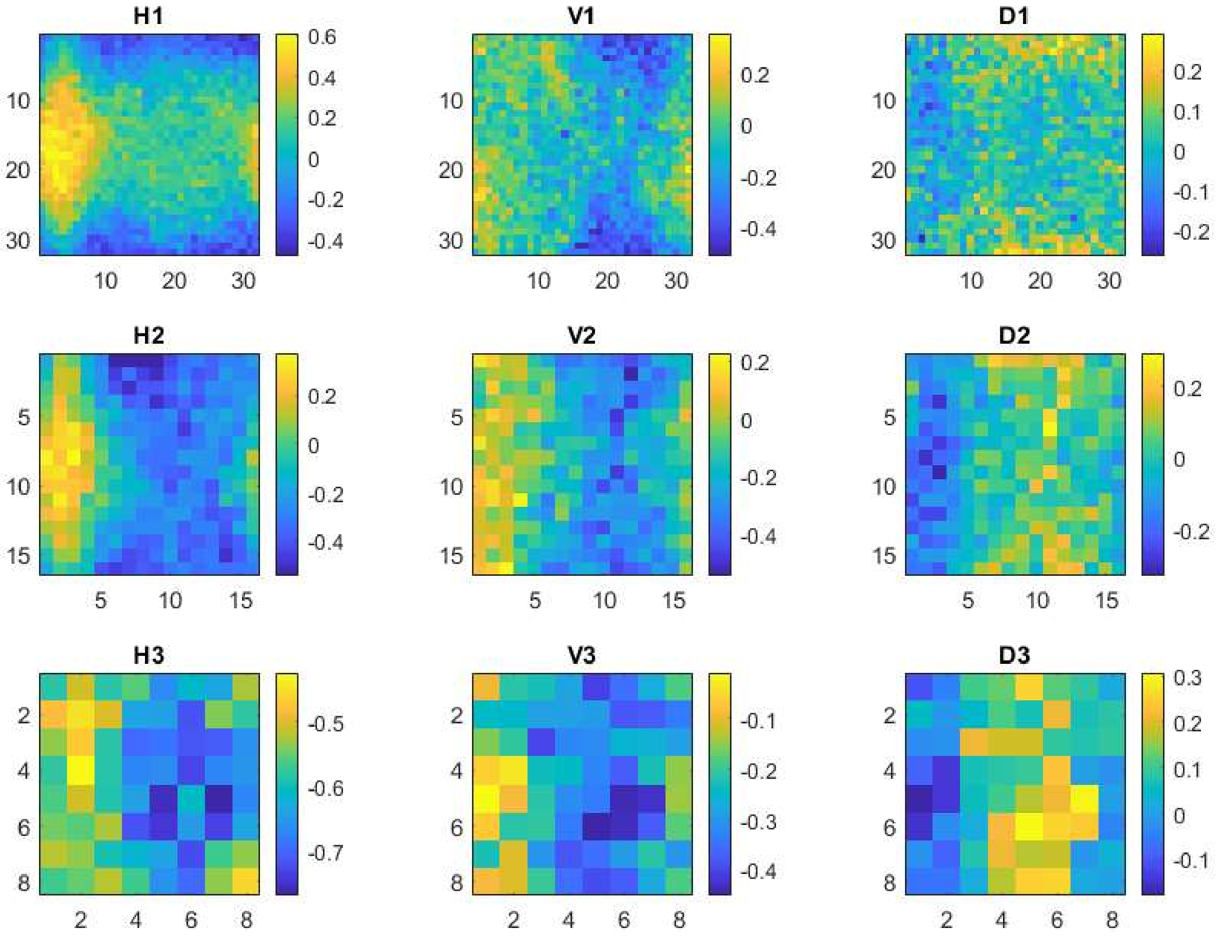

Figure 124: Estimated Multiscale Correlations of Baseline Full Covariance Data - Plant D, Light Wind

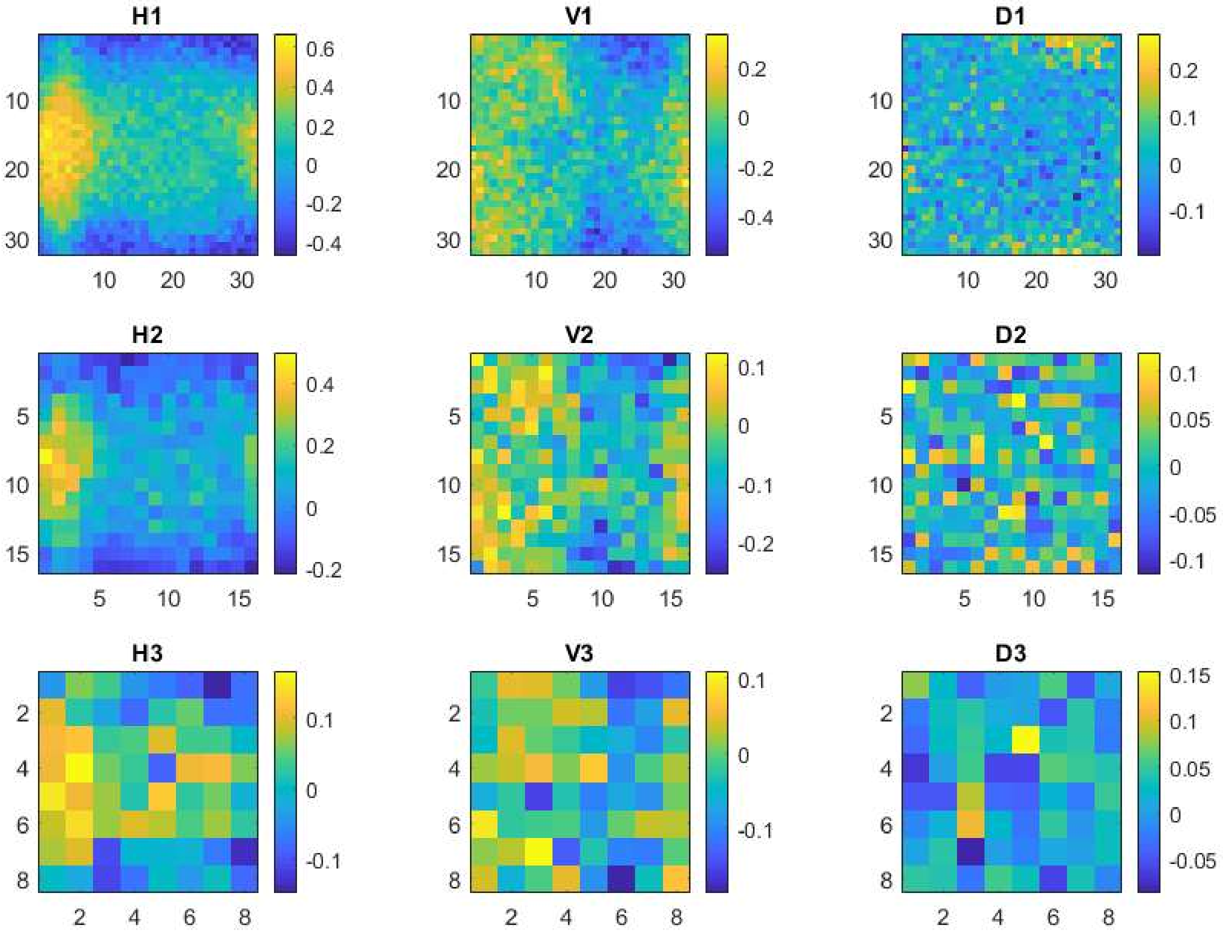

Figure 125: Estimated Multiscale Correlations of Method 1 Data - Plant D, Light Wind

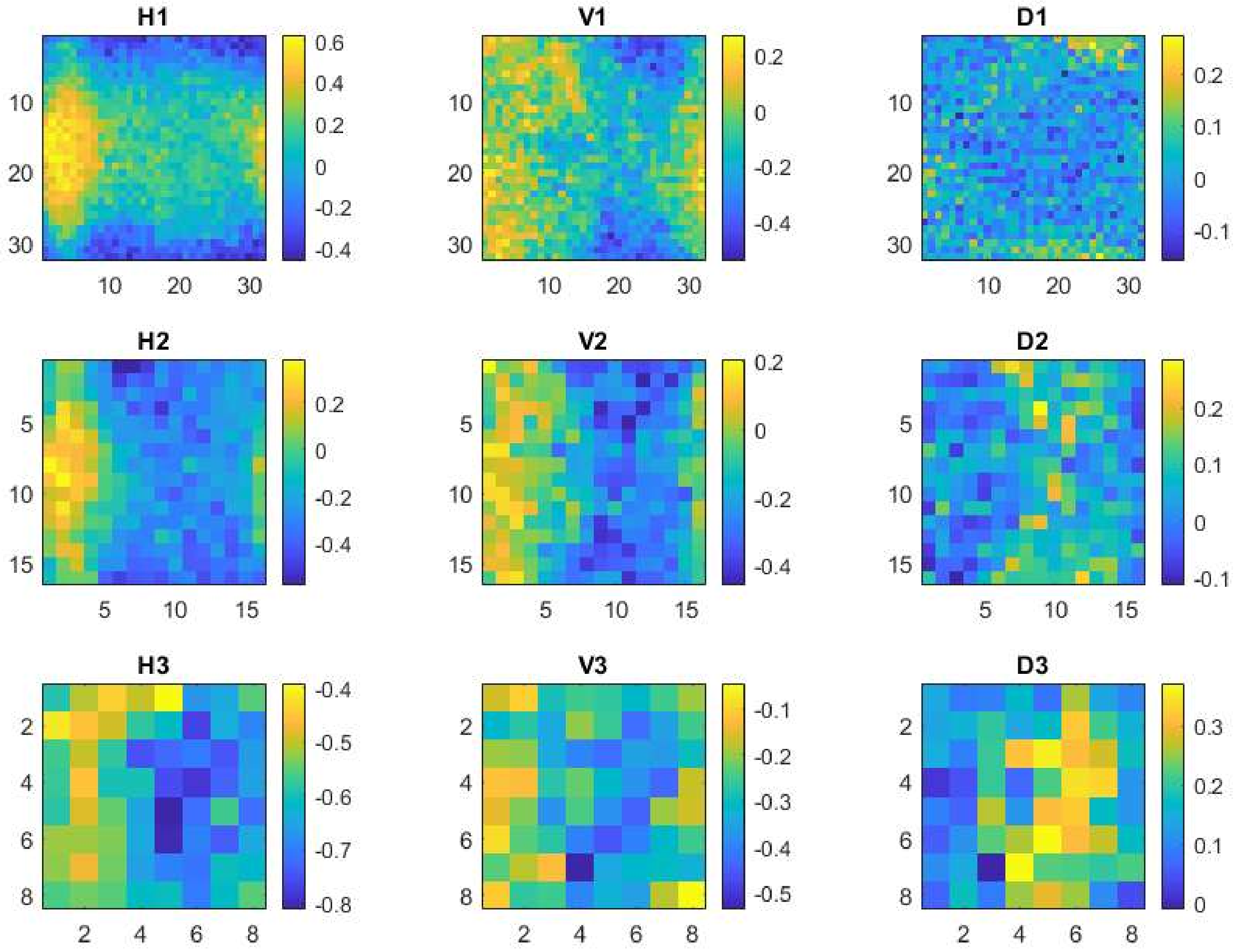

Figure 126: Estimated Multiscale Correlations of Method 2 Data - Plant D, Light Wind

KL Divergence by Pixel and Image Area

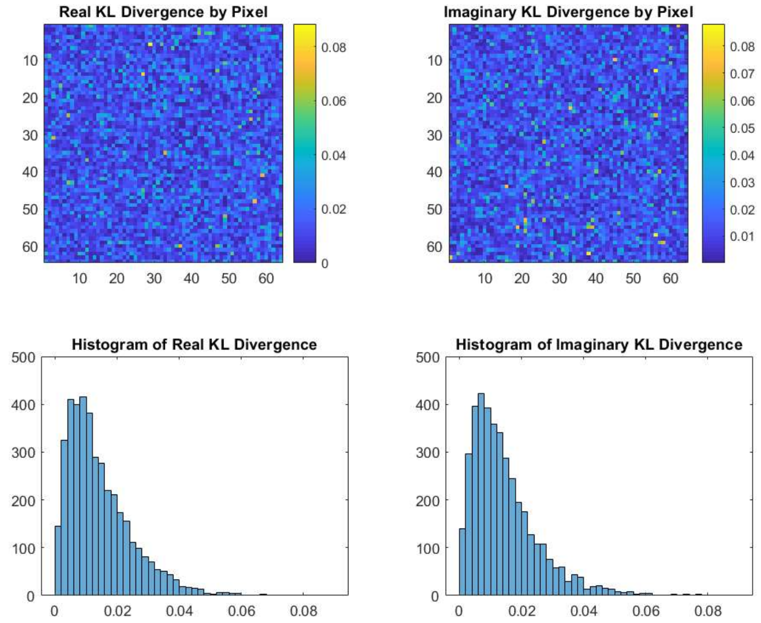

Figure 127: KL Divergence per Pixel for Data Baseline Full Covariance Data - Plant D, Light Wind

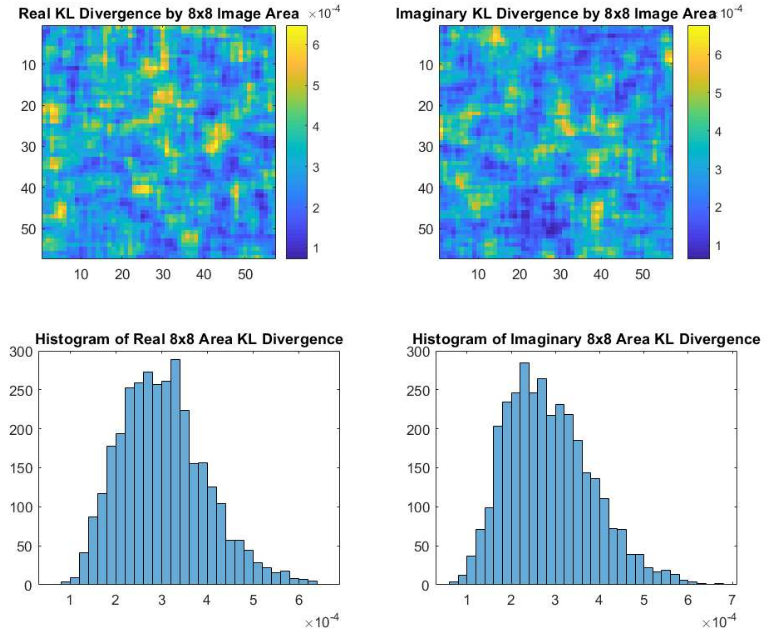

Figure 128: KL Divergence over 8x8 Image Area for Baseline Full Covariance Data - Plant D, Light Wind

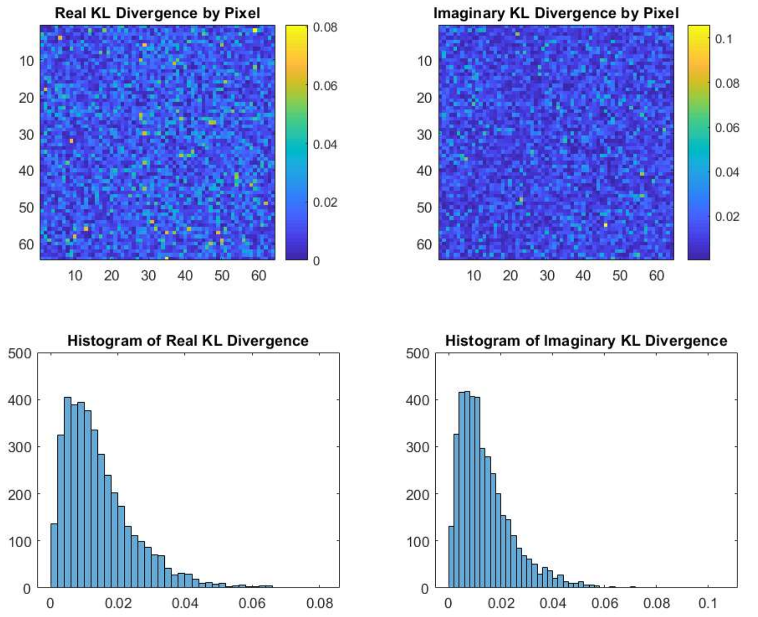

Figure 129: KL Divergence per Pixel for Method 1 Data - Plant D, Light Wind

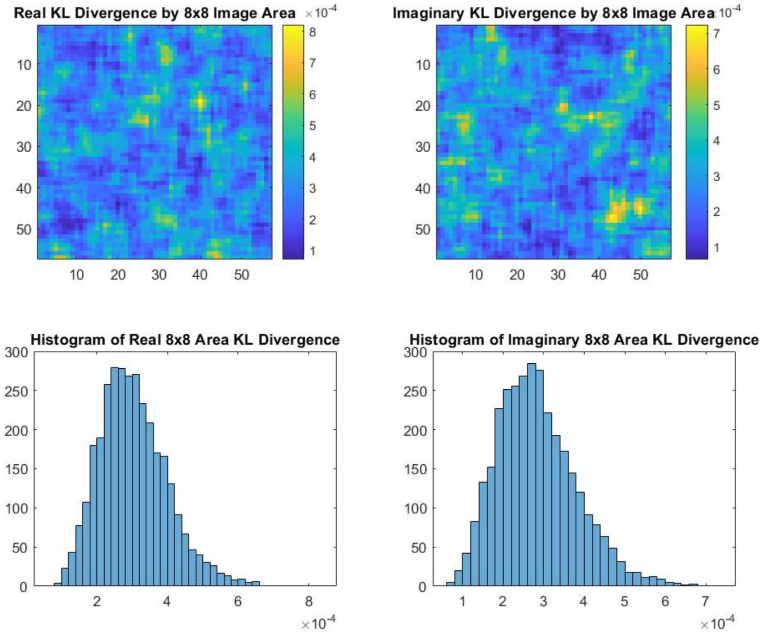

Figure 130: KL Divergence over 8x8 Image Area for Method 1 Data - Plant D, Light Wind

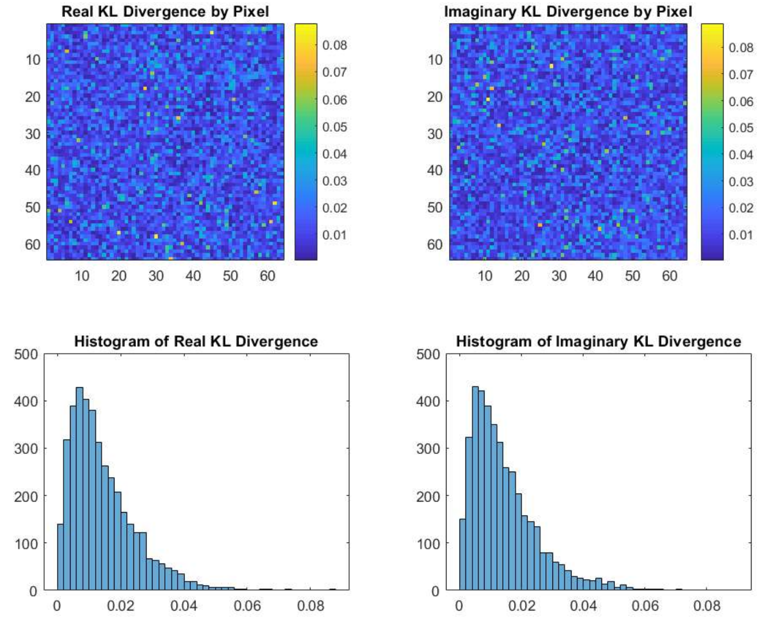

Figure 131: KL Divergence per Pixel for Method 2 Data - Plant D, Light Wind

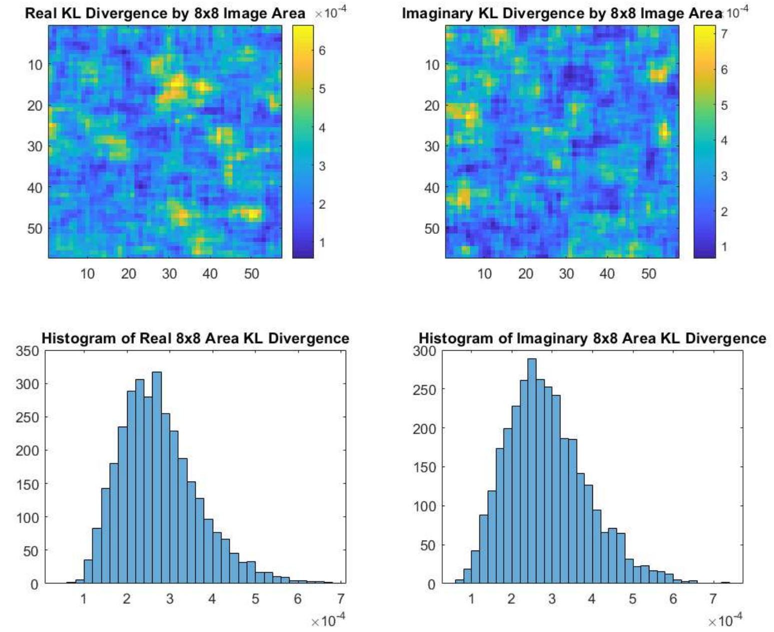

Figure 132: KL Divergence over 8x8 Image Area for Method 2 Data - Plant D, Light Wind

SIMILARITY METRICS FOR SIMULATION OF MEASURED DATA – PLANT D, LIGHT WIND

Correlation Matrix Similarity to Original Data

Table 29: Correlation Matrix Similarity for Baseline Full Covariance Data and Measured Data – Plant D, Light Wind

Baseline Full Covariance Data	Method 1 Data	Method 2 Data
0.2673	0.9745	0.9711

Multiscale Directional Correlation Similarity to Original Data

Table 30: MSE of Estimated Multiscale Directional Correlations from Measured Data – Plant D, Light Wind

MSE between Original Data and Generation Methods	Baseline Full Covariance Data	Method 1 Data	Method 2 Data
RH1	4.17%	4.88%	4.91%
RV1	5.44%	4.95%	5.16%
RD1	4.34%	7.91%	7.91%
RH2	4.10%	26.72%	5.76%
RV2	5.33%	17.27%	5.16%
RD2	4.30%	10.71%	10.25%
RH3	2.88%	64.37%	5.28%
RV3	5.16%	27.35%	6.57%
RD3	5.29%	15.58%	9.16%

SIMULATION OF MEASURED DATA – PLANT D, MEDIUM WIND

Estimated Multiscale Directional Correlation Maps

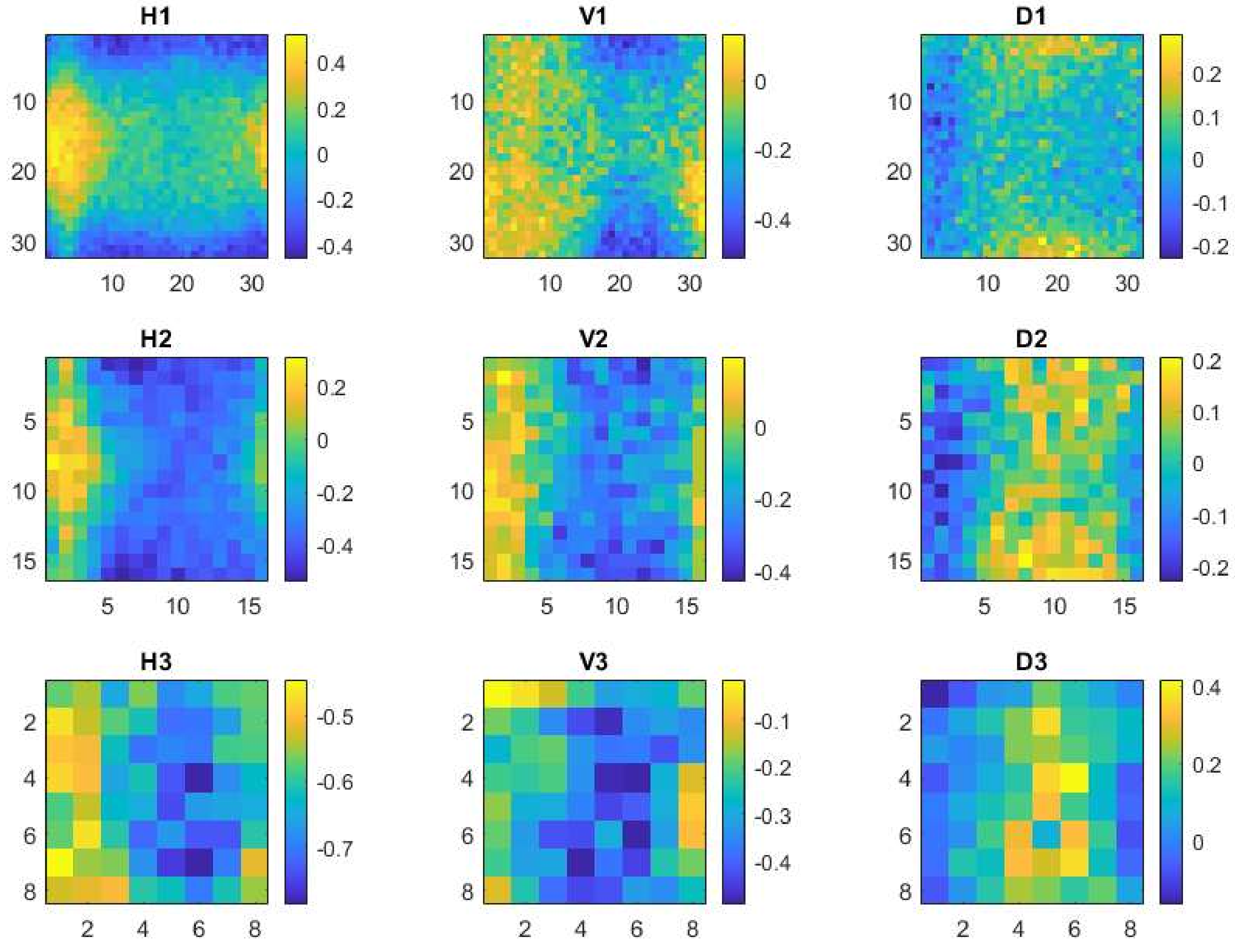

Figure 133: Estimated Multiscale Correlations of Measured Data - Plant D, Medium Wind

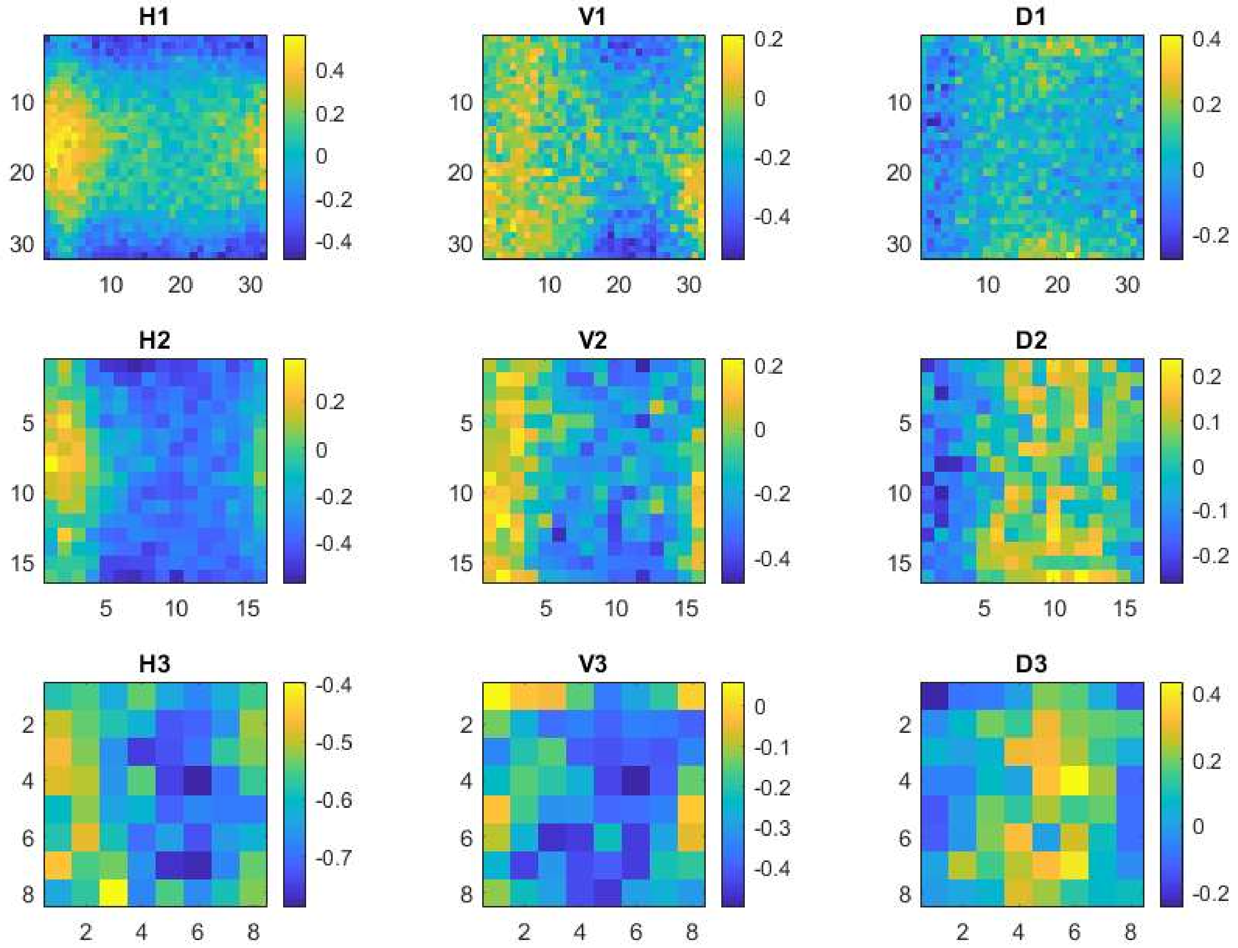

Figure 134: Estimated Multiscale Correlations of Baseline Full Covariance Data - Plant D, Medium Wind

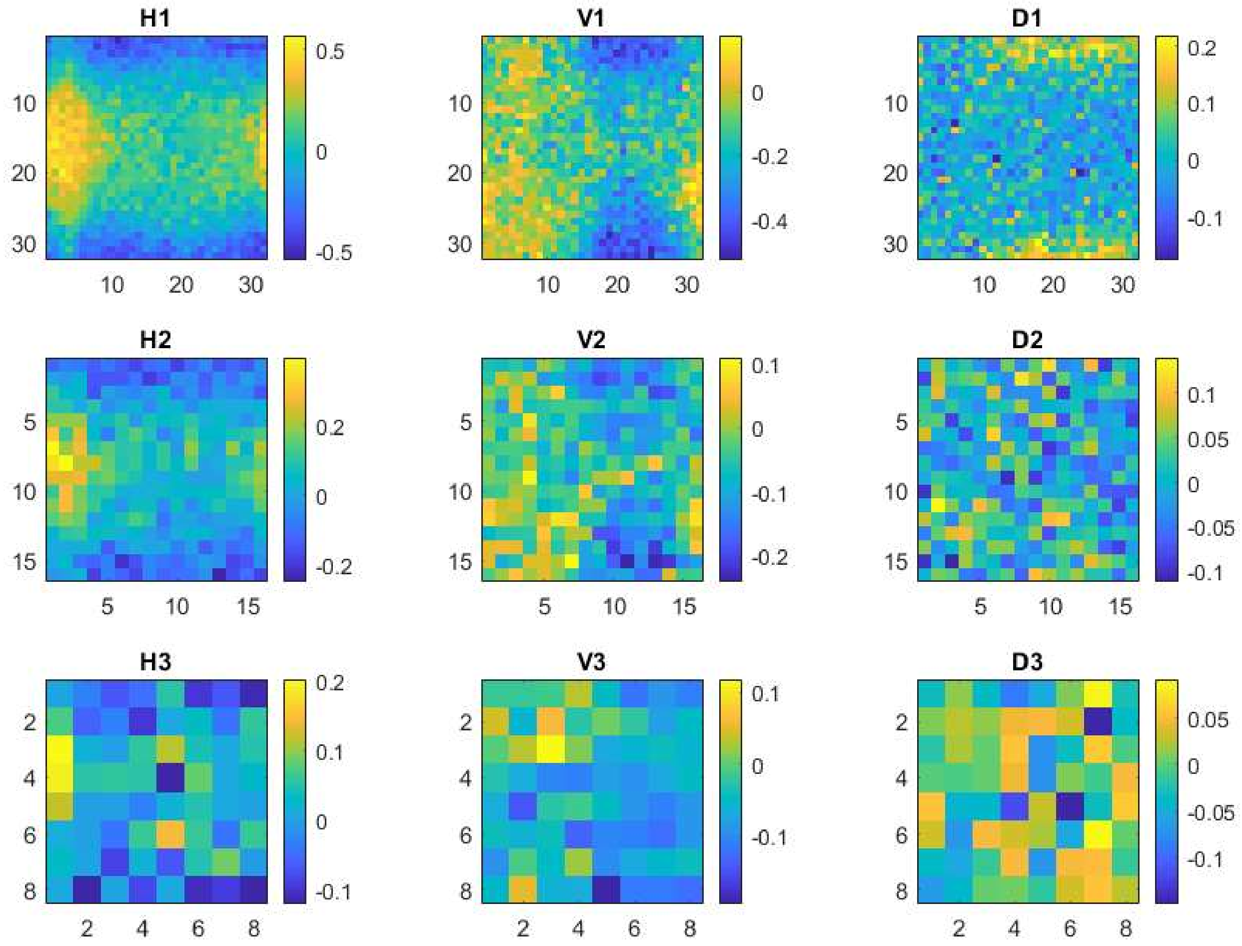

Figure 135: Estimated Multiscale Correlations of Method 1 Data - Plant D, Medium Wind

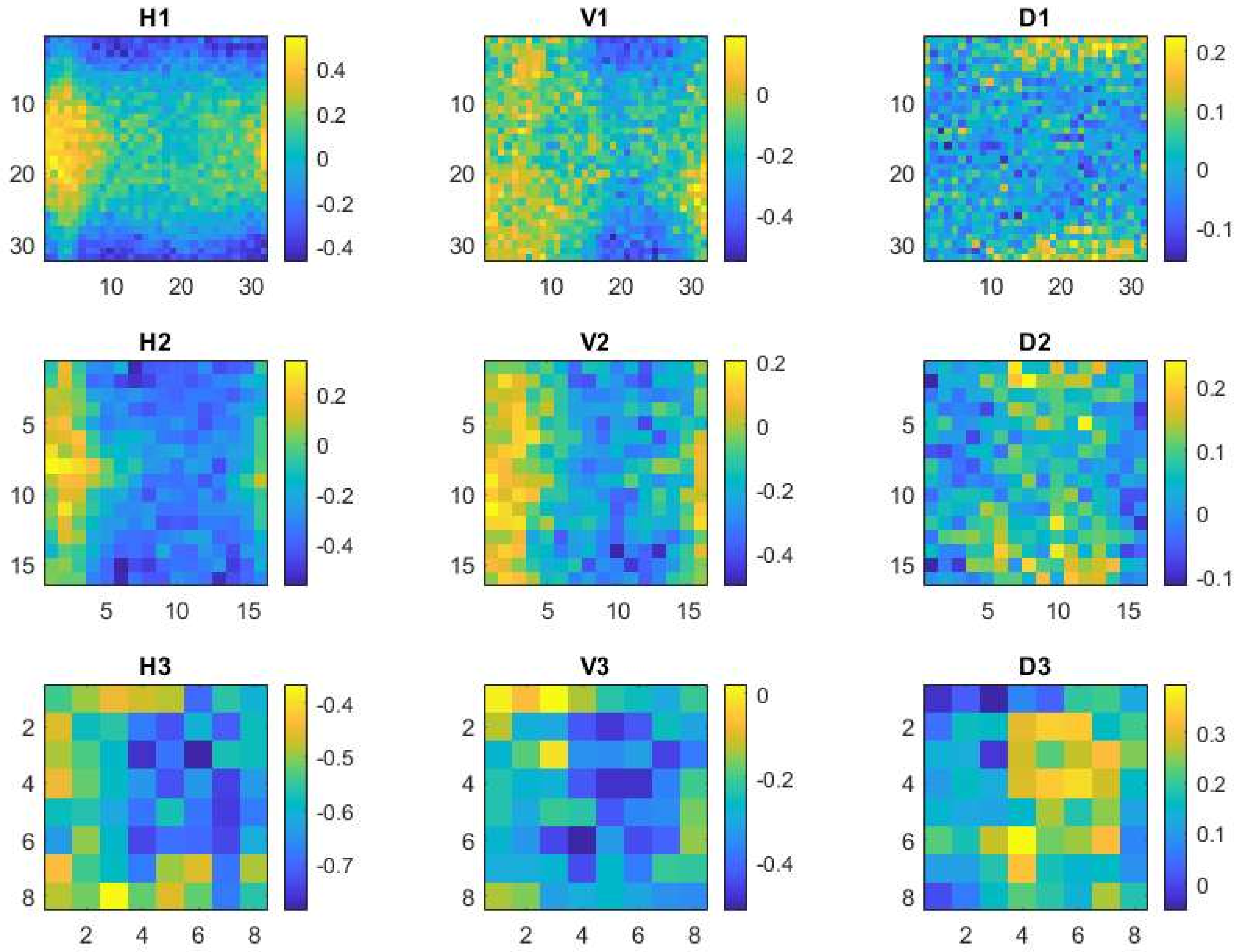

Figure 136: Estimated Multiscale Correlations of Method 2 Data - Plant D, Medium Wind

KL Divergence by Pixel and Image Area

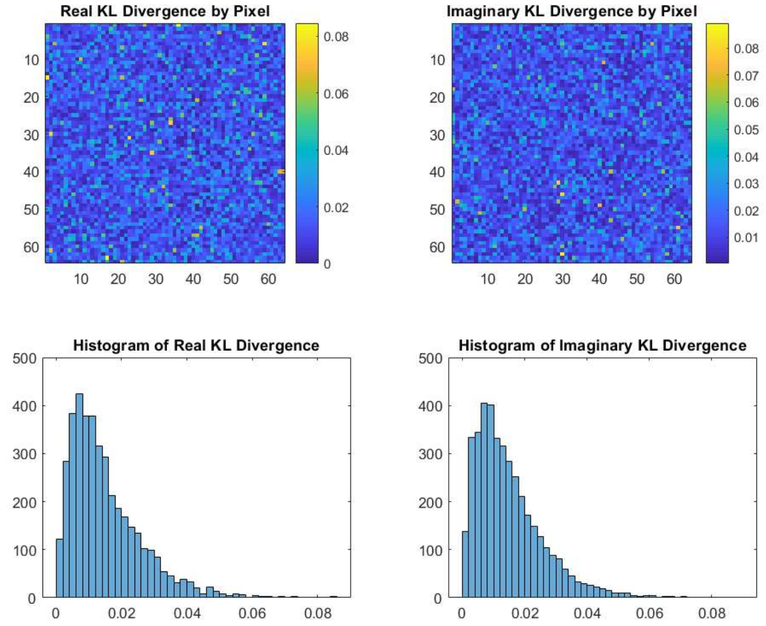

Figure 137: KL Divergence per Pixel for Full Covariance Baseline Data - Plant D, Medium Wind

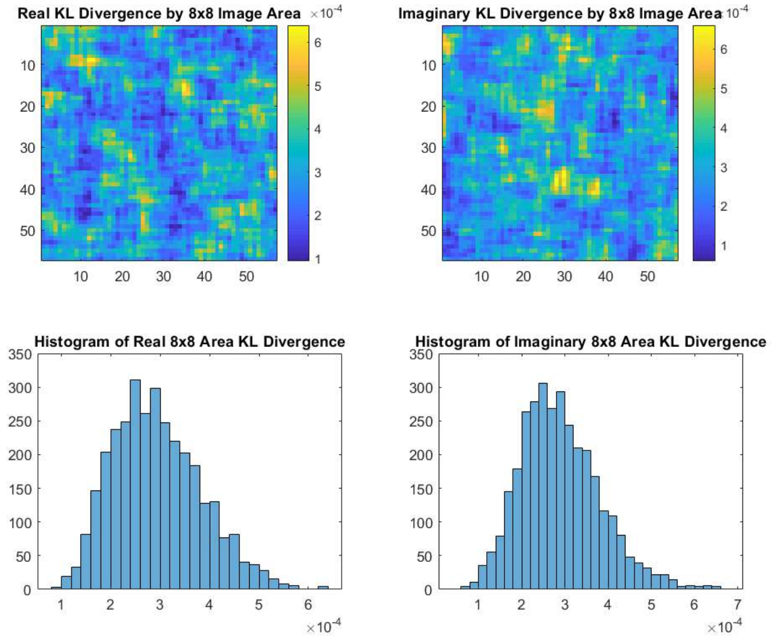

Figure 138: KL Divergence over 8x8 Image Area for Full Covariance Baseline Data - Plant D, Medium Wind

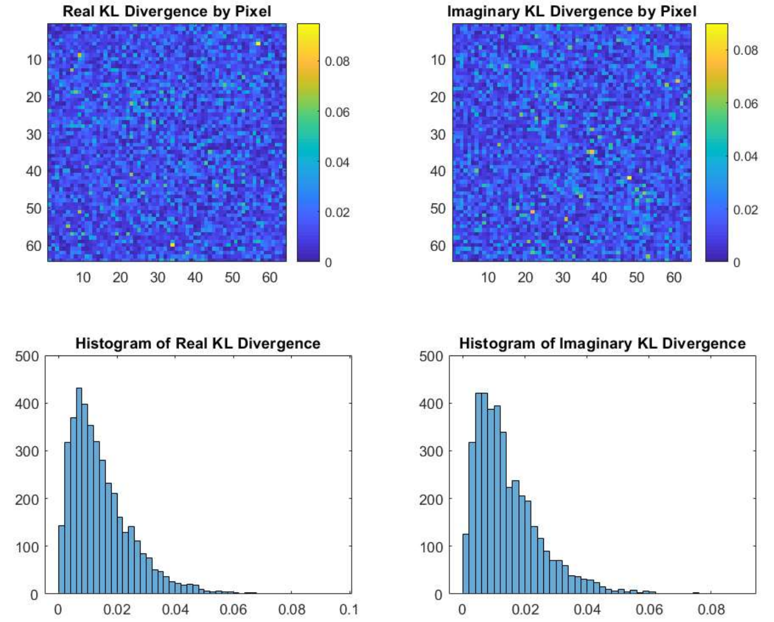

Figure 139: KL Divergence per Pixel for Data Generation Method 1 - Plant D, Medium Wind

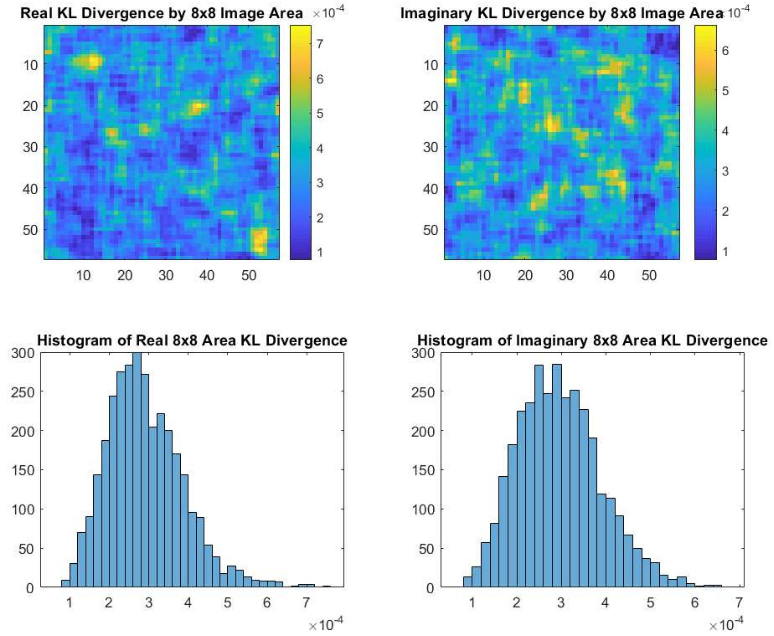

Figure 140: KL Divergence over 8x8 Image Area for Data Generation Method 1 - Plant D, Medium Wind

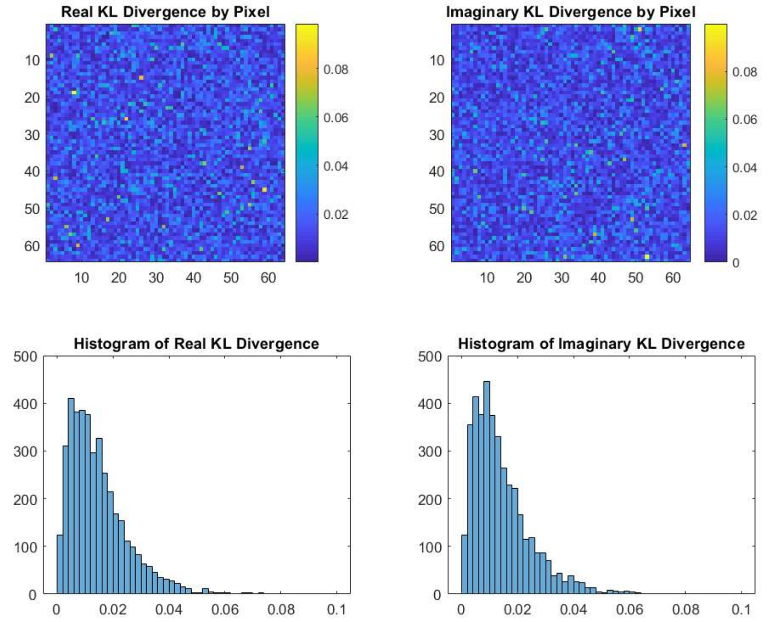

Figure 141: KL Divergence per Pixel for Data Generation Method 2 - Plant D, Medium Wind

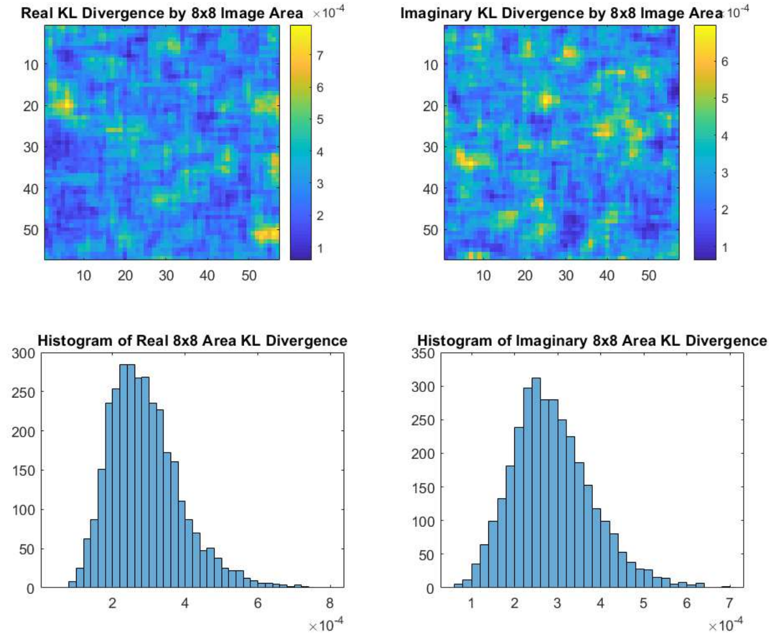

Figure 142: KL Divergence over 8x8 Image Area for Data Generation Method 2 - Plant D, Medium Wind

SIMILARITY METRICS FOR SIMULATED MEASURED DATA – PLANT D, MEDIUM WIND

Correlation Matrix Similarity to Original Data

Table 31: Correlation Matrix Similarity for Baseline Full Covariance Data and Measured Data – Plant D, Medium Wind

Baseline Full Covariance Data	Method 1 Data	Method 2 Data
0.2652	0.9744	.9719

Multiscale Directional Correlation Similarity to Original Data

Table 32: MSE of Estimated Multiscale Directional Correlations from Measured Data – Plant D, Medium Wind

MSE Between Original Data and Generation Methods	Baseline Full Covariance Data	Method 1 Data	Method 2 Data
RH1	4.35%	4.88%	4.86%
RV1	5.34%	4.86%	4.85%
RD1	4.58%	7.97%	7.98%
RH2	3.99%	29.19%	5.74%
RV2	5.31%	14.76%	5.35%
RD2	4.33%	11.57%	10.23%
RH3	3.73%	64.53%	8.63%
RV3	5.60%	29.12%	5.96%
RD3	5.89%	17.68%	10.3%

SIMULATED MEASURED DATA – PLANT E, LIGHT WIND

Estimated Multiscale Directional Correlation Maps

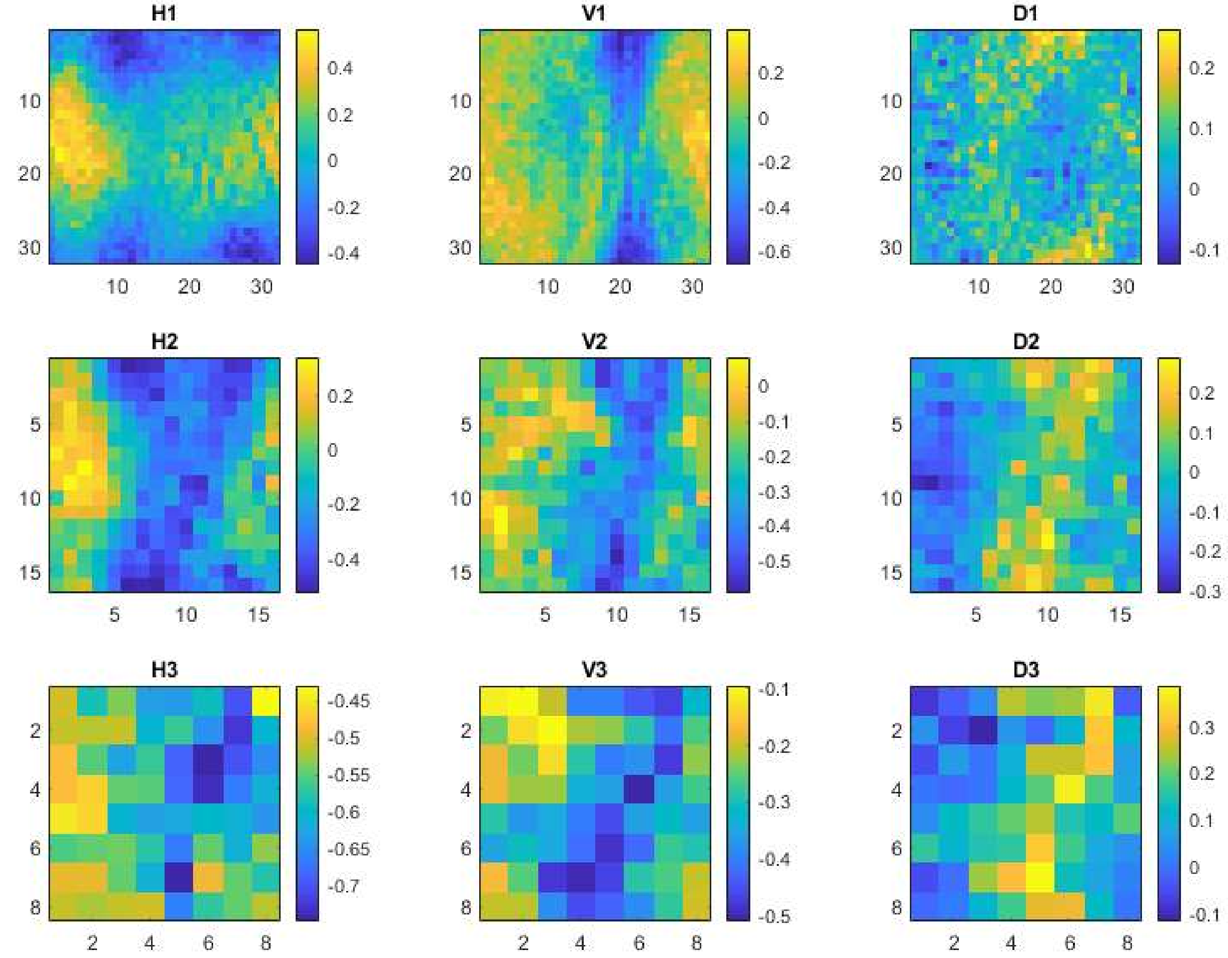

Figure 143: Estimated Multiscale Correlations of Measured Data - Plant E, Light Wind

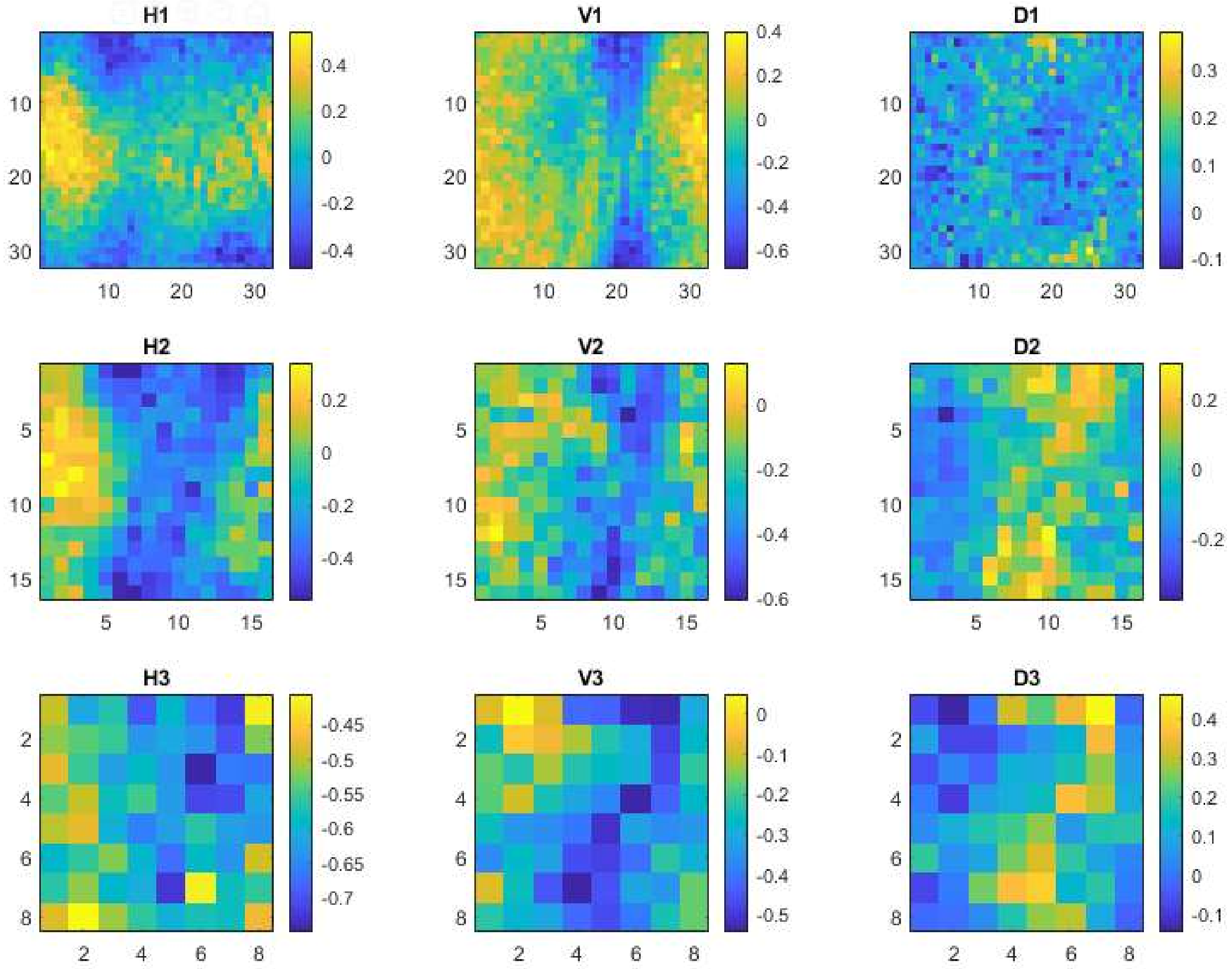

Figure 144: Estimated Multiscale Correlations of Baseline Full Covariance Data - Plant E, Light Wind

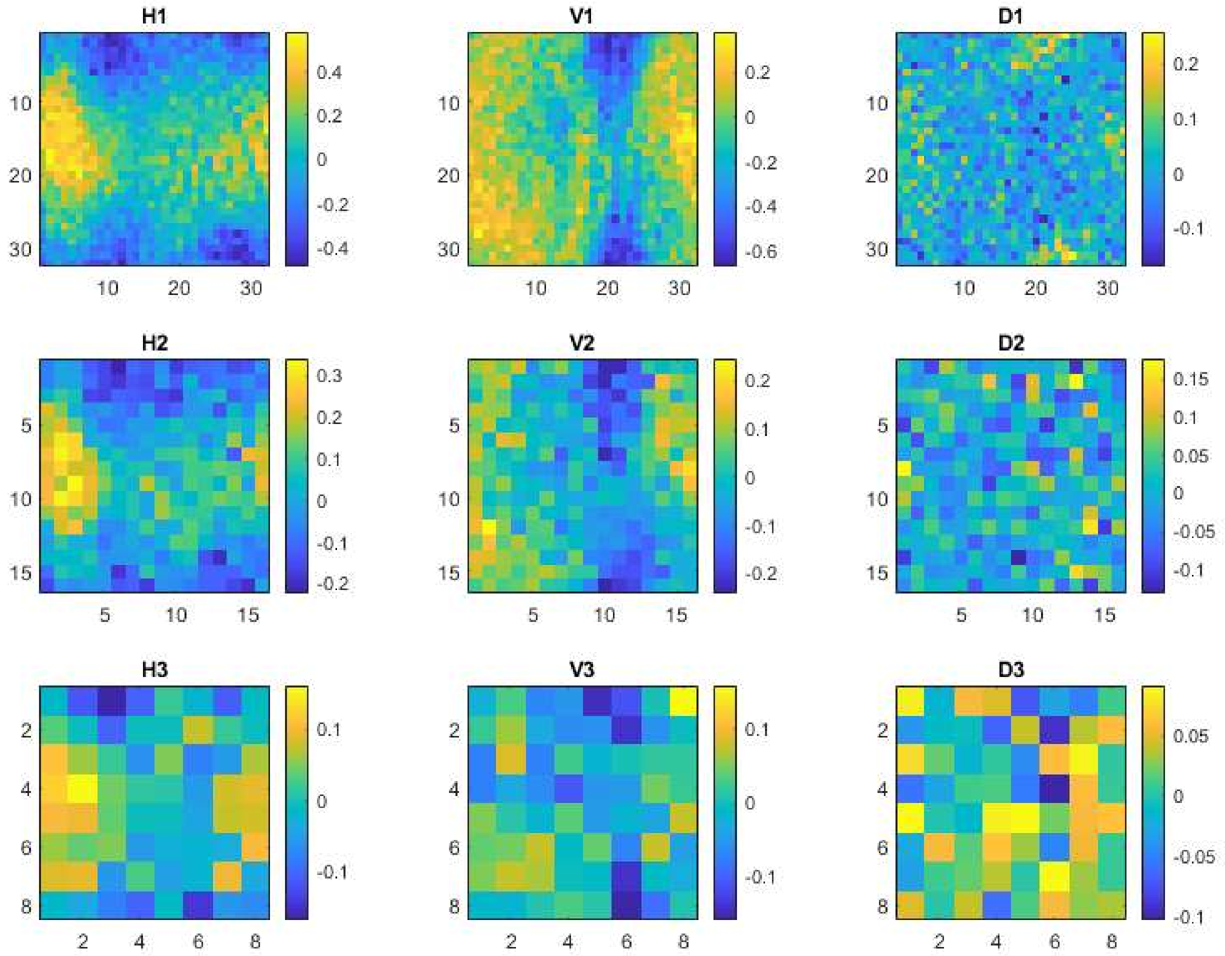
H1 V1 D1

H2 V2 D2

H3 V3 D3

Figure 145: Estimated Multiscale Correlations of Method 1 Data - Plant E, Light Wind

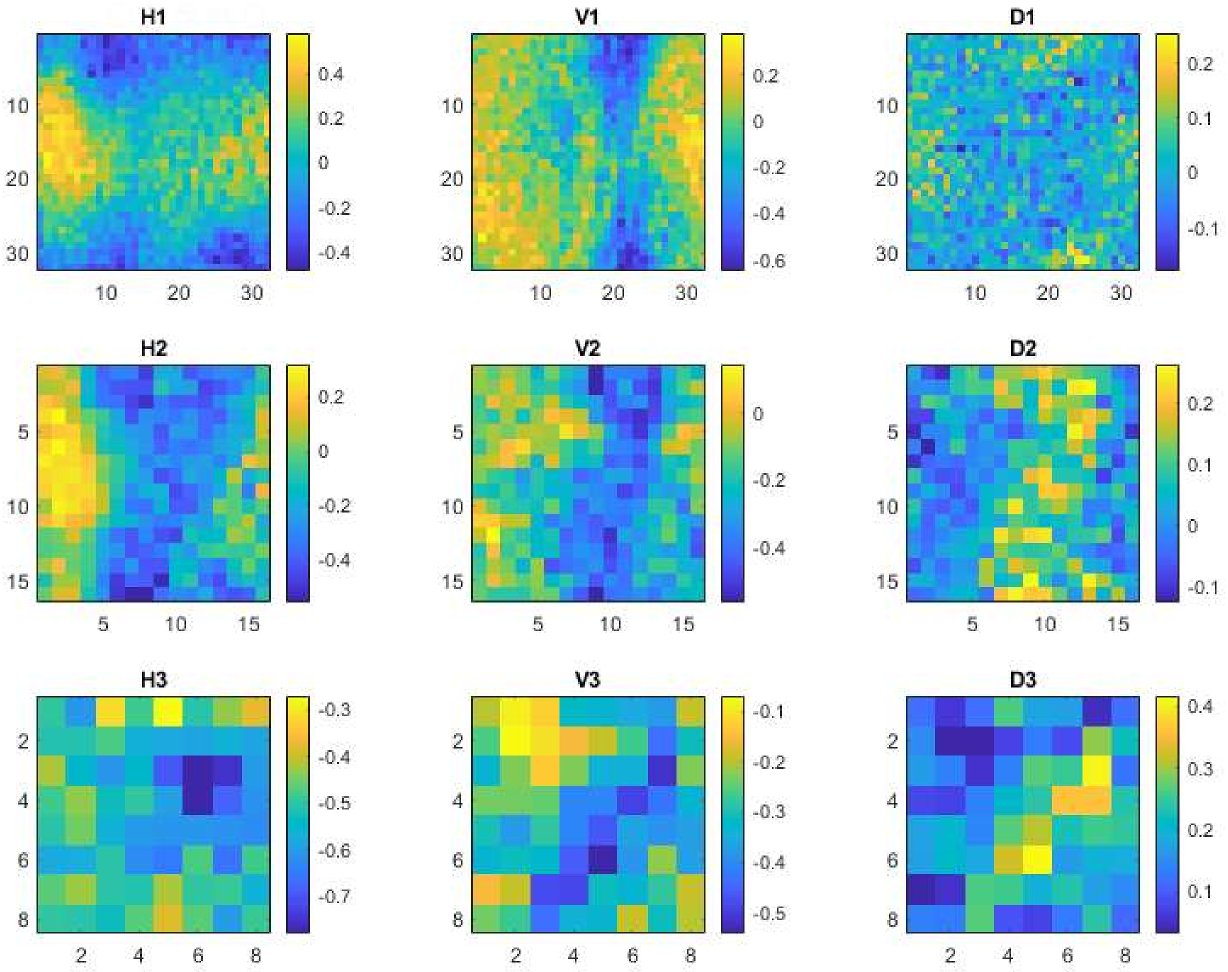

Figure 146: Estimated Multiscale Correlations of Method 2 Data - Plant E, Light Wind

KL Divergence by Pixel and Image Area

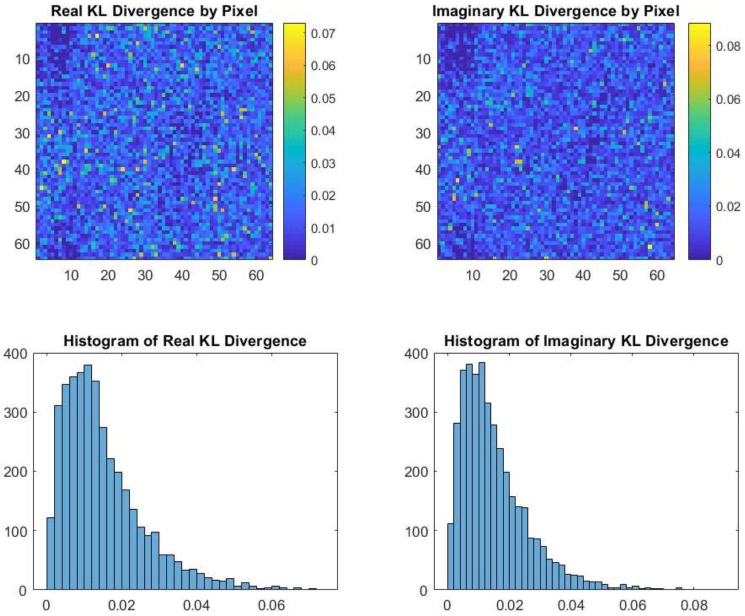

Figure 147: KL Divergence per Pixel for Baseline Full Covariance Data - Plant E, Light Wind

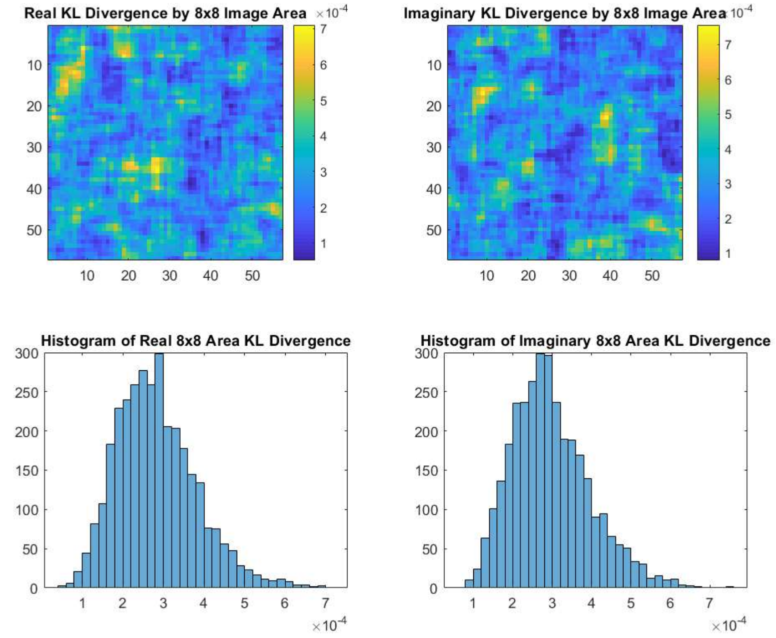

Figure 148: KL Divergence over 8x8 Image Area for Baseline Full Covariance Data - Plant E, Light Wind

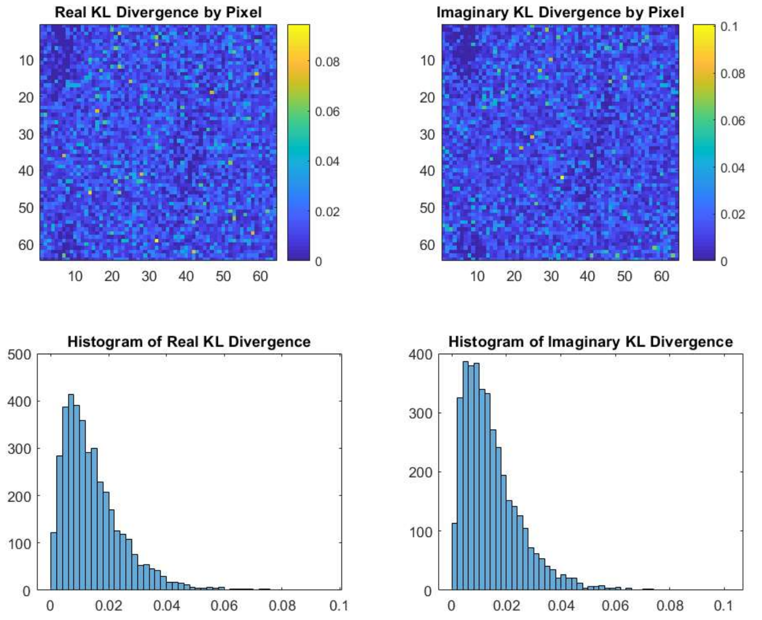

Figure 149: KL Divergence per Pixel for Method 1 Data - Plant E, Light Wind

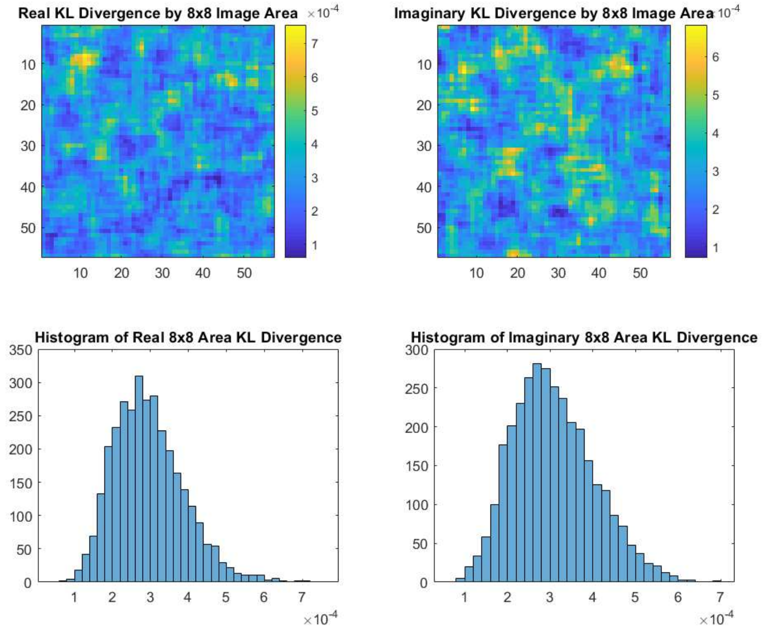

Figure 150: KL Divergence over 8x8 Image Area for Method 1 Data - Plant E, Light Wind

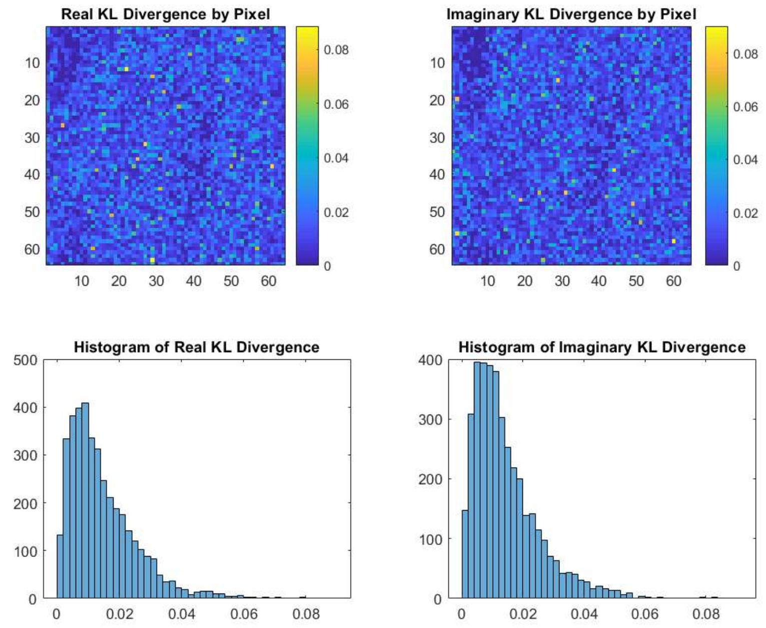

Figure 151: KL Divergence per Pixel for Method 2 Data - Plant E, Light Wind

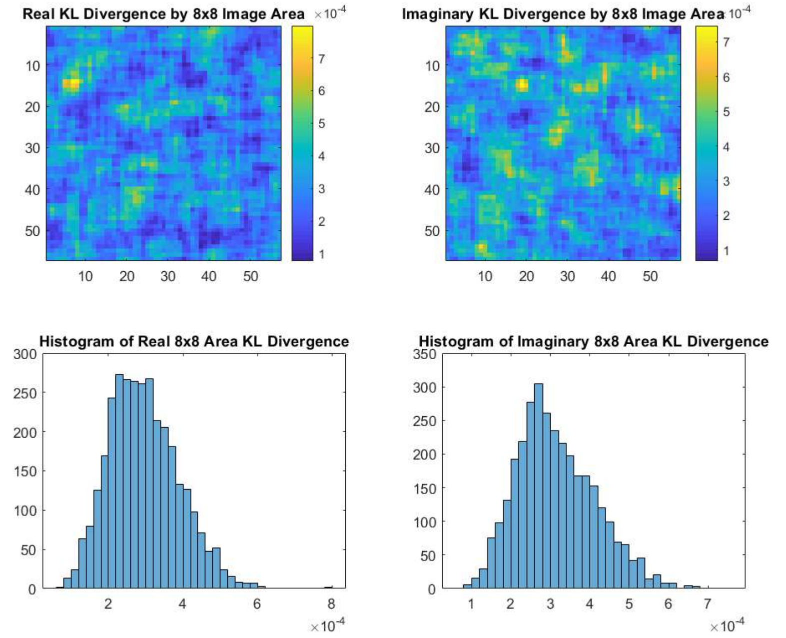

Figure 152: KL Divergence over 8x8 Image Area for Method 2 Data - Plant E, Light Wind

SIMILARITY METRICS FOR SIMULATED MEASURED DATA – PLANT E, LIGHT WIND

Correlation Matrix Similarity to Original Data

Table 33: Correlation Matrix Similarity for Baseline Full Covariance Data and Measured Data – Plant E, Light Wind

Baseline Full Covariance Data	Method 1 Data	Method 2 Data
0.25	0.9761	0.9705

Multiscale Directional Correlation Similarity to Original Data

Table 34: MSE of Estimated Multiscale Directional Correlations from Measured Data – Plant E, Light Wind

MSE Between Original Data and Generation Methods	Baseline Full Covariance Data	Method 1 Data	Method 2 Data
RH1	4.62%	5.15%	5.04%
RV1	4.86%	4.93%	5.49%
RD1	4.12%	9.07%	9.17%
RH2	4.13%	25.03%	6.16%
RV2	5.69%	26.16%	5.05%
RD2	4.10%	13.25%	11.28%
RH3	3.57%	58.96%	9.58%
RV3	5.86%	32.54%	6.27%
RD3	5.60%	17.23%	11.14%

SIMULATION OF MEASURED DATA – PLANT E, MEDIUM WIND

Estimated Multiscale Directional Correlation Maps

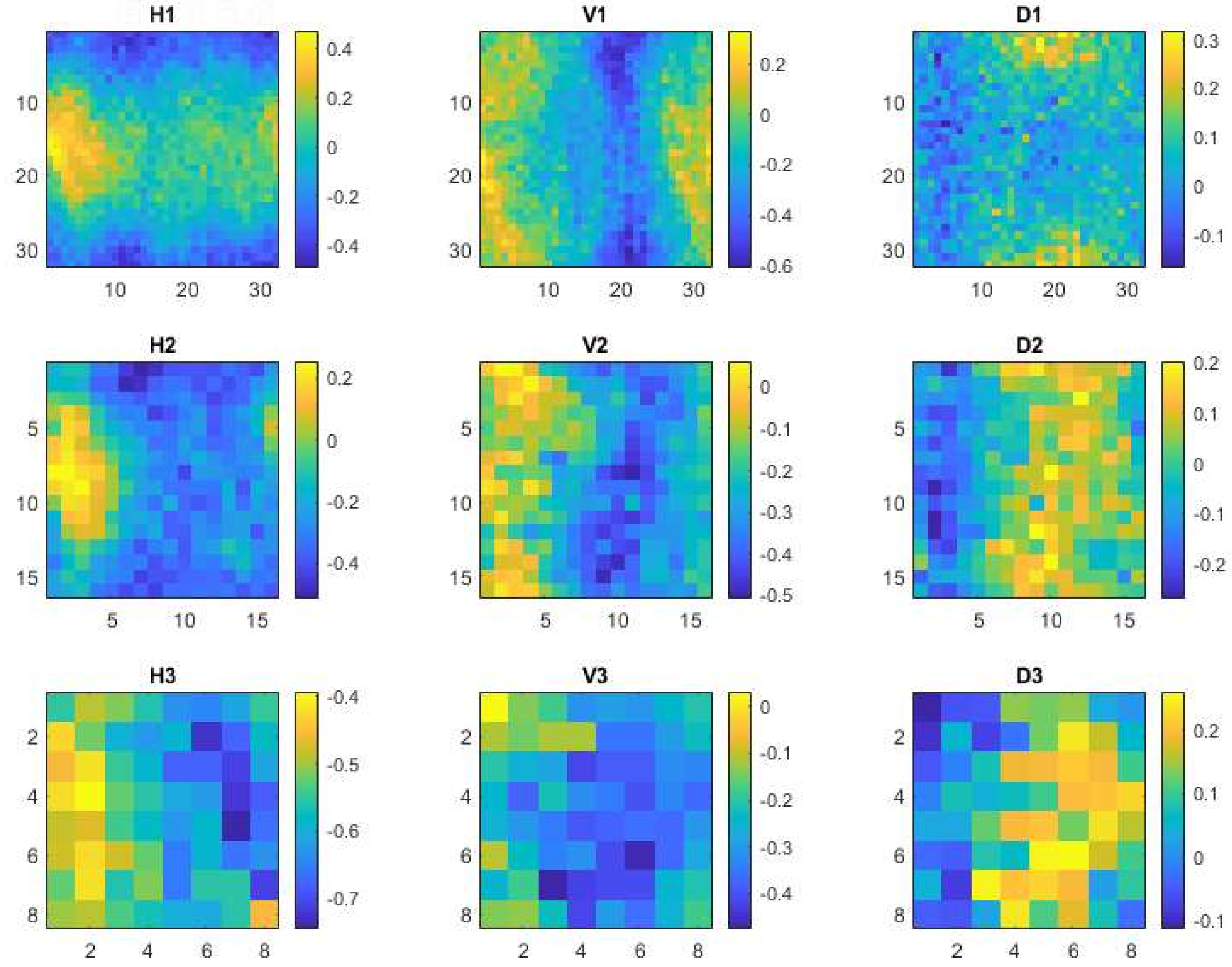

Figure 153: Estimated Multiscale Correlations of Measured Data - Plant E, Medium Wind

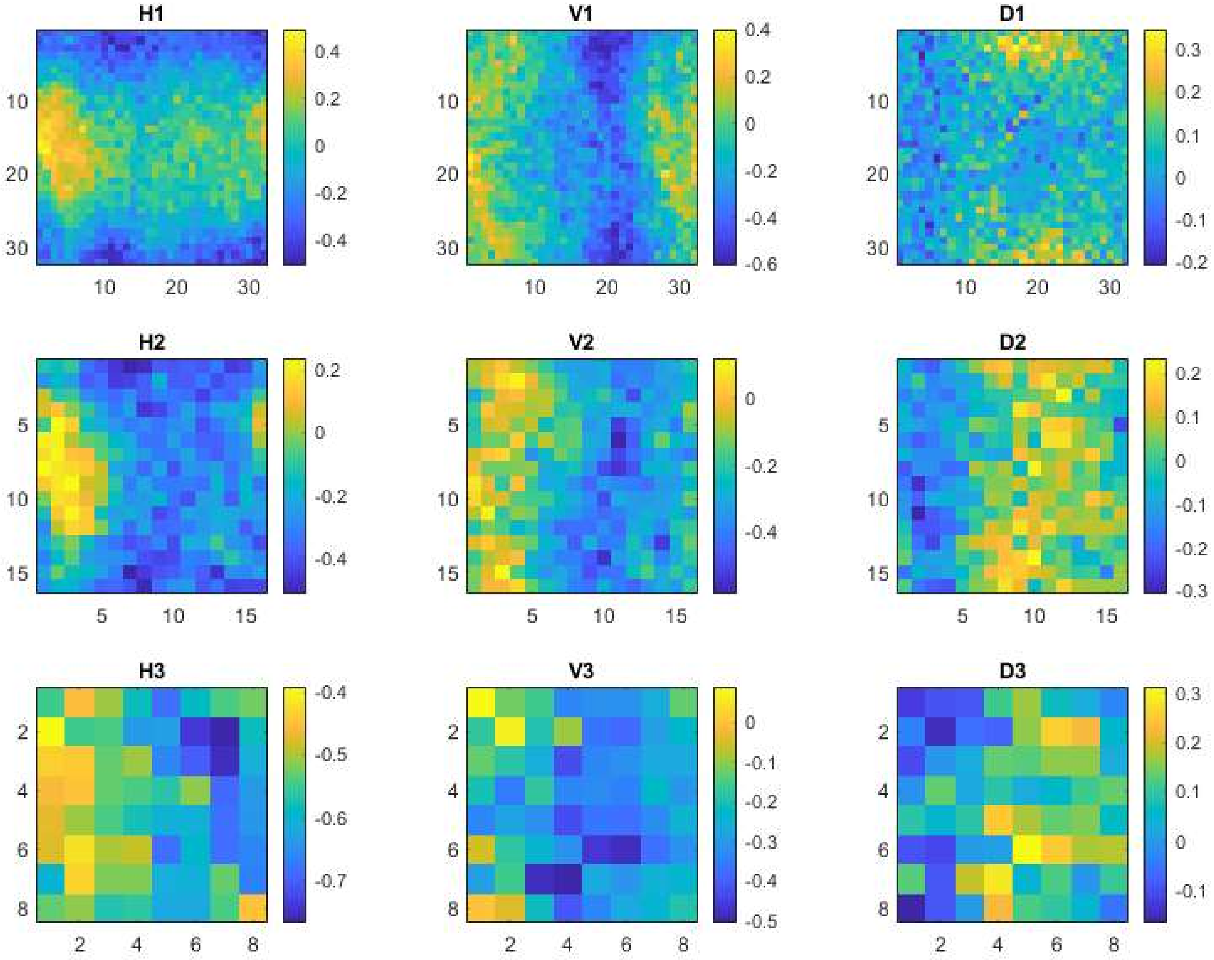

Figure 154: Estimated Multiscale Correlations of Baseline Full Covariance Data - Plant E, Medium Wind

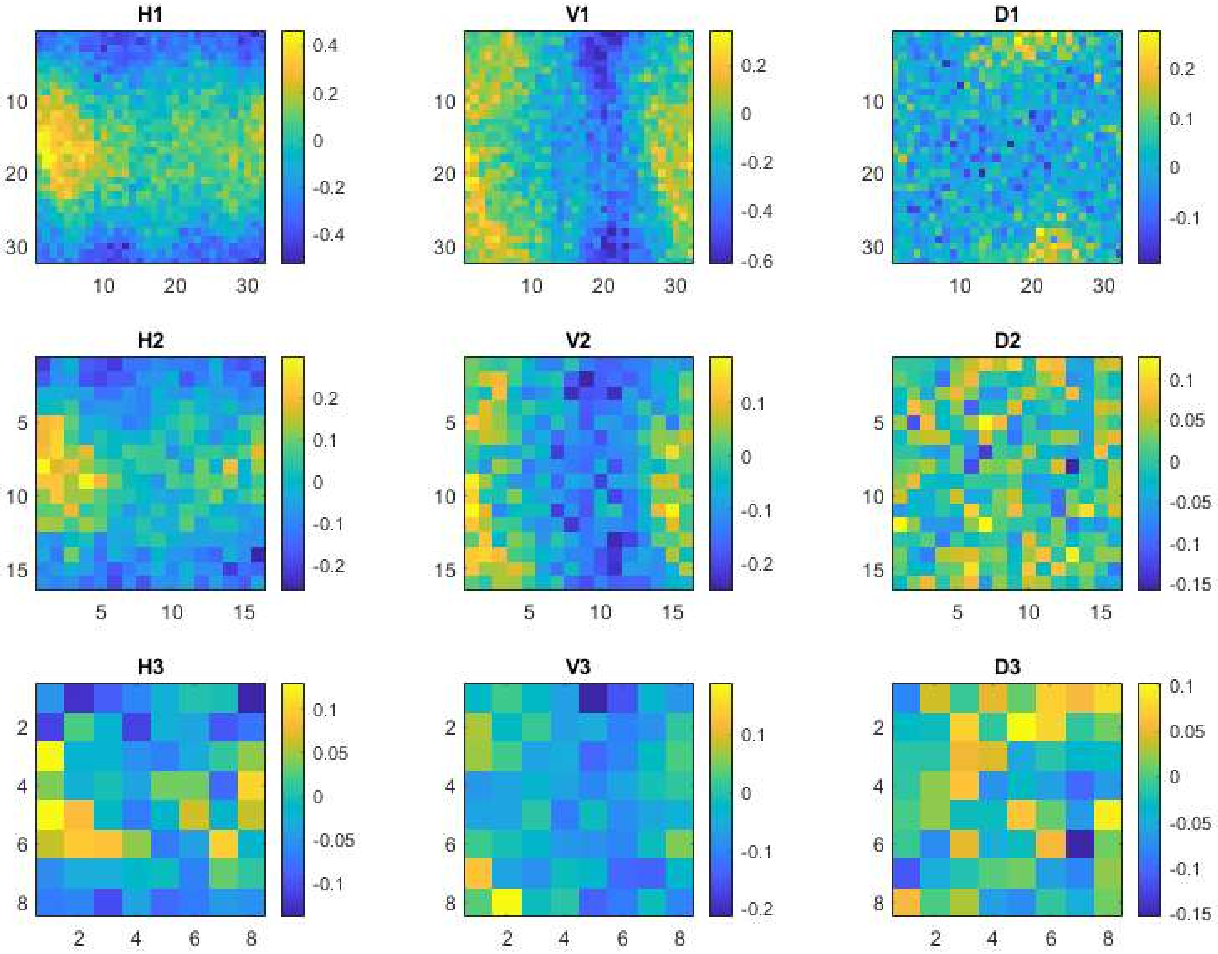

Figure 155: Estimated Multiscale Correlations of Method 1 Data - Plant E, Medium Wind

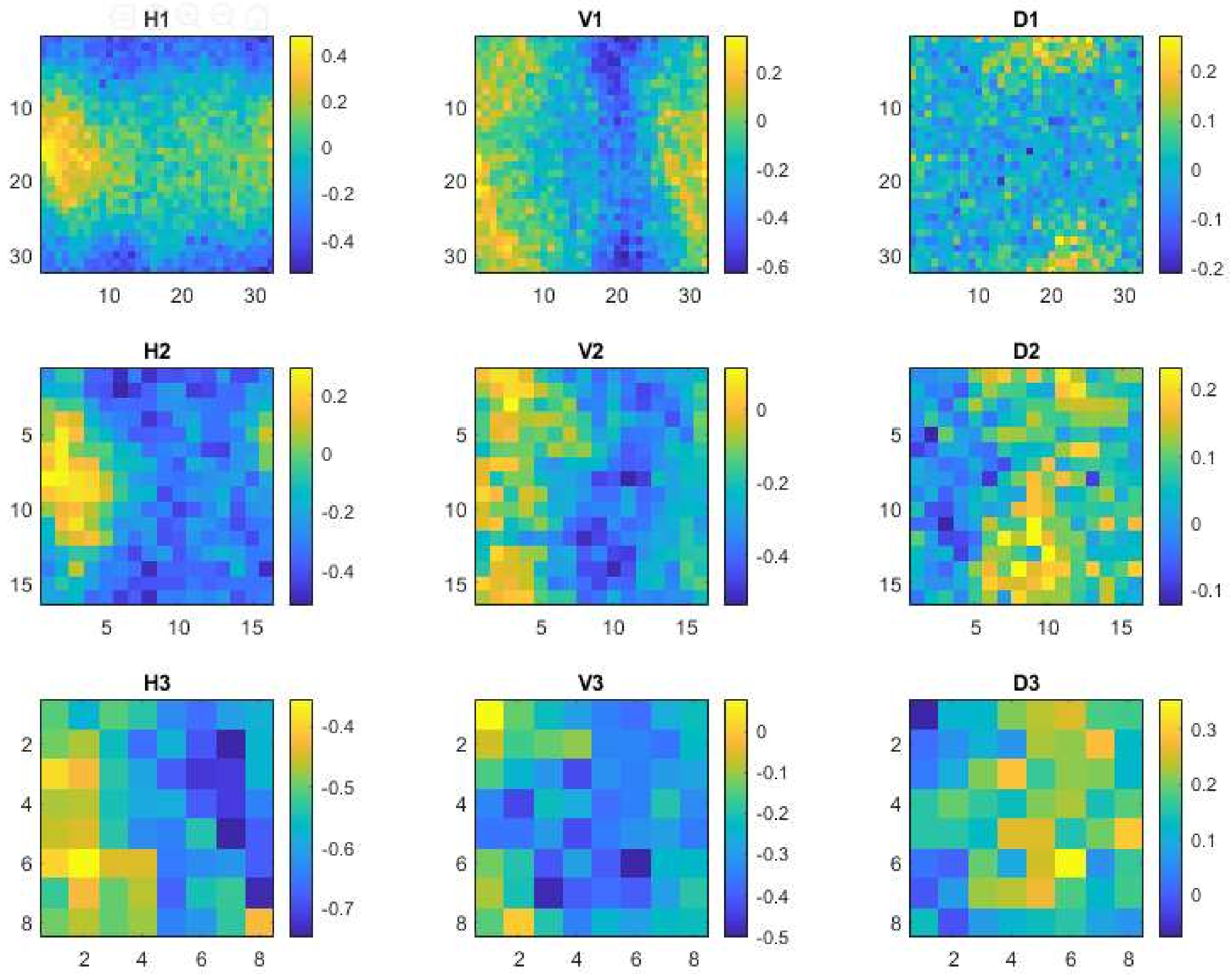

Figure 156: Estimated Multiscale Correlations of Method 2 Data - Plant E, Medium Wind

KL Divergence by Pixel and Image Area

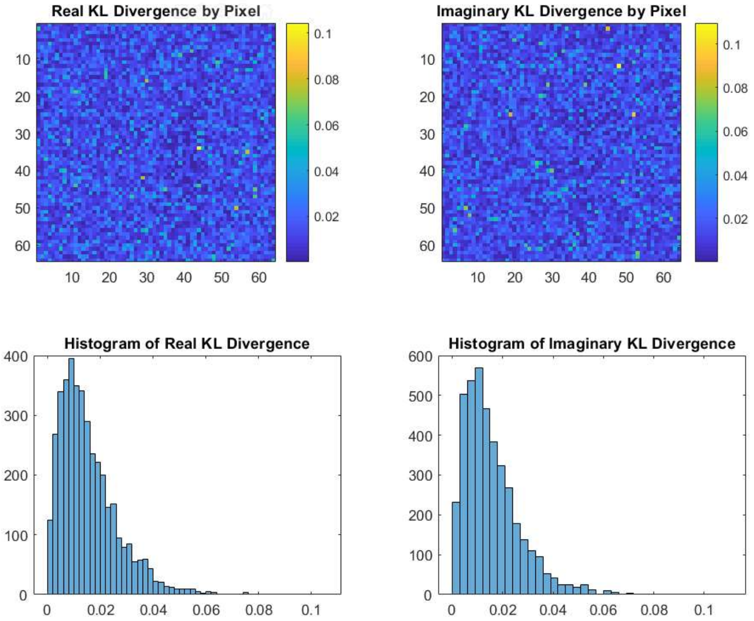

Figure 157: KL Divergence per Pixel for Baseline Full Covariance Data - Plant E, Medium Wind

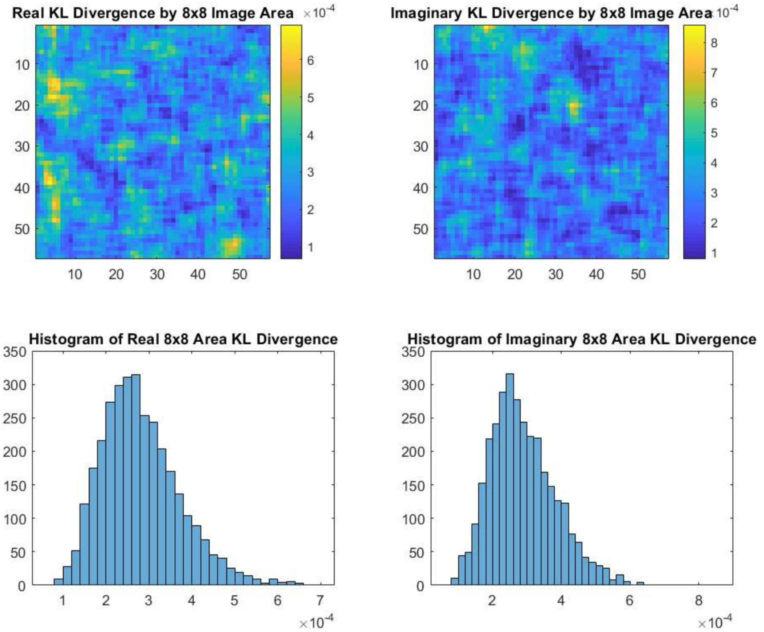

Figure 158: KL Divergence over 8x8 Image Area for Baseline Full Covariance Data - Plant E, Medium Wind

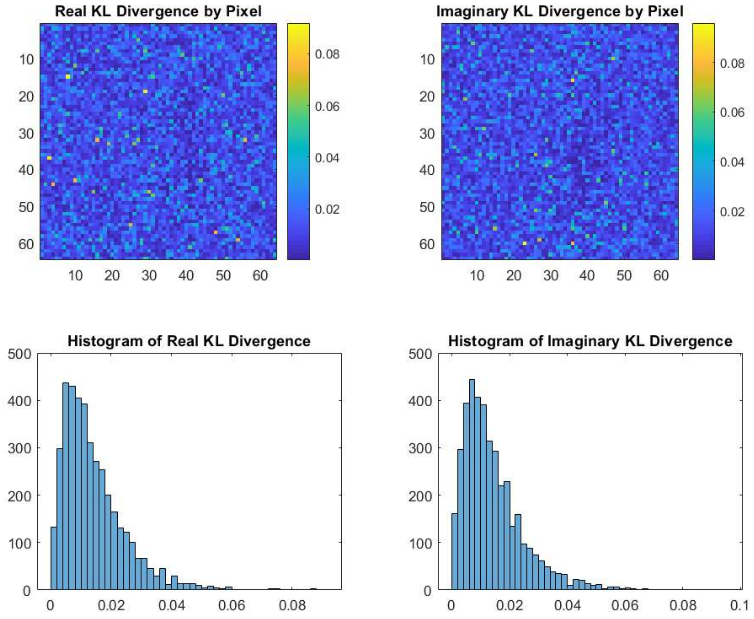

Figure 159: KL Divergence per Pixel for Method 1 Data - Plant E, Medium Wind

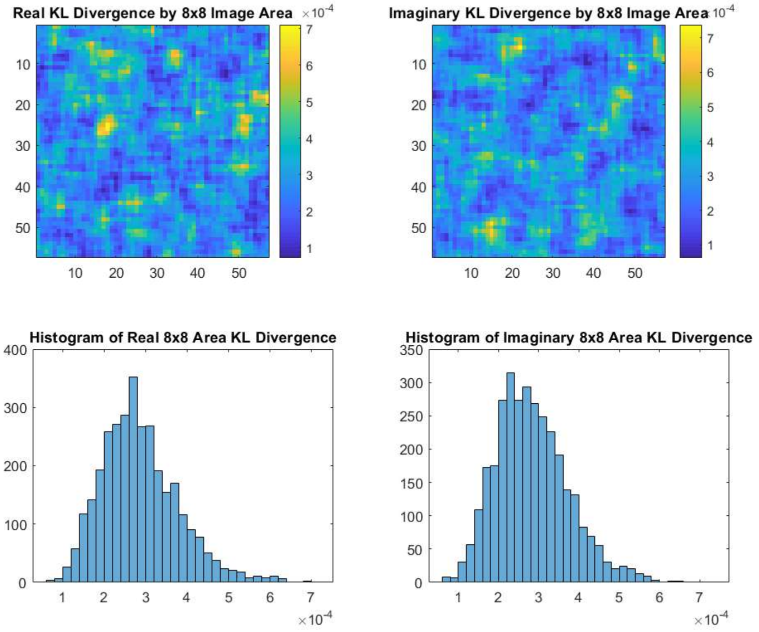

Figure 160: KL Divergence over 8x8 Image Area for Method 1 Data - Plant E, Medium Wind

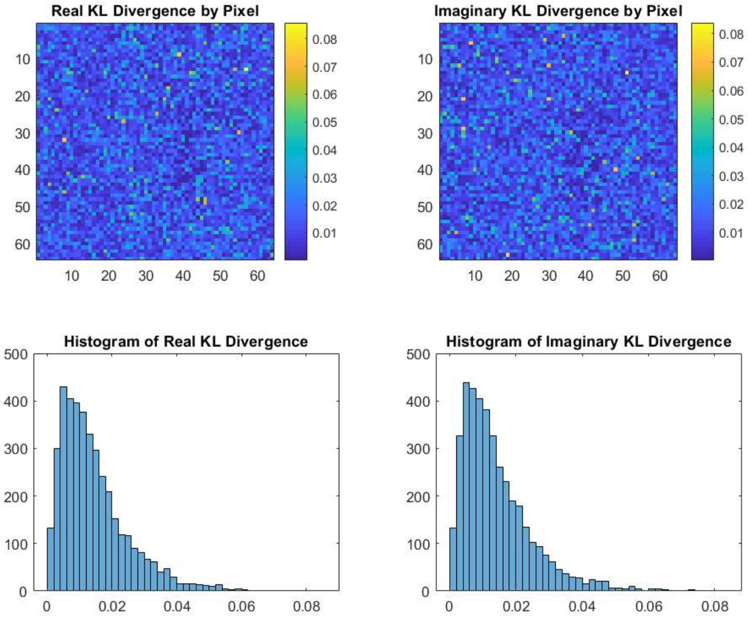

Figure 161: KL Divergence per Pixel for Method 2 Data - Plant E, Medium Wind

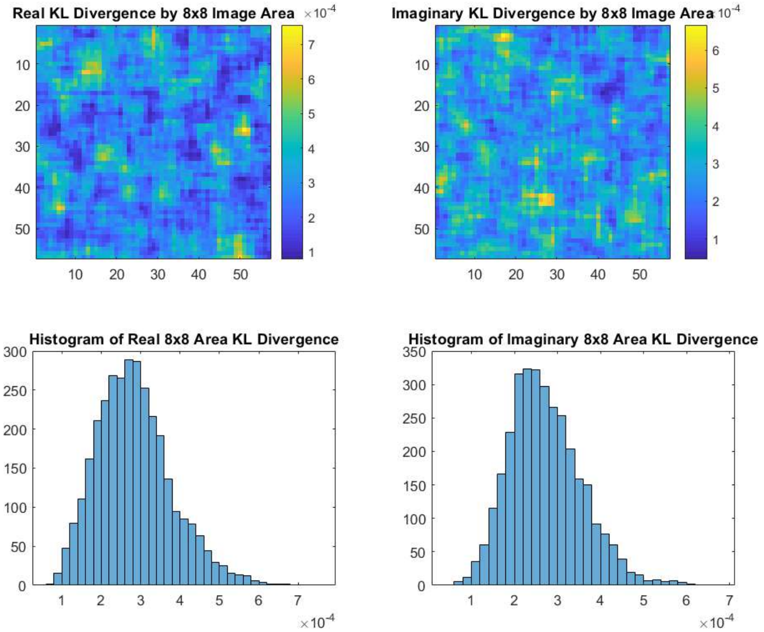

Figure 162: KL Divergence over 8x8 Image Area for Method 2 Data - Plant E, Medium Wind

SIMILARITY METRICS FOR SIMULATED MEASURED DATA – PLANT E, MEDIUM WIND

Correlation Matrix Similarity

Table 35: Correlation Matrix Similarity for Baseline Full Covariance Data and Measured Data – Plant E, Medium Wind

Baseline Full Covariance Data	Method 1 Data	Method 2 Data
0.2651	0.9738	0.9704

Multiscale Directional Correlation Similarity

Table 36: MSE of Estimated Multiscale Directional Correlations from Measured Data – Plant E, Medium Wind

MSE Between Original Data and Generation Methods	Baseline Full Covariance Data	Method 1 Data	Method 2 Data
RH1	4.40%	4.93%	4.82%
RV1	5.25%	4.93%	4.95%
RD1	4.37%	8.07%	7.98%
RH2	4.31%	24.65%	5.18%
RV2	5.51%	21.11%	5.06%
RD2	4.52%	10.91%	9.70%
RH3	3.77%	56.89%	4.67%
RV3	4.97%	26.01%	4.69%
RD3	5.34%	14.10%	10.06%